D-state Rydberg electrons interacting with ultracold atoms

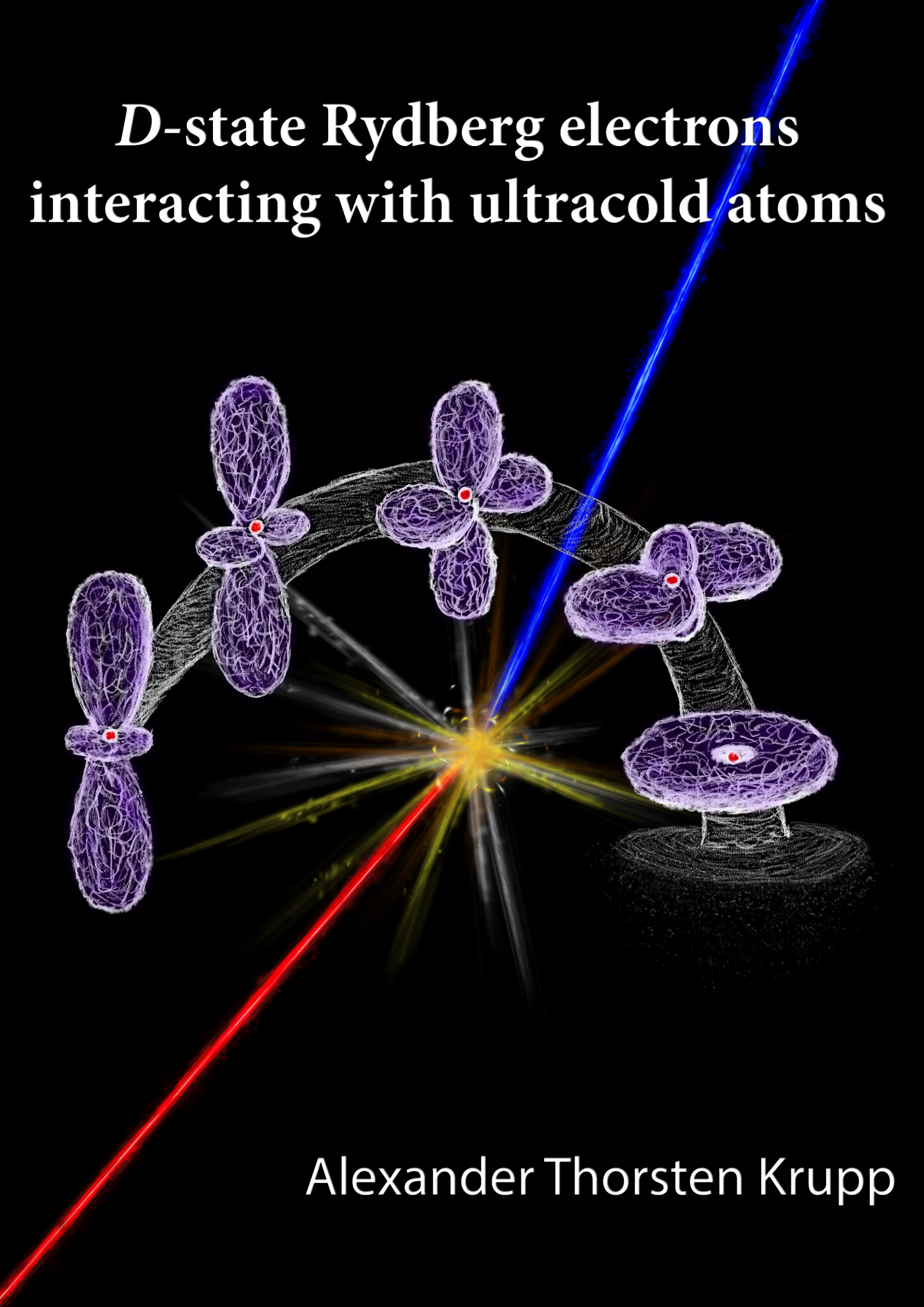

Alexander Thorsten Krupp

D-state Rydberg electrons interacting with ultracold atoms

Von der Fakultät Mathematik und Physik der Universität Stuttgart
zur Erlangung der Würde eines Doktors der
Naturwissenschaften (Dr. rer. nat.) genehmigte Abhandlung

vorgelegt von

Alexander Thorsten Krupp

aus Nürnberg

Hauptberichter:	Prof. Dr. Tilman Pfau
Mitberichter:	Prof. Dr. Bernhard Keimer
Prüfungsvorsitzender:	Prof. Dr. Günter Wunner
Tag der mündlichen Prüfung:	02.10.2014

5. Physikalisches Institut
Universität Stuttgart
2014

Hiermit erkläre ich, dass ich diese Arbeit selbständig verfasst und keine anderen als die von mir angegebenen Quellen und Hilfsmittel verwendet habe.

I hereby declare that this submission is my own work and that, to the best of my knowledge and belief, it contains no material written by another person, except where due acknowledgment has been made in the text.

Alexander Krupp

Zusammenfassung

Diese Arbeit ist in dem Themengebiet der Atomphysik angesiedelt und verbindet die Teilgebiete der ultrakalten Gase und der Rydberg Atomphysik miteinander, um neuartige Quantenzustände und -objekte zu untersuchen. Auf beide Teilgebiete wird im Folgenden genauer eingegangen, immer im Hinblick auf unsere Experimente und Ergebnisse. Letzere werden anschließend zusammenfassend präsentiert.

Die Definition von 'ultrakalt' wird im Allgemeinen für Temperaturen unter einem Millikelvin, einem tausendstel Kelvin, verwendet, wo quantenmechanische Phänomene an Bedeutung gewinnen. In diesem Temperaturregime zu arbeiten hat den Vorteil, dass sich die Atome während der typischen Dauer eines Experiments (im Mikrosekunden Bereich) in Ruhe befinden, wir sozusagen eine Momentaufnahme der Atome studieren können. Deswegen wird dieses Regime auch als 'frozen gas' − 'eingefrorenes Gas'-Regime bezeichnet. Somit kann das Verhalten der Atome und die Wechselwirkung zwischen den Atomen leichter untersucht und auch durch das Anlegen externer elektrischer oder magnetischer Felder kontrolliert werden. Wenn es gelingt, eine dichte Atomwolke weiter in den Bereich von hunderten von Nanokelvin abzukühlen, findet ein Phasenübergang statt, bei dem ein sogenanntes Bose-Einstein-Kondensat entsteht. Dieser einzigartige Materiezustand ist dadurch charakterisiert, dass alle Atome sich im gleichen quantenmechanischen Grundzustand befinden und zusammen als eine einzelne Materiewelle beschrieben werden können. Hier wird sofort der Welle-Teilchen Dualismus deutlich, der unter anderem auf A. Einstein zurückgeht [1]. Das erste Bose-Einstein-Konsensat wurde erstmalig 1995 erzeugt (Nobel-Preis 2001 für E. Cornell, C. Wieman und W. Ketterle [2, 3]) und wird seitdem erfolgreich zur Erforschung einer Vielzahl grundlegender physikalischer Fragestellungen eingesetzt.

Der zweite wichtige Bestandteil dieser Arbeit ist die Anregung von Rydberg-Atomen. Dies sind Atome, bei denen mindestens ein Elektron in einen hochenergetischen Zustand nahe am Ionisationslimit angeregt wird. Dieses Elektron umkreist den ionischen Kern dann auf weit entfernten Bahnen und verhält sich somit ähnlich dem Elektron des Wasserstoffatoms, das als einziges Atom vollständig analytisch quantenmechanisch beschrieben werden kann. Der einzige Unterschied besteht darin, dass Rydberg-Atome anstatt eines einzelnen Protons im Kern viele Protonen, Neutronen und weitere Elektronen besitzen. Letztere sorgen dafür, dass es Abweichungen vom Wasserstoffmodell gibt, wenn sich das Rydberg-Elektron nahe dem Kern befindet, weshalb bei der Berechnung der effektiven Hauptquantenzahl der sogenannte Quantendefekt eingeführt wurde [4]. Das hochangeregte Elektron verleiht den Rydberg Zuständen ihre besonderen Eigenschaften. So sind sie sehr leicht durch elektrische Felder beeinflussbar und auch die Wechselwirkung zwischen zwei Rydberg-Atomen ist um viele Größenordnungen stärker als die Wechselwirkung zwischen zwei Grundzustandsatomen. Durch

diese starke Wechselwirkung ist es bei einer festen Laseranregungsfrequenz nur möglich zwei Rydberg-Atome in einem Mindestabstand, dem sogenannten Blockade-Radius, zu erzeugen. Dieser Blockade-Effekt spielt bei unseren Experimenten auch eine bedeutende Rolle, auf die später genauer eingegangen wird. Wichtig ist, dass durch die Wahl der Hauptquantenzahl n viele Eigenschaften der Rydberg-Atome kontrolliert werden können, wie zum Beispiel ihre Größe und Wechselwirkung. Ein limitierender Punkt ist die relativ kurze Lebensdauer von Rydberg-Atomen, die maximal nur wenige Millisekunden lang ist. Heutzutage spielen Rydberg-Atome in der Quanteninformation und -kommunikation eine große Rolle. Die Zielsetzung ist hier die Verarbeitung, die Speicherung und das Versenden von Informationen in Form von quantenmechanischen Zuständen, um schlussendlich einen Quantencomputer zu verwirklichen. Außerdem können Rydberg-Atome auch als hochempfindliche Sensoren dienen, wie vor kurzem mit der zerstörungsfreien Detektion von einzelnen Photonen gezeigt wurde (Nobel-Preis für S. Haroche 2012 [5]).

In dieser Arbeit verknüpfen wir nun diese beiden Teilgebiete der ultrakalten Gase und Rydberg-Atome miteinander, indem wir Rydberg-Anregungen im Bose-Einstein-Kondensat mit Dichten von $10^{14}\,\mathrm{cm}^{-3}$ bei hohen Hauptquantenzahlen $n > 100$ und in der thermischen Wolke bei Dichten um $10^{12}\,\mathrm{cm}^{-3}$ bei niedrigen $n = 40 - 50$ erzeugen. In unserem Experiment wird das Alkali Metall Rubidium ^{87}Rb verwendet.

Im ersten Teil der Arbeit widmen wir uns den Rydberg-Molekülen, die aus einen Rydberg-Atom und mindestens einem Grundzustandsatom bestehen. Deren Existenz wurde im Jahr 2000 von C. Greene und seinen Mitarbeitern prognostiziert. Der Bindungsmechanismus dieser langreichweitigen Moleküle basiert auf der niederenergetischen Streuung des Rydberg-Elektrons an den Grundzustandsatomen. Dabei werden die Grundzustandsatome im Potential der Elektronenwellenfunktion gefangen und können durch diese attraktive Wechselwirkung eine Bindung eingehen. Mit anderen Worten werden die Grundzustandsatome im elektrischen Feld des Elektrons polarisiert und dadurch an das Rydberg-Atom gebunden. Dieser Bindungsmechanismus ist einzigartig, denn er unterscheidet sich fundamental von der van-der-Waals und ionischen Bindung. Um das Bindungspotential zu beschreiben, kann E. Fermis Pseudopotentialansatz verwendet werden, welcher auf das Jahr 1934 zurückgeht. Dieses Potential ist proportional zur Aufenthaltswahrscheinlichkeit des Elektrons und der Elektron-Grundzustandsatom-Streulänge. Die Eigenschaften dieser Moleküle sind durch die des Rydberg-Elektrons gegeben, weswegen sie sich leicht durch elektrische Felder beeinflussen lassen.

Im Jahr 2009 wurden diese Moleküle das erste Mal durch einen Photoassoziationsprozess in einer ultrakalten thermischen Wolke aus Rubidiumatomen erfolgreich erzeugt und nachgewiesen [6]. Außerdem wurde gezeigt, dass die Moleküle kohärent generiert und dissoziiert werden können [7] und dass sie ein permanentes elektrisches Dipolmoment besitzen, obwohl es sich um zwei Atome gleichen Typs handelt, die sich zu einem Molekül verbinden [8]. Kürzlich wurden sogar Pentamere nachgewiesen, bestehend aus einem Rydberg-Atom und vier Grundzustandsatomen [9]. Außerdem besitzen sie einen Durchmesser von bis zu mehreren Mikrometern bei hohen n und gehören damit zu den größten bekannten Molekülen, vergleichbar mit der Größe von Bakterien oder großer Viren, die im Gegensatz dazu aus Billionen Atomen bestehen. Bei all diesen Experimenten wurden S-Zustands-Rydberg-Elektronen benutzt, die eine vollständig symmetrische Wellenfunktion besitzen.

In dieser Dissertation wird erstmalig über die Erzeugung diatomarer Moleküle, bestehend aus einen D-Zustands-Rydberg-Atom und einen Grundzustandsatom, berichtet. Diese Moleküle sind rotationssymmetrisch entlang der z-Achse (Magnetfeld- und Lichtfeldachse), aber weisen eine Abhängigkeit vom polaren Winkel Θ auf und können deshalb nur an bestimmten Stellen im Rydberg-Elektronen-Orbital erschaffen werden. Wir untersuchen zwei verschiedene Klassen von D-Zustands-Molekülen für die Hauptquantenzahlen $n = 40 - 50$, den $D_{5/2}, m_J = 1/2$ Zustand, dessen Elektronenorbital sich hantelförmig entlang der z-Achse ersteckt und einen kleinen Torus im Zentrum besitzt, und den $D_{5/2}, m_J = 5/2$ Zustand, dessen Elektronenorbital die Form eines großen Donut aufweist und in der x-y-Ebene liegt. In Zusammenarbeit mit M. Kurz von der Universität Hamburg haben wir die 2-dimensionalen Potentiallandschaften (in Abhängigkeit von R und Θ) für diese beiden Zustände ausgerechnet und die Bindungsenergien der darin liegenden Moleküle bestimmt. So gibt es zwei verschiedene Klassen von Molekülen, die in dem Elektronenorbital des $D_{5/2}, m_J = 1/2$ Zustands gebunden werden können: die axialen Moleküle in den tiefen Potentialtöpfen weit außen in den Spitzen der Keulen des Elektronenorbitals und die toroidalen Moleküle, die sich in den flachen Potentialtöpfen im Torus formen. Im Gegensatz dazu können im $D_{5/2}, m_J = 5/2$ Zustand nur toroidale Moleküle gebunden werden. Mit unseren schmalbandigen Lasern können wir exakt auswählen, welches spezifische Molekül wir anregen wollen. Dabei detektieren wir in unseren hochauflösenden Spektren auch höherangeregte Rovibrationszustände. Ein Vergleich der experimentellen Bindungsenergien der Moleküle mit den theoretischen zeigt eine gute Übereinstimmung. Eine weitere besondere Eigenschaft der D-Zustands-Moleküle ist ihr spezielles Alignment, ihre räumliche Ausrichtung. Generell ist das Alignment von Molekülen von Forschungsinteresse, denn speziell ausgerichtete Moleküle zeigen im Vergleich zu nicht ausgerichteten Molekülen ein anderes Verhalten bei chemischen Reaktionen oder können die Effizienz von chemischen Reaktionen erheblich beeinflussen. Zur Ausrichtung der Moleküle werden normalerweise starke elektrische, magnetische Felder oder Lichtfelder verwendet, während in unserem Fall die Rydberg-Moleküle allein durch den Anregungsprozess in unserem schwachen Magnetfeld eine spezielle Ausrichtung haben. So weisen die axialen Moleküle ein fast perfektes Alignment entlang der z-Achse auf, während die toroidalen Moleküle genau senkrecht zu dieser Achse ausgerichtet sind, und daher ein niedriges Alignment besitzen. Ein weiterer wichtiger Aspekt ist, dass unsere Moleküle während ihrer kurzen Lebensdauer stationär sind.

In weiteren Versuchen haben wir ein zusätzliches elektrisches Feld angelegt, um die Potentiale und Bindungsenergien der Moleküle zu verändern und zu kontrollieren. Dabei legten wir den Fokus auf das Mischen der $D_{5/2}, m_J = 1/2$ und $D_{5/2}, m_J = 5/2$ Zustände und den daraus entstehenden Molekülen. Während die atomaren Zustände aufgrund der Dipolauswahlregeln nicht koppeln, mischen sich die Elektronen-Orbitale für die Moleküle und ermöglichen die Erzeugung von Rydberg-Molekülzuständen, die eine neue Abhängigkeit vom azimutalen Winkel φ aufweisen. Wir beobachteten experimentell, dass die Bindungsenergie des toroidalen Grundzustandsmoleküls bis zu dem Punkt, wo sich die beiden Zustände kreuzen, adiabatisch anwächst und danach wieder abnimmt, wenn wir langsam das angelegte elektrische Feld erhöhen. Das Verhalten kann mit einem einfachen 2-Niveau-Modell, bestehend aus den Wellenfunktionen des $D_{5/2}, m_J = 1/2$ und $D_{5/2}, m_J = 5/2$ Zustandes, verstanden werden. Es findet eine adiabatische Transformation des Elektronenorbitals des $m_J = 1/2$ Zustandes in das des $m_J = 5/2$ Zustandes statt, bei der die axialen Keulenstrukturen immer kleiner

werden, während sich bei dem Torus in der x-y-Ebene zwei keulenartige Auswölbungen ausbilden, die stetig weiter wachsen, was den Anstieg der Bindungsenergie des toroidalen Moleküls erklärt. Ab dem Kreuzungspunkt der beiden Zustände nimmt die Ausdehnung der zwei ausgebildeten Auswüchse in der x-y-Ebene wieder leicht ab und die Auswölbungen formen sich zu dem kompletten Torus des $m_J = 5/2$ Zustandes um. Dies führt zu einer kleinen Abnahme der Bindungsenergie des Moleküls. Im Gegensatz dazu beobachteten wir für die axialen Moleküle eine nahezu konstante Bindungsenergie, was sich damit erklären lässt, dass das Elektronenorbital des $m_J = 5/2$ Zustands keinen Beitrag in axialer z-Richtung besitzt. Somit bleiben die axialen Rydberg-Moleküle immer im $m_J = 1/2$ Orbital, welches auch zu einem gewissen Anteil im Kreuzungspunkt und darüber hinausgehend existiert. Qualitativ beschreibt das Modell das Verhalten des toroidalen Moleküls gut, aber quantitativ gibt es Abweichungen. Zur Verbesserung des Modells müssen die benachbarten m_J-Zustände auch berücksichtigt werden, da sie die Wellenfunktionen unserer beiden Zustände beeinflussen.

Der zweite Teil dieser Arbeit beschäftigt sich mit D-Zustands-Rydberg-Elektronen im Bose-Einstein-Kondensat für Hauptquantenzahlen $n > 100$. Die Grundlage für diese Untersuchungen bildet die vorangegangene Studie über die wiederholte Anregung einzelner S-Zustands-Rydberg-Elektronen im Bose-Einstein-Kondensat [10, 11]. Für diese hohen Hauptquantenzahlen ist der Blockade-Radius der Rydberg-Atome größer als die Ausdehnung unseres Kondensates, weswegen immer nur ein einzelnes Rydberg-Atom zur gleichen Zeit im Kondensat existieren kann. Da die Effizienz unseres Ionendetektors für die Detektion einzelner Ionen nicht ausreichend ist, müssen wir uns auf die Aufnahme von Absorptionsbildern nach einer Flugzeit des Kondensates von 50 Millisekunden verlassen und Atomverluste in diesen Bildern analysieren. Damit wir signifikante Atomverluste im Kondensat detektieren können, müssen wir die Anregung eines einzelnen Rydberg-Atoms 300-500 Mal wiederholen.

In den vorangegangenen Messungen zu den S-Zuständen fanden wir heraus, dass die Atomverluste einerseits durch die Kopplung des Elektrons an Phononen, Dichtewellen im Kondensat, und andererseits durch das Herausschlagen von Kondensatatomen herrühren. Der erste Effekt erzeugt in den Absorptionsbildern auch Atomverluste und kann somit von dem zweiten Effekt nicht unterschieden werden. Die zweite wichtige Beobachtung war eine Energieverschiebung zwischen der Position der maximalen Atomverluste im Kondensat und der Rydberg-Linie, die im Spektrum einer thermischen Wolke gemessen wurde. Diese Energieverschiebung lässt sich vollständig durch die Streuung des Rydberg-Elektrons an den einzelnen Grundzustandsatomen im Kondensat mit dem Modell von E. Fermi [12] erklären und ist proportional zur mittleren Dichte der Kondensatatome. Nach allen bisherigen Beobachtungen ist die Wechselwirkung des positiv geladenen Rydberg-Kerns mit den Kondensatatomen vernachlässigbar.

In den Messungen für diese Dissertation verlagerten wir unseren Fokus nun auf die Anregung von D-Rydberg-Atomen im Kondensat, die etwa den gleichen Radialteil, aber einen unterschiedlichen Winkelanteil in ihren Wellenfunktionen im Vergleich zu den S-Zuständen besitzen. In den Lebensdauermessungen der Rydberg-Elektronen beobachteten wir keine signifikanten Unterschiede zwischen S- und D-Zuständen, da derselbe bisher ungeklärte limitierende Prozess die Lebensdauer der Rydberg-Atome im Kondensat auf 7-10 Mikrosekunden beschränkt. Eine zentrale Rolle bei diesem Prozess spielt die Dichte des Kondensats. In den Verlustmessungen der Atome im Kondensat zeigten unsere Messungen Unterschiede zwischen den untersuchten S- und D-Zuständen, die nicht durch die unterschiedlichen 2-Photon-Rabi-

Frequenzen erklärt werden können. Messungen der kollektiven Oszillationen im Kondensat zeigen, dass der Hauptgrund für diesen Effekt das gepulste Einstrahlen unseres Rydberg-Anregungslasers mit der Wellenlänge von 780 Nanometern ist, und nicht die Anregung der Rydberg-Atome. Aus diesem Grund änderten wir die Anregungssequenz und schalteten diesen Laser nun adiabatisch ein. Damit konnten wir das Oszillationssignal, was durch den 780 Nanometer Laser erzeugt wird, minimieren und wiesen signifikante Oszillationen bedingt durch die Anregung von Rydberg-Atomen im Kondensat nach. Um die verschiedenen Signalstärken der Oszillationen für die D-Zustände im Vergleich zu dem S-Zustand zu verstehen, müssen weitere Messungen und vor allem theoretische Simulationen für dieses Experiment durchgeführt werden. In Zusammenarbeit mit der Gruppe von K. Rzążewski wurde bereits ein stochastisches Modell, basierend auf der Gross-Pitaevskii Gleichung, erfolgreich zur Beschreibung der Anregung von S-Zustands-Rydberg-Atomen im Kondensat eingesetzt. Die Erweiterung dieses Modells auf D-Zustände und die Implementierung des adiabatischen Einschaltens des 780 Nanometer Lasers sind geplant und werden uns dabei helfen, die bisher ungeklärten physikalischen Prozesse besser zu verstehen.

Dieses interessante physikalische System, bestehend aus einem Elektron im Bose-Einstein-Kondensat bildet den Ausgangspunkt für weitere zukünftige Experimente. Insbesondere die Aufnahme eines einzelnen Elektronen-Orbitals, eingeprägt in die Dichteverteilung des Kondensats, erscheint vielversprechend. Hierbei wird durch die Anregung eines Rydberg-Atoms im Kondensat ein Potential erzeugt, dass in einer Verformung der Dichte des Kondensats resultiert. Diese Dichteverteilung, die die Form des Elektronen-Orbitals wiederspiegelt, kann durch in-situ Abbildungen des Kondensats sichtbar gemacht werden. Im Hinblick auf die Rydberg-Moleküle ist als neues Projekt geplant, S-Zustände mit hohen l-Zuständen zu mischen, um neuartige Rydberg-Moleküle mit großen permanenten Dipolmomenten zu erzeugen oder die sogenannten 'Trilobite'-Zustände [13] nachzuweisen.

Publications

In the framework of this thesis, the following articles have been published:

- T. Karpiuk, M. Brewczyk, K. Rzążewski, J. B. Balewski, A. T. Krupp, A. Gaj, R. Löw, S. Hofferberth, T. Pfau, *Detecting and imaging single Rydberg electrons in a Bose-Einstein condensate*, arXiv:1402.6875 (submitted February 2014)

- A. Gaj, A. T. Krupp, J. B. Balewski, R. Löw, S. Hofferberth, T. Pfau, *From molecular spectra to a density shift in dense Rydberg gases*, Nature Communications, **5**, 4546 (2014)

- A. T. Krupp, A. Gaj, J. B. Balewski, P. Ilzhöfer, S. Hofferberth, R. Löw, T. Pfau, M. Kurz, P. Schmelcher, *Alignment of D-state Rydberg molecules*, Physical Review Letters, **112**, 143008 (2014)

- J. B. Balewski, A. T. Krupp, A. Gaj, S. Hofferberth, R. Löw and T. Pfau, *Rydberg dressing: Understanding of collective many-body effects and implications for experiments*, New Journal of Physics, **16**, 063012 (2014)

- J. B. Balewski, A. T. Krupp, A. Gaj, D. Peter, H. P. Büchler, R. Löw, S. Hofferberth and T. Pfau, *Coupling a single electron to a Bose-Einstein condensate*, Nature, **502**, 664–667 (2013)

- J. Nipper, J. B. Balewski, A. T. Krupp, S. Hofferberth, R. Löw and T. Pfau, *Atomic pair-state interferometer: Controlling and measuring an interaction-induced phase shift in Rydberg-atom pairs*, Physical Review X, **2**, 031011 (2012)

- J. Nipper, J. B. Balewski, A. T. Krupp, B. Butscher, R. Löw and T. Pfau, *Highly resolved measurements of Stark-tuned Förster resonances between Rydberg atoms*, Physical Review Letters, **108**, 113001 (2012)

Contents

Introduction

The title of this thesis 'D-state Rydberg electrons interacting with ultracold atoms' contains all the important aspects of this work, which I will now flesh out briefly to provide a short overview of all major topics.

Ultracold atoms

The definition of 'ultracold' is generally used for all temperatures below $1\,\mathrm{mK}$ where quantum mechanical processes start to play a crucial role. The considerable advantage to work in this temperature regime is that the atoms are stationary on the µs timescale of the conducted experiments. It is convenient to work in this timescale with regard to the switching time of the electronics and optical elements. Thus the behavior and interaction of ultracold atoms can be understood and controlled easily and the fundamental atom−atom interactions can be probed. The field of ultracold atom physics dates back to 1975 when T. Hänsch and A. Schawlow proposed that neutral atoms could be cooled via the radiation pressure of a laser beam tuned to an atomic resonance [14]. Independently D. Wineland and H. Dehmelt suggested the same cooling method for trapped ions [15]. In 1987 the first simultaneous trapping and cooling of atoms was realized in a magneto-optical trap (MOT) consisting out of six pairwise counterpropagating laser beams [16]. This device is commonly used today as a building block for many experiments on ultracold atoms, which allows to reach temperatures of about $10 - 100\,\mu\mathrm{K}$. With the help of the novel evaporative cooling technique in combination with the adiabatic relaxation of the atoms in the trapping potential, it was possible to cool neutral atoms down to less than $1\,\mathrm{nK}$ [17] (Nobel prize for C. Chu, C. Cohen-Tannoudji and W. Phillips in 1997 [18, 19, 20]). This led in 1995 to the first creation of a Bose-Einstein condensate (BEC) in a dilute gas of rubidium by the group of E. Cornell, C. Wieman [2] and of sodium by W. Ketterle and coworkers [3], which marked a milestone in the young research field of ultracold atoms. In a Bose-Einstein condensate the de Broglie wavelength of the bosons is larger than their interparticle distance so that the whole ensemble of particles can be described as a macroscopic matter wave, in which all atoms possess the same ground state energy.

Recent research in the field of Bose-Einstein condensation deals with more exotic particles than atoms: The Bose-Einstein condensation of quasiparticles in solid state systems, for example for microcavity exciton-polaritons [21, 22, 23] and recently the Bose-Einstein condensation of photons have been realized [24]. Even a BEC out of positronium, a bound state of an electron and a positron, was proposed lately as a source for a self-amplified gamma-ray laser [25]. Furthermore the non-linear properties of Bose-Einstein condensates have been investigated resulting in the observation of dark [26] and bright solitons [27], self-reinforcing wave packets, which maintain their shape while they travel at constant speed. Vortices, density singularities analogue to vortices in superfluids, were as well studied in Bose-Einstein condensates [28, 29].

A promising application of Bose-Einstein condensates is the creation of an atom laser which produces a coherent monoenergetic beam of atoms, extracted from the condensate [30]. One main topic in this thesis are the measurements in which we excite Rydberg atoms of high principal quantum number n directly in a Bose-Einstein condensate of rubidium (^{87}Rb).

Rydberg atoms

This directly links to the second buzzword 'Rydberg electrons' used in the title. Rydberg atoms are atoms where at least one electron, the Rydberg electron, is excited to a very high principal quantum number n, close to the ionization border. Many properties of these atoms stem from this highly excited electron [31]. They are very sensitive to electric fields and the interaction between two of these Rydberg atoms is about twelve orders of magnitude higher than of their ground state counterparts (comparing the $100S$ to the $5S$ state).

Historically Rydberg atoms were discovered in 1885 by J. Balmer who found absorption lines in hydrogen and postulated afterwards a formula to describe them [32]. These lines, which are in the visible light spectrum, were named after him describing the transition from principal quantum number $n = 2$ to higher lying levels. Later J. Rydberg systematically analyzed and classified the spectral lines of several elements, mainly alkali atoms, and found an empirical formula, which fully described their energy transitions. In this formula he introduced a general constant, valid for all elements, which was named after him [31, 33]. The physical significance of these highly excited states became clear when N. Bohr postulated his model of the atoms in 1913 [34, 35]. In his well-known model, he describes the atom as a negatively charged electron classically orbiting around the positively charged core. A crucial discovery in his work was the quantization of the angular momentum in units of the reduced Planck constant $\hbar$, which allowed the derivation of the energy formula of J. Rydberg. This made it possible to relate the spectroscopic Rydberg constant to the fundamental physical constants of the mass of an electron, the Planck constant, the electron charge and the permittivity of free space.

In 1934 another important experiment was conducted by E. Amaldi and E. Segré [36, 37] and independently by C. Füchtbauer and coworkers [38, 39, 40], which has a particular relevance for this thesis. They systematically investigated the influence of different noble gases, specifically hydrogen, neon, helium and argon at variable densities on the spectra of sodium and potassium. Note that for densities of up to $10^{20}\,\mathrm{cm}^{-3}$ thousands of these foreign gas particles exist in the orbit of one Rydberg atom. They detected that their spectral lines get red or blue shifted depending on the used type of foreign gas and observed a broadening of these lines. For a higher density of the noble gas they saw larger line shifts, which could be explained in the same year by the theoretical work of E. Fermi [12]. He studied the interaction between the Rydberg electron and its ionic core on the foreign gas atoms. One result was, that the effect of the ionic core on the background perturber atoms can be neglected. E. Fermi treated the interaction between electron and atom as a scattering event, introducing a two particle scattering length. One can identify the scattering length as a phase shift between ingoing and outgoing wavefunction of the two particles from the region of interaction. With this concept the linear dependence of the energy shift on the density of the background gas could be explained. The same theory can be applied to our measurements, studying the influence of Rydberg electrons on a dense Bose-Einstein condensate. In our case, the condensed ground state atoms take the role of the dense buffer gas used in E. Amaldi's and E. Segré's experiment.

To realize the excitation of only a single Rydberg atom in our condensate we have to go to very high principal quantum numbers $n > 100$. Here an additional important feature of the Rydberg atoms comes into play: the so-called blockade radius. Due to the strong van der Waals interaction between two Rydberg atoms, the minimum distance between two Rydberg atoms is limited when a fixed laser frequency is used for the excitation. Only at radii larger than the blockade radius, another excitation is possible. For $n > 100$ the blockade radius is larger than the extent of our condensate, which guaranties that we only excite one Rydberg atom at a time in our Bose-Einstein condensate. This effect is especially important for the novel field of quantum information processing. Here the goal is to transfer, process and store information as quantum mechanical states with the ultimate goal to realize a quantum computer in the future [41, 42, 43, 44]. For example Rydberg atoms have been used recently as probes for the nondestructive counting of photons and the recording of field quantum jumps (Nobel prize for S. Haroche in 2012 [5]).

Rydberg molecules

In the last paragraph we considered Rydberg atoms in very dense background gases (E. Amaldi and E. Segré) or in a dense condensate at very high quantum numbers $n > 100$. If we now go to the other extreme with thermal cloud densities of $10^{12}\,\mathrm{cm}^{-3}$ at a temperature of a few $\mu\mathrm{K}$ and low principal quantum numbers, we end up with only a few ground state atoms (on average) in the orbit of a Rydberg atom. In 2000 C. Greene and coworkers proposed that for ultracold gases the interaction between Rydberg electrons and neutral atoms can give rise to the formation of molecules. The unique binding mechanism of these so-called Rydberg molecules originates from the scattering of the low energy Rydberg electron with at least one neutral ground state atom. The ground state atom gets thereby trapped in the scattering potential of the Rydberg electron. This novel binding mechanism differs from the van der Waals or ionic interaction and can again be described by Fermi's pseudopotential where instead of the density of the background gas now the square of the electron wavefunction appears. Due to the negative triplet scattering length of rubidium the interaction becomes attractive, allowing for the binding of these molecules. In 2009 these Rydberg molecules were created for the first time via a photoassociation process, using S-states at principal quantum numbers of around $n = 36$ [6, 45]. They are a fascinating species due to their exaggerated properties, which stem from their constituent Rydberg atom. The Rydberg molecules possess sizes of up to several $\mu\mathrm{m}$, which is the size of bacteria or large viruses [9], which in contrast to the Rydberg molecules consist of trillions of atoms. Even pentamers − four ground state atoms bound to one Rydberg atom − have recently been successfully created [9]. Furthermore Rydberg molecules can be coherently created and dissociated [7] and they show even a permanent dipole moment [8], which is remarkable for a homonuclear diatomic molecule. In this thesis molecules consisting of a D-state Rydberg electron were investigated for the first time, offering new opportunities for novel developments in the emerging field of ultracold quantum chemistry.

This thesis

In the previous brief introductory parts I gave a short overview of all the multifaceted fields, which are covered in this thesis. This dissertation comprises of two main topics: the creation of D-state Rydberg molecules of ^{87}Rb in an ultracold thermal cloud and the excitation of single D-state Rydberg electrons in a Bose-Einstein condensate.

The main difference between the so far studied S-state molecules and the D-state molecules is the different angular part in their wavefunctions. While the electron orbit of the S-state molecules is spherical symmetric, the electron orbits of the two $D_{5/2}$ molecules, which we study in this thesis, are either shaped like a dumbbell along the z-axis with a small torus in the center, or they look like a doughnut lying in the x-y-plane. To separately study the different m_J substates, we apply a magnetic field of about $14\,\mathrm{G}$ to energetically split these states, utilizing the Zeeman effect (see subsection 1.3.2). Since the potentials of the molecules depend on the squared wavefunctions of the Rydberg electrons they have entirely different energy landscapes compared to the S-states. There is now a dependence on the polar angle Θ, giving rise to two different species, toroidal and axial molecules, which have different alignments, i.e. angular confinements. They also possess completely different binding energies, which could be resolved in our high resolution spectra. These measurements are presented in chapter 8. In a collaboration with M. Kurz from the University of Hamburg we calculated the potential energy landscapes and the binding energies of the containing molecular D-states (see chapter 2). Additionally we investigated these two types of D-state molecules under the influence of an electric field in section 8.3. Here we show that we can alter the potential energy surfaces and thus their binding energies adiabatically giving rise to novel molecules, which also possess a dependence on the azimuthal angle φ.

In the second experimental part in chapter 9 we excited D-state Rydberg atoms in a Bose-Einstein condensate and compare the results to previous S-state measurements at high principal quantum numbers n. To be able to conduct experiments at these high principal quantum numbers a precise control of our electric fields is necessary, since the polarizability of the Rydberg atoms scales as n^7. Due to our separately addressable field plates we can compensate stray electric fields in all spatial directions and thus reach n up to 202. Since for these high principal quantum numbers the Rydberg blockade radius is bigger than the extent of our condensate, only one Rydberg excitation at a time is possible in the condensate. Our low ion detector efficiency forced us to utilize the time of flight absorption imaging technique to get information about the condensate atoms. More about our compensation method of stray electric fields, the used experimental sequences and the setup of our experiment in general can be found in the setup part II of this thesis. For the comparison between S- and D-state Rydberg atoms in a condensate we use states which have approximately the same radial wavefunctions and only differ in the angular part. We show differences in the condensate atom losses and prove that the successive excitation of Rydberg atoms creates shape oscillations due to the coupling of the Rydberg electron to the phonons in the Bose-Einstein condensate. These measurements can be found in chapter 9.

In collaboration with the group of K. Rzążewski we developed a stochastic model, based on the evolution of the Gross-Pitaevskii equation, which simulates the successive excitation of Rydberg atoms in the condensate. A comparison with the previous conducted S-state measurements [10] shows a very good agreement between experimental data and theoretical

calculations, presented in section 3.3 of the theory chapter in part I. Simulations of the D-state Rydberg electrons in the condensate are underway. In chapter 1, basics about Rydberg atoms are discussed, including their coupling to a light field (section 1.2), their response to electric and magnetic fields (section 1.3), their lifetimes (section 1.4) and their interaction with each other (section 1.5). Chapter 2 deals with Rydberg electron−ground state interaction, including the formation of molecules and the calculation of their binding energies. In the last chapter 3 of the theory part, the Gross-Pitaevskii equation is introduced to characterize Bose-Einstein condensates, which is needed for the developed statistical model to describe the excitation of single Rydberg atoms in the condensate.

In the conclusion of this thesis in chapter 10, the most important results of this dissertation are summarized and in chapter 11 a brief outlook about ideas for future projects and follow-up studies, directly based on the investigations described in this thesis, is given. This thesis is followed by a comprehensive appendix, which contains further explicit theoretical calculations (section A) and supplementary experimental measurement results (section B), providing additional information for the interested reader.

To avoid any problems with admixing different unit systems, all formulas in this thesis apart from section 2.2 and 2.3 are given in SI units. In this dissertation the electric field is denoted as $\mathcal{E}$ to avoid confusion with the energy E. All values of the energy E are always provided in units of 'Hz'.

Part I

Theoretical Basics

Your theory is crazy, but it's not crazy enough to be true.

Niels Bohr

1 Rydberg atoms

In this chapter the theoretical description of Rydberg atoms, their interaction with each other and with electric, magnetic and light fields, are presented. Starting point is a recapitulation of the basic properties of Rydberg atoms and their scaling behavior with principal quantum number n in section 1.1. In section 1.2 follows the theoretical description of the Rydberg excitation process, first starting off with a two-level system, which is then extended to a three-level system to describe the experimental two-photon transition appropriately. After that we investigate the influences of magnetic and electric fields on these highly excited atoms in section 1.3. Section 1.4 is dedicated to the lifetime and possible decay processes of these species. The last section 1.5 deals with Rydberg−Rydberg interactions and explains important phenomena like the Rydberg blockade effect and the collective Rabi frequency.

1.1 Basics about Rydberg atoms

In Rydberg atoms the outermost electron(s) is/are excited to a state with high principal quantum number n close to the ionization limit. Many properties of these atoms stem for this highly excited electron [31]. Since the electron is far away from the ionic core they can be similarly treated as the hydrogen atom, which is the only element that has a fully analytical solution to its quantum mechanical description. Rydberg atoms were the first time discovered in 1885 by J. Balmer who detected absorption lines in hydrogen and postulated afterwards a formula to describe them [32]. These lines, which are in the visible light spectrum, were named after him, describing the transition from principal quantum number $n = 2$ to higher lying levels. All these series of lines are linked to the energy of the hydrogen atom described by the Bohr atom model [34, 35]

$$E'_n = -hc\frac{R_H}{n^2} = -13.6\,\mathrm{eV} \cdot \frac{1}{n^2}; \tag{1.1}$$

with the Rydberg constant for hydrogen

$$R_H = R_\infty \frac{M_p}{m_e + M_p} \approx R_\infty = \frac{e^4 m_e}{8c\epsilon_0^2 h^3} = 10979731\,\mathrm{m}^{-1}. \tag{1.2}$$

Here R_∞ is the Rydberg constant [33], M_p the mass of the proton, m_e the electron mass, ϵ_0 the vacuum permittivity, e the electron charge and h the Planck constant. We now want to shift our focus to alkali Rydberg atoms, especially to rubidium, since we are using this element in our experiment. Rubidium possesses one valence electron in the outermost shell whereas the inner closed electron shells, consisting out of 35 electrons, screen the charge of the nucleus. With the excitation of the valence electron to a high principal quantum number n, Rydberg atoms behave hydrogen-like and thus have similar characteristics and properties as hydrogen atoms.

State	$n^2S_{1/2}$	$n^2P_{1/2}$	$n^2P_{3/2}$	$n^2D_{3/2}$	$n^2D_{5/2}$	$n^2F_{5/2}$	$n^2F_{7/2}$
δ_0	3.1311804	2.6548849	2.6416737	1.34809171	1.34646572	0.0165192	0.0165437
δ_2	0.1784	0.2900	0.2950	-0.60286	-0.59600	-0.085	-0.086

Table 1.1: Quantum defect parameters for ^{85}Rb, taken from references [46, 47, 48].

Nevertheless we have to take into account that the core of the Rydberg atom is not simply one proton but consists of many additional particles. The electrons in the inner shells influence the Rydberg electron when it is close to the core. To describe this deviation, quantum defect theory is employed [4], which introduces an effective quantum number $n^\star = n - \delta_{nlj}$ in equation (1.1) leading to

$$E_n = -hc\frac{R_\infty}{n^{\star 2}} = -hc\frac{R_\infty}{(n-\delta_{nlj})^2}. \tag{1.3}$$

The quantum defect δ_{nlj} represents the energy shift between the hydrogen atom and the hydrogen-like Rydberg atom and is given by the Rydberg-Ritz formula [49]

$$\delta_{nlj} = \delta_0 + \frac{\delta_2}{(n-\delta_0)^2} + \frac{\delta_4}{(n-\delta_0)^4} + \dots \tag{1.4}$$

It is important that this quantum defect strongly depends on the orbital angular momentum l. For low-l ($l \leq 3$) states the Rydberg electron has a high probability to penetrate the inner shells effectively increasing the potential and thus increasing the binding energy. Since for high-l states the Rydberg electron probability density is larger far away from the core, they behave more hydrogen-like and thus feature a smaller quantum defect. In Table 1.1 the quantum defects for rubidium are shown up to the second order; higher order terms do not significantly change the quantum defect anymore. All values were acquired empirically by millimeter spectroscopy measurements [46, 47] or by thermionic ionization detection [48].
The scaling laws of the fundamental parameters of Rydberg atoms are the same as for hydrogen,

Property		Scaling	^{87}Rb $42D_{5/2}$
Binding energy	$E_{n^\star}$ (1.3)	$n^{\star -2}$	-8.23 meV
Level separation	$E_{n^\star} - E_{n^\star-1}$	$n^{\star -3}$	101.7 GHz
Rydberg radius	$r_{n^\star}$ (1.5)	$n^{\star\,2}$	1652.7 a_0
Mean orbit radius	$\langle r_{n^\star}\rangle \approx \frac{1}{2}(3(n^\star)^2 - l(l+1))$	$n^{\star\,2}$	2476.1 a_0
Polarizability	$\alpha \propto \frac{\lvert\vec{d}\rvert^2}{E_{n^\star}-E_{m^\star-1}}$	$n^{\star\,7}$	61.6 MHz/(V/cm)^2
Radiative lifetime	$\tau_{\text{rad}} = \tau' n^{\star\gamma}$ (1.40)	$n^{\star\,3}$	69.1 µs

Table 1.2: Scaling laws and fundamental properties of Rydberg atoms with effective principal quantum number $n^\star$ and explicitly calculated values for the rubidium $42D_{5/2}$ state, which will play an important role in the measurements.

just with the quantum defect applied. The radius of Rydberg atoms is given by

$$r_{n^\star} = \frac{4\pi\epsilon_0\hbar^2}{m_e e^2} = a_0 n^{\star 2}, \tag{1.5}$$

where $a_0 = 5.29 \times 10^{-11}\,\mathrm{m}$ is the Bohr radius and m_e is the electron mass. Additional scaling laws and selected properties are summarized in Table 1.2. A very important parameter is the polarizability α, which scales with $n^{\star\,7}$ and thus renders Rydberg atoms very sensitive to external fields at high principal quantum numbers. That is the reason why the electric field control plays a crucial role for the experiment (see chapter 7 for details).

1.2 Atom-light interaction

All experiments with Rydberg atoms in this thesis are based on a two photon excitation scheme via two diode lasers (see chapter 5). A semiclassical treatment was chosen to describe the interaction of light with our atoms. Since our laser excitation pulses contain many photons, the use of quantum mechanical creation and annihilation operators for the quantization of the light field is not necessary here and we can treat the light field classically. Starting from a simple two-level system, where important parameters like the Rabi frequency are introduced, we continue with the discussion of the ac Stark shift and advance later to a three-level system precisely describing our excitation process used in the experiment. We show that this three-level system can be treated as an effective two-level system with modified parameters. A two-level system will also play an important role for the intermixing of the molecular wavefunctions in subsection 8.3.2.

1.2.1 Two-level system

We describe our atom as a two-level system with the ground state $|g\rangle$ and excited state $|e\rangle$, visualized in the sketch in Figure 1.1(a). Via the coupling to the light field the ground state atom can be coherently transferred into the excited state. The evolution of this system is characterized by the time-dependent Schrödinger equation

$$i\hbar\frac{\partial}{\partial t}\Psi(\vec{r},t) = H\Psi(\vec{r},t). \tag{1.6}$$

The total Hamiltonian $H = H_0 + H_l$ consists of two parts: the Hamiltonian H_0, which describes the unperturbed free atom and H_l, which characterizes the coupling to the light field. Note that the states $|g\rangle$ and $|e\rangle$ are eigenstates of the Hamiltonian H_0. Furthermore we use the dipole approximation stating that the spatial change of the electric field can be neglected at the position of the atom since the atom size is at least a factor 100 smaller than the laser wavelength [50]. Thus we can describe the oscillating electric field as

$$\vec{\mathcal{E}}(t) = \vec{\varepsilon}\,\mathcal{E}_0\cos(\omega t), \tag{1.7}$$

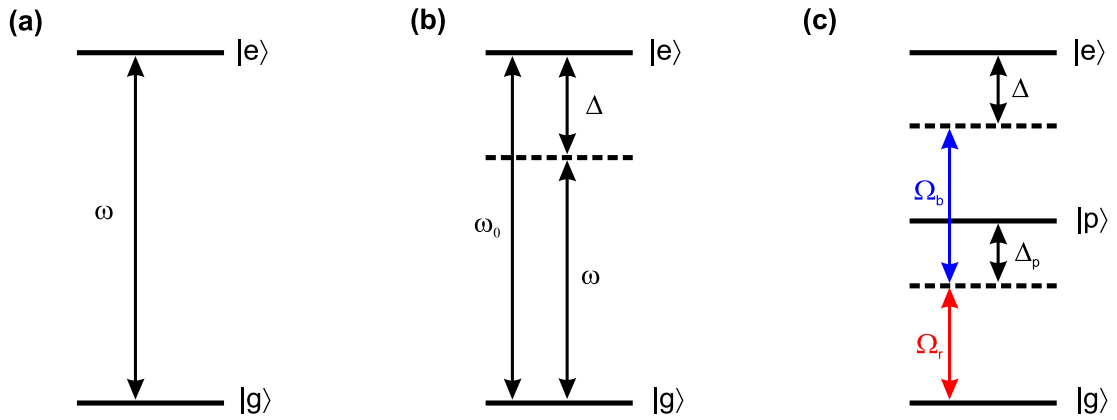

Figure 1.1: Sketch of the different level systems. In (a) the ground state $|g\rangle$ is coupled by a light field ω to the excited state $|e\rangle$. In (b) an additional detuning Δ of the laser from the excited state $|e\rangle$ was introduced. In (c) a third level, the intermediate state $|p\rangle$, was added to exactly describe the two-photon excitation process we perform in the experiment. Two laser fields with Rabi frequencies Ω_r (red laser) and Ω_b (blue laser) are coupling the ground state to the excited state with a total detuning of Δ. The lower transition frequency Ω_r is detuned by Δ_p from the intermediate state.

where $\vec{\varepsilon}$ is the normalized polarization vector, $\mathcal{E}_0$ the amplitude and ω the angular frequency of the light field. The light field coupling Hamiltonian takes now the form of $H_l = -\vec{d} \cdot \vec{\mathcal{E}}(t)$ with the electric dipole moment $\vec{d} = -e\vec{r}$, where $\vec{r}$ is the position of the electron with respect to the atom's center of mass. Now we can express the Hamiltonian of the light field as

$$H_l = e\vec{r} \cdot \vec{\varepsilon}\, \mathcal{E}_0 \cos(\omega t). \tag{1.8}$$

1.2.2 Rabi oscillations

The goal of our description is to calculate the time evolution of the two-level system under the effect of a light field. As an ansatz to solve the time dependent Schrödinger equation (1.6) we use the general wavefunction

$$\Psi(\vec{r}, t) = c_g(t) e^{-i\omega_g t} |g\rangle + c_e(t) e^{-i\omega_e t} |e\rangle \,, \tag{1.9}$$

in which $c_g(t)$ and $c_e(t)$ are the time dependent amplitudes of the eigenvectors $|g\rangle$ and $|e\rangle$. Inserting this equation into (1.6) and multiplying the resulting equation from the left either by $e^{i\omega_g t} \langle g|$ or $e^{i\omega_e t} \langle e|$ yields two coupled differential equations for the time dependent coefficients $\dot{c}_g(t)$ and $\dot{c}_e(t)$:

$$i\dot{c}_g(t) = \Omega \cos(\omega t) e^{-i\omega_0 t} c_e(t) = \frac{\Omega}{2} \left(e^{i(\omega-\omega_0)t} + e^{-i(\omega+\omega_0)t} \right) c_e(t); \tag{1.10}$$

$$i\dot{c}_e(t) = \Omega^* \cos(\omega t) e^{i\omega_0 t} c_g(t) = \frac{\Omega^*}{2} \left(e^{-i(\omega-\omega_0)t} + e^{i(\omega+\omega_0)t} \right) c_g(t). \tag{1.11}$$

Here we introduced the resonance frequency $\omega_0 = \omega_e - \omega_g$ and the Rabi frequency Ω:

$$\Omega = \frac{\langle g \left| e\mathcal{E}_0 \vec{r} \cdot \vec{\varepsilon} \right| e \rangle}{\hbar} = \frac{e\mathcal{E}_0}{\hbar} \int \psi_g(r) \vec{r} \cdot \vec{\varepsilon} \psi_e(r) d^3\vec{r} \,. \tag{1.12}$$

Experimentally relevant is the case in which the radiation frequency ω is close to the atomic resonance at ω_0, resulting in a very small detuning $\Delta = \omega - \omega_0$ of the laser frequency from the atomic resonance (see Figure 1.1(b)). Therefore all rapidly oscillating terms with frequencies $\omega_0 + \omega$ are neglected since they do not significantly influence the coupling of the two-level system. This approximation is generally called rotating-wave approximation. We can simplify equations (1.10) and (1.11) to

$$i\dot{c}_g(t) = \frac{\Omega}{2} e^{i\Delta t} c_e(t); \tag{1.13}$$

$$i\dot{c}_e(t) = \frac{\Omega^*}{2} e^{-i\Delta t} c_g(t). \tag{1.14}$$

These two coupled differential equations can now be converted into a decoupled second order differential equation of the form

$$\ddot{c}_e(t) + i\Delta\dot{c}_e(t) + \frac{\Omega^2}{4} c_e(t) = 0. \tag{1.15}$$

By assuming that only the ground state is populated at the beginning $c_g(0) = 1; c_e(0) = 0$, we can solve equation (1.15) acquiring the following evolution for the excited state [51]

$$c_e(t) = \frac{A\,\Omega}{\sqrt{\Omega^2 + \Delta^2}} e^{-i\Delta t/2} \sin\left(\frac{\sqrt{\Omega^2 + \Delta^2}}{2} t\right), \tag{1.16}$$

where A is a normalization parameter. Accounting for the normalization $|c_g|^2 + |c_e|^2 = 1$ we can calculate the probability to find the system in the excited state:

$$|c_e(t)|^2 = \frac{\Omega^2}{\Omega_{\text{eff}}^2} \sin^2\left(\frac{\Omega_{\text{eff}}}{2} t\right) = \frac{\Omega^2}{2\Omega_{\text{eff}}^2} \left(1 - \cos\left(\Omega_{\text{eff}} t\right)\right). \tag{1.17}$$

We find that the system undergoes so-called Rabi oscillations with the effective non-resonant Rabi frequency $\Omega_{\text{eff}} = \sqrt{\Omega^2 + \Delta^2}$ and amplitude $\Omega^2/(2\Omega_{\text{eff}}^2)$. If the laser frequency is not detuned from the transition ($\Delta = 0$) the system oscillates exactly with the resonant Rabi frequency Ω between ground and excited state.

1.2.3 Light shift / ac Stark effect

The light field has not only an effect on the population of the states but also changes the energy of the levels, which is called light shift or ac Stark effect. If we change the bases of our system to $\tilde{c}_g(t) = c_g(t)$ and $\tilde{c}_e(t) = e^{i\Delta t} c_e(t)$, we can get rid of the exponential functions in equations (1.13) and (1.14). We can rewrite these two coupled differential equations now as matrix

equation:

$$i\hbar\frac{\partial}{\partial t}\begin{pmatrix}\tilde{c}_g\\ \tilde{c}_e\end{pmatrix} = \underbrace{\hbar\begin{pmatrix}0 & \Omega/2\\ \Omega^*/2 & -\Delta\end{pmatrix}}_{H}\begin{pmatrix}\tilde{c}_g\\ \tilde{c}_e\end{pmatrix}. \tag{1.18}$$

Here we multiplied both sides with $\hbar$ to acquire an expression for the Hamiltonian H of the system. A diagonalization of this Hamiltonian provides the eigenenergies of the dressed two-level system, the ac Stark shift:

$$E_{1/2} = \Delta_{\text{ac}} = \frac{\hbar}{2}\left(-\Delta \pm \sqrt{|\Omega|^2 + \Delta^2}\right). \tag{1.19}$$

These are the energies of the dressed ground and excited state for the Rabi frequency Ω and the laser detuning Δ. For large frequency detunings $|\Delta| \gg \Omega$ the effect of absorption can be neglected and the light shift results in

$$E_{1/2} = \Delta_{\text{ac}} = \pm\frac{\hbar\Omega^2}{4\Delta}. \tag{1.20}$$

Note that for positive/negative detunings the distance between the dressed states decreases/increases compared to the unperturbed states. Exploiting the normalization condition of the eigenstates, the excited state fraction of the new ground state can be calculated by

$$f = \frac{|\Omega|^2}{|\Omega|^2 + 2\Delta^2 + 2\Delta\sqrt{|\Omega|^2 + \Delta^2}}. \tag{1.21}$$

For weak dressing $|\Delta| \gg \Omega$, this expression simplifies to $f \approx |\Omega|^2/(4\Delta^2)$.

1.2.4 Three-level system as an effective two-level system

In the experiment we perform a two-photon excitation from the ground state, over a far detuned intermediate, to our final Rydberg state. Thus the obvious choice to model this scheme is a three-level system, which is coupled by two separate light fields. We will show that this system can be treated similar to the two-level model, investigated in the previous subsections. This additional level leads to various interesting physical phenomena, like the electromagnetically induced transparency (EIT) [52], coherent population trapping and stimulated Raman adiabatic passage (STIRAP) [43], Autler-Townes splitting [53] and Raman transitions [54]. A scheme of the two-photon process is depicted in Figure 1.1(c), where a red laser with a wavelength of $780\,\text{nm}$ employs a Rabi frequency Ω_r to drive the lower transition from the ground state $|g\rangle$ to the intermediate state $|p\rangle$. The detuning of this laser to the intermediate level Δ_p is large to avoid the population of this state. The decay rate of this state is typically high; e.g. the $5P_{3/2}$ ^{87}Rb state used as the intermediate state in the experiment has a decay rate $\Gamma = 2\pi \cdot 6.067\,\text{MHz}$ [55]. A blue laser, possessing a wavelength of $480\,\text{nm}$, drives the upper transition with the Rabi frequency Ω_b. The detuning of the complete two-photon transition to the excited state is given by Δ. Using the same approximations as in subsection 1.2.2, we can write the three-level

Hamiltonian, consisting of the ground state $|g\rangle$, intermediate state $|p\rangle$ and excited state $|e\rangle$ as

$$H = \hbar \begin{pmatrix} 0 & \Omega_r/2 & 0 \\ \Omega_r/2 & -\Delta_p & \Omega_b/2 \\ 0 & \Omega_b/2 & -\Delta \end{pmatrix}. \tag{1.22}$$

To simplify the expression we assumed that all Rabi frequencies have only a real part. According to equation (1.21) we know that for large detunings $\Delta_p \gg \Omega_r$ for the lower transition, the excited state fraction scales as $\Omega_r^2/(4\Delta_p^2)$ giving rise to a very low population of the intermediate state. Equation (1.17) illustrates that the effective non-resonant Rabi frequency of this transfer $\Omega_{\text{eff}} = \sqrt{\Omega_r^2 + \Delta_p^2}$ is very fast, thus on time average we constantly find only a tiny fraction of population in the intermediate state $|p\rangle$. Therefore the intermediate state can be virtually eliminated by setting the time derivative coefficient to zero ($\dot{c}_p(t) = 0$) and substituting all terms with $c_p(t)$ into terms with only $c_g(t)$ and $c_e(t)$. This enables us to rewrite the Hamiltonian in the basis of $|g\rangle$ and $|e\rangle$ with its time dependent coefficients $c_g(t)$ and $c_e(t)$ as

$$H = \hbar \begin{pmatrix} \frac{\Omega_r^2}{4\Delta_p} & \frac{\Omega_r\Omega_b}{4\Delta_p} \\ \frac{\Omega_r\Omega_b}{4\Delta_p} & \frac{\Omega_b^2}{4\Delta_p} - \Delta \end{pmatrix}. \tag{1.23}$$

By comparing this Hamiltonian with the Hamiltonian of the two-level system (1.18) we can determine the effective resonant Rabi frequency, coupling the ground to the excited state of our system:

$$\Omega_{\text{eff},0} = \frac{\Omega_r\Omega_b}{2\Delta_p}. \tag{1.24}$$

For the effective non-resonant Rabi frequency we have to take into account the effective detuning Δ_{eff} which consists of the two-photon detuning to the excited state Δ and the light shift Δ_{ac}:

$$\Omega_{\text{eff}} = \sqrt{\Omega_{\text{eff},0}^2 + \Delta_{\text{eff}}^2}\,; \quad \Delta_{\text{eff}} = \Delta + \underbrace{\frac{\Omega_r^2 - \Omega_b^2}{4\Delta_p}}_{\Delta_{\text{ac}}}. \tag{1.25}$$

The effective resonant Rabi frequency $\Omega_{\text{eff},0}$ plays a crucial role for the experiment and is calculated from the single Rabi frequencies of both laser systems. In the experiment the intermediate level detuning Δ_p is much larger than the single photon Rabi frequencies Ω_r and Ω_b, enabling us to neglect the ac Stark shift Δ_{ac}. Thereby the effective detuning Δ_{eff} becomes Δ.

1.3 Electric and magnetic fields and their influence on Rydberg atoms

As discussed in section 1.1, the polarizability of Rydberg atoms scales with $\propto n^{\star\,7}$, thus small electric fields influence the Rydberg atoms tremendously. We first treat the electric and the magnetic fields separately as a perturbation to the atomic Hamiltonian, which is sufficiently precise for weak electric and magnetic fields. Later we present a way of dealing with the whole Hamiltonian. The Stark map and B-field splitting is exemplarily shown in the following subsections for the ^{87}Rb $42D_{5/2}$ state.

To characterize our Rydberg states we use the set of quantum numbers (n, l, J, m_J) taking into account the fine splitting, where l is the angular quantum number, J the total quantum number including the spin s and m_J the magnetic quantum number. In contrast to the fine structure splitting, the hyperfine splitting does not play a role for Rydberg states, since it is very small in comparison to the fine splitting. The hyperfine structure scales as $\propto 1/n^{\star\,3}$ [46, 56] for S and P-states. Using the formula $\Delta_{\text{hfs}} = 33.59\,\text{GHz} \times n^{\star -3}$ for ^{87}Rb from reference [56] we calculate a hyperfine structure splitting of around 572 kHz for the $42S$ state. Since we are only interested Rydberg D-states in this thesis, which have a much smaller hyperfine structure which has not even been measured for $l > 1$ [46] yet, we can neglect the hyperfine splitting in the description of our Rydberg atoms.

1.3.1 Stark effect

Exposing the Rydberg atoms to an electric field results in the appearance of an additional term $H_{\mathcal{E}}$ in the Hamiltonian

$$H = H_0 + H_{\mathcal{E}} = H_0 + \vec{d} \cdot \vec{\mathcal{E}}, \tag{1.26}$$

which consists of the dipole moment $\vec{d} = -e\vec{r}$ and the electric field vector $\vec{\mathcal{E}}$. The Hamiltonian H_0 denotes the field-free Hamiltonian, including the kinetic energy term and the effective potential, which is the perturbed Coulomb potential of the core. In a first approximation we consider weak fields so that we can treat the additional electric Hamiltonian as a perturbation. This is valid if the Stark shift caused by the applied $\mathcal{E}$-field is small compared to the level spacing of the unperturbed system. In this case we can expand the dipole moment in powers of the electric field $\mathcal{E}$ and get for the first order term in non-degenerate perturbation theory

$$\Delta E_{\text{linear Stark}} = \left\langle \psi_i \left| \vec{d} \cdot \vec{\mathcal{E}} \right| \psi_i \right\rangle, \tag{1.27}$$

in which ψ_i is the initial state and an eigenfunction of the field-free Hamiltonian H_0. This wavefunction is defined as

$$\psi_i = |nlm\rangle = R_{n,l}(r) Y_l^m(\Theta, \varphi) \tag{1.28}$$

and comprises of the radial part of the electron wavefunction $R_{n,l}(r)$ and the spherical harmonic $Y_l^m(\Theta, \varphi)$, representing the angular part of the Rydberg state. Due to electric dipole transition rules, only transitions with $\Delta l = \pm 1$ are allowed, which cancel this first order term. Only high-l

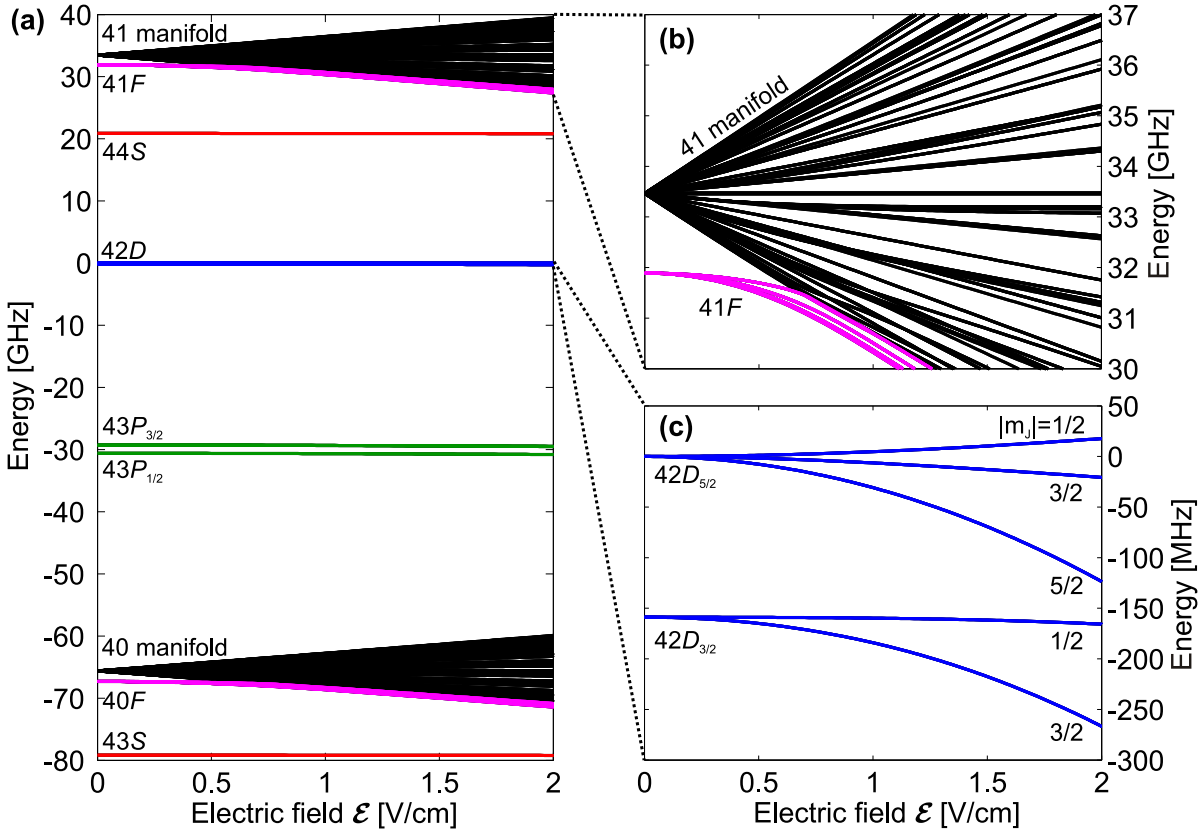

Figure 1.2: Stark maps showing all states in vicinity to the $42D$ state without any applied B-field. In (a) an overview of the Rydberg states in the energetic vicinity of the $42D$ state is given, color-coded depending on their angular momentum quantum number l. The zoom into the area around 33 GHz in (b) depicts the 41 high-l state manifold, which shows a linear Stark effect. For small electric fields the high-l states show a quadratic behavior which changes into a linear one for larger fields, clearly visible for the $41F$ state. All $l \leq 4$ states show only a quadratic Stark effect as depicted in (c) where exemplarily a magnification of the $42D$ states are shown. For all three graphs the atomic $42D_{5/2}$ state was chosen as the zero level for the energy axis. The Stark map was calculated with the program `rydLib` [57].

states ($l > 4$) which are degenerate and possess basis states with different parity feature a linear Stark effect like hydrogen atoms. All other states exhibit a quadratic Stark effect in the electric field $\mathcal{E}$ given by the second order term

$$\Delta E_{\text{quadratic Stark}} = \sum_{f \neq i} \frac{\left| \left\langle \psi_f \left| \vec{d} \cdot \vec{\mathcal{E}} \right| \psi_i \right\rangle \right|^2}{E_f - E_i} = -\frac{1}{2} \alpha |\vec{\mathcal{E}}|^2, \tag{1.29}$$

where α is the polarizability (in general it is a matrix) and ψ_i, ψ_f are the initial and final states, respectively. Here the sum goes over all possible final states and is divided by $E_f - E_i$, the corresponding energy difference between final and initial state. Thus only states near to the initial state have a sufficiently large contribution to the Stark effect.

For large electric fields when the Stark effect becomes of the same order of magnitude

as the fine structure splitting, perturbation theory is no longer valid and the whole electric Hamiltonian $H_{\mathcal{E}}$ needs to be diagonalized to calculate the Stark effect, since the off-diagonal entries begin to play an important role. This diagonalization was carried out for the calculation of a Stark map, for which the eigenenergies of the states are plotted versus the electric field. We used the program `rydLib` (see reference [57] for details) to obtain the Stark map, which is depicted in Figure 1.2. Due to their degeneracy, high-l states depict a linear Stark effect. This gives rise to the fan-like structure in Figure 1.2(b). The $l \leq 3$ states show only a quadratic Stark effect, clearly visible for the $42D$ states in Figure 1.2(c). They split in the electric field and can be described by the magnetic quantum number $|m_J|$, which is the absolute value of the projection of the total angular momentum J on the quantization axis of our system.

A large electric field is used for our ion detection. Here we ionize the Rydberg atom in order to strip the Rydberg electron from its ionic core. More about ionization and detection can be found in the setup section 6.1.

1.3.2 Zeeman shift and Paschen-Back regime

Applying a weak magnetic field, one can again consider the additional Hamiltonian H_B as a perturbation similar to the treatment of the weak electric field in the previous subsection 1.3.1. The total Hamiltonian can be written as

$$H = H_0 + H_B = H_0 - \vec{\mu} \cdot \vec{B}, \tag{1.30}$$

where H_0 is the field-free Hamiltonian, $\vec{\mu}$ is the magnetic dipole moment and B the applied external magnetic field. For the magnetic dipole transition the rules for the quantum numbers are $|\Delta n| = 0$, $|\Delta L| = 0$, $|\Delta J| = 0, 1$ and $|\Delta m_J| = 0, 1$. Thus the first order approximation is sufficient and not vanishing. We define the total angular momentum $J = L + S$ as the sum of the orbital momentum L and the spin momentum S. We can now split the magnetic dipole moment into these two contributions:

$$\vec{\mu} = -\mu_B \vec{J} = -g_l \mu_B \vec{L} - g_s \mu_B \vec{S}. \tag{1.31}$$

Here $g_l = 1$ is the Landé g-factor of the orbital angular momentum, $g_s \approx 2$ of the spin angular momentum and μ_B is the Bohr magneton. In the vector model we now project the magnetic moment onto $\vec{J}$, choosing z as quantization axis of the magnetic field ($\vec{B} = B\hat{e}_z$) [50]:

$$H_B = \frac{\left\langle \vec{L} \cdot \vec{J} \right\rangle + 2 \left\langle \vec{S} \cdot \vec{J} \right\rangle}{J(J+1)} \mu_B B J_z. \tag{1.32}$$

Evaluating the time averages and projections onto the states, the Zeeman energy can be calculated:

$$E_{ZE} = g_J m_J \mu_B B. \tag{1.33}$$

State	g	m	ΔE_{ZE}	ΔE_{split}
$nD_{5/2}$	$g_J = \frac{6}{5}$	$m_J = \frac{5}{2}$	$6\mu_B B = 113.8\,\text{MHz}$	$\frac{6}{5}\mu_B B = 22.8\,\text{MHz}$
$nD_{3/2}$	$g_J = \frac{4}{5}$	$m_J = \frac{3}{2}$	$\frac{12}{5}\mu_B B = 45.5\,\text{MHz}$	$\frac{4}{5}\mu_B B = 15.2\,\text{MHz}$
$nS_{1/2}$	$g_J = 2$	$m_J = \frac{1}{2}$	$2\mu_B B = 37.9\,\text{MHz}$	$2\mu_B B = 37.9\,\text{MHz}$
$5S_{1/2}$	$g_F = \frac{1}{2}$	$m_F = 2$	$2\mu_B B = 37.9\,\text{MHz}$	$\frac{1}{2}\mu_B B = 9.5\,\text{MHz}$

Table 1.3: Zeeman energy shifts for the experimentally relevant Rydberg states $nD_{5/2}$, $nD_{3/2}$, $nS_{1/2}$ (in the basis of (n, L, J, m_J)) and the ground state $5S_{1/2}$ (in the basis of (n, L, F, m_F)). Furthermore the Landé factors, secondary magnetic moments, the total Zeeman splitting and the energy difference between two neighboring Zeeman split states are shown. The values for the energies were calculated for a magnetic field of $B = 13.55\,\text{G}$, which was used in all experiments conducted in this thesis.

Here m_J is the secondary magnetic quantum number and the Landé factor g_J is given by

$$g_J = \frac{3}{2} + \frac{S(S+1) - L(L+1)}{2J(J+1)}. \tag{1.34}$$

Note that the Zeeman shift depends only linear on the magnetic field B and that $|m_J|$ defines the energy splitting. In the experiments in this thesis we always used the maximum possible magnetic offset field of $B = 13.55\,\text{G}$ and focused on investigating $D_{5/2}$-states. In Table 1.3 the calculated Zeeman splittings for different states are shown. Additionally the energy of the Zeeman splitting between two neighboring m_J levels ΔE_{split} is given, which can be compared to actual measurements.

In Figure 1.3 a spectrum of the $42D_{5/2}$ state is presented, revealing the six Zeeman split m_J states ranging from $-5/2$ to $+5/2$ (peaks labeled in black) with an average energy difference of $22.1\,\text{MHz}$ between neighboring levels. This experimental value shows only a deviation of $2.8\,\%$ to the theoretically predicted one (see Table 1.3), which is explained by the uncertainty of our experimentally applied B-field of $13.55 \pm 0.1\,\text{G}$ and the error in the determination of the peak positions of the spectral lines. In the spectrum there are also additional peaks visible (green labeled), which stem from the transitions from the state $5S_{1/2}$ ($F = 2, m_F = 1$) to the excited $42D_{5/2}$ Rydberg state. The reason for the small population of this other m_F ground state arises from the cooling process and is in detail discussed in chapter 4. A very high laser power was used to acquire this spectrum in order to resolve also the weakly coupled states. Due to the σ^--polarization of the blue $480\,\text{nm}$ laser the $m_J = 1/2$ state is the most populated state, not so clearly visible in the spectrum since the detector was saturated. Additionally sidebands of $\pm 20\,\text{MHz}$ apart from the spectral lines can be detected in the spectrum, which arise from the Pound-Drever-Hall locking scheme of our lasers, explained in chapter 5.

It is important that the applied perturbation theory is only valid if the energy shift caused by the Zeeman effect is small compared to the fine structure splitting of the spin-orbit coupling. The spin-orbit coupling can be estimated using the Landé formula, which is an empirical

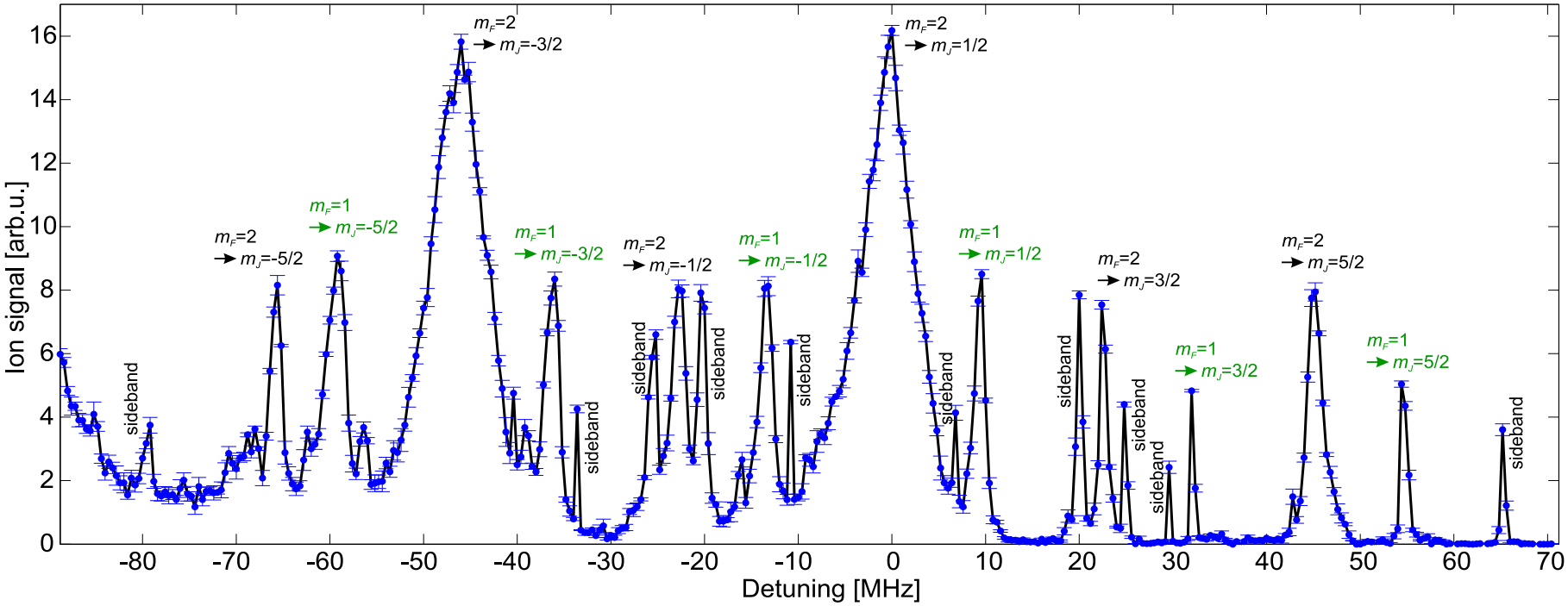

Figure 1.3: Spectrum of the $42D_{5/2}$-state taken with σ^--polarized 480 nm laser light. This spectrum was recorded with a very high laser power and for a high magnetic offset field of 13.55 G, so that all transitions from the ground state $5S_{1/2}(F = 2, m_F = 2)$ to the different $42D_{5/2}(m_J = -5/2 \ldots + 5/2)$ levels are visible. Since we have a small finite population of the $5S_{1/2}(F = 2, m_F = 1)$ ground state atoms in our samples, we also excite their transitions to the final m_J-states. This is the reason for the additional lines, shifted by $\mu_B B/(2h) = 9.5\,\mathrm{MHz}$ from the lines excited by the $F = 2, m_F = 2$ ground state atoms. Furthermore we also see some of the modulated sidebands $\pm$ 20 MHz apart from the transition lines, generated by our Pound-Drever-Hall locking scheme (see chapter 5). The strongest transition $5S_{1/2}(F = 2, m_F = 2) \rightarrow 42D_{5/2}(m_J = 1/2)$ marks the origin of the spectrum. The black line connecting the data points is a guide to the eye. The error bars (standard deviation) were determined from 5 independent measurements.

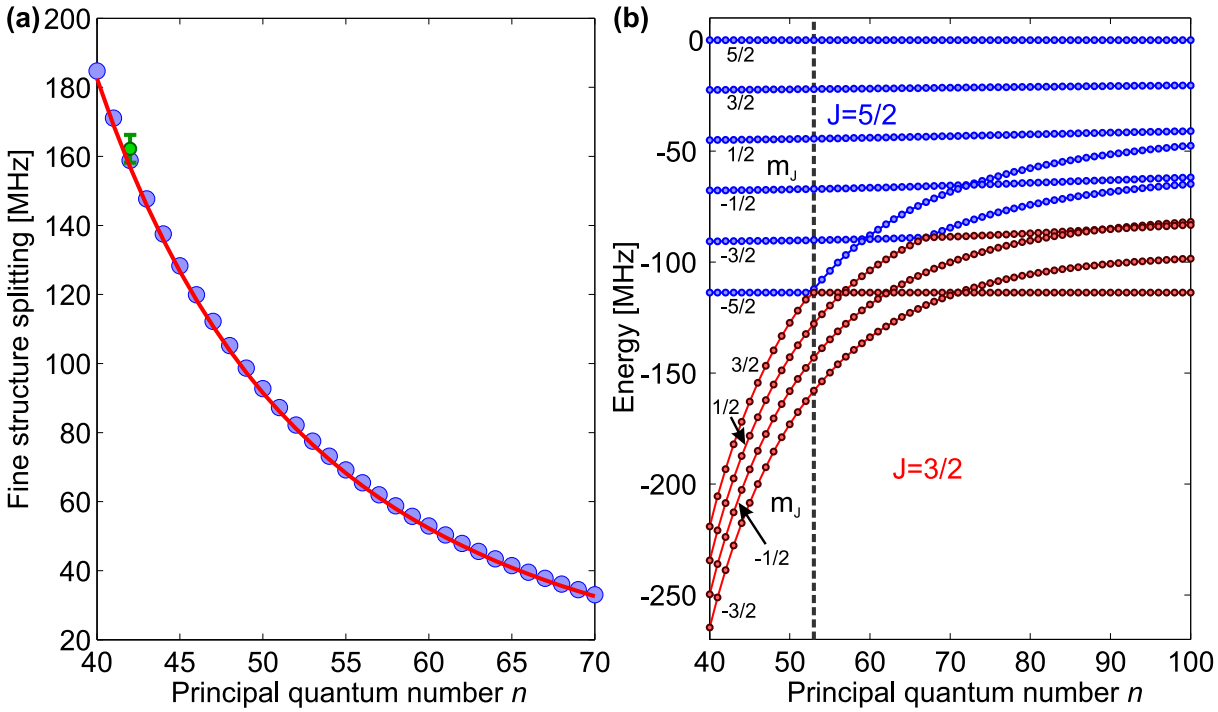

Figure 1.4: In (a) the fine structure splitting between the $nD_{5/2}$ and $nD_{3/2}$ state was calculated in two different ways. A computation of the fine structure by the program `rydLib` (details in the text) yielded the blue circles for principal quantum number n ranging from 40 to 70, whereas the red line was acquired using the empirical formula (1.35) with the effective atomic number $Z_{\text{eff}} = 19$. The effective atomic number was obtained by fitting this integer parameter to the measured data point for $n = 42$ (green circle). In (b) the energies of the ten different m_J sublevels of $nD_{5/2}$ and $nD_{3/2}$ are shown with increasing principal quantum number n, causing a decrease in the fine structure splitting as seen in (a). Note that the finite resolution of the energy axis is responsible that these m_J levels seem to cross. These are no 'real' crossings. The $nD_{5/2}, m_J = 5/2$ state always marks the zero energy position and a magnetic field of 13.55 G was used for the calculation. The lines connecting the calculated data points are guides to the eye.

modification of the hydrogen formula [50]:

$$\Delta E_{FS} = \frac{Z_{\text{eff}}^2}{(n^\star)^3 l(l+1)} \alpha^2 hcR_\infty. \tag{1.35}$$

Here $\alpha = e^2/(4\pi\epsilon_0\hbar c) \approx 1/137$ is the fine-structure constant, R_∞ the Rydberg constant (1.2) and Z_{eff} is the effective atomic number. The latter tends to the value of the atomic number Z in the approximation $r \to 0$, in our case for rubidium towards 37, while in the other limit, when the electron is far away from the core, Z_{eff} goes to 1. Since there is no way to predict this number apart from sophisticated numerical simulations of the core potential, we use this unknown integer variable as a fitting parameter to the experimental data point. In Figure 1.4(a) the green circle marks the experimental measurement of the fine structure between the $42D_{5/2}$ and $42D_{3/2}$ state. Using the effective atomic number $Z_{\text{eff}} = 19$ in equation (1.35) (red line in Figure 1.4(a)) we acquire the best match with the experimental data point. Furthermore we cal-

culated the fine structure using the program `rydLib`, which uses an effective core potential to calculate the field-free Hamiltonian H_0 in equation (1.26) (see [57] for details). These results are represented by the blue circles in Figure 1.4(a) and they match very well to the empirical formula (red line) and experimental data point (green circle).

It is crucial to know quantitatively when the perturbation theory to calculate the Zeeman shift breaks down and is not valid anymore. As we stated as a general remark before, as long as the Zeeman splitting is small compared to the fine structure splitting of the spin-orbit coupling, perturbation theory is sufficient. To test its limit we use a constant magnetic field of $B = 13.55\,\mathrm{G}$ and increase the principal quantum number n to lower the fine structure splitting further and further. Since the fine structure splitting scales with $\Delta E_{FS} \propto {n^\star}^{-3}$ we thus come into a regime where the Zeeman splitting is equal to the fine structure splitting and perturbation theory becomes invalid. We calculated the experimental accessible fine structure between the $nD_{5/2}$ and $nD_{3/2}$ states with the program `rydLib` (see [57] for details) by diagonalizing the full Hamiltonian of our system. The result can be seen in Figure 1.4(b). The six blue states are the m_J-split states of $nD_{5/2}$, whereas the four red states are the states of $nD_{3/2}$. At $n = 53$, marked as the dashed gray line in Figure 1.4(b), the Zeeman splitting of the fine structure deviates more than 5 % from its original value (see Table 1.3). Starting at this value of n the perturbation theory cannot be trusted any longer and one has to fully diagonalize the Hamiltonian (1.30) to gain the correct results for the energy splitting of the states. This behavior of the states at high n is the same as if one would apply a very large magnetic field for low n states. We then enter the so called Paschen-Back regime, in which the electron spin S and angular momentum L do not couple to a total angular momentum J anymore because J is no longer a good quantum number. Here S and L have to be treated independently from each other, leading to non-equidistant energy splittings as seen in Figure 1.4(b) for $n \geq 53$. From a more mathematical point of view, when we enter the Paschen-Back regime the off-diagonal terms in B-field Hamiltonian H_B are not zero anymore but start to mix with the Zeeman energies in the diagonal of the matrix.

1.3.3 Combined electric and magnetic fields

In our experiment the atoms are held in a magnetic trap, which means that we always have to deal with a finite magnetic offset field. Applying an additional electric field, for example for recording Stark maps, we end up with a Hamiltonian, in which both fields have to be included. The Hamiltonian of the system

$$H = H_0 + H_\mathcal{E} + H_B \tag{1.36}$$

is then composed of the field-free Hamiltonian H_0 and the interaction Hamiltonian with the electric $H_\mathcal{E}$ and magnetic field H_B. For small electric and magnetic fields and low principal quantum numbers, these terms can be treated perturbatively with respect to H_0. As soon as the intermixing starts and the shifts are comparable, the best way to treat this problem is a diagonalization of the full Hamiltonian, in detail described in the thesis of B. Butcher [57]. In the experiment the electric field is always applied along the z-axis which is also the axis of our magnetic field. Since no setup is perfect a slight misalignment or inhomogeneities might cause a small deviation of the angle $\Theta_{\mathcal{E}B}$ between the electric and magnetic field vectors from zero degrees. This leads to an admixture of electric and magnetic dipole matrix elements. One now has

to calculate the projection of the electric and magnetic dipole moment onto the z-axis as conducted in [57, 58] and then diagonalize the full Hamiltonian of the problem. These additional couplings can trigger avoided crossings [59] whose strength depends on the angle $\Theta_{\mathcal{E}B}$.

1.4 Lifetimes of Rydberg atoms

Two main decay processes define the lifetimes of Rydberg atoms: the spontaneous decay and black-body radiation induced decay. The effective lifetime τ_{eff} can be calculated by

$$\tau_{\text{eff}} = \left(\frac{1}{\tau_{\text{rad}}} + \frac{1}{\tau_{\text{bb}}} \right)^{-1}, \tag{1.37}$$

where τ_{rad} is the radiative lifetime caused by spontaneous decay and τ_{bb} is the black-body radiation part, which is only important for temperatures $T > 0\,\text{K}$. For a simple two level system the radiative lifetime τ_{rad} of the excited state $|nl\rangle$ is determined by the inverse of the Einstein A-coefficient:

$$\tau_{\text{rad}} = \frac{1}{A(n, l \to n', l')} = \frac{3\pi\epsilon_0\hbar c^3}{\omega^3_{n,l,n',l'} |\langle n'l'| \vec{d} |nl\rangle|^2}. \tag{1.38}$$

Here $|n'l'\rangle$ stands for the target state of the decay, $\omega_{n,l,n',l'} = |E_{n',l'} - E_{nl}|/\hbar$ is the transition frequency and $\langle n'l'| \vec{d} |nl\rangle$ the dipole matrix element of the two level system, which can be obtained from the program `rydLib` (see [57] for details). Since there is not only one state, to which the excited state can decay we have to sum over all lower lying states $|n'l'\rangle$ to get the radiative lifetime:

$$\tau_{\text{rad}} = \left(\sum_{|E_{n,l}| < |E_{n',l'}|} A(n, l \to n', l') \right)^{-1}. \tag{1.39}$$

First measurements and theoretical calculations of the radiative lifetimes for alkali atoms date back to the 1970s [60, 61]. An empirical formula found by J. Deech and coworkers [61] with two fitting parameters yields a good approximation to the experimentally measured lifetimes and thus is still used nowadays [62]:

$$\tau_{\text{rad}} = \tau' n^{\star\gamma}. \tag{1.40}$$

Here τ' and γ are the two parameters fitted to the experimentally obtained lifetimes. A Table comparing the experimental and theoretical values for these parameters can be found in [57]. In general the radiative lifetime scales with $n^{\star 3}$ for low-l states [31]. For high l states the scaling of the average radiative lifetime changes to $\bar{\tau}_{\text{rad}} \propto n^{\star 4.5}$ [31].

As soon as the temperature is non-zero, black-body radiation begins to play a role since the excited state can couple to neighboring states due to the thermal energy in the system. W. Cooke and T. Gallagher extended the lifetime radiation model by introducing this new decay mechanism [63]. In the presence of thermal radiation the stimulated emission rate $W(n, l \to n', l')$ can be calculated as the number of photons in the black-body radiation

multiplied by the Einstein A-coefficient for the spontaneous decay:

$$W(n, l \to n', l') = \tilde{N}(\omega_{n,l,n',l'}, T) \cdot A(n, l \to n', l'). \tag{1.41}$$

The photon number per mode

$$\tilde{N}(\omega_{n,l,n',l'}, T) = \frac{1}{\exp\left(\frac{\hbar\omega_{n,l,n',l'}}{k_B T}\right) - 1} \tag{1.42}$$

is obtained by using the Planck distribution at temperature T. For the black-body radiation we have to consider both, lower and higher lying states for the sum over all possible transitions. In analogy to the equation for the spontaneous decay (1.39) we can write τ_{bb} as

$$\tau_{\text{bb}} = \left(\sum_{n'l'} W(n, l \to n', l')\right)^{-1} = \left(\sum_{n'l'} \frac{A(n, l \to n', l')}{\exp\left(\frac{\hbar\omega_{n,l,n',l'}}{k_B T}\right) - 1}\right)^{-1}. \tag{1.43}$$

In first approximation the black-body induced lifetimes scales as $\tau_{\text{bb}} \propto n^{\star 2}$ [31]. Knowing both contributions, the effective lifetime according to equation (1.37) can be calculated. An analytical equation containing the numerical fitting parameters A, B, C, D, τ' and γ, derived from fits to numerical simulations, was given by I. Beterov and coworkers [64]:

$$\tau_{\text{eff}} = \left(\frac{1}{\tau' n^{\star\gamma}} + \frac{A}{n^{\star D}} \frac{21.4}{\exp\left(315780B/(n^{\star C}T)\right) - 1}\right)^{-1} [\text{ns}]. \tag{1.44}$$

Note that this equation is given in the units of nanoseconds and was only tested up to $n = 80$ by a comparison to numerical simulations. Nevertheless we use this formula as an estimate for the lifetimes of our high $n > 100$ Rydberg atoms. In subsection 9.2.1, the estimated lifetimes calculated by equation (1.44) will be compared to the lifetimes obtained by the experimental measurements for the $S_{1/2}$- and $D_{5/2}$-states at very high principal quantum numbers around $n = 110$ and 180. Furthermore, we will discuss additional mechanisms reducing the lifetimes in the Bose-Einstein condensate measurements.

1.5 Interactions between Rydberg atoms

Due to the Rydberg electrons being very close to the ionization limit, the interaction between two Rydberg atoms is very strong, which makes them the ideal building block for quantum information and simulation [41]. In Figure 1.5(a) the famous plot of the review article by M. Saffman and T. Walker [41] is depicted, where the binary interaction strength is plotted versus the interparticle distance R of two ground state rubidium atoms, Rb atoms excited to the $100S$-state and ions (Coulomb interaction). It is noteworthy that the interaction strength of two Rydberg atoms at high principal quantum number is more ion-like, due to the far out electron, and is twelve orders of magnitude larger than the interaction strength of two ground state atoms. Just by the excitation of Rydberg atoms it is possible to change between these two interaction regimes, offering a powerful tool to manipulate the interaction strength in the system.

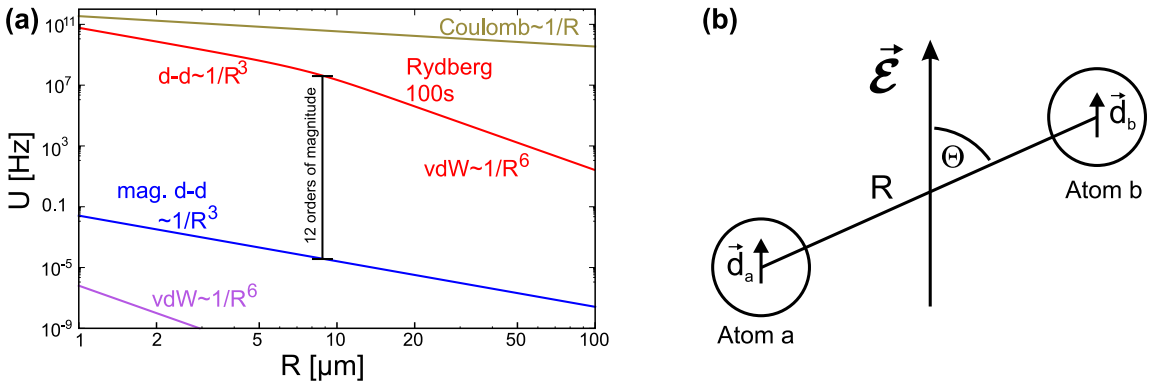

Figure 1.5: (a) Comparison of the two-body interaction strength for ground-state rubidium atoms, Rb atoms excited to the $100S$-state and ions. This Figure was taken from [41]. (b) Geometry of the Rydberg atoms a and b with their dipole moments $\vec{d}_a$ and $\vec{d}_b$ and quantization axis along the electric field $\vec{\mathcal{E}}$. The angle Θ is defined between the electric field direction and the interatomic axis.

We now define two non-overlapping Rydberg atoms a and b in their respective states $|n_a l_a j_a m_a\rangle$ and $|n_b l_b j_b m_b\rangle$ with their electric dipole moments $\vec{d}_a$ and $\vec{d}_b$. Then their interaction energy is given by the dipole-dipole interaction operator [65]

$$V_{\text{dd}} = \frac{\vec{d}_a\vec{d}_b - 3(\vec{d}_a\vec{n})(\vec{d}_b\vec{n})}{4\pi\epsilon_0 R^3}, \tag{1.45}$$

where $\vec{R} = R\vec{n}$ is the vectorial distance between atoms a and b. The dipole moment $\vec{d} = (d_x, d_y, d_z)$ can be written in a spherical basis as

$$d_+ = \frac{1}{\sqrt{2}}(d_x + id_y)\ ; \quad d_- = \frac{1}{\sqrt{2}}(d_x - id_y)\ ; \quad d_z = d_z. \tag{1.46}$$

Using the coordinate system depicted in Figure 1.5(b), we can express the unit vector connecting the atoms as $\vec{n} = \sin\Theta \cdot \vec{e}_x + \cos\Theta \cdot \vec{e}_z$, where $\vec{e}_{x,z}$ are the unit vectors in x- and z-direction. Following the steps of [66], the dipole-dipole interaction operator can be rewritten as

$$\begin{aligned} V_{\text{dd}} =& \frac{d_{a+}d_{b-} + d_{a-}d_{b+} + d_{az}d_{bz}(1 - 3\cos^2\Theta)}{4\pi\epsilon_0 R^3} \\ &- \frac{\frac{3}{2}\sin^2\Theta(d_{a+}d_{b+} + d_{a+}d_{b-} + d_{a-}d_{b+} + d_{a-}d_{b-})}{4\pi\epsilon_0 R^3} \\ &- \frac{\frac{3}{\sqrt{2}}\sin\Theta\cos\Theta(d_{a+}d_{bz} + d_{a-}d_{bz} + d_{az}d_{b+} + d_{az}d_{b-})}{4\pi\epsilon_0 R^3}. \end{aligned} \tag{1.47}$$

The first subscript of the electric dipole moment denotes the atom a or b, whereas the second subscript indicates the polarization, which can either be circular $(+,-)$ or linear (z). We now want to focus on the case where the two Rydberg atoms a and b are excited to the same energy level, so that $n_a = n_b$, $l_a = l_b$, $j_a = j_b$. The dipole-dipole interaction causes the reaction [67]

$$|n_a l_a j_a\rangle + |n_a l_a j_a\rangle \rightarrow |n_s l_s j_s\rangle + |n_t l_t j_t\rangle \tag{1.48}$$

with the energy difference

$$\Delta_F = E(n_s l_s j_s) + E(n_t l_t j_t) - 2E(n_a l_a j_a) \tag{1.49}$$

between the initial (a,a) and final (s,t) two-atom states. This energy difference is the so-called Förster energy defect.

For the first case we want to investigate we assume a large interatomic distance R and a non-zero Förster defect. Then the energy shifts of the initial states are determined by the van der Waals interaction [67]

$$H_{\text{vdW}} = -\sum_{s,t} \frac{V_{\text{dd}} \left|st\right\rangle \left\langle st\right| V_{\text{dd}}}{\Delta_F} = -\frac{C_6}{R^6} D, \tag{1.50}$$

derived in second order perturbation theory where the sum goes over all possible final states s and t including the full set of quantum numbers. The variable D contains all the angular properties of the states. It is crucial that this operator acts on a degenerate set of Zeeman sublevels of the two-atom initial state $|aa\rangle$. Note that the degeneracy of the Zeeman substates was not taken into account in reference [66]. There are various collision channels, like for example $D_{5/2} + D_{5/2} \rightarrow P_{3/2} + F$, for which this degeneracy plays an important role. A list with all relevant and possible channels can be found in reference [67]. The calculation of the van der Waals interaction can be split into the computation of the radial part, the C_6 coefficient

$$C_6 = \sum_{n_s, n_t} \frac{e^4}{(4\pi\epsilon_0)^2 \Delta_F} (R^{n_s l_s}_{n_a l_a} R^{n_t l_t}_{n_a l_a})^2, \tag{1.51}$$

where $R^{n_s l_s}_{n_a l_a}$ are the multiplied radial electron wavefunctions of the states a and s and a part D (1.50), containing all the angular properties of the states. We define the $(2j+1)^2$ two-atom eigenstates for the operator D as $|\varphi\rangle$ with the eigenenergies D_φ giving rise to the eigenvalue equation [67]

$$H_{\text{vdW}} \left|\varphi\right\rangle = \frac{C_6}{R^6} D_\varphi \left|\varphi\right\rangle . \tag{1.52}$$

Since the interaction Hamiltonian (1.50) is indirectly proportional to the energy defect, only nearby levels need to be considered for the calculations. The sign of this energy defect Δ_F makes the interaction either attractive or repulsive. Due to the scaling of the dipole moment $\vec{d} \propto n^{\star\,2}$ and $\Delta_F \propto n^{\star\,-3}$ the van der Waals coefficient C_6 scales like $n^{\star\,11}$. The angular dependence D in equation (1.50) will be important for the studied D-states in this thesis. For all different reaction channels, calculations for the eigenvalues of operator D can be found in [67].

In the second case we analyze the interaction for a very small Förster defect $\Delta_F \rightarrow 0$, leading to a strong dipole-dipole coupling. In this limit the energy shift is given by [67]

$$V_{\text{Förster}} = \pm \frac{C_3}{R^3} \sqrt{D_\varphi}. \tag{1.53}$$

Here the most important fact with respect to our experiment is, that by changing the energy defect between two pair states, one can change the character of the interaction from a van der Waals $1/R^6$ type to a pure dipole-dipole type, which scales as $1/R^3$. One can also alter the sign of the interaction by going to different sides of the Förster resonance. To tune these Rydberg states in or out of resonance small electric fields [68, 69, 70, 71, 72, 73, 74] or microwaves [75, 76] are sufficient. This resonant energy transfer process plays an important role in biological systems (e.g. light harvesting complexes [77]) and was recently modeled and observed in a cloud of Rb Rydberg atoms [78]. A more detailed discussion of this topic can be found in reference [58].

Rydberg blockade and collective oscillations

The strong van der Waals or dipole-dipole interaction between Rydberg atoms has a strong impact on a large sample of atoms which can be excited to the Rydberg state. If one Rydberg atom is excited by Rabi frequency Ω to the Rydberg state, the excitation of another one is only possible at a certain distance r_B, the so-called blockade radius. The reason is the interaction energy shift of the Rydberg level depicted in Figure 1.6. Thus, without detuning the excitation laser, an excitation of a second Rydberg atom in distance r to the first excited Rydberg state is only possible if the excitation bandwidth $\hbar\Delta\omega$ of the laser is larger than the interaction energy E_{int}

$$\hbar\Delta\omega \geq |E_{\text{int}}|. \tag{1.54}$$

If we assume an isotropic van der Waals interaction ($D = 1$ in equation (1.50)) for E_{int}, the blockade radius can be estimated by

$$r_B = \sqrt[6]{\frac{C_6}{\hbar\Delta\omega}} \tag{1.55}$$

and defines a sphere around the first Rydberg atom, in which any further excitation is forbidden. Sources for the excitation bandwidth of the laser can be power broadening or the Fourier width of the laser pulse. This dipole blockade effect plays an important role in quantum information and simulation [41] and also in our experimental work described in chapter 9. One has to be careful using formula (1.55), since it neglects the angular dependence of the dipole moments and it thus only valid for S-states. If we go to D-states, which we studied in the experiment, we have to take into account the angle Θ, defined between the quantization axis (in our case the z-axis determined by the excitation lasers) and the internuclear axis between the pair states (see Figure 1.5(b)). A calculation for our D-Rydberg states, taking into account the degeneracy of the Zeeman substates in our magnetic field of $13.55\,\text{G}$ and an angle $\Theta \neq 0$, is very sophisticated, since we end up with more than 20000 eigenstates, which makes the diagonalization cumbersome [79]. One has to come up with a transformation to an advantageous basis for the eigenstates to reduce the computing time significantly and we would have to perform this calculation for all possible angles Θ to obtain an estimate for the van der Waals interaction and thereby the blockade radius. This goes beyond the scope of this thesis and was not carried out by any theory group yet.

If there is more than one single ground state atom inside the blockade radius, the excita-

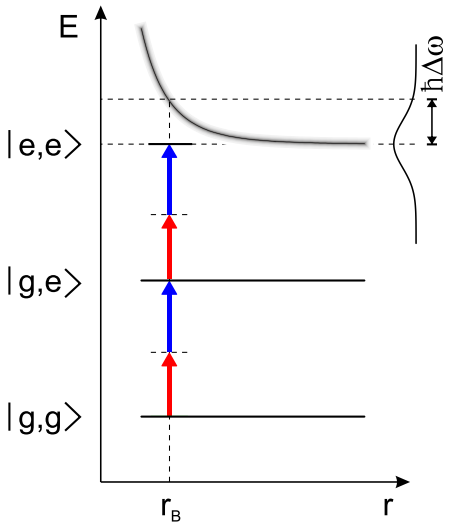

Figure 1.6: Two-photon excitation scheme, illustrating the Rydberg blockade effect. The energies of a pair of ground state atoms $|g,g\rangle$, one excited and one ground state atom $|g,e\rangle$ and two Rydberg atoms $|e,e\rangle$ are plotted against the distance r between these two partners. Both two-photon excitations are marked with two arrows. Due to the interaction potential of the two Rydberg atoms (black line) additional energy is needed for the second excitation. Only for radii equal or larger than the blockade radius r_B the laser bandwidth $\hbar\Delta\omega$ provides sufficient energy to overcome the interaction potential and enables a second excitation.

tion dynamic of the two-level system is altered, due to the indistinguishability of the bosons. The excitation then becomes delocalized and equally shared between all N atoms inside the blockade sphere. We end up with a collective state given by

$$\left|\psi^{(N,1)}\right\rangle = \frac{1}{N}\sum_{i=1}^{N}|g_1, g_2, \ldots, e_i, \ldots, g_N\rangle, \tag{1.56}$$

where $|g\rangle$ denotes the ground and $|e\rangle$ the excited state. The notation $\psi^{(N,1)}$ indicates that the state consists of N atoms and one excited state/photon. In equation (1.56) all relative phases between the states have been set to the value 1. This approximation is valid as long as the distance between the atoms is smaller than the excitation wavelength. If we now treat this system as a two level system (see subsection 1.2.1) and calculate the matrix element for the transition between ground state $\psi^{(N,0)}$ and excited state $\psi^{(N,1)}$

$$\left\langle\psi^{(N,1)}\right| H_l \left|\psi^{(N,0)}\right\rangle = \sum_{i=1}^{N}\frac{\hbar}{2\sqrt{N}}\Omega = \sqrt{N}\frac{\hbar}{2}\Omega = \frac{\hbar}{2}\Omega_c, \tag{1.57}$$

we obtain an enhancement of the Rabi frequency by a factor $\sqrt{N}$, compared to the single atom matrix element in equation (1.18). The so-called collective Rabi frequency $\Omega_c = \sqrt{N}\Omega$ drives this effective two-level system, occasionally named 'super atom' [42]. This enhancement factor of the collective Rabi oscillation was observed for two atoms in 2009 in the group of P. Grangier [80] and more recently in 2012 for multiple atoms by A. Kuzmich and coworkers [81].

One has to be careful with the super atom description and the blockade effect, since this model takes into account only binary interactions. Already in case of three atoms and dipole interaction, there are configurations where the dipole blockade of the atoms can break down and two excitations are possible at the same time [82]. As soon as there are disturbances by electric field gradients or inhomogeneities in the density of the atoms, the atoms in one blockade sphere become distinguishable and this model of the collective excitation breaks down.

2 Formation of ultralong-range Rydberg molecules

Molecules are complex quantum-mechanical systems compared to single atoms due to their richer energy level structure. They feature vibrational and rotational degrees of freedom which arise from the fact that they consist of more than one atom. The spatial configuration of their constituent atoms is significant because based on their alignment and orientation chemical reactions can be enhanced or altered. Controlling their properties is a challenging task. Nevertheless they open new scientific directions such as the precise control of chemical reactions [83, 84, 85], studies of dynamics in low-energy collisions [86] or can even be building blocks of quantum systems for quantum information processing and computing [87, 88]. Furthermore molecules with different constituents offer even more flexibility with regard to their energy structure [89]. In ultracold environments the dynamics of particles are dominated by s-wave scattering and are thus easier to describe and control, as I am going to illustrate in this chapter. Our study of Rydberg molecules offers new opportunities for novel developments in the emerging field of ultracold quantum chemistry.

In the framework of this thesis we investigate the so-called species of Rydberg molecules, formed by a Rydberg atom and at least one ground state atom. They possess various interesting properties, like their enormous size, which is in the order of a few $\mu\mathrm{m}$, their high polarizability and many others, inherited by their constituent Rydberg atom. The binding mechanism is unique and different to the known classical chemical binding mechanisms of covalent, ionic and van der Waals binding and will be explained in detail in this chapter. Theoretically predicted in 2000 by C. Greene and coworkers [13], they were first discovered experimentally in 2009 in our group with the same experimental setup as used in this thesis [6]. Over the last years, many of their properties were analyzed, like their lifetimes, decay processes [90], the quantum reflection binding mechanism [45] and the emergence of a permanent dipole moment in homonuclear diatomic rubidium molecules [8]. Moreover the photoassociation of dimers and trimers was shown [45] and recently also the creation of pentamers [9], where four ground state atoms are bound to one Rydberg atom.

We extended the study from S- to D-state molecules, which possess different angular wavefunctions and are not anymore spherically symmetric and thus show new properties. Before showing the results of the measurements in section 8.1, the principle of the molecular binding mechanism (section 2.1) as well as the calculation of the potential energy landscapes, in which the molecules are formed (section 2.2), are presented. The calculations of these adiabatic potential energy landscapes (APES) were done in cooperation with M. Kurz and P. Schmelcher from the University of Hamburg. In section 2.3 the calculations of the binding energy of the rovibrational states in the APES, computed by a finite difference method, are presented and finally the last section 2.4 illustrates why the ion$-$ground state atom interaction can be neglected.

2.1 Electron-ground state atom interaction

As C. Greene and coworkers proposed in 2000 [13], the binding mechanism of ultralong-range Rydberg molecules originates from the scattering of the low energy Rydberg electron with ground state atoms. The treatment of such a scattering process goes back to E. Fermi who introduced in 1934 the concept of the scattering length and pseudopotential, which has been named after him [12, 91]. In the simplest approximation this potential can be written in the Fermi style

$$V_{\text{pseudo}}(\vec{r},\vec{R}) = \frac{2\pi\hbar^2 a}{m_e}\delta(\vec{r}-\vec{R}), \tag{2.1}$$

where $\vec{r}$ ($\vec{R}$) is the position of the Rydberg electron (ground state atom) relative to the ionic core, m_e the mass of the electron, a the s-wave scattering length between electron and ground state atom and δ the Dirac delta function. The derivation of formula (2.1) is described in detail in [11] and [92]. Here only the important assumptions, which lead to the pseudopotential equation are laid out. For this approximation it is important that the scattering event is treated as a binary interaction between the electron and the ground state atom. This is valid if the effective interaction range is small compared to the interparticle distance. For our experimentally achievable densities of up to $10^{14}\,\mathrm{cm}^{-3}$ this is well fulfilled, since the absolute value of the relevant triplet atom-electron scattering length for ^{87}Rb is $16.1\,a_0$ [93] and very small compared to the interparticle distance of 4000 to 19000 a_0, estimated by the formula $\bar{d} = \rho^{-1/3}$ for our densities. The second important fact is that the triplet scattering length $a_{\uparrow\uparrow} = -16.1\,\mathrm{a_0}$ has a negative sign, giving rise to an attractive potential, which is needed to bind these molecules. The small singlet scattering length $a_{\uparrow\downarrow} = 0.627\,\mathrm{a_0}$ has a positive sign and is thus repulsive. But due to its small value it does not play any role here and can be neglected in the further calculations. For the triplet scattering length the spins of the Rydberg electron and ground state atom are parallel, whereas for the singlet scattering length, they are anti-parallel. To calculate the corresponding scattering lengths with the short-ranged interaction potential which scales with $\propto 1/r^4$, more involved theory is needed [93]. The last approximation made is that all back-action effects of the ground state atoms on the Rydberg electron wavefunction were neglected. This effect is small, but can nevertheless lead to a permanent electric dipole moment in the case of a diatomic molecule [8].

Directly connected to formula (2.1) are the historic measurements of E. Amaldi and E. Segré, conducted in 1934, which led to the development of E. Fermi's theory of the pseudopotentials. In their measurements they observed a shift of the Rydberg absorption line due to the high pressure background buffer gas [36, 37]. Depending on the used type of background gas, they detected a red or a blue shift of the spectral line. If we sum equation (2.1) over all positions of the ground state atoms in the radius of the Rydberg atom and assume a constant density ρ of the background gas we get:

$$\Delta E(\rho) = \frac{2\pi\hbar^2 a}{m_e}\rho. \tag{2.2}$$

This formula describes well the dependence of the observed energy shift on the density of the background gas of E. Amaldi's measurements. Independently from E. Amaldi and E. Segré,

C. Füchtbauer and coworkers also detected the same red shifts for an argon buffer gas and blue shifts for helium and neon [40] in their experiments with the Alkali metals sodium and potassium. This behavior can be explained again by equation (2.2) with the different magnitude and sign of the scattering lengths: argon has, like rubidium, a negative scattering length, leading to a red shift, whereas helium and neon have a positive scattering length, giving rise to a blue shift [94]. To put it another way, one can identify the scattering length as a phase shift between ingoing and outgoing wavefunction from the region of interaction. Depending on whether the wavefunction is shifted inwards (negative scattering length) or outwards (positive scattering length) this gives rise to an attraction or repulsion of the two particles, respectively. In our experimental situation the rubidium ground state atoms adopt the role of the background gas and for a dense Bose-Einstein condensate we end up with a similar situation as E. Amaldi and E. Segré. We observed a red shift as well as a broadening of our spectral lines for Rydberg S-states at high principal quantum numbers $n > 80$ [9, 10]. For principal quantum numbers below 71 we could still resolve individual molecular lines in the thermal cloud spectra. Between these two numbers a change in the description of the system from discrete bound states to a mean field approximation is required [9]. In this thesis we extend the investigation from S- to D-state Rydberg atoms in a condensate which have a different angular electron distribution. The results of this study are presented in chapter 9.

Our goal is still the calculation of the molecular potential. We have seen that equation (2.1) transforms into (2.2) if many particles are inside the orbit of the Rydberg electron leading to a potential, which is proportional to the density of the background atoms. The other extreme is reached when there is on average only one or a few atoms inside the Rydberg electron wavefunction. To calculate now the molecular potential of one single ground state atom at position $\vec{R}$ we integrate equation (2.1) over the electron density $|\psi(\vec{r})|^2$:

$$V_{\text{mol}}(\vec{R}) = \int V_{\text{pseudo}}(\vec{r} - \vec{R})|\psi(\vec{r})|^2 d\vec{r} = \frac{2\pi\hbar^2 a}{m_e}|\psi(\vec{R})|^2. \tag{2.3}$$

In this equation $\psi(\vec{R})$ is the wavefunction of the Rydberg electron evaluated at the position of the ground state atom. Note that the molecular potential describes only the contribution to the 0^{th} order in the electron momentum $\hbar k$, the so-called s-wave contribution.

To include higher order effects, the scattering length a can be expanded by a modified effective range theory (MERT) [95, 96] into an energy dependent scattering length

$$a(k) = a_s + \frac{\hbar^2}{m_e e^2 a_0^2} \cdot \frac{\pi}{6}\alpha\, k(R) + \mathcal{O}(k^2), \tag{2.4}$$

where α is the polarizability of the ground state atom and $\hbar k$ the momentum of the Rydberg electron. If we include this scattering length up to first order in k into equation (2.3) we obtain

$$V_s(\vec{R}) = \frac{2\pi\hbar^2}{m_e}\left(a_s + \frac{\hbar^2}{m_e e^2 a_0^2}\frac{\pi}{6}\alpha k\right)|\psi(\vec{R})|^2. \tag{2.5}$$

This is the term for pure s-wave scattering just taking into account terms up to the first order of the electron momentum $\hbar k$. With the semiclassical approximation [97], the momentum of the

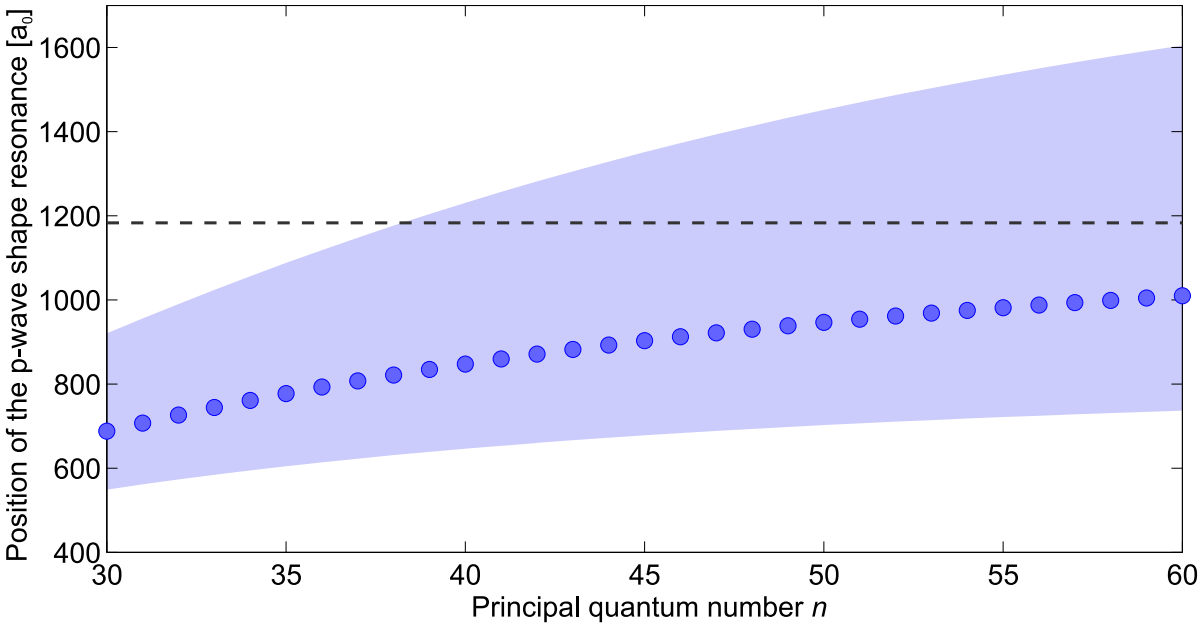

Figure 2.1: Position of the triplet p-wave scattering resonance. This position in units of a_0 was calculated for $nD_{5/2}$-states with a kinetic energy of the electron of 23 meV for principal quantum numbers $n = 30 - 60$. The affected area where this effect of the anticrossing has an influence is shaded in blue color. For high principal quantum numbers n the resonance position asymptotically goes to 1183 a_0, depicted as a black dashed line in the graph.

Rydberg electron can be calculated

$$\hbar k(R) = \sqrt{2E_{\text{kin}}(R)m_e} = \sqrt{-\frac{2m_e R_\infty hc}{n^{\star 2}} + \frac{e^2 m_e}{2\pi\epsilon_0 R}}; \quad \text{with} \quad E_{\text{kin}}(R) = -\frac{R_\infty hc}{n^{\star 2}} + \frac{e^2}{4\pi\epsilon_0}\frac{1}{R}. \tag{2.6}$$

If we allow for the second order term in the expansion of the electron−ground state atom interaction calculated by A. Omont [97], and sum up all terms to the first order of electron momentum $\hbar k$, the p-wave contribution to the molecular potential yields

$$V_p(\vec{R}) = -\frac{2}{5}\frac{e^2\pi^2}{(4\pi\epsilon_0)^2}\frac{\alpha}{k}|\vec{\nabla}\psi(\vec{R})|^2. \tag{2.7}$$

It is important that this equation is only valid if there is no nearby resonance. For rubidium there is a so-called p-wave shape resonance found at an electron energy of about 23-25 meV [98, 99]. Due to an anticrossing at this position the treatment of the interaction between the Rydberg electron and ground state atoms with the pseudopotential approximation is no longer valid. In Figure 2.1 the position of this shape resonance is shown for principal quantum numbers ranging from 30 to 60 for Rydberg $nD_{5/2}$-state electrons. The light blue shaded area depicts values $\pm 10\,\text{meV}$ around this resonance where the scattering potential is still affected [100, 101]. In the experiment, we studied Rydberg $D_{5/2}$-state molecules from $n = 40$ to $n = 50$, bound

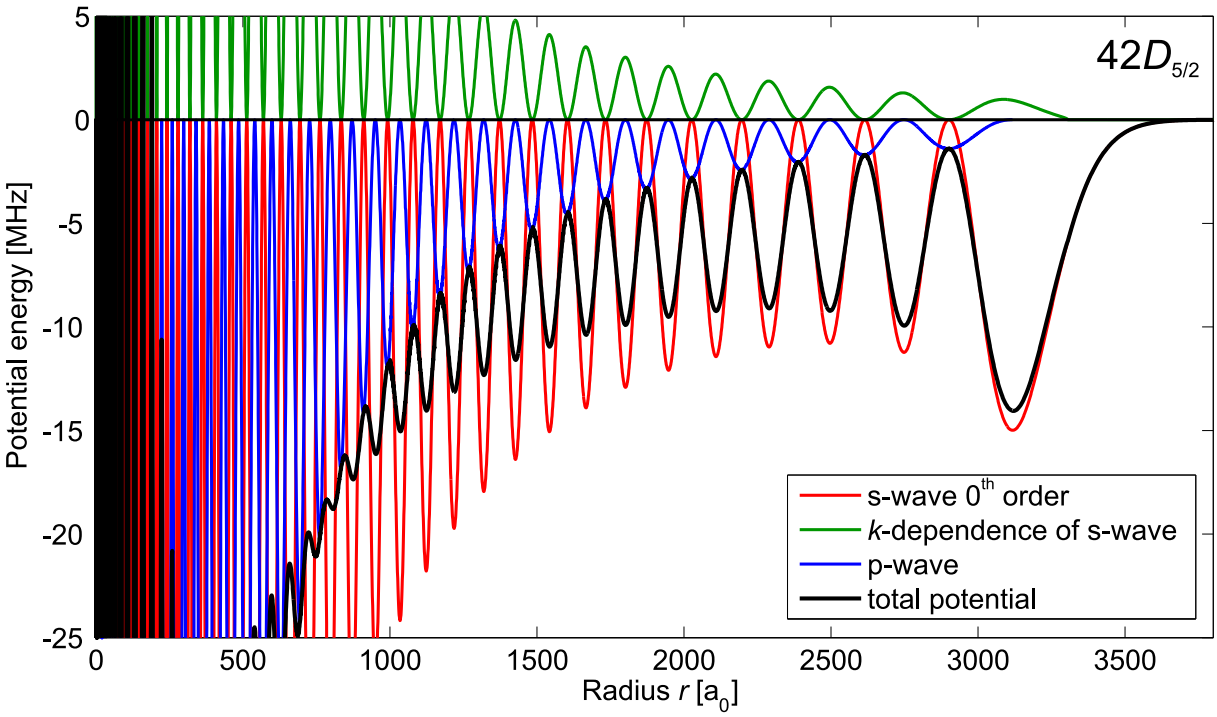

Figure 2.2: Total scattering potential of the Rb $42D_{5/2}$ state with its different contributions, shown for $\Theta = \pi/2$. The total scattering potential (black) is consisting of the 0^{th} order s-wave scattering potential (red), the k-dependent first order part (green) from the s-wave contribution and the p-wave contribution (blue). The different sign in the k-dependent second term of formula (2.5) is causing the positive green potential curve in the plot. For the calculations of these potentials we assumed a constant zero energy electron-atom scattering length of $a_s = -16.1\,\mathrm{a_0}$ [93]. Note that for $r < 1500\,\mathrm{a_0}$ this calculation cannot be trusted since the pseudopotential ansatz breaks down.

in the outermost potential wells, which are far away ($R \geq 2000\,\mathrm{a_0}$) from the p-wave shape resonance area. Only highly excited molecules with large vibrational excitation numbers might be effected, but this is not relevant for our experimental observations. Nevertheless this feature gives rise to bound excited S-state molecules via internal quantum reflection observed in 2010 by V. Bendkowsky and coworkers [45].

In Figure 2.2 the total potential $V_{\text{tot}}(\vec{R}) = V_s(\vec{R}) + V_p(\vec{R})$ and its relevant contributions are exemplarily depicted for the $42D_{5/2}$ state and the polar angle $\Theta = \pi/2$, just taking into account the triplet scattering length. We assumed a ^{87}Rb triplet scattering length of $a_s = -16.1\,\mathrm{a_0}$ [93] for the calculations. The total potential is not dependent on the azimuthal angle φ because $|e^{im\varphi}| = 1$ for all φ. The electron momentum $\hbar k$ is approximated semi-classically by equation (2.6) and the radial part of the Rydberg wavefunction was calculated with the program `rydLib` [57]. Immediately evident from Figure 2.2, the main contribution to the total scattering potential stems from the 0^{th} order s-wave scattering potential. The k-dependent contribution to the scattering length has a positive sign in equation (2.5), causing a positive potential and thus reducing the depth of the total potential. The p-wave contribution is negative but out of phase by π compared to the other contributions and thus shrinks the heights of the oscillations of the potential, making it shallower with decreasing quantum number n.

Since the p-wave shape resonance influences the potential for $r < 1500\,\mathrm{a_0}$ the calculation of the potential cannot be trusted in this region because the whole pseudopotential ansatz becomes invalid. However we are only interested in the molecules with low excitation numbers, which are bound in the outermost deepest potential wells. Thus we should not be bothered by this effect.

2.2 Calculation of the potential energy landscapes

In the following we want to utilize the pseudopotential to calculate the adiabatic potential energy surfaces (APES) and the rovibrational levels of the $D_{5/2}$-Rydberg molecules with principal quantum numbers n ranging from 41 to 49 and $m_J = 5/2$ and $m_J = 1/2$, which we observed experimentally. For the calculations the same magnetic field as in the experiment $B = 13.55\,\mathrm{G}$ was used. This theory work was done in collaboration with M. Kurz and P. Schmelcher from the University of Hamburg. Note that in this section and the next section 2.3 atomic units are used.

Starting point is the Hamiltonian of our system, consisting of the Rydberg electron, its ionic core and the ground state atom

$$H = \frac{\vec{P}^2}{M} + H_{\mathrm{el}} + V_{\mathrm{tot}}(\vec{r}, \vec{R}), \tag{2.8}$$

where $(\vec{P}, \vec{R})$, $(\vec{p}, \vec{r})$ denote the relative momenta and positions of the ground state atom and Rydberg electron, with respect to the ionic core. M is the mass of atomic Rb and $V_{\mathrm{tot}} = V_s + V_p$ is the total scattering potential (see equations (2.5) and (2.7) with $\delta-$functions instead of the absolute squared wavefunctions) between the Rydberg electron and the ground state atom, including the energy dependance of $k(R)$ and the p-wave contribution. The wavenumber $k(R)$ is again determined by the semi-classical approximation (2.6). The electronic Hamiltonian

$$H_{\mathrm{el}} = H_0 + \frac{1}{2}\vec{B}(\vec{L} + 2\vec{S}) + \frac{1}{8}(\vec{B} \times \vec{r})^2 \tag{2.9}$$

consists of the field-free Hamiltonian H_0 and the paramagnetic and diamagnetic terms of an electron in a static external magnetic field $\vec{B} = B\vec{\mathrm{e}}_z$. Note that the paramagnetic term contains the Zeeman interaction. The field-free Hamiltonian

$$H_0 = \frac{\vec{p}^{\,2}}{2m_e} + V_L(\vec{r}) + H_{\mathrm{fs}} \tag{2.10}$$

includes the Rydberg quantum defect due to the L-dependent electron-core potential $V_L(r)$ and the fine structure term H_{fs}. For the principal quantum numbers $n = 41$ to 49, the total angular momentum $\vec{J} = \vec{L} + \vec{S}$ is still a good quantum number since the fine structure splitting is much larger than the Zeeman splitting, directly visible from Figure 1.4 and Table 1.3. We use the Born-Oppenheimer approximation to split the total wavefunction into two parts

$$\Psi_{\kappa u}^{(n,m_J)}(\vec{r}, \vec{R}) = \psi_{n,m_J}(\vec{r}; \vec{R})\phi_{\kappa u}^{(n,m_J)}(\vec{R}). \tag{2.11}$$

The first one describes the electronic molecular wavefunction in the presence of a ground state atom while the second part determines the rovibrational state of the perturbing ground state atom. Here κ is the rovibrational excitation number and u is an integer number, which will become important later. With this adiabatic approximation we obtain

$$\underbrace{\left[H_0 + \frac{B}{2}(J_z + S_z) + V_{\text{tot}}(\vec{r}, \vec{R})\right]}_{H_{\text{tot}}} \psi_{n,m_J}(\vec{r}; \vec{R}) = \epsilon_{n,m_J}(\vec{R})\psi_{n,m_J}(\vec{r}; \vec{R}), \tag{2.12}$$

$$\underbrace{\left(\frac{\vec{P}^2}{M} + \epsilon_{n,m_J}(\vec{R})\right)}_{H_{\text{rv}}} \phi_{\kappa u}^{(n,m_J)}(\vec{R}) = E_{\kappa u}^{(n,m_J)} \phi_{\kappa u}^{(n,m_J)}(\vec{R}), \tag{2.13}$$

where $\epsilon_{n,m_J}(\vec{R})$ is the energy of the electron forming the APES and $E_{\kappa u}^{(n,m_J)}$ the energy of the perturbing ground state atom. Note that we neglected the diamagnetic term in equation (2.12) due to the small B-field applied in the experiment. It is of importance that the APES $\epsilon_{n,m_J}(\vec{R}) = \epsilon_{n,m_J}(R, \Theta)$ possess rotational symmetry around the z-axis, which means that they only depend on the polar angle of inclination Θ between the B-field vector and the internuclear axis, and the radial distance R. It is easier to perform the following calculations in a cylindrical coordinate system so that the APES become functions of $(z, \rho = R\sin\Theta)$.

The next step is to define a basis set of wavefunctions which we need for the diagonalization of the electronic Hamiltonian H_{tot} (2.12). The goal is to calculate the electronic potentials for the Rydberg $D_{5/2}$ states for principal quantum numbers n ranging from 41 to 49 and for the two magnetic substates $m_J = 5/2, 1/2$, which were observed in the experiment. We use the eigenstates of H_0

$$|\psi_{n,m_J}\rangle = \sum_{n,m_J} C_{n,m_J}(\vec{R})\chi_{n,m_J}(\vec{r}) = \sum_{n,m_J} C_{n,m_J}(\vec{R}) \left| n, J = L \pm \frac{1}{2}, m_J, L = 2, s = \frac{1}{2} \right\rangle \tag{2.14}$$

to obtain the APES $\epsilon_{n,m_J}(z, \rho)$, where $C_{n,m_J}(\vec{R})$ is a coefficient and $\chi_{n,m_J}(\vec{r})$ contains the radial and angular wavefunction. Note that ξ_{n,m_J} is the energy of the field-free Hamiltonian $H_0\chi_{n,m_J} = \xi_{n,m_J}\chi_{n,m_J}$ and that we also take into account a possible coupling to the state $J = 3/2$. That's why we use for the basis states $J = 3/2, 5/2$ and write them explicitly as

$$\begin{aligned} |n, J, m_J, L, s\rangle &= \left| n, L \pm \frac{1}{2}, m_J, 2, \frac{1}{2} \right\rangle = \\ &= R_{n,J,2}(r) \left(\pm\sqrt{\frac{\frac{5}{2} \pm m_J}{5}} Y_2^{m_J - \frac{1}{2}}(\Theta, \varphi) \,|\uparrow\rangle + \sqrt{\frac{\frac{5}{2} \mp m_J}{5}} Y_2^{m_J + \frac{1}{2}}(\Theta, \varphi) \,|\downarrow\rangle \right) \equiv \\ &\equiv R_{n,J,2}(r)\big(\alpha(J, m_J) Y_2^{m_J - \frac{1}{2}}(\Theta, \varphi)|\uparrow\rangle + \beta(J, m_J) Y_2^{m_J + \frac{1}{2}}(\Theta, \varphi)|\downarrow\rangle\big). \end{aligned} \tag{2.15}$$

Here $R_{n,J,L}(r)$ are the radial wavefunctions of the Rydberg states which were calculated by the program `rydLib` [57] and $Y_L^m(\Theta, \varphi)$ are the spherical harmonics. $\alpha(m_J)$ and $\beta(m_J)$ are the

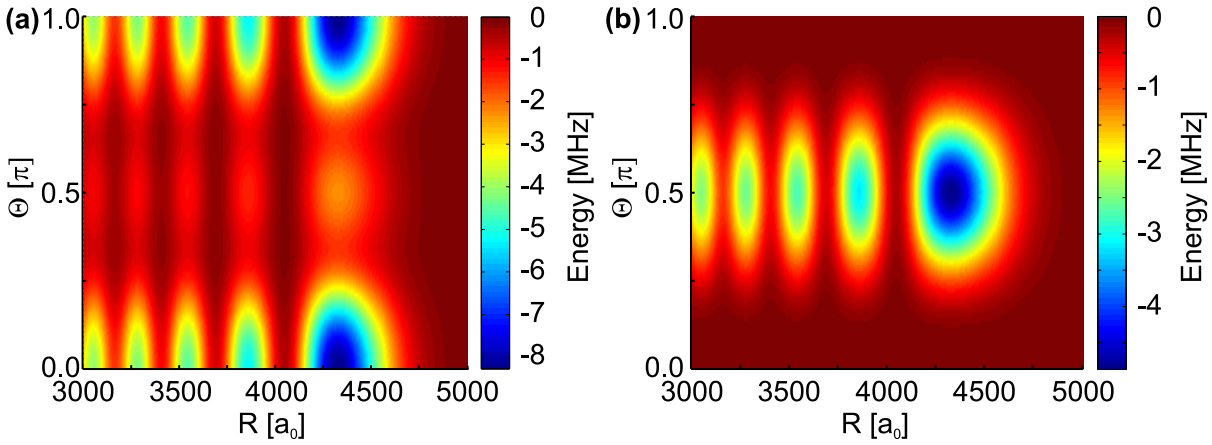

Figure 2.3: Adiabatic potential energy surfaces (APES) for the states $49D_{5/2}$, $m_J = 1/2$ (a) and $49D_{5/2}$, $m_J = 5/2$ (b) as a function of (R,Θ). In (a) the potential provides bound states in potential wells localized at $\Theta = 0, \pi$ (axial states) and at $\Theta = \pi/2$ (toroidal states). For the stretched state $m_J = 5/2$ (b), only one series of toroidal potential wells can be identified at $\Theta = \pi/2$.

Clebsch-Gordon coefficients and $|\uparrow\rangle$, $|\downarrow\rangle$ indicate the two different electronic spin states. With these eigenfunctions of H_0 we can solve the following eigenvalue problem:

$$\left[\xi_{n,m_J} - \epsilon_{n,m_J}(\vec{R})\right] C_{n,m_J} + \sum_{n',m'_J} C_{n',m'_J} \left\langle n, J, m_J, L, s \left| \frac{B}{2}(J_z + S_z) + V_{\text{tot}}(\vec{r}, \vec{R}) \right| n', J', m'_J, L', s' \right\rangle = 0. \quad (2.16)$$

We calculate the APES $\epsilon_{n,m_J}(z, \rho)$ in polar coordinates for the $m_J = 5/2$ and $m_J = 1/2$ substates, which we investigated in the experiment. In Figure 2.3(a) and (b) we exemplarily show the calculated potential surfaces for the $49D_{5/2}, m_J = 1/2$ and $49D_{5/2}, m_J = 5/2$ states. For the $49D_{5/2}$, $m_J = 1/2$ state we distinguish between two series of potential wells, the deeper ones at $\Theta = 0, \pi$ and the shallower one at $\Theta = \pi/2$. Two classes of molecules, the axial and the toroidal can be bound in these series of potential wells, respectively. In contrast to this, for the $49D_{5/2}, m_J = 5/2$ state, only one series of potential wells exists at $\Theta = \pi/2$ because of the different electron orbit, shown in Figure 8.1(b) and (c). While the electron orbit of the $m_J = 1/2$ state exhibits a dumbbell shape with a small torus in the x-y-plane, the $m_J = 5/2$ has the shape of a big doughnut. This gives rise to the different angles Θ where the ground state atom is bound in the electronic wavefunction. It is important that these potential surfaces are rotationally symmetric to the z-axis, thus independent of the azimuthal angle φ. A similar plot for $n = 41$ can be seen in Figure 8.2 in the D-state molecule section 8.1.

2.3 Rovibrational levels and binding energies

For a comparison with the experimentally obtained spectroscopy data we need to calculate the binding energies of the Rydberg molecules. To solve the Hamiltonian equation (2.13) we choose the following ansatz for the rovibrational wavefunctions of the ground state atom:

$$\phi_{\kappa u}^{(n,m_J)}(\vec{R}) := \frac{F_{\kappa u}^{(n,m_J)}(\rho,z)}{\sqrt{2\pi\rho}}\mathrm{e}^{iu\varphi}, \quad u \in \mathbb{Z},\ \kappa \in \mathbb{N}_0. \tag{2.17}$$

Here κ is the rovibrational excitation number, u is an integer number and $F_{\kappa u}^{(n,m_J)}(\rho,z)$ are the molecular wavefunctions. Using this expression we can rewrite the rovibrational Hamiltonian equation (2.13) as:

$$\left(-\frac{\partial_\rho^2+\partial_z^2}{M}+\frac{u^2+\frac{1}{4}}{M\rho^2}+\epsilon_{n,m_J}(\vec{R})\right)F_{\kappa u}^{(n,m_J)}(\rho,z)=E_{\kappa u}^{(n,m_J)}F_{\kappa u}^{(n,m_J)}(\rho,z). \tag{2.18}$$

The derivation of this equation can be found in the appendix A.1. To solve this differential equation and to calculate the molecular wavefunctions $F_{\kappa m}^{(n,m_J)}$ and corresponding eigenenergies $E_{\kappa u}^{(n,m_J)}$ we use a finite difference method [102]. Basically the finite difference method is a numerical method to approximate the solutions to a differential equation, which is converted into a system of difference quotient equations that can be solved numerically. For a fixed u we label the eigenenergies from the highest to the lowest absolute value with the rovibrational excitation number $\kappa = 0, 1, 2, \ldots$ and define the binding energy $E_{\kappa u}^{(n,m_J)} = E_B^{(\kappa)}$ of an eigenstate as the value between the eigenenergy and the dissociation limit of the APES, as in the experiment. Since the APES are symmetric with respect to the x-y-plane $\epsilon_{n,m_J}(\rho,-z)=\epsilon_{n,m_J}(\rho,z)$, the molecular wavefunctions $F_{\kappa m}^{(n,m_J)}$ fulfill the equation $F_{\kappa u}^{(n,m_J)}(\rho,-z) = \pm F_{\kappa u}^{(n,m_J)}(\rho,z)$, which means their probability densities have also a mirror symmetry in respect to the x-y-plane $|F_{\kappa u}^{(n,m_J)}(\rho,-z)|^2 = |F_{\kappa u}^{(n,m_J)}(\rho,z)|^2$. For the following calculations we fixed the value of u to zero.

For the stretched states, $m_J = 5/2$ the binding energies of the molecules were calculated around the outermost deepest potential well (at $\Theta = \pi/2$; see Figure 2.3(b)). This approach is considered to behave well if the wavefunctions are assumed to be (nearly) zero at the boundary of the considered potential domain at $R = 2000\,\mathrm{a_0}$. In our case this is fulfilled as long as the bound states lie deep within the potential wells. This is the case for the toroidal states $\kappa = 0-9$ whose absolute binding energies are listed in Table 2.1 for the $42D_{5/2}$ state; for the other principal quantum numbers n the Tables can be found in the appendix A.2. Note that the binding energies were calculated only for the states investigated in the experiment.

For the $m_J = 1/2$ states, we performed two separate calculations to obtain the rovibrational levels for the associated potential curves. For states localized in the deeper potential wells at $\Theta = 0, \pi$ in Figure 2.3(a) the region of interest was set to $z > 1500\,\mathrm{a_0}$ and $R > 2000\,\mathrm{a_0}$, whereas for the shallower potential wells at $\Theta = \pi/2$ the region $z < 1500\,\mathrm{a_0}$ and $R > 2000\,\mathrm{a_0}$ was investigated. Due to the p-wave shape resonance (see section 2.1 and Figure 2.1) influencing the calculations for $R < 2000\,\mathrm{a_0}$, we introduced an artificial boundary for the wavefunctions by setting the probability density to zero in this region. We have to be careful if we calculate states with higher rovibrational excitation number κ, which possess non-zero probability den-

$42D_{5/2}$	$m_J = 1/2$ Axial states	$m_J = 1/2$ Toroidal states	$m_J = 5/2$ Toroidal states
κ	$\lvert E_B^{(\kappa)}\rvert$[MHz]	$\lvert E_B^{(\kappa)}\rvert$[MHz]	$\lvert E_B^{(\kappa)}\rvert$[MHz]
0	14.42	3.27	7.05
1	13.24	2.78	6.42
2	12.04	2.31	5.74
3	10.84	1.85	5.18
4	9.64	1.39	4.60
5	8.47	0.93	4.01
6	7.32		3.69
7	6.90		3.58
8	6.48		3.04
9	6.20		2.79
10	5.93		
11	5.83		
12	5.37		
13	5.12		
14	4.87		
15	4.77		
16	4.31		
17	4.21		
18	4.10		
19	3.83		
20	3.74		

Table 2.1: Binding energies (absolute values) of the $42D_{5/2}$ state, calculated by a finite element method. The dark red color indicates for which binding energies the numerical calculation did not converge nicely (more details in the text). Thus these binding energies have to be treated with caution.

sity in the vicinity of our artificial border. Due to the large fluctuations of the APES in this area around the border the numerically calculated wavefunctions do not converge nicely. We would have to change the grid size for the calculation of the rovibrational wavefunctions and binding energies with the finite difference method to get more accurate and trustworthy results, which would result in very time consuming calculations. The states which are affected by this and have to be treated with caution are marked dark red in the absolute binding energy lists for the axial molecules, which can be found in Table 2.1 ($42D_{5/2}$ state) or in the appendix A.2 (other states). For the toroidal states of $m_J = 1/2$ it was sufficient to calculate the binding energies up to $\kappa = 5$, since they are already very close to the atomic line and thus are very hard to resolve experimentally. Since these states are far away from our artificial border they could be calculated without any difficulties by our finite difference method. The comparison with the experimental measurements and detailed discussions can be found in section 8.1.

To illustrate where the two different types of molecules are formed we qualitatively depict the scaled probability densities of the axial and toroidal molecules for $42D_{5/2}, m_J = 1/2$ in

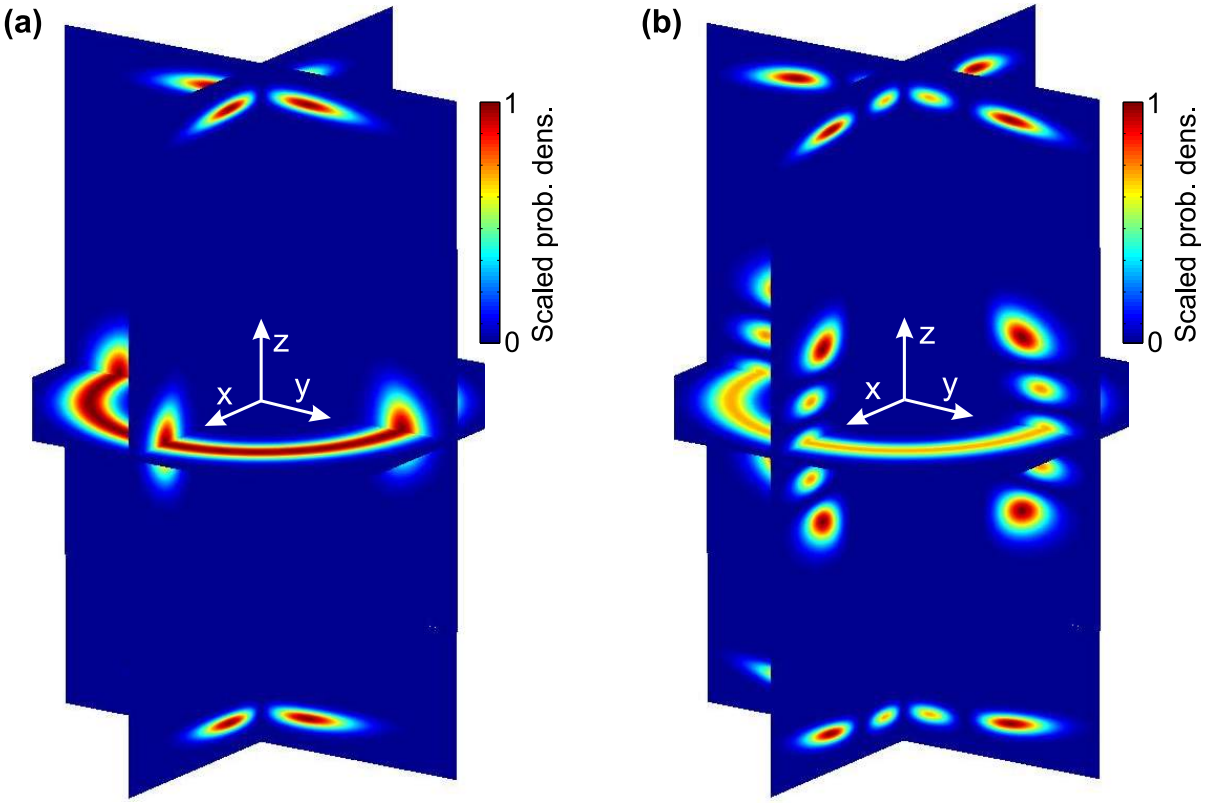

Figure 2.4: Qualitative 3-D plots of the scaled rovibrational probability densities of the toroidal and the axial molecules of the $42D_{5/2}, m_J = 1/2$ state. In (a) the plot shows the scaled probability density of the $\kappa = 0$ axial and $\kappa = 0$ toroidal molecule and in (b) the scaled probability density of the $\kappa = 1$ axial and $\kappa = 4$ toroidal molecule are depicted. Both plots illustrate where the ground state molecules and the higher excited molecules are formed in the energy landscape and are not true to scale.

Figure 2.4. In panel (a) the axial and toroidal ground state molecule can be seen, whereas in panel (b) higher excited states are shown. We observe that on the one hand, the toroidal states in the x-y-plane spread out into z-direction for the higher excited molecules. On the other hand, the axial states are created far out in the z-direction advancing into radial direction for higher excitation numbers κ. Note that the toroidal and axial states have completely different binding energies (see Table 2.1) and cannot be excited with our two excitation lasers at the same time. The positions where these molecules are formed are crucial for the study of their alignment (angular confinement), in detail described and discussed in section 8.2.

2.4 Ion-ground state atom interaction

In this section, it is shown that the influence of the ionic core on the ground state atoms is negligible compared to the electron-atom interaction, presented in section 2.1. A simple estimate of this effect was already given by E. Fermi [12]. The energy shift of the Rydberg state due to the polarization of the surrounding ground state atoms by the ionic core of the Rydberg atom can be described by

$$\Delta E_{\text{pol}} = -\frac{\alpha e^2}{2(4\pi\epsilon_0)^2}\ s\left(\frac{4\pi}{3}\right)^{4/3}\rho^{4/3}, \tag{2.19}$$

treating the Rydberg core and the ground state atoms as point-like and assuming a homogeneous gas of density ρ. In this equation, $\alpha = 0.0794\,\mathrm{Hz}/(\mathrm{V}/\mathrm{cm})^2$ [55] is the polarizability of the ground state rubidium atoms and $s \approx 2.6$ [12] is a numerical correction factor for the mean interparticle distance, taking into account all particles further away. For our typical BEC densities of $\rho = 10^{14}\,\mathrm{cm}^{-3}$ we estimate a line shift of $-67.1\,\mathrm{kHz}$. This value is more than two orders of magnitude smaller than the impact of the Rydberg electron and thus the effect of ion-atom interaction can be neglected in our case. In the experiment we observe line shifts of up to $10\,\mathrm{MHz}$ for principal quantum numbers $n > 100$ (see subsections 9.2.2 and 9.3.1). Compared to the linear density scaling for the electron-ground state interaction (2.2), the ion-atom interaction scales with $\rho^{4/3}$ meaning that only for very high densities, this effect becomes important. In the experiments of E. Amaldi and E. Segré [36, 37] densities of the noble gas atoms of up to $10^{20}\,\mathrm{cm}^{-3}$ have been reached resulting in a visible contribution of this effect.

In other experiments the ion-atom interaction is crucial. Combining a Paul trap with a cold atom system, it was possible to study the influence of one single ion on a Bose-Einstein condensate (BEC) [103]. The dynamics of the ion in the condensate was investigated and it was demonstrated that a single ion can be used to probe the density profile of a BEC [104]. A problem in these experiments is still the micromotion of the ion leading to atom losses and unwanted heating [105, 106, 107]. To overcome this obstacle we present in the outlook in section 11.2 a proposal how we could in principle realize a single ion in a BEC with some minor modifications to our current experimental setup.

3 Bose-Einstein condensates

In this chapter the fundamental basics and characteristics of Bose-Einstein condensates (BEC) are recapitulated, only going into details where it is needed for the following sections. The crucial part in this chapter is the presentation of a stochastic model in section 3.3, based on the Gross-Pitaevskii equation and Fermi's pseudopotential, which describes the process of exciting single Rydberg atoms in a BEC. We show that this model reproduces very well our experimental data of the losses in the condensate, the line shifts and the broadening of the spectra [10]. Before explaining the model we give a brief introduction to the Gross-Pitaevskii equation and its derivation in section 3.1. Using the Thomas-Fermi approximation to neglect the kinetic energy in this equation, we can also describe the time of flight expansion of a BEC (section 3.2), which is important for our time of flight imaging technique, used in the experiment (see section 6.2). In the end of this chapter in section 3.4 we briefly discuss the shape oscillations and their different modes in a BEC, since one specific oscillatory mode was measured experimentally (see subsection 9.3.2).

A so called Bose-Einstein condensate can be formed when a system of bosons is undergoing a critical phase transition into a regime where all particles possess the same quantum mechanical ground state energy and can be described as a giant matter wave. This process is illustrated in Figure 3.1. Starting at a high temperature (top panel) the bosons can be treated as particles with a certain velocity distribution given by the thermal temperature. Due to the wave-particle duality [109], another way to describe the particles is to define them as a matter wave with an extent of the order of the de Broglie wavelength $\lambda_{\mathrm{dB}} = h/(mv) = h/\sqrt{2\pi m k_B T}$, where v is the velocity and m is the mass of the atom, k_B the Boltzmann constant and T the temperature. If we increase the phase space density and reduce the temperature, the de Broglie wavelength becomes comparable to the interparticle distance $d \propto \rho^{-1/3}$ (ρ is the particle density) and the transition to the BEC takes place, where the individual particles can no longer be distinguished and their matter waves start

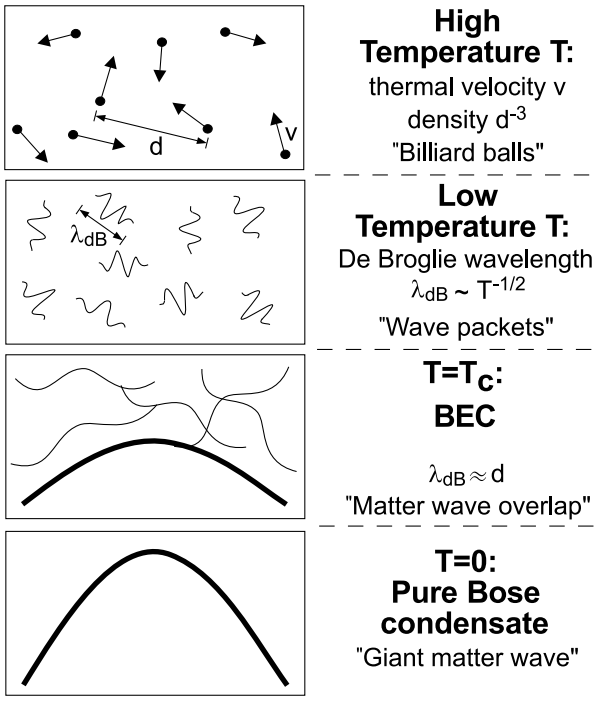

Figure 3.1: from top to bottom: formation of a Bose-Einstein condensate reducing the temperature and increasing the phase space density of the system. T_C is the critical temperature, at which the condensation starts. This scheme was taken from [108].

to overlap. To put it another way, the uncertainty of the particles gets larger as their momentum and associated kinetic energy decrease. In an ideal case at $T = 0$ (bottom panel of Figure 3.1) we end up with a pure condensate and the whole system can be described as a macroscopic matter wave. Assuming a three-dimensional harmonic oscillator potential the critical temperature needed for the onset of condensation can be estimated by [110]

$$T_C \approx \frac{\hbar\bar{\omega}}{k_B}\left(\frac{N}{\zeta(3)}\right)^{\frac{1}{3}}; \qquad \bar{\omega} = \sqrt[3]{\omega_x\omega_y\omega_z}\,; \qquad \zeta\,(3) \approx 1.202, \tag{3.1}$$

where N is the total number of bosons and $\bar{\omega}$ is the mean trapping frequency, consisting of the trapping frequencies for each spatial direction, forming a harmonic oscillator potential for the atoms. $\zeta(s)$ is the Riemann zeta function defined by $\zeta(s) = \sum_{n=1}^{\infty} n^{-s}$. For the experimental parameters of our magnetic trap ($\omega_x = \omega_y = \omega_r = 2\pi \cdot 82\,\mathrm{Hz}$, $\omega_z = 2\pi \cdot 22\,\mathrm{Hz}$, $B = 13.55\,\mathrm{G}$) and averaged number of condensed atoms of $N = 8 \cdot 10^4$ we calculate a critical temperature of about $103\,\mathrm{nK}$, which is quite small due to the high magnetic offset field. More details about our magnetic trap can be found in chapter 4.

This condensation phenomenon of bosons has already been predicted 1924 by A. Einstein [111], based on earlier work by S. Bose [112]. Experimentally the first Bose-Einstein condensate was created 1995 by E. Cornell, C. Wieman and coworkers for rubidium ^{87}Rb [2] and in the group of W. Ketterle for sodium ^{23}Na [3]. The crucial steps which enabled the condensation were the newly developed magnetic trapping methods for neutral atoms [113] and evaporative cooling [114]. Later Bose-Einstein condensation of quasiparticles in solid state systems, for example for microcavity exciton-polaritons [21, 22, 23] and recently the Bose-Einstein condensation of photons have been realized [24]. Even a BEC out of positronium, a bound state of an electron and a positron, was proposed lately as a source for a self-amplified gamma-ray laser [25].

3.1 Gross-Pitaevskii equation

We describe the Bose-Einstein condensate as a nonuniform dilute gas consisting of N bosons. If we consider two of these particles at low energies and temperatures their interaction can be described by the coupling constant

$$g = \frac{4\pi\hbar^2 a}{m}, \tag{3.2}$$

where m is the mass of one atom and a is the constant s-wave scattering length. We treat this many particle problem with a Hartree or mean-field approach, assuming that the wavefunction can be composed of a product of normalized single-particle wavefunctions:

$$\Psi(\vec{r}_1, \vec{r}_2, \ldots, \vec{r}_N) = \prod_{i=1}^{N} \phi(\vec{r}_i). \tag{3.3}$$

All bosons are in the same single particle state $\phi(\vec{r})$. Taking only binary interactions into account (3.2), we can write the effective Hamiltonian as [110]

$$H = \sum_{i=1}^{N} \left[\frac{\vec{P}_i^2}{2m} + V_e(\vec{r}_i) \right] + g \sum_{i<j} \delta(\vec{r}_i - \vec{r}_j), \tag{3.4}$$

where $V_e(\vec{r})$ is an external potential (it will be the magnetic trapping potential later). The second term sums over all possible ways of forming two particle interactions among the N particles. The total energy of the state $\Psi(\vec{r})$, the expectation value of (3.4), is given by

$$E = N \int d\vec{r} \left[\frac{\hbar^2}{2m} |\vec{\nabla}\phi(\vec{r})|^2 + V_e(\vec{r})|\phi(\vec{r})|^2 + \frac{N-1}{2} g|\phi(\vec{r})|^4 \right]. \tag{3.5}$$

We now introduce the wavefunction $\psi(\vec{r})$ of the condensed state

$$\psi(\vec{r}) = \sqrt{N}\phi(\vec{r}); \qquad n(\vec{r}) = |\psi(\vec{r})|^2, \tag{3.6}$$

where n is the density of the particles. If we substitute the single particle wavefunction $\phi(\vec{r})$ with the condensate wavefunction $\psi(\vec{r})$ in equation (3.5) and neglect all terms of the order $1/N$ assuming a large number of particles in the condensate, we end up with

$$E(\psi) = \int d\vec{r} \left[\frac{\hbar^2}{2m} |\vec{\nabla}\psi(\vec{r})|^2 + V_e(\vec{r})|\psi(\vec{r})|^2 + \frac{1}{2} g|\psi(\vec{r})|^4 \right]. \tag{3.7}$$

The next step is to minimize this energy functional in respect to the independent variations of $\psi(\vec{r})$ and its complex conjugate $\psi^*(\vec{r})$ under the condition that the total number of particles stays constant:

$$N = \int d\vec{r} |\psi(\vec{r})|^2. \tag{3.8}$$

Calculating the variation of $E(\psi) - \mu N = 0$ with respect to $\psi^*(\vec{r})$ results in the time-independent Gross-Pitaevskii equation (GPE) [110]

$$\left[-\frac{\hbar^2}{2m}\nabla^2 + V_e(\vec{r}) + g|\psi(\vec{r})|^2 \right] \psi(\vec{r}) = \mu\psi(\vec{r}), \tag{3.9}$$

where μ is the chemical potential of the condensate, i.e. the energy to which all particles of the condensate sum up to, taking into account the interaction g between each other. The GPE has the form of a Schrödinger equation, in which the potential acting on the particles is the sum of the external potential $V_e(\vec{r})$ and a second term $g|\psi(\vec{r})|^2$ describing the the mean-field acting on a single particle produced by the other surrounding bosons. The time-dependent Gross-Pitaevskii equation, derived in [115], can be written as

$$i\hbar \frac{\partial}{\partial t}\psi(\vec{r},t) = \left[-\frac{\hbar^2}{2m}\nabla^2 + V_e(\vec{r}) + g|\psi(\vec{r},t)|^2 \right] \psi(\vec{r},t). \tag{3.10}$$

Further details about the derivation of the GPE and other properties of the Bose-Einstein condensate can be found in [108, 110, 115, 116].

3.2 Thomas-Fermi approximation and time of flight expansion

For sufficiently large clouds and therefore slowly varying particle density in space, the kinetic energy term in the Gross-Pitaevskii equation (3.9) can be neglected [108], yielding the equation

$$\left[V_e(\vec{r}) + g|\psi(\vec{r})|^2\right]\psi(\vec{r}) = \mu\psi(\vec{r}). \tag{3.11}$$

The density $n(\vec{r})$ can be calculated by

$$n(\vec{r}) = |\psi(\vec{r})|^2 = \max\left(\frac{\mu - V_e(\vec{r})}{g}, 0\right), \tag{3.12}$$

taking into account the normalization condition (3.8). Physically the Thomas-Fermi approximation can be understood that if we add a particle at any point in the BEC the increase of energy is the same. This energy is the chemical potential given by the sum of the external potential $V_e(\vec{r})$ and the interaction potential $gn(\vec{r})$. The name of this approximation comes from the similarity to the Thomas-Fermi atom model, in which the electrons are treated like a gas, possessing an uniform electron density. To visualize the density profile one can think of particles filling up the bottom of the trapping potential to the value of the chemical potential μ [108].

We now want to investigate the condensate density in the cylindrical trapping potential we use in our experiment. The BEC has a cigar-shaped form since the radial trap frequency $\omega_r = 2\pi \cdot 82\,\mathrm{Hz}$ is about a factor of four larger than the axial $\omega_z = 2\pi \cdot 22\,\mathrm{Hz}$. Inserting the the external trap potential

$$V_e(\vec{r}) = \frac{1}{2}m(\omega_r^2(x^2+y^2) + \omega_z^2 z^2) \tag{3.13}$$

into the condensate density equation (3.12) we get a parabolic density profile

$$n(\vec{r}) = \max\left(n_0\left[1 - \frac{x^2+y^2}{r_0^2} - \frac{z^2}{z_0^2}\right], 0\right) \tag{3.14}$$

with the peak density

$$n_0 = \frac{\mu}{g} = \frac{m\mu}{4\pi\hbar^2 a} \tag{3.15}$$

and the Thomas-Fermi radii

$$r_0 = \sqrt{\frac{2\mu}{m\omega_r^2}}; \quad z_0 = \sqrt{\frac{2\mu}{m\omega_z^2}}. \tag{3.16}$$

Using the normalization condition for the density (3.8) the chemical potential can be calculated:

$$\mu = \left(\frac{15\hbar^2}{2^{5/2}}m^{1/2}\omega_r^2\omega_z a N\right)^{2/5}. \tag{3.17}$$

The peak density n_0 scales therefore with the total condensate particle number N as $n_0 \propto N^{2/5}$.

Bose-Einstein condensate in time of flight expansion

With the help of the Thomas-Fermi approximation we can study the time evolution of the BEC when the magnetic trap is switched off for $t > 0$. Starting point is the time-dependent GPE (3.10). Applying the Thomas-Fermi approximation yields

$$i\hbar\frac{\partial}{\partial t}\psi(\vec{r},t) = \left(V_e(\vec{r}) + g|\psi(\vec{r},t)|^2\right)\psi(\vec{r},t). \tag{3.18}$$

We now use the model of a classical gas to define the force each particle in the BEC experiences [117], created by the trapping potential and the mean-field interaction, as

$$\vec{F}(\vec{r},t) = -\vec{\nabla}\left[V_e(\vec{r},t) + gn(\vec{r},t)\right]. \tag{3.19}$$

At the time $t = 0$ the atoms are in an equilibrium position and there is no effective force $\vec{F}(\vec{r},t) = 0$ acting on them. Thus we obtain the following relation between density and trap potential:

$$g\vec{\nabla}n(\vec{r},0) = -\vec{\nabla}V_e(\vec{r},0). \tag{3.20}$$

For $t > 0$ the trap potential $V_e(\vec{r}, t > 0)$ is zero, since the trap is instantaneously switched off. In case of a harmonic trap potential an exact solution for this classical model can be obtained [117], resulting in a dilatation of the gas, moving along the trajectory

$$R_j(t) = \lambda_j(t)R_j(0)\,; \qquad (j = 1,2,3), \tag{3.21}$$

where the integer j denotes the three spatial directions and $\lambda_j(t)$ is the time-dependent scaling parameter. This means for the evolution of the density:

$$n(\vec{r},t) = \frac{1}{\lambda_1(t)\lambda_2(t)\lambda_3(t)}\; n\left(\left(\frac{r_1}{\lambda_1(t)},\frac{r_2}{\lambda_2(t)},\frac{r_3}{\lambda_3(t)}\right),0\right). \tag{3.22}$$

Inserting our equation for the force (3.19) and the trajectory equation (3.21) into Newton's law $m\ddot{R}_j(t) = F_j(\vec{R}(t),t)$ and using equation (3.20) to substitute the derivative of the density with the derivative of the trap potential, we obtain

$$m\ddot{\lambda}_j(t)R_j(0) = \frac{1}{\lambda_j(t)\lambda_1(t)\lambda_2(t)\lambda_3(t)}\partial_{r_j}V_e(\vec{R}(0),0) - \partial_{r_j}V_e(\vec{R}(t),t). \tag{3.23}$$

For harmonic trap potentials both sides of this equation are proportional to $R_j(0)$ justifying the self-consistent chosen ansatz (3.21). Using the axially symmetric trap potential from our experiment (3.13), we obtain a system of coupled differential equations for the scaling parameters λ_r and λ_z:

$$\ddot{\lambda}_r(t) = \frac{\omega_r^2(0)}{\lambda_r^3\lambda_z} - \omega_r^2(t)\lambda_r\,; \qquad \ddot{\lambda}_z(t) = \frac{\omega_z^2(0)}{\lambda_r^2\lambda_z^2} - \omega_z^2(t)\lambda_z. \tag{3.24}$$

If the switching off of the trap potential occurs instantaneously for $t > 0$, the second term in both equations becomes zero, since $\omega_r(t > 0) = \omega_z(t > 0) = 0$. We can solve these equations by expanding them in powers of the aspect ratio $\epsilon = \omega_z(0)/\omega_r(0)$ of the trap at $t = 0$. By taking the radial expansion parameter to the 0^{th} order of ϵ and the axial one to the second order, we

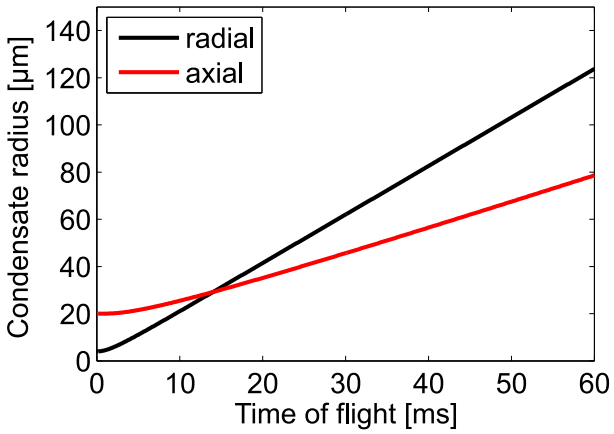

Figure 3.2: Simulated time of flight expansion of the cigar-shaped condensate from our experiment. The radial trap frequency is $\omega_r = 2\pi \cdot 82\,\mathrm{Hz}$, whereas the axial one is $\omega_z = 2\pi \cdot 22\,\mathrm{Hz}$. As starting parameters for the expansion, a radial diameter of $8\,\mu\mathrm{m}$ was chosen and for the axial extent of the condensate a value of $40\,\mu\mathrm{m}$. The two equations (3.25) were used for the calculation of the time of flight evolution.

obtain for the evolution of the BEC radii [108, 117]:

$$\begin{aligned} r_r(t) &= \sqrt{1+\omega_r^2(0)t^2}\;\; r_r(0); \\ r_z(t) &= \left[1+\epsilon^2\left(\omega_r(0)t\cdot\arctan\left(\omega_r(0)t\right)-\ln\sqrt{1+\omega_r^2(0)t^2}\right)\right] r_z(0). \end{aligned} \tag{3.25}$$

It is important that for our trap parameters in the experiment, the radial trap frequency $\omega_r = 2\pi \cdot 82\,\mathrm{Hz}$ is around a factor of four larger than the axial trap frequency $\omega_r = 2\pi \cdot 22\,\mathrm{Hz}$. Thus the expansion in the radial direction is much faster than in axial direction leading to an inversion of the condensate's aspect ratio ϵ at time of flights above $14\,\mathrm{ms}$. So the radial axis becomes the elongated one which can be clearly seen in Figure 3.2, where the axial and radial extent of the condensate is plotted. The used trap parameters are those of the experiment.

If we evaluate the time of flight pictures from our absorption imaging (see section 6.2) and extract the condensate size in axial and radial direction, these two equations can be used to calculate the initial BEC dimensions. Furthermore the temperature, condensate density and BEC atom number are determined from the analysis of the absorption pictures. How this is done is explained in detail in reference [108].

3.3 Modeling single Rydberg excitations in a Bose-Einstein condensate via the Gross-Pitaevskii equation

Our goal in this section is to find a theoretical model which describes the experimental procedure of exciting single S-state Rydberg atoms in the condensate for high principal quantum numbers ranging from $n = 110$ to 200 and to reproduce our experimental findings [10]. For these high quantum numbers, 700 to 20000 ground state atoms can be found within the radius of a Rydberg atom. To explain the atom losses in the condensate in our experimental work [10], we introduced Bogoliubov excitations, resulting in a coupling between the Rydberg electron and phonons, quantized density modulations in the BEC. It was shown that additionally free particles contribute to the total number of atom losses since in the time of flight imaging, they cannot be distinguished from the phonon induced losses. Details about the theory of Bogoliubov

excitations can be found in [11, 110, 116].

This theory work was done in a collaboration with the group of K. Rzążewski and culminated in a joint paper [118]. Starting point of this model is the time-dependent Gross-Pitaevskii equation (3.10) with an added pseudopotential term V_{Ryd} to describe the interaction between the Rydberg electron and the condensate [118]:

$$i\hbar\frac{\partial}{\partial t}\Psi(\vec{r},t) = \left[-\frac{\hbar^2}{2m}\nabla^2 + V_e(\vec{r}) + g|\Psi(\vec{r},t)|^2 + f(t)V_{\text{Ryd}}(\vec{r}-\vec{R})\right]\Psi(\vec{r},t). \tag{3.26}$$

Here m is the mass of a condensate ground state atom and $\vec{R}$ the position of the Rydberg atom. Note that we do not use relative coordinates here in contrast to the previous section 2.2, where the adiabatic potential energy landscapes for the molecules have been calculated. We renamed the pseudopotential V_{mol} from equation (2.3) to V_{Ryd} to avoid misunderstandings, since we now have to deal with an energy shift instead of a molecular binding potential [9]. To calculate this energy shift we integrate over the ground state atom density $\rho(\vec{r})$:

$$\Delta E(\vec{R}) = \int d^3\vec{r}\, V_{\text{Ryd}}(\vec{r}-\vec{R})\rho(\vec{r}). \tag{3.27}$$

Due to the blockade radius (1.55) being larger than the extent of our condensate only one Rydberg excitation at a time is possible. The pseudopotential term V_{Ryd} in equation (3.26) is multiplied with the function $f(t)$, which assumes only the values of 1 or 0, depending on whether a Rydberg atom at position $\vec{R}$ is present, or not. The Rydberg interaction on the condensate atoms is only existent during the lifetime of the Rydberg atom.

In the experiment [10], the 1 µs long excitation pulse is repeated 300 to 500 times, depending on the principal quantum number n, to obtain a sufficiently large amount of atom losses in the condensate. Using an effective two-level system for the excitation dynamics of the two photon transition (see subsection 1.2.4), the probability to find an excited Rydberg atom at position $\vec{R}$ is given by equation (1.17), rewritten as:

$$p(\vec{R},t) = \frac{\Omega_{\text{eff},0}^2}{\Omega_{\text{eff}}^2(\vec{R},t)}\sin^2\left(\frac{\Omega_{\text{eff}}(\vec{R},t)}{2}\,t\right); \quad \Omega_{\text{eff},0} = \frac{\Omega_r\Omega_b}{2\Delta_p}. \tag{3.28}$$

In this equation $\Omega_{\text{eff},0}$ is the effective resonant Rabi frequency which is in the kHz regime in the experiment and depends on the single atom Rabi frequencies Ω_r and Ω_b, which stand for the lower and upper photon transition, respectively (see Figure 1.1(c)). Ω_{eff} denotes the effective non-resonant Rabi frequency, which takes into account the local detuning Δ:

$$\Omega_{\text{eff}}(\vec{R},t) = \sqrt{\Omega_{\text{eff},0}^2 + \Delta^2(\vec{R},t)}\,; \quad \Delta(\vec{R},t) = \Delta\omega_L - \frac{\Delta E(\vec{R},t)}{\hbar}. \tag{3.29}$$

The local detuning Δ consists of the laser detuning $\Delta\omega_L$ from the unperturbed Rydberg level and of the density dependent shift of the Rydberg level $\Delta E(\vec{R},t)$, given by equation (3.27). It is important that the condensate density is significantly disturbed by the successive excitation of Rydberg atoms. This leads to a time dependence in the local detuning (3.29) and therefore also in the Rydberg atom excitation probability (3.28). Equation (3.28) is valid for short

times t and low single atom Rabi frequencies. Since the single atom Rabi frequencies are small compared to the detuning from the intermediate state Δ_p, the ac Stark shift Δ_{ac} (1.19) can be neglected (see subsection 1.2.4).

So far, in equation (3.28) the probability to find an excited atom at position $\vec{R}$ neither considers the Rydberg blockade, nor the interaction of the Rydberg atom with the ground state atoms in the dense cloud. In order to account for the latter we identify the coupling as a projection onto the basis of single excited Rydberg atoms. Thus we treat this interaction as a kind of measurement process, in which the excited atom breaks off from the large matter wave and localizes spatially. At this point the coherent evolution of the excitation stops and the probability to excite another Rydberg atom becomes zero due to the blockade effect. Based on experimental measurements for all investigated Rydberg states [10], the lifetime of the Rydberg atom in the BEC is limited to about 10 µs, during which no further excitation is possible. In first approximation we adopt this value in our model, fixing the time during which the Rydberg electron interacts with a ground state atom and thus the time in which $f(t) = 1$ in equation (3.26). We choose time steps of 200 ns for the dynamical evolution of our model since this is the estimated duration between two scattering events between a Rydberg electron and ground state atom (see supplemental material of reference [118]). For the model we use a 3-dimensional grid with an axial size of 0.18 µm and a radial of 0.15 µm to calculate the density $\rho(\vec{r}, t) = |\Psi(\vec{r}, t)|^2$ from the condensate wavefunction at each grid point. The total condensate atom number is fixed to the averaged experimental value of about $N = 80000$. To determine if and where a Rydberg atom is excited, we use the following procedure:

1. According to the density distribution $\rho(\vec{r})$ of the condensate atoms we pick a position of a possible excitation on the grid.
2. We draw a random number between 0 and 1 (with a sufficiently small step size) and compare it to the calculated excitation probability (3.28) to determine if an excitation at this grid position takes place.
    - If yes, the function $f(t)$ changes its value from 0 to 1, activating the pseudopotential term in equation (3.26) and the time evolution of the density and condensate wavefunction continues for the 10 µs long lifetime of the Rydberg atom.
    - If not, the steps 1. and 2. are repeated until the number of trials reaches 80000, the total number of atoms in the BEC, or until one atom is successfully excited.

If none of the 80000 trials results in a successful excitation, we evolute the condensate wavefunction in equation (3.26) for one time step of 200 ns with $f(t) = 0$. Since the experimental pulse length is 1 µs, we repeat the stochastic procedure described above for five more times, so, in total six times for one single laser pulse, under the condition that no Rydberg atom was excited. In case of a successful excitation the evolution of the condensate wavefunction continues with $f(t) = 1$ for 10 µs, based on the measured lifetime. The time between two successive Rydberg laser pulses was set to the experimental value of 16 µs. After a successful or non-successful Rydberg excitation, in the rest time until the next excitation takes place the condensate wavefunction propagates without the pseudopotential ($f(t) = 0$). This whole procedure is repeated for 300 or 500 times (total number of excitation pulses used in the experiment), depending on the principal quantum number. We end up with a certain density

distribution at the end of the sequence.

In equation (3.26) we used a capital Ψ to indicate that the interpretation of the complex wavefunction $\Psi(\vec{r},t)$ is different from before. Here it characterizes all atoms in the condensate as well as in the thermal cloud. Now the question arises how to split the wavefunction into a part for the condensate and the thermal cloud. To solve this problem we use the definition proposed originally by O. Penrose and L. Onsager [119]: the condensate is assigned to the eigenvector corresponding to the dominant eigenvalue of an one-particle density matrix, given by

$$\rho^{(1)}(\vec{r},\vec{r}';t) = \frac{1}{N}\Psi(\vec{r},t)\Psi^*(\vec{r}',t). \tag{3.30}$$

In this equation N is the total number of particles and Ψ^* is the complex conjugate of Ψ. This equation is however only a spectral decomposition of an one-particle density matrix, still changing nothing on the fact, that all particles would nonetheless be in the condensate [120]. For the splitting between condensate and thermal cloud we need to average equation (3.30) over time and/or space resulting in a partial loss of information contained in the classical field $\Psi(\vec{r},t)$ [121]. This process is also known as coarse-graining with the mixed state emerging from the pure one by a loss of information. The condensate atom losses therefore stem from the process of averaging and the thereby involved loss of information. This can be understood from the fact that the high energy solutions of the GPE (3.27) oscillate rapidly in time and space, whereas the detection process, for which the wavefunction is evaluated at a specific time and position, is always performed with limited spatial and temporal resolution (uncertainty principle). Therefore each measurement process involves a kind of averaging, leading to a loss of information. All in all, the splitting of the system into condensed and non-condensed components is a result of Bose statistics, interaction and the measurement process.

In the experiment, we use a time of flight absorption imaging technique along one of the radial condensate axes to observe the influence of the Rydberg atoms on the BEC (see section 6.2). Thus for our model we need to integrate over this axis to obtain the coarse-grained/averaged one-particle density matrix

$$\bar{\rho}(x,z,x',z';t) = \frac{1}{N}\int dy \Psi(x,y,z,t)\Psi^*(x',y,z',t). \tag{3.31}$$

Due to the information loss via averaging, we can calculate the dominant eigenenergy, which is the eigenenergy of the condensate, by a diagonalization of this density matrix. All other eigenenergy values belong to the thermal cloud.

For a comparison with the experimentally detected losses we calculate the difference in BEC atom number between the start and end of the sequence. At the end of the evolution only the particles which are in the dominant eigenstate of the wavefunction Ψ belong to the condensate. To make the comparison with the experimental data easier, we divide the BEC losses by the number of excitation pulses: 300 for $n = 110$ and 125, and 500 for the rest of the principal quantum numbers $n > 130$. For the computation of the atom losses, the trap frequencies from the magnetic trap of our experiment were used (see chapter 4). We study the losses per Rydberg laser pulse as a function of principal quantum number n and laser detuning $\Delta\omega_L$, depicted in Figure 3.3(a). Due to the large time consumption of the calculations

only one realization of the stochastic model was calculated for the losses at each detuning. For all principal quantum numbers it is clearly visible that the maximum of the atom losses in the condensate is shifted away from the resonant laser detuning at $\Delta\omega_L = 0$. To explain this behavior we depict histograms of the excited S-state Rydberg atoms in real space in the three panels (b) to (d) in Figure 3.3, exemplarily shown for $n = 110$ and three different laser detunings. In panel (d) at $\Delta\omega_L = 1\,\mathrm{MHz}$ we see a nearly homogenous excitation of Rydberg atoms in the whole condensate, meaning that most of Rydberg atoms are created in the low density parts at the edges of the condensate, featuring fewer losses. At a laser detuning of -9 MHz the Rydberg atoms are excited mainly in the center of the condensate (see panel (c)), in which the density is the highest in the cloud, leading to the highest condensate losses. The maximum is roughly at the position where $\Delta\omega_L = \Delta E(\vec{R}, t)/\hbar$, calculated at the center of the cloud. If we go to a larger absolute detuning of $-13\,\mathrm{MHz}$ we still excite most Rydberg atoms in the center of the condensate, but the number of excited Rydberg atoms decreases significantly, clearly visible if we compare panels (b) and (c) of Figure 3.3. On the blue side of the maximum

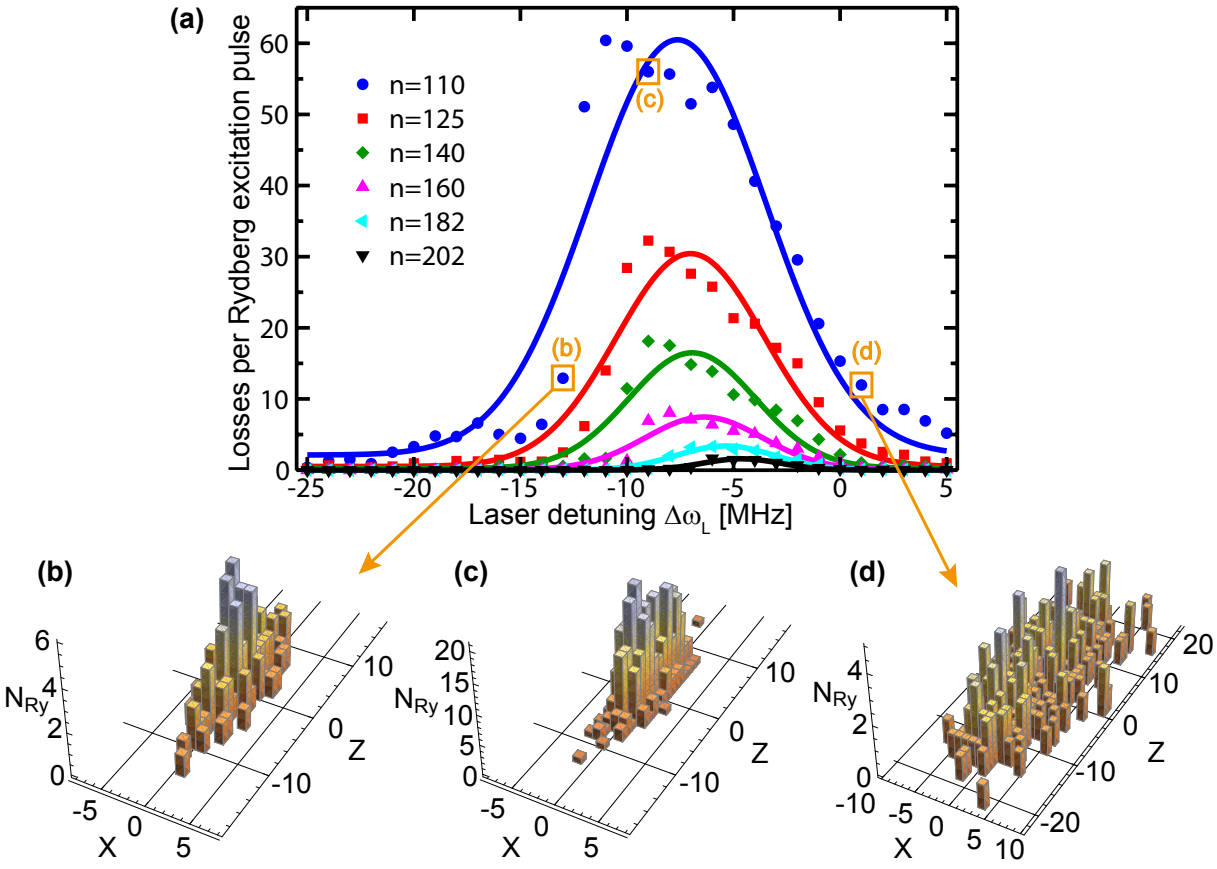

Figure 3.3: (a) Condensate atom losses calculated by one realization of the stochastic model, normalized to the number of excitation pulses, plotted against the laser detuning $\Delta\omega_L$ for different principal quantum numbers n. The solid lines are Gaussian fits to the computed data. (b)-(d) Single realization of the complete excitation sequence showing the real space distribution of the successfully excited Rydberg atoms in the x-z-plane for $n = 110$ and $\Delta\omega_L = -13\,\mathrm{MHz}$ (b), $-9\,\mathrm{MHz}$ (c) and $+1\,\mathrm{MHz}$ (d). The cigar-shaped condensate extends around $40\,\mu\mathrm{m}$ in the axial z-direction and $8\,\mu\mathrm{m}$ in the radial x-direction.

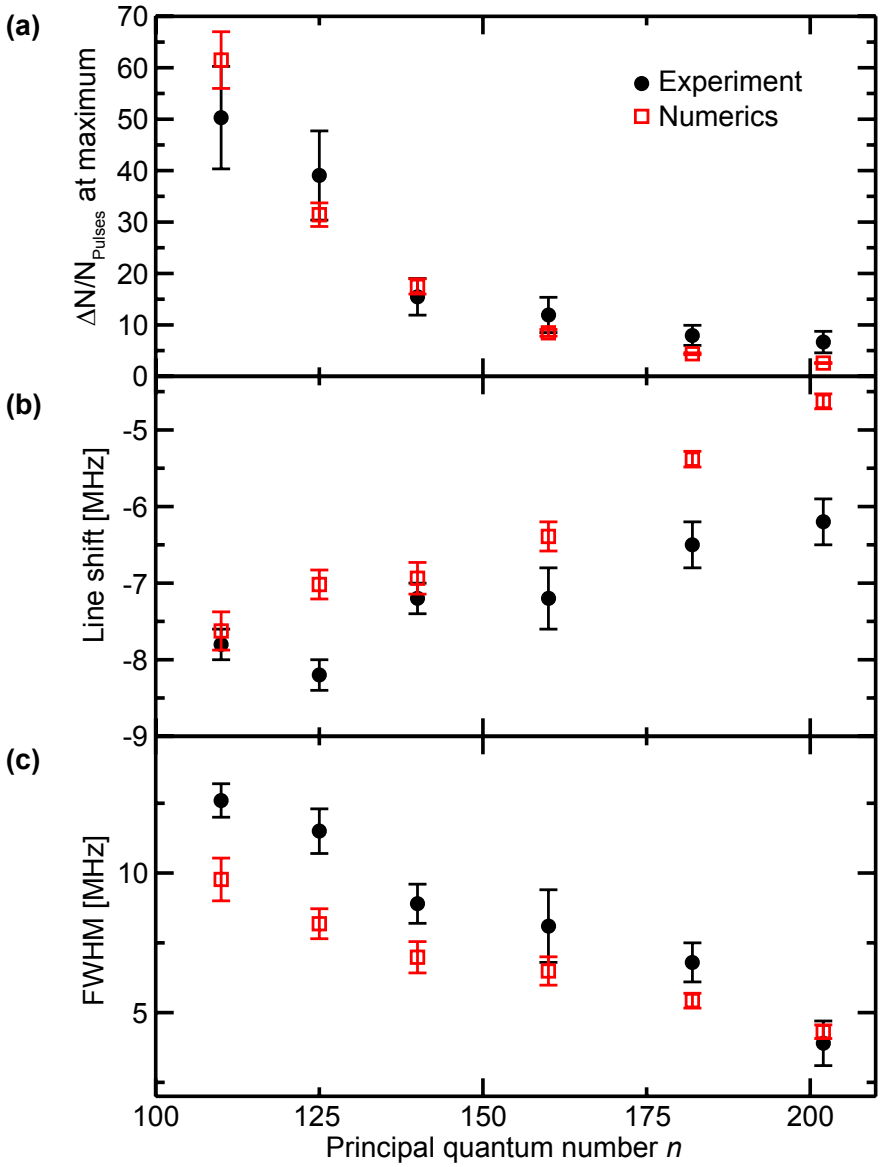

Figure 3.4: Comparison between theoretical (red open squares) and experimental results (black dots) from [10] for principal quantum numbers $n = 110$ to 202. In (a) the maximum condensate atom losses per number of excitation pulses are shown. For (b) and (c) Gaussian fits to the numerical computed data from Figure 3.3(a) have been conducted to obtain values for the line shift (b) and the full width half maxima (FWHM) (c). The error bars result from the Gaussian fits.

loss peak nearly every laser pulse creates a Rydberg atom whereas on the red side fewer Rydberg atoms are excited. If we take for example the $n = 110$ state, at $\Delta\omega_L = -12\,\mathrm{MHz}$ about $2/3$ of the excitation pulses create a Rydberg atom while at $\Delta\omega_L = -16\,\mathrm{MHz}$ only $1/7$ of all excitations are successful.

In Figure 3.4 the numerical data from the theory calculations are compared to the experimental data from [10] for S-states with principal quantum numbers n ranging from 110 to 202. In panel (a) the maximum losses per number of excitation pulses are shown, followed by the line shift (b) and the full width half maximum (FWHM) in (c). The line shift and

FWHM were extracted from Gaussian fits to the simulated losses from Figure 3.3(a). The line shift is the deviation of the position of the maximum of the detected losses from the resonance $\Delta\omega_L = 0$ position; here it equals the laser detuning at the maximum position of the Gaussian fit. It is remarkable that the theoretical calculations match so well to the experimental data considering that only the experimental trap frequencies, Rabi frequencies, lifetime, pulse length and duration, but no further free parameters were used.

Now that we have demonstrated that our theory model agrees well with the experimental findings we take a step forward and propose the imaging of single electron orbitals by the imprint of the electron wavefunction into the condensate, showing simulations with our stochastic model. This proposal is discussed in detail in [118] and its supplementary material and briefly in the outlook of this thesis in section 11.1.

3.4 Shape oscillations in a Bose-Einstein condensate

Another feature of Bose-Einstein condensates is the excitation of collective oscillations of the whole condensate wavefunction, mainly influenced by the trap geometry. In the experimental part (in subsection 9.3.2) we show that due to the excitation of Rydberg atoms in the condensate we evoke quadrupole oscillations. To understand where they originate from, we show in this section how to calculate these oscillation frequencies for our cylindrically shaped condensate with the trap potential given by equation (3.13). We only present the crucial steps in the derivation of these frequencies, details can be found in reference [122]. Starting point to describe the evolution of a Bose-Einstein condensate is the time-dependent Gross-Pitaevskii equation (3.10). In contrast to the previous section 3.3, ψ is the pure condensate wavefunction. We now introduce the condensate density $\rho(\vec{r},t) = |\psi(\vec{r},t)|^2$ and the velocity field

$$\vec{v}(\vec{r},t) = \frac{\hbar}{2mi\rho(\vec{r},t)}\left(\psi(\vec{r},t)\vec{\nabla}\psi^*(\vec{r},t) - \vec{\nabla}\psi(\vec{r},t)\psi^*(\vec{r},t)\right) \tag{3.32}$$

to rewrite the time-dependent Gross-Pitaevskii equation in these macroscopic observables:

$$\partial_t\rho + \rho + \vec{\nabla}(\vec{v}\rho) = 0; \tag{3.33}$$

$$m\partial_t\vec{v} + \vec{\nabla}\left(\delta\mu + \frac{1}{2}m\vec{v}^{\,2}\right) = 0. \tag{3.34}$$

Here, $\delta\mu$ is the change of the chemical potential with respect to its ground state value μ:

$$\delta\mu = V_e(t) + g\rho - \frac{\hbar^2}{2m\sqrt{\rho}}\vec{\nabla}^2\sqrt{\rho} - \mu. \tag{3.35}$$

The next step is the negligence of the kinetic energy term $\frac{\hbar^2}{2m\sqrt{\rho}}\vec{\nabla}^2\sqrt{\rho}$ in equation (3.35) like it was done in the Thomas-Fermi approximation in section 3.2. This approximation is valid in case of dynamical processes if the total number of atoms N in the BEC is sufficiently large so that the restoring force of the collective excitation is dominated by the trap potential and the

atomic interaction g. For a vanishing velocity field $v(\vec{r},t) = 0$ we get the solution from the Thomas-Fermi approximation (3.12) for the density

$$\rho_0 = \frac{\mu - V_e(\vec{r})}{g}. \tag{3.36}$$

A linearization of equations (3.33) and (3.34) with respect to small density changes $\delta\rho(\vec{r},t) = \rho(\vec{r},t) - \rho_0(\vec{r})$ results in the equation:

$$\partial_t^2 \delta\rho(\vec{r},t) = \vec{\nabla}\left[\frac{g}{m}\rho_0(\vec{r})\,\vec{\nabla}\delta\rho(\vec{r},t)\right] = \vec{\nabla}\left[c(\vec{r})\,\vec{\nabla}\delta\rho(\vec{r},t)\right]. \tag{3.37}$$

In absence of a trapping potential, equation (3.37) simplifies to

$$\partial_t^2 \delta\rho(\vec{r},t) = \frac{\mu}{m}\vec{\nabla}^2\delta\rho(\vec{r},t), \tag{3.38}$$

where $c = \sqrt{\rho_0 g/m} = \sqrt{\mu/m}$ is the sound velocity of the homogenous Bose Einstein condensate [108, 110]. We now want to return to our experimental situation (see section 4) where we have a harmonic trap potential given by

$$V_e(\vec{r}) = \frac{1}{2}m(\omega_r^2(x^2+y^2) + \omega_z^2 z^2). \tag{3.39}$$

Inserting this potential into equation (3.37) yields the differential equation

$$\partial_t^2 \delta\rho(\vec{r},t) = \vec{\nabla}\left[\left(\frac{\mu}{m} - \frac{1}{2}\omega_r^2(x^2+y^2) - \frac{1}{2}\omega_z^2 z^2\right)\vec{\nabla}\delta\rho(\vec{r},t)\right], \tag{3.40}$$

which can be solved by using the spherical harmonics in an oscillatory ansatz

$$\delta\rho(\vec{r},t) = \mathrm{e}^{-i\omega t} f(r) r^L Y_L^{m_L}(\Theta,\varphi), \tag{3.41}$$

where L is the angular momentum and m_L the corresponding magnetic quantum number. Note that the projection of m_L onto the symmetry axis z is still a good quantum number. The derivation of the solution can be found in [122]. We acquire different solutions depending on L and m_L:

$$m_L = \pm L \quad : \quad \omega^2 = L\omega_r^2\,; \tag{3.42}$$

$$m_L = \pm(L-1) : \quad \omega^2 = (L-1)\omega_r^2 + \omega_z^2. \tag{3.43}$$

The solutions of equations (3.42) and (3.43) provide a full description of the dipole excitation modes with $L = 1$. Their frequencies are $\omega = \omega_r$ for $m_L = \pm 1$ and $\omega = \omega_z$ for $m_L = 0$, corresponding exactly to the values of an unperturbed harmonic oscillator since their modes are purely radial or axial. If we go to the quadrupole modes $(L = 2)$, equations (3.42) and (3.43) yield $\omega = \sqrt{2}\omega_r$ for $m_L = \pm 2$ and $\omega = \sqrt{\omega_r^2 + \omega_z^2}$ for $m_L = \pm 1$. To determine the $m_L = 0$ solution for the quadrupole mode, we need to use a different ansatz to solve the differential equation (3.40), which involves the coupling between a quadrupole $(L = 2)$ and a monopole mode $(L = 0)$. Decoupling those modes results in the following solution for the quadrupole

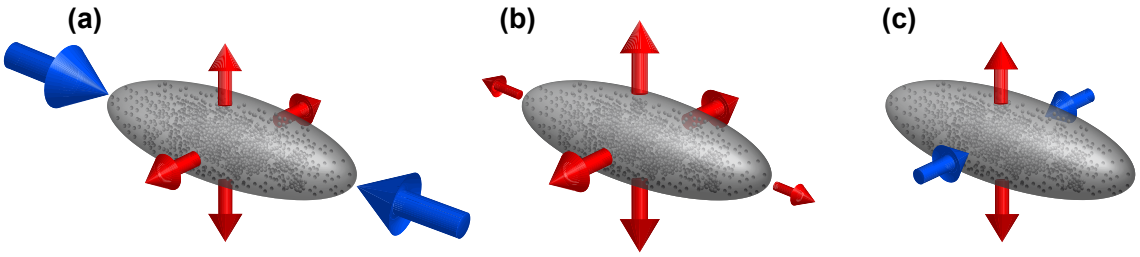

Figure 3.5: Shape of the three experimentally most relevant quadrupolar ($L = 2$) oscillation modes [108]. The oscillations of the slow quadrupole $m_L = 0$ mode (a) at $\omega \approx \sqrt{5/2}\omega_z$ in radial and axial direction are opposed to each other. The fast quadrupole mode $m_L = 0$ (b) oscillates with a frequency of $\omega \approx 2\omega_r$ and in contrast to (a) the phase in the axial and the radial direction is the same. However, the axial oscillation amplitude nearly vanishes compared to the radial one. The $m_L = \pm 2$ quadrupolar mode at $\omega = \sqrt{2}\omega_r$ performs only oscillations in radial direction, but out of phase, as depicted in (c).

mode [122]:

$$L = 2\,; m_L = 0: \quad \omega^2 = \omega_r^2 \left(2 + \frac{3}{2}\lambda^2 \pm \frac{1}{2}\sqrt{9\lambda^4 - 16\lambda^2 + 16}\right) \;; \quad \lambda = \frac{\omega_z}{\omega_r}. \tag{3.44}$$

For our cigar-shaped condensate ($\lambda << 1$), the two solutions of equation (3.44) become $\omega \approx \sqrt{5/2}\omega_z$ and $\omega \approx 2\omega_r$.

After having calculated all the different frequencies for the different oscillation modes of the Bose Einstein condensate, we present in Figure 3.5 the shapes of the experimentally relevant modes for our elongated BEC. The slow (3.5(a)) and fast (3.5(b)) quadrupolar $m_L = 0$ mode, as well as the $m_L = \pm 2$ mode (3.5(c)) have been observed experimentally by inducing modulations to the trapping potential [108, 123, 124], by introducing a random potential via a laser speckle pattern [125] and by frequency modulating the evaporative cooling process [126]. In our experiment we generate collective oscillations by consecutively exciting Rydberg atoms in the BEC for our S- and D-states. We only observe the slow quadrupole $m_L = 0$ mode since the other modes are unlikely due to their asymmetry ($m_L = \pm 2$) or too high frequency $\omega \approx 2\omega_r$ for the $m_L = 0$ mode. The experimental measurements and the comparison with the calculated oscillation frequencies can be found in subsection 9.3.2.

Part II

Experimental Setup

You have to learn the rules of the game. And then you have to play better than anyone else.

Albert Einstein

This part of the thesis deals with the current experimental setup of the cold Rydberg BEC apparatus. With the starting point of building the experiment dating more than ten years back, meanwhile seven generations of PhD students [127, 128, 129, 92, 57, 58, 11] were conducting successful experiments with this apparatus. While the main chamber, the core of the experiment, is still unchanged since that time, other parts of the experiment got changed tremendously. It is fascinating that this apparatus, inspired by the original Bose-Einstein condensate (BEC) apparatus of W. Ketterle [130], still generates great results and there is no plan in the near future to shut this cold Rydberg experiment down. A new setup in our group which improved especially the design of the main chamber to have a better optical access and a higher ion detection efficiency, is starting to produce promising data and will soon start to coexist with the 'old' setup.

Especially two improvements of the setup in the last years allowed to advance to new interesting physics: the Rydberg laser system is now locked to a high finesse ultra low expansion (ULE) cavity, giving rise to a combined laser linewidth of below $30\,\mathrm{kHz}$ and the compensation of the stray $\mathcal{E}$-fields was improved and is now controlled by an eight channel USB voltage analog output device, which applies voltages to six field plates with mV precision. The precise control of the $\mathcal{E}$-field in all spatial directions made it possible to investigate Rydberg states at very high principal quantum numbers up to $n = 202$. Furthermore high resolution spectroscopy, based on the narrow linewidth laser system, enabled us to detect Rydberg molecules with binding energies of $50 - 100\,\mathrm{kHz}$ paving the way for the study of D-state Rydberg molecules in all their various facets.

Part II of this thesis, describing the experimental setup, is consisting of four chapters (4-7). Chapter 4 outlines the preparation of our rubidium samples and the cooling processes required to reach BEC temperatures. Chapter 5 deals with the Rydberg excitation process and on the technical side with the Rydberg laser system, its stabilization and the optical setup around the main vacuum chamber. The two types of detection methods we used to acquire data are in detail explained in chapter 6: the first one is the detection of Rydberg ions via a micro channel plate and the second one is the recording of absorption images after a certain time of flight. The final chapter 7 deals with the newly implemented eight channel USB voltage analog output device, its integration into our setup, the characterization of its precision and long time stability. This device is used for the electric field compensation in order to investigate Rydberg states at high principal quantum numbers.

Other parts of the setup, like the laser system used for cooling, are only discussed briefly, but references to previous theses with detailed descriptions are given.

4 Preparation of samples of ultracold rubidium atoms

In this chapter all processes are described which lead to a magnetically trapped sample of rubidium atoms at thermal cloud or BEC temperatures, which is the starting point for all experiments. The core of the setup is a BEC chamber based on a modified design from the group of W. Ketterle at MIT [130] where everything from trapping, cooling, detecting and imaging is done. The main differences are eight additional separately addressable field plates and the ion detector inside the chamber (details later).

Starting point of the rubidium atoms in the vacuum setup is an oven, heated up to $150\,^{\circ}\mathrm{C}$, in which an ampule of rubidium was placed. The hot atoms are then decelerated in a $85\,\mathrm{cm}$ long Zeeman slower [131] guiding the atoms to the main chamber where a magneto-optical trap (MOT) catches and traps the atoms possessing the right velocity. From the oven part to the main chamber a differential pumping system is installed starting at a pressure of $10^{-7}\,\mathrm{mbar}$ and ending at a pressure below $10^{-11}\,\mathrm{mbar}$ in the main chamber. A mechanical shutter separates the oven part from the main vacuum chamber. After the $2\,\mathrm{s}$ of loading the MOT, a metal plate is turned into the beam path by a mechanical arm to block the hot atoms from accessing the Zeeman slower. The MOT consists of three pairs of orthogonal counterpropagating laser beams nearly resonant to the cooling transition and a quadrupole magnetic field, generated by the pinch coils (see Figure 4.1(b)). All light needed for the trapping and cooling of the ^{87}Rb atoms is provided by a Titanium-Sapphire laser system[1] with the main cooling transition $5S_{1/2}(F = 2) \rightarrow 5P_{3/2}(F = 3)$. Since the transition is not closed and atoms also decay to the $5S_{1/2}(F = 1)$ state, additionally a repumping laser[2] for the MOT and Zeeman slower is necessary, driving the transition $5S_{1/2}(F = 1) \rightarrow 5P_{3/2}(F = 2)$. Atoms in the $5P_{3/2}(F = 2)$ state decay with a probability of 50% to the $5S_{1/2}(F = 2)$ state and are thus part of the cooling cycle again. More details about these laser systems can be found in [58] and [127].

After the loading process several 10^9 atoms, possessing a temperature of a few mK, are trapped in the chamber. To increase the density further, a dark MOT phase of $20\,\mathrm{ms}$ was introduced (see [58, 132] for details). Afterwards the magnetic field for the MOT is completely switched off for a $15\,\mathrm{ms}$ long molasses cooling phase [127, 133], for which the laser light is slightly detuned to the red. This causes a loss of around 50% of the atoms, but also permits to reach temperatures of around 10s of µK. Since there is no B-field and thus no quantization axis anymore, all different m_F levels of the $5S_{1/2}(F = 2)$ state get populated. Therefore the depolarized atoms of the molasses need to be optically pumped to the $(F = 2, m_F = 2)$ state using circular polarized pumping light at a small axial offset field.

The next step is to load the atoms into the magnetic trap by ramping up the magnetic

[1] Coherent MBR-110 Single-Frequency Ti:Sapphire Laser system pumped by a $10\,\mathrm{W}$ Verdi laser

[2] Self-built diode laser with a wavelength of $780\,\mathrm{nm}$

field for $5\,\mu s$. To obtain a large number of atoms in the magnetic trap the mode was matched to the shape and size of the MOT. A scheme of the arrangement of the coils generating the magnetic field can be seen in Figure 4.1(b). The two pinch coils (green) generate the axial trapping confinement whereas the cloverleaf coils (black) create a minimum in the magnetic field landscape exactly in the middle between them, at the position of the atoms. The bias coils (blue) are compensating the high offset field generated at the minimum position of the magnetic field. The shape of the magnetic trap can be varied by changing the offset field (bias coils) from a steep trap with an offset field of around $B_0 = 0.8\,\mathrm{G}$ to a shallow one with the highest possible offset field of $B_0 = 13.55\,\mathrm{G}$ when no compensation current is applied to the bias coils. This highest offset field exists due to a misalignment of the coils, which can be compensated with the bias coils. More information about the magnetic field generation can be found in [127, 134], whereas the system of power supplies generating the magnetic fields is in detail described in reference [129]. During the ramping procedure of the magnetic field, the atoms are compressed to a cigar-shaped cloud.

The last and longest step to reach the BEC regime is the evaporative cooling procedure [114]. Thereto an off-resonant radio frequency (RF) drives transitions between the m_F and $m_F \pm 1$ substates of the $5S_{1/2}(F = 2)$ ground state atoms, which are split in the magnetic field. In a $40\,\mathrm{s}$ long scanning ramp of the RF from $45\,\mathrm{MHz}$ down to below $1\,\mathrm{MHz}$, atoms are transferred to the untrapped $m_F \leq 0$ states. The detuned frequency ramp is chosen in a way that only hot atoms which reach the border of the magnetic trap and therefore experience a large Zeeman shift are transferred to the untrapped states. By loosing the hottest atoms the rest of the atoms rethermalizes and the overall temperature of the atom cloud is reduced. Crucial for the evaporative cooling is that the atoms have a high density since this increases the efficiency of the rethermalization process due to collisions, which is needed for this cooling cycle to generate hot removable atoms again. Depending on the final frequency of the RF scanning ramp, either a cold thermal cloud with temperatures of a few μK and peak densities of $10^{12}\,\mathrm{cm}^{-3}$ can be realized or a BEC at temperatures of a few hundreds of nK and peak densities of about $10^{14}\,\mathrm{cm}^{-3}$. The typical condensate atom number is about $(7 - 10) \times 10^4$. It also needs to be mentioned that additionally to the $5S_{1/2}(F = 2, m_F = 2)$ state the $5S_{1/2}(F = 2, m_F = 1)$ state is also populated and trapped to a small extent. These atoms generate additional peaks in the spectra (see Figure 1.3).

After the evaporative cooling the magnetic offset field at the center of the magnetic trap can be ramped from its initial value of about $0.8\,\mathrm{G}$ to the highest possible value of $B_0 = 13.55\,\mathrm{G}$, by ramping down the current in the bias coils, used for compensation. During this process the RF frequency needs to be increased to adjust for the higher Zeeman splitting so that still only the hottest atoms are removed. One has to be careful with the RF ramp so that the BEC survives this procedure and that no shape oscillations are excited. To circumvent these problems the increase of the offset field is done in a smooth S-form shaped ramp lasting $400\,\mathrm{ms}$. All experiments conducted in this thesis were done at the highest possible offset field of $B_0 = 13.55\,\mathrm{G}$; this is especially crucial for the D-state molecule measurements where this high magnetic field is needed to split and address the different m_J states separately (see section 8.1). For this offset field the axial trapping frequency is $\omega_z = 2\pi \cdot 22\,\mathrm{Hz}$, whereas the radial trapping frequency has the value $\omega_r = 2\pi \cdot 82\,\mathrm{Hz}$. These trap frequencies were

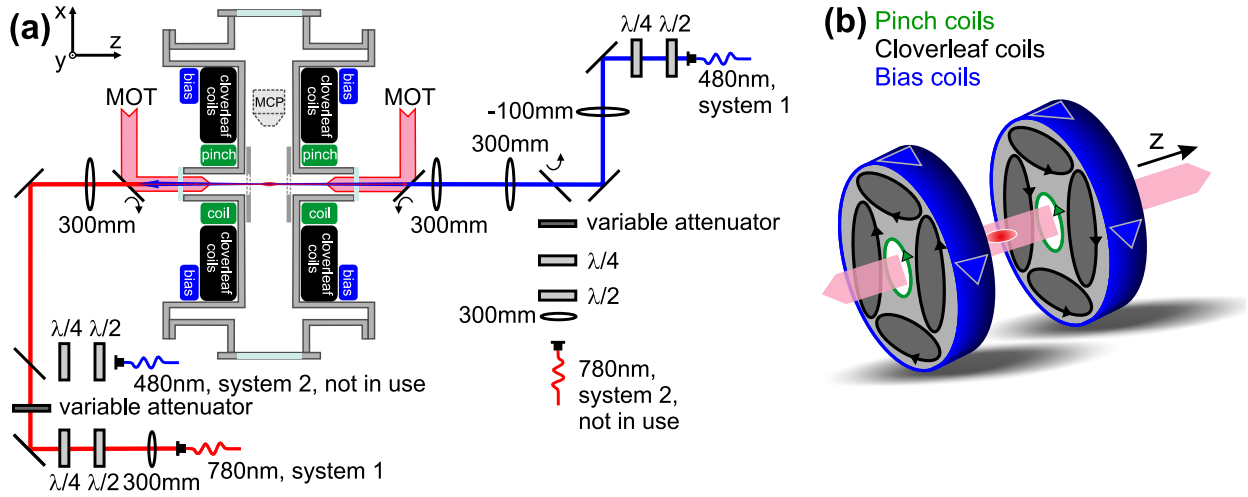

Figure 4.1: (a) Top down view of the Rydberg excitation laser setup around the main chamber. The pinch (green), bias (blue) and cloverleaf coils (black) are wound around the outside of the vacuum main chamber. During the MOT loading phase, motorized mirrors are flipped up to let the axial MOT beams enter the chamber. Afterwards they are turned down to open the pathway for the counterpropagating Rydberg excitation lasers. For the experiments in this thesis only one Rydberg excitation laser system was used. A variable attenuator is used to adjust the power of the red laser with a wavelength of 780 nm. In (b) the magnetic field coils are shown in detail including the winding directions of the coil wires (same colors as in (a)).

measured by applying a short strong $\mathcal{E}$-field pulse in the x- or z-direction in order to create trap oscillations of the atoms. From time of flight absorption imaging (see section 6.2) at different hold times the trap frequency can obtained from sinusoidal fits to these oscillations.

5 Rydberg excitation

The excitation of the Rb Rydberg states is performed by a two-photon excitation process as depicted in the scheme of Figure 5.1. A σ^+-polarized $780\,\mathrm{nm}$ laser drives the transition from the $5S_{1/2}\,(F = 2, m_F = 2)$ ground state to the intermediate $5P_{3/2}\,(F = 3, m_F = 3)$ state. The upper transition is conveyed by a σ^+- or σ^-- polarized $480\,\mathrm{nm}$ laser to address Rydberg D- and S-states. The red laser is Δ_p =$500\,\mathrm{MHz}$ blue detuned from the intermediate state to prevent its population. This allows us to treat this three level system as a simple two level system with an effective resonant Rabi frequency $\Omega_{\text{eff},0}$ (1.24), realizing a coherent coupling between ground and Rydberg state (see subsection 1.2.4). Note that the Rabi frequency of the lower transition Ω_r is limited by off-resonant scattering from the intermediate level

$$\Gamma_{\text{scat}} = \frac{\Omega_r^2}{4\Delta_p^2}\Gamma_p, \tag{5.1}$$

which depends on the intermediate detuning Δ_p and the decay rate of the P-state Γ_p [135]. In contrast to that, the Rabi frequency of the upper transition was chosen to be as high as possible to maximize the effective resonant two-photon Rabi frequency (1.24). Here the constraint arises from the technical side since the maximum output power of our frequency doubled $480\,\mathrm{nm}$ laser is limited to around $400\,\mathrm{mW}$[1], from which about $120\,\mathrm{mW}$ are focused onto the atoms. An acousto-optic modulator (AOM), a 20 m long fiber and other optics consume the majority of the total useable power. Besides, increasing the frequency of the $480\,\mathrm{nm}$ laser to reach higher Rydberg states $n > 100$ results in a small drop of output power due to a less efficient doubling in the cavity.

Since neither the polarization of the light, nor the spin polarization of the atomic states in the experiment are perfect there are always unwanted polarization components resulting in the excitation of other magnetic substates m_J. Already mentioned in chapter 4, the evaporative cooling creates a small population of atoms in the weakly trapped $5S_{1/2}(F = 2, m_F = 1)$ state. This gives rise to additional small peaks in the spectrum shifted by $\mu_B B/(2h)$ to the blue from the lines created by the excitation from the $5S_{1/2}(F = 2, m_F = 2)$ state (see Figure 1.3). This feature can be utilized to our advantage for the calibration of the offset field of the magnetic trap.

A detailed description of the laser system used for the experiments in this thesis can be found in [136]. For the locking and stabilization of the laser frequencies a commercial cavity was used[2]. As spacer material for this cavity, premium grade ultralow expansion (ULE) glass is used, which allows us to completely neglect thermal drifts of the resonance frequency, even on the kHz scale. The cavity has a finesse > 10000 and its mirrors possess a quad-band coating

[1] Toptica TA-SHG pro system, consisting of a $970\,\mathrm{nm}$ infrared diode laser whose frequency is doubled in a ring cavity

[2] Stable Laser Systems ATF 6020-4; cavity serial number: 0018

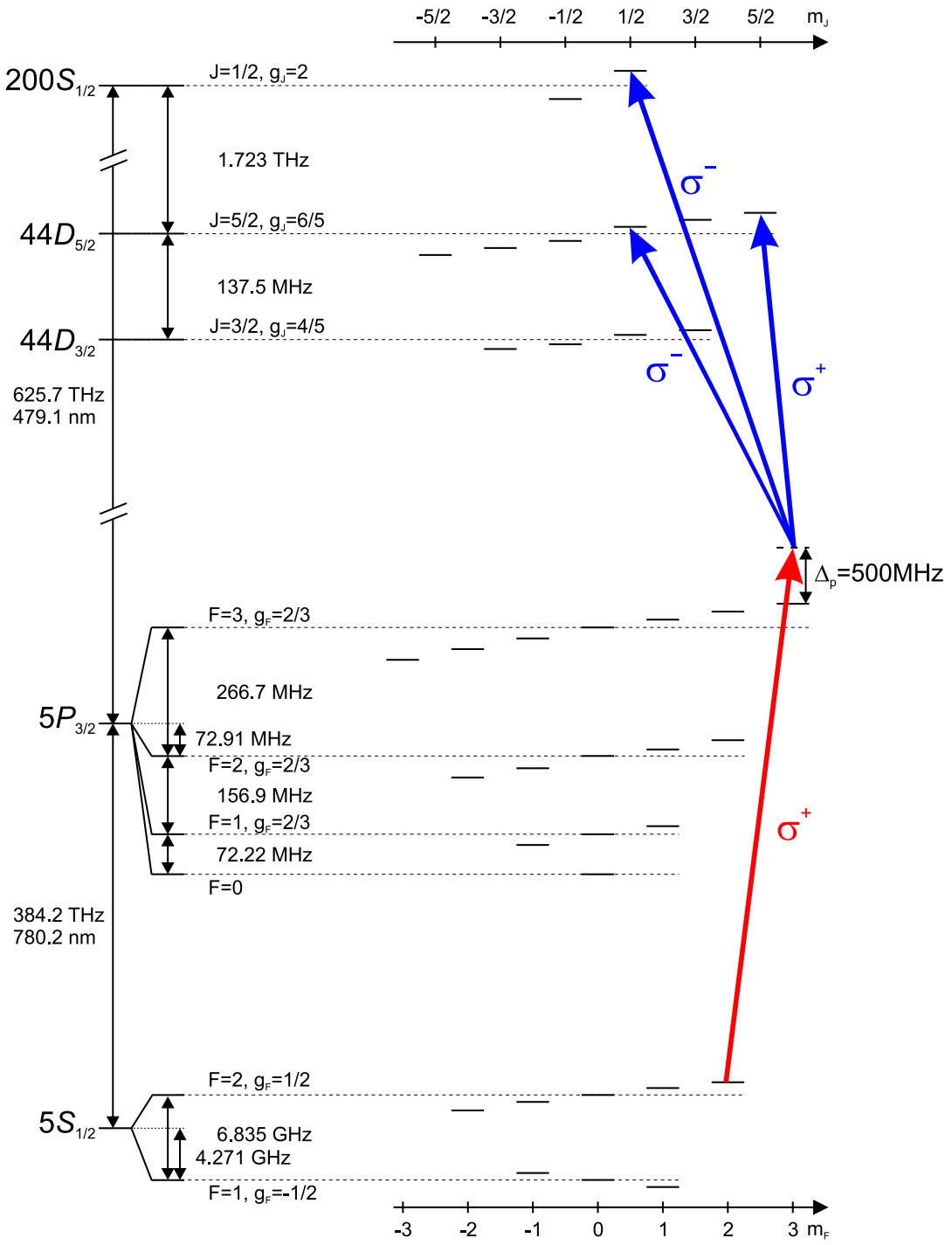

Figure 5.1: Level scheme for the Rydberg excitation of ^{87}Rb, including the ground state $5S_{1/2}$, the intermediate state $5P_{3/2}$ and exemplarily the Rydberg states $44D_{3/2}$, $44D_{5/2}$ and $200S_{1/2}$. On the left side the hyperfine splittings for the ground and intermediate state are shown, whereas for the Rydberg states only the fine splitting is depicted since the hyperfine structure can be neglected. On the right side the splitting of the states in a magnetic field is shown, indicated by the magnetic quantum number m_F (ground and intermediate state) and m_J (Rydberg states). Via a two-photon excitation process, Δ_p =500 MHz blue detuned from the intermediate $5P_{3/2}\,(F = 3, m_F = 3)$ state, Rydberg atoms are excited. By changing the polarization of the upper transition D-states (σ^+- and σ^--polarization) and S-states (σ^--polarization) can be addressed. In the scheme only the strongest excitation path is highlighted. The hyperfine structure splittings are taken from [55].

providing a simultaneous stabilization of four lasers with the wavelengths of $780, 840, 960$ and $1020\,\mathrm{nm}$ to this cavity. Thus an additional laser system using the inverted excitation scheme, which uses the $6P_{3/2}$ as intermediate state instead of the $5P_{3/2}$, can be stabilized additionally to our existing laser system. To control the frequencies of the lasers, sidebands at a variable frequency are locked to the TEM_{00} cavity mode. A commercial Pound-Drever-Hall module[3] provides a $20\,\mathrm{MHz}$ signal which is modulated by a fiber coupled electro-optic modulator (EOM) on the laser frequency. The scanning of this sideband frequency is done by using a system of direct digital synthesizers (DDS)[4], assembled in the electronics workshop at the university. A heterodyne linewidth measurement with a second laser revealed that the linewidths of both lasers are below the detection limit of $20\,\mathrm{kHz}$. Further details about the setup can be found in [136].

The blue and red laser beams for the Rydberg excitation are shone from the opposite direction onto the atoms in the main chamber to reduce the Doppler broadening (see Figure 4.1(a)). In contrast to a collinear setup the counterpropagating beam setup reduces the Doppler broadening more than a factor of 3 to around $19\,\mathrm{kHz}$ for a temperature of $1\,\mu\mathrm{K}$. Two installed motorized flipping mirrors are used to switch between the axial MOT beams, shone in during the MOT loading phase, and the two Rydberg excitation laser beams (see Fig. 4.1(a)). For the experiments conducted in this thesis only one Rydberg laser system was used (system 1), but by using dichroic mirrors a second laser system can be used simultaneously for two color Rydberg experiments in the future. The red $780\,\mathrm{nm}$ laser beam is focused to a beam waist of $500\,\mu\mathrm{m}$, whereas the blue $480\,\mathrm{nm}$ beam initially had a beam waist of $10\,\mu\mathrm{m}$ at the position of the atoms, including the focusing telescope. The goal of this focusing was to increase the two-photon Rabi frequency but it was found that this leads to an additional potential for the atoms generated by the blue laser. This caused an unwanted dimple in the harmonic trap potential. To get rid of this effect, the position of the $300\,\mathrm{mm}$ lens directly in front of the chamber was shifted away to defocus the beam and generate a harmonic trap potential again. Thus we ended up with a calculated beam waist of about $60\,\mu\mathrm{m}$ for the $480\,\mathrm{nm}$ laser. Nevertheless we still detected an influence of the potential caused by the blue laser on the BEC atoms, leading to unwanted shape oscillations. This problem could be overcome by switching the laser on adiabatically during the ramping of the magnetic offset field.

For the alignment of the lasers on the thermal cloud, it is sufficient to change the beam direction of the blue laser until the maximum detector signal is found (see section 6.1 for information about the ion detection). But detecting a maximum in the ion signal does not automatically mean that the excitation beams exactly hit the BEC atoms. Therefore a different technique was applied: a back reflection mirror was placed in $-z$-direction directly behind the chamber (see Figure 4.1(a)) so that the blue laser beam creates a lattice for the atoms and is reflected back into the fiber. A pulsing of the optical lattice for about $10\,\mu\mathrm{s}$ creates a diffraction pattern in the BEC if the blue laser is aligned exactly on the condensate atoms. Detecting a maximum of these diffraction peaks in the time of flight absorption images (details in section 6.2) guarantees a precise alignment of the lasers on the BEC atoms. Further details can be found in [11].

[3] Toptica PDD 110
[4] ELAB 70/10

When I started writing this thesis, a new laser setup was built consisting of two diode lasers with the wavelengths $1020\,\mathrm{nm}$ and $420\,\mathrm{nm}$ using the $5S_{1/2} \rightarrow 6P_{3/2}$ as lower transition, the so-called inverted scheme. The big advantage of this system is that a higher laser power of about $1000 - 1500\,\mathrm{mW}$ is currently available technically for the upper transition ($1020\,\mathrm{nm}$ light). A drawback is that the light for the lower transition at $420\,\mathrm{nm}$ can ionize a Rb atom in a two-photon process leading to additional losses [137, 138]. Taking into account the dipole matrix elements for these two transitions, a factor of $2 - 3$ can be gained by using this new laser system in comparison to the currently used laser system.

6 Detection methods

There are two different kind of detection methods we use to obtain information about the Rydberg atoms. The first method is to detect Rydberg atoms via a field ionization process counting the number of arriving ions at a micro channel plate detector. For the second method, absorption imaging is used in a time of flight (TOF) experiment. These two methods are now discussed in detail.

6.1 Ion detection

After the laser excitation of the Rydberg atoms we apply a sufficiently large voltage to the opposing field plates B and H (see Figure 7.1(b)) generating an electric field in order to ionize the Rydberg atoms. Details about the field plates and stray $\mathcal{E}$-field compensation can be found in chapter 7. The ionization field also accelerates the ions towards a micro channel plate (MCP) detector. The energy needed for a successful ionization can be estimated by a classical calculation taking into account the Coulomb potential of the Rydberg core and the Stark potential caused by the external electric field. In the resulting potential plot electrons with energies above the local maximum (saddle point in 3D) are ionized. One obtains for the classical ionization field [31]:

$$\mathcal{E}_{\text{ion}}(n) = \frac{1}{16}\frac{e}{4\pi\epsilon_0 a_0^2}\, n^{\star\,-4}. \tag{6.1}$$

Here $n^\star$ is the effective principal quantum number (see section 1.1) and a_0 the Bohr radius. This formula yields an ionization field of $\mathcal{E}_{\text{ion}} = 312\,\mathrm{V/cm}$ for $n = 35$ which requires high voltages of a few kV for the field plates. In the experiment two high voltage power supplies and switches[1] are used. For the measurements conducted at high principal quantum numbers $n > 100$ only electric fields smaller than $6\,\mathrm{V/cm}$ are needed for the ionization. Thus a faster low voltage switch[2] is used in connection with two low voltage power supplies which provide voltages of some 10s of volts. Note that the voltages applied to the two field plates are not the same. The reasons could be stray $\mathcal{E}$-fields which are only compensated at the positions of the atoms or maybe some slight misalignment of the MCP detector during the assembly of the main chamber. The voltages applied to the field plates were optimized on the ion signal of the detector. Details about the MCP detector, its calibration and functionality can be found in [11, 127, 139]. The signal of the MCP is recorded by a PCI digitizer card[3]. Since the overall detector efficiency is only about $2\,\%$ [139], hundreds of Rydberg atoms need to be ionized in the cloud to get a reliable ion signal. That is the reason why this measurement technique

[1] 2 Heinzinger LNC 3000-20pos. power supplies and 2 Behlke HTS 61-03-GSM high voltage push pull switches
[2] CGC instruments NIM-AMX500-3F digital threefold analogue switch
[3] ADLINK Technology PCI-9812

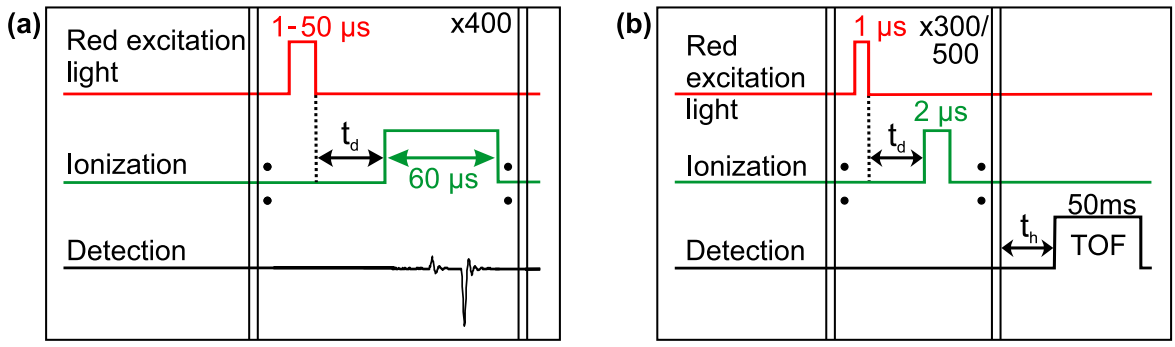

Figure 6.1: Sketches of two different experimental sequences used for the experiments conducted in this thesis. In (a) the sequence for a spectroscopy measurement is depicted. An experimental cycle consists of a typically 1-50 µs long laser excitation pulse and a 60 µs long ionization pulse. During this time a signal on the MCP can be detected. This cycle is repeated 400 times, each time with a different laser detuning, yielding in combination with our small laser bandwidth a high resolution spectrum. For lifetime measurements an additional variable delay time t_d is introduced in the sequence before the ionization pulse. In (b) the excitation sequence of Rydberg atoms in the BEC regime is shown. After a 1 µs long excitation laser pulse, a 2 µs long ionization pulse is used to remove residual population in the Rydberg state or any possibly existing ions. Between the excitation and ionization pulse there is a fixed delay time t_d which is typically 10 µs (more details in the text). This cycle is repeated 300 or 500 times, depending on the principal quantum number n, and at the end, a time of flight absorption image is recorded from the BEC cloud. Comparing the atom losses of this absorption image with a reference image, information about the Rydberg atoms is obtained. An additional hold time t_h before the TOF was introduced for the oscillation measurements.

only works for large thermal clouds and not for the BEC in our present setup. Nevertheless this method has its advantages since in one single experimental run (one atomic cloud), a whole spectrum as shown in Figure 1.3 can be obtained by scanning the frequency of the red excitation laser. In combination with our narrow linewidth excitation laser system high resolution spectroscopy data can be obtained. Note that we cannot do a state selective field ionization with our detector since the detector efficiency is too low.

Our standard sequence for recording a spectrum with the ion detector is depicted in Figure 6.1(a). After the cloud is prepared in the magnetic trap and cooled down to a few µK (see chapter 4), the two excitation lasers create Rydberg atoms in the whole thermal cloud for typically 1-50 µs. Next follows a 60 µs long ionization field pulse, during which the ion signal is detected at the MCP. This whole cycle of excitation, ionization and detection is repeated 400 times in one single cloud (one experimental run), while the red laser frequency is changed after each cycle. This allows us to obtain a complete spectrum in a total experimental runtime of about 50 seconds. If the power of the red laser is not chosen too high, the cloud does not get depleted during the 400 excitation laser pulses, since the fraction of extracted Rydberg atoms is small compared to the total atom number of typically 3×10^6. In the present configuration the time between two consecutive laser pulses is set to 6 ms, including an additional wait time so that there is no problem with the rearm time of the digitizer card. For the lifetime measurements in the thermal cloud, an additional variable delay time t_d is added between excitation and

ionization. Increasing the wait time results in a smaller detected Rydberg atom number from which the lifetime, using an exponential fit to the data, can be extracted. The measurements of the lifetimes, the analysis and a discussion about possible decay mechanisms, can be found in subsection 9.2.1, whereas a short section on the theory of Rydberg atom lifetimes is presented in section 1.4.

6.2 Time of flight imaging

As stated in the previous section, for measurements in the BEC regime, the ion detection method is not applicable since our detector efficiency is simply too small ($\sim 2\,\%$). Considering that we aim for the excitation of single Rydberg atoms in a BEC, the signal of one or a few Rydberg ions is not high enough for the current setup. Even if it would be possible, there is the problem of a small thermal cloud surrounding the BEC which also generates an ion signal. Since we cannot separate these two signal sources, no valuable information can be obtained. Therefore a different approach was realized, using an absorption imaging technique.

The idea behind this method is to observe an atom loss in the absorption image taken from the BEC in a time of flight (TOF) experiment [108, 127, 128] and compare it with a reference picture taken at a different laser detuning for a subtraction of the background. For this measurement technique we switch off the magnetic trap and let the atoms fall down in the gravitational field of earth for about $50\,\mathrm{ms}$. Due to the different expansion velocities of the thermal cloud and BEC atoms during the TOF, we are mainly left with the condensate atoms and only a small fraction of the surrounding thermal could. Since the size of the condensate increases by a factor of about 8 after the TOF, it is possible to resolve changes in the condensate atom number via absorption imaging. The theory of the expansion of a BEC, including the equations of motion, can be found in section 3.2. To realize this scheme we have to make sure to create enough atom losses so that we can detect a difference between the two images. This is done by consecutively exciting Rydberg atoms in the BEC, waiting for them to interact with the ground state atoms and then getting rid of any ions or Rydberg excitations by field ionization. Repeating this process for 300-500 times, we end up with sufficiently large losses. It is important to note that all measurements conducted in the BEC were done for principal quantum numbers $n > 100$, so that the blockade radius of one single Rydberg atom is exceeding the condensate in all spatial directions. Thus the creation of further Rydberg atoms in one excitation pulse is forbidden due to the blockade effect (see section 1.5).

The experimental sequence for this high n measurement is shown in Figure 6.1(b). After the $1\,\mu\mathrm{s}$ long red Rydberg laser excitation pulse, a $2\,\mu\mathrm{s}$ long ionization field pulse is applied to the field plates B and H (see Figure 7.1(b)). Note that the blue laser is already switched on adiabatically over $400\,\mathrm{ms}$ during the ramping of the magnetic offset field. For the ionization at these high n, it is sufficient to apply $50\,\mathrm{V}$ and $46\,\mathrm{V}$ to the field plates B and H, respectively, in order to create an ionization field of about $18\,\mathrm{V/cm}$. The voltages were adjusted to get the maximum ion count signal from the detector. The ionization is done to get rid of any ions or still existing Rydberg atom in the BEC. Between the excitation laser pulse and field ionization a fixed delay time t_d was introduced in order to provide enough time for the Rydberg electron to interact with the condensate ground state atoms in its orbit.

In our standard BEC loss measurements, this time was set to $10\,\mu s$, which is adapted to the longest lifetime of all measured Rydberg states in the BEC (see subsection 9.2.1). Thus we chose a time interval of $16\,\mu s$ between two successive red excitation pulses. This cycle of excitation and ionization is continuously repeated for $300 - 500$ times, depending on the excited Rydberg state. For the measured states above $n = 160, 500$ cycles were used to enhance the losses, whereas for states below this principal quantum number, 300 cycles were sufficient. After a TOF of $50\,ms$ at the end of the cycles, an absorption picture is taken from the released condensate atoms. An advantage here is that the hotter, faster thermal cloud atoms are mainly gone and via fitting routines described in [108, 128], the absolute number of BEC atoms can be extracted from the image. If we now take one image with both excitation lasers on and another one with the red laser switched off, we can get the BEC losses from the subtraction of the corresponding atom numbers. However it turned out that this method is very sensitive to atom number fluctuations and the additional losses from the red laser, which are not present in the second image, lead to an overestimation of the total number of losses. The trick is to record two TOF images each time with both lasers switched on, but one recorded at the Rydberg excitation resonance and the other one off-resonant. Thereby the losses due to the red Rydberg laser are showing up in both images. Furthermore we improved the data analysis to extract the atom losses and the aspect ratio of the condensate (ratio between radial and axial extent of the condensate) from the images, using the following procedure:

First the intensity per pixel in the condensate was calculated by summing over all pixels in a rectangle, in which the condensate was detected and normalizing this value to one pixel. For the background a larger area around the rectangle was chosen and the pixels were again summed up and normalized (to one pixel). These two values were then subtracted from each other, yielding an intensity per pixel, caused by the condensate. This value was also calculated for the reference image taken $50 - 90\,MHz$ away from the laser detuning for which we detected the condensate atom losses. To compute now the percentage of lost atoms, the intensity per pixel value from the reference image is subtracted from the actual measured value, normalized to the value of the reference image. The method with the reference picture has the advantage to minimize the influence of atom losses due to off-resonant scattering from the intermediate state and deformations of the trap caused by stray magnetic fields. The reference images were always taken directly before or after the 'real' loss images. Note that in a standard measurement we took 20 TOF images (10 of them are reference images) for one detuning value of the blue Rydberg laser and averaged over them to compensate for fluctuations in the BEC atom number and to get better statistics. Thus for a typical BEC atom loss measurement, including 30 different laser detunings, around 9 hours of uninterrupted data acquiring is needed. To calculate the aspect ratio, one-dimensional Thomas-Fermi fits along the axial and radial direction were conducted. To obtain the profile for the axial/radial fit, it was averaged over 11 pixel rows in axial/radial direction. Apart from the limited optical access, another factor reducing the resolution of the taken condensate images is the pixel size of $6.45\,\mu m$ of the camera[4]. We take 1/4 of the camera resolution as an estimated error for the determination of the radial and axial extent of the condensate in these images. The measurement results with this pulsed excitation sequence are discussed in section 9.2.

[4]Pixelfly from PCO

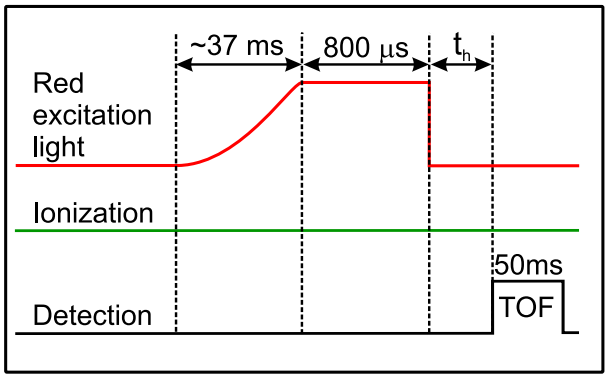

Figure 6.2: Experimental sequence for the oscillation measurements. Instead of pulsing the red laser light as in Figure 6.1(b), the red laser light is adiabatically ramped to its maximum in about 37 ms and kept at this level for 800 µs. In the experiment different ionization pulses were tested, but in the end we got rid of all ionization pulses. After a variable hold time t_h, the 50 ms TOF absorption imaging is the same as in the pulsed sequence (see Figure 6.1(b)).

A slightly different type of measurement was conducted to determine the lifetime of the Rydberg atoms in the BEC. Here measurements were taken for different delay times t_d (see Figure 6.1(b)), saturating for longer wait times at a constant atom number value. Fitting an exponential function yields the lifetime of the Rydberg atoms (see subsection 9.2.1 for the measurements). In these measurements the time between two successive red laser pulses was fixed to 70 µs in order to allow measurements with a maximal delay time t_d of 60 µs.

The goal of the third type of measurement conducted in the BEC regime is to get information about the condensate oscillations induced by the Rydberg electron-phonon coupling. The first measurements were done using the pulsed excitation sequence depicted in Figure 6.1(b) where an additional hold time t_h was introduced. This wait time was varied during the data taking, showing distinct shape oscillations in the condensate (see subsection 9.2.3 for the measurements). However, it was found that these oscillations are mainly caused by the pulsing of the red laser, not by the excitation of Rydberg atoms. Thus we changed our excitation sequence to the one depicted in Figure 6.2. The main difference to the pulsed sequence in Figure 6.1(b) is, that the red laser is now adiabatically switched on over 37 ms in order to minimize the effect of the red laser light to create unwanted condensate oscillations. Additionally, for most of the oscillation measurements, we do not use an ionization field pulse in order to get rid of any effects that could influence the oscillatory behavior of the condensate. The red light is on its maximum level for 800 µs which corresponds to 50 cycles in the pulsed sequence. Furthermore a fixed hold time t_h of 5 up to 90 ms was introduced before the TOF to observe the time dependent oscillations of the condensate. The 50 ms long TOF is the same as in the other sequences. The measurements of the shape oscillations in the condensate with this adiabatic ramping sequence can be found in subsection 9.3.2.

7 $\mathcal{E}$-field control and compensation

For the detection of Rydberg atoms at high principal quantum numbers $n > 100$, the control of the stray electric field starts to become crucial, since the polarizability of the high Rydberg states scales like $n^{\star 7}$ [140]. An advantage of the chamber design is that the field plates and the atomic cloud are far away from the chamber walls and thus surface charges do not negatively influence the $\mathcal{E}$-field compensation and ionization of Rydberg atoms. Thus the investigation of Rydberg states even at $n = 200$ is feasible with our current setup. For the $\mathcal{E}$-field compensation, six out of eight separately addressable field plates are currently used to compensate fields in all three spatial directions at the position of the atoms (see Figure 7.1(b)).

In Figure 7.1(a) the measured Stark map for the $160S$ state is shown as an example, used for the $\mathcal{E}$-field compensation. To acquire the color coded data, a spectroscopy measurement in a thermal cloud was conducted for different applied electric fields. Theoretical calculations (black lines) yield the energies of the $n = 157$ manifold crossing the $160S$ state and show that already for small electric fields of around $5\,\mathrm{mV/cm}$, deviations from the quadratic behavior occur. The reason for the vanishing Stark curve is a broadening caused by the coupling to the manifold and by the inhomogeneity of the electric field.

The electric field compensation is done by scanning the $\mathcal{E}$-fields in x-, y- and z-direction by applying voltages to specific field plates in detail mentioned in the next paragraph. In each single spectrum in the Stark map, a Gaussian is fitted to the signal. Then a parabolic function

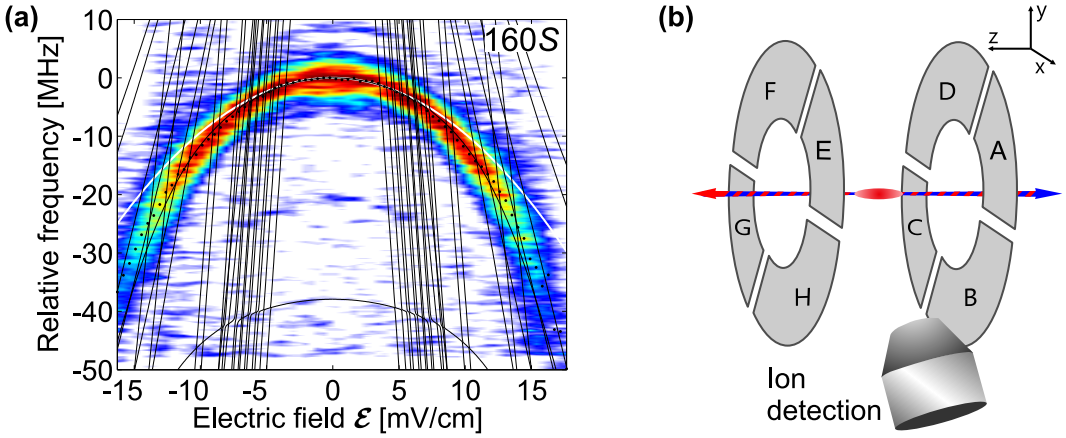

Figure 7.1: In (a) an example of a Stark map for the $160S$ state can be seen, taken from [11]. On top of the measured color coded signal, the theoretically predicted energies of other states, crossing the $160S$ state are shown as black lines. The small black dots are the maxima of fitted Gaussians to the data and the white line is a parabolic fit to the theory at low electric fields, where the Stark effect is purely quadratic. In (b) the geometry of the eight separately addressable field plates positioned around the atomic cloud to control the $\mathcal{E}$-fields is sketched. The micro channel plate in its housing is also shown.

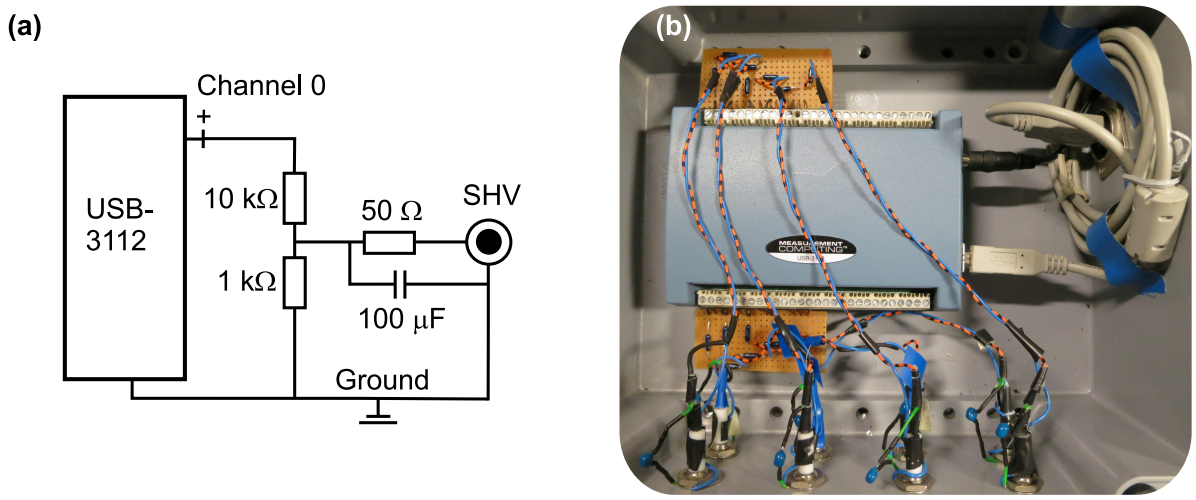

Figure 7.2: (a) Circuit diagram of the connection from one channel of the USB-3112 device to a SHV (safe high voltage) connector. A detailed description is given in the text. (b) Picture taken from the Measurement Computing USB-3112 device inside a box showing the circuit depicted in (a) for all eight channels. In addition the USB connection and power supply connection is visible.

is fitted to the maxima positions of these Gaussian fits in the region where the Stark shift is still quadratic. Its maximum position, which coincides with the smallest linewidth in the spectrum, yields the compensation voltage. The reason for this is that at the maximum of the parabola the best compensation of stray $\mathcal{E}$-fields including gradients is achieved and the atomic line gets thus less broadened. Repeating this procedure several times for all spatial directions results in a 3-D compensation of all stray $\mathcal{E}$-fields. Increasing the principal quantum number from $n = 110$ in steps of about 20, the compensation was performed until $n = 202$ was reached. At this value the limit of our compensation is reached and $\mathcal{E}$-field gradients now play a crucial role which need to be compensated as well to be able to go to higher n. This would require a new method of compensation and was not implemented yet since $n = 202$ was sufficient for all experimental purposes. The electric field can be controlled within $1\,\mathrm{mV/cm}$ and is stable for around one week. This is especially crucial for $n > 180$ where a recompensation needs to be done regularly. For lower n it is stable for a few months and one has to do the compensation again when a significant broadening of the linewidth of the atomic states is detected. All these measurements need to be done in thermal samples of around 1 µK and low laser powers so that scattering effects at the intermediate level and heating effects are reduced and do not lead to an artificial broadening of the acquired linewidth.

Initially the voltages for the field compensation were provided by three different arbitrary waveform generators, supporting a voltage resolution of $1\,\mathrm{mV}$. Since only one of them was implemented into the computer control, the other two had to be operated manually what made a scanning run of them very tedious. To gain more flexibility, higher long term stability and a PC control, these function generators were replaced by an eight channel USB voltage analog output device[1]. This device was integrated into our Labview control sequence enabling us to define an output voltage for each channel individually, which is then provided to the field plates. Currently channel 0 is connected to the field plates D and F supporting an $\mathcal{E}$-field

[1]Measurement Computing USB-3112, 8-Channel, 16-Bit, High-Drive Analog Output Device

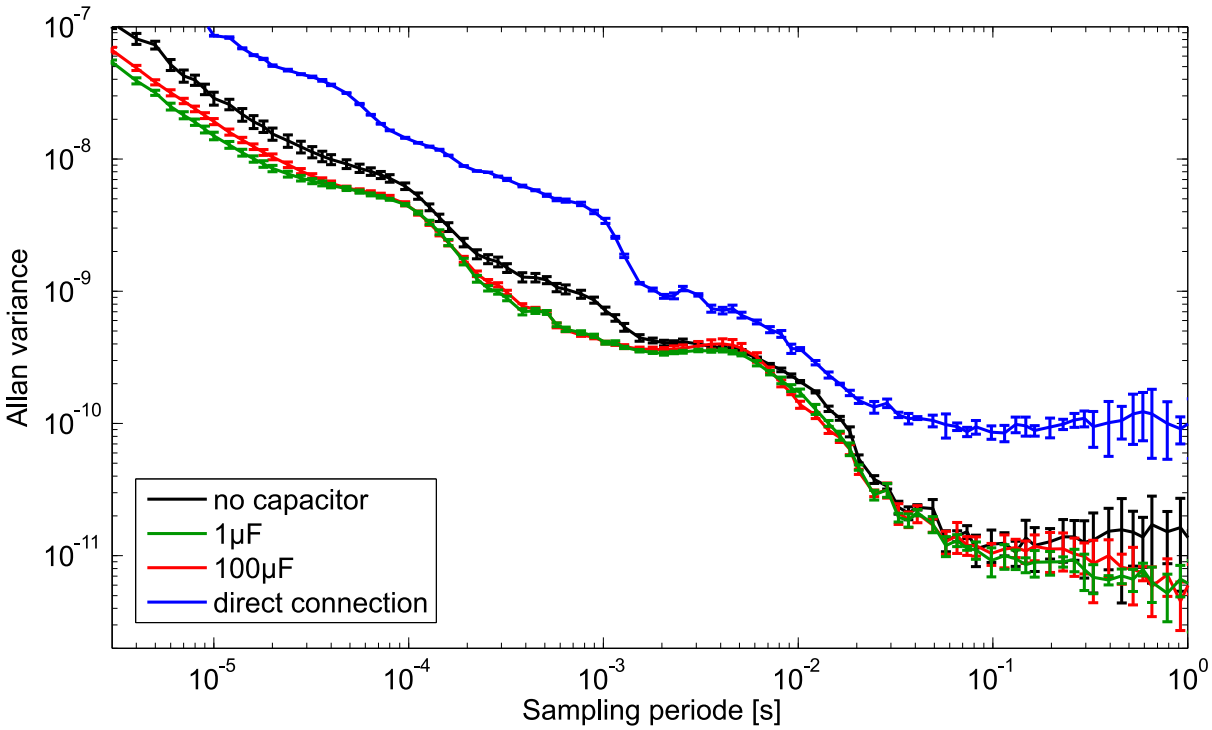

Figure 7.3: Allan variance shown for different sampling periods measured over a total time of $10\,\mathrm{s}$ in a double logarithmic plot. Only the part of this plot for sampling times $\leq 1\,\mathrm{s}$ is depicted. The Allan variance illustrates the frequency stability of different sampling periods for our eight channel USB voltage analog output device. Exemplarily for one channel, at which a voltage of $500\,\mathrm{mV}$ was applied, four different configurations are shown: the blue line shows the situation in which the output of the voltage device was directly connected to our oscilloscope, whereas the other three lines depict measurements of the setup with the voltage divider and different capacitors implemented.

compensation in x-direction, plates A and C are used for the z-direction and plates G and E are individually addressed by channel 2 and 3 for an $\mathcal{E}$-field compensation in y-direction (see Figure 7.1(b)).

Exemplarily the connection circuit for one channel of the USB-3112 device to a SHV (safe high voltage) connector is depicted in Figure 7.2(a) and an authentic picture of it is shown in Figure 7.2(b). First of all, the USB-3112 device, the ground of the SHV connector and the box, in which the whole assembly was put, are all on the same ground. There is a $1:10$ voltage divider installed between the channel output and the SHV connector to reach a higher resolution for low output voltages needed for the compensation. The maximum output voltage per channel is now about $909\,\mathrm{mV}$. Furthermore a $50\,\Omega$ resistor is used to match the impedance of the SHV cable and a capacitor of $100\,\mu\mathrm{F}$ is integrated to smooth out and cut off voltage spikes in the signal.

One way of characterizing the stability of the output voltage is to measure the Allan variance, which provides information about the stability of certain frequencies. The Allan variance is defined as

$$\sigma_y^2(\tau) = \frac{1}{2}\left\langle (\bar{y}_{n+1} - \bar{y}_n)^2 \right\rangle , \tag{7.1}$$

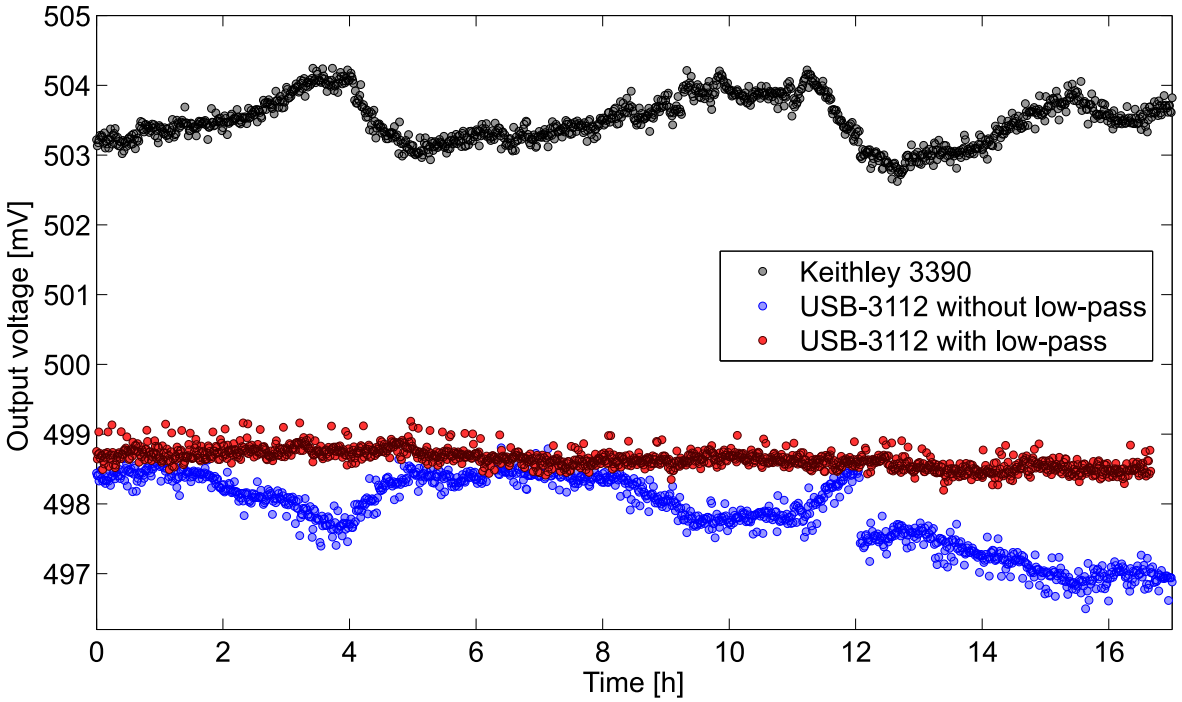

Figure 7.4: Long-term stability test of the USB-3112 device. Over a run time of 17 h the voltage outputs of a Keithley 3390 arbitrary waveform generator (black) and the USB-3112 device, one time with an integrated 100 µF capacitor (red) and the other time without (blue), are shown. All voltages were measured by a LeCroy oscilloscope.

where τ is the observation period and $\bar{y}_n$ the n-th measured voltage value. In Figure 7.3 the Allan variance is plotted against the sampling period. For each measurement run the same output voltage of 500 mV was set with the USB-3112 device and recorded with an oscilloscope[2] over a time of 10 s. Four different measurement setups were tested: for the black line there was no capacitor connected, whereas for the red trace a 100 µF and for the green line a 1 µF capacitor was installed. In the blue trace the output of the USB-3112 device was directly connected to the oscilloscope without any impedance matching, voltage divider or capacitor. It is clearly visible that the Allan variance of this blue line is for all sampling times larger than for the other three lines, meaning that the fluctuations are larger. The integration of a capacitor into the circuit improves the Allan variance further compared to the measurement without any (black line). The size of the capacitor does not affect the measurement a lot and the Allan variance is pretty much the same for 1 or 100 µF, since the 50 Ω capacitor is particularly defining the cutoff frequency as a recently done simulation showed. The final design decision was to build in 100 µF capacitors for each channel as we thought that we could decrease the cutoff frequency this way.

The long term stability was tested in a run of about 17 h, in which every 36 s one data point was measured, and is shown in Figure 7.4. At the same time we recorded the DC voltage of an arbitrary waveform generator[3] (black line) and of the USB-3112 device, one time with

[2] LeCroy Waverunner 64XI
[3] Keithley 3390, 50MHz Arbitrary Waveform/Function Generator

a low-pass filter with a cutoff frequency of $370\,\mathrm{kHz}$ installed (red line) and the other time without any (blue line). The devices were all set to an output voltage of $500\,\mathrm{mV}$. It can clearly be seen that the red line exhibits the fewest noise of less than $1\,\mathrm{mV}$ compared to the other two configurations. Thus we can be sure that our new voltage device has a better long term stability than the formerly used arbitrary function generator (black line). Furthermore the origin of the noise could also stem from the oscilloscope we use for the data recording.

Part III

Experimental results

Everything is possible.
The impossible just takes longer.

Dan Brown, *Digital Fortress*

8 Ultracold long-range Rydberg molecules

Ultralong-range Rydberg molecules are an exotic species of molecules, formed by the low energy scattering of ground state atoms from the Rydberg electron (see chapter 2 for details). They inherit their exceptional properties from their constituent Rydberg atom. Thus they are again very sensitive to electric fields due to their high polarizability and have a large extent up to a few $\mu\mathrm{m}$, so that they exceed the size of bacteria. First time observed experimentally in Stuttgart in 2009 [6, 45], these molecules sparked not only the interest of experimentalists to conduct research along this line [141, 142, 143], but also led to many proposals from theory groups [8, 99, 144, 145]. Recently a two-qubit quantum gate with Rydberg dimer molecules has been proposed [88].

In section 8.1 of this chapter we present the first measurement of Rydberg D-state molecules, published recently [146]. We specifically studied the $D_{5/2}, m_J = 1/2$ and $m_J = 5/2$ states for principal quantum numbers n ranging from 41 to 49. We distinguish between two classes of D-state molecules, the axial and toroidal ones, depending in which lobes of the Rydberg electron orbits they form bound states. Moreover we compare their binding energies with the theoretically calculated ones from section 2.2 and show their good agreement with each other. In section 8.2 we explain and discuss the specific alignments of our molecules, which are in general very important since they can, for example, affect the reaction dynamics in chemical systems. In the last part of this chapter in section 8.3 we apply an electric field to our Rydberg molecules and study its influence on their binding energies.

8.1 Measurement of *D*-state molecules

In contrast to the previously investigated S-state Rydberg molecules, D-state molecules provide new interesting features. The main difference between them is the different angular part of their electronic wavefunctions, which directly influences the molecular potential (see equation (2.3)). For the S-states the wavefunctions and electron orbitals are completely isotropic in Θ- and φ-direction, whereas the D-states display an angular dependence on the polar angle Θ. D-states show like S-states a rotational symmetry along the z-axis. We investigate and address two different $D_{5/2}$-state configurations by changing the polarization of our $480\,\mathrm{nm}$ laser: the $m_J = 1/2$ states by using σ^+ and the $m_J = 5/2$ states by using σ^--polarized light. We study the diatomic molecules of these states for principal quantum numbers n ranging from 41 to 49. The experiment was conducted in magnetically trapped thermal clouds ($2\,\mu\mathrm{K}$) of ^{87}Rb with a typical peak density of $\sim 10^{12}\mathrm{cm}^{-3}$. The average atom number for our samples was about 1.4×10^6. To photoassociate Rydberg molecules we use our

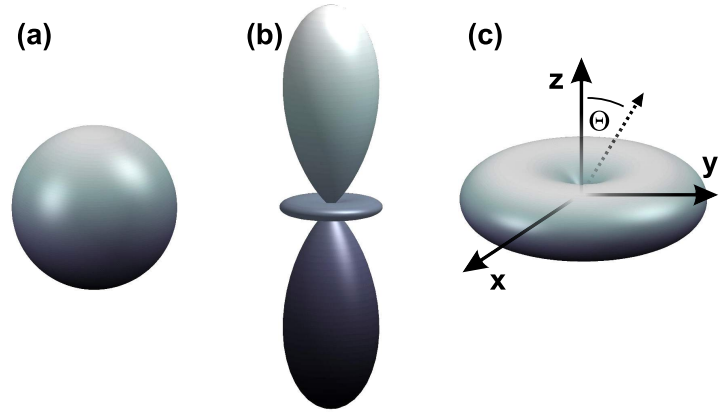

Figure 8.1: Relevant electron orbits displaying the dependence on the spherical harmonics. (a) The S-states show a completely symmetric angular behavior $|Y_0^0|^2$, whereas the D-state angular distributions $|Y_2^{(0,2)}|^2$, (b,c), respectively, are Θ-dependent. The latter possess a dumbbell-shape in z-direction with a small torus in the equatorial plane (b) or just a toroidal shape (c).

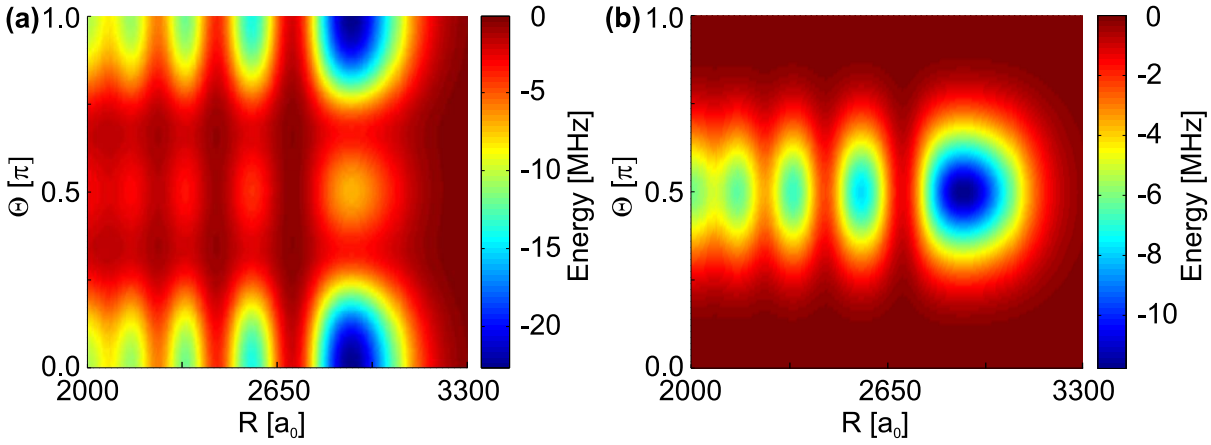

Figure 8.2: Adiabatic potential energy surfaces (APES) for the states $41D_{5/2}$, $m_J = 1/2$ (a) and $41D_{5/2}$, $m_J = 5/2$ (b) as a function of (R,Θ). In (a) the potential provides bound states in potential wells localized at $\Theta = 0, \pi$ (axial states) and at $\Theta = \pi/2$ (toroidal states). For the stretched state $m_J = 5/2$ (b), only one series of toroidal potential wells can be identified at $\Theta = \pi/2$.

standard two-photon excitation scheme (see chapter 5 for details). The experimental sequence used for our Rydberg molecule measurements in a thermal cloud is explained in detail in section 6.1. In the 400 cycles of excitation, ionization and detection we scan the red $780\,\mathrm{nm}$ laser and extract the ion signal from our micro channel plate detector, yielding one complete spectrum.

As illustrated in Figure 8.1, the shapes of the relevant angular part of the electron wavefunctions of the two different D-states deviate tremendously from each other and from the S-state. In case of the $l = 2, m = 0$ state, visible in Figure 8.1(b), the electron orbit features the shape of a dumbbell with a small torus in the equatorial plane, whereas for the stretched state (Figure 8.1(c)) it exhibits only a toroidal shape. This is in stark contrast to the S-state (Figure 8.1(a)), which possesses a spherical symmetry. In Figure 8.1(b) we only show the electron orbit for the dominant triplet scattering term, since the singlet term is negligibly small in comparison. More information about the scattering length and the molecular binding mechanism can be found in section 2.1. Since the D-states, in addition to their R-dependence, feature a Θ-dependence, we show the potential energy surfaces in Figure 8.2 in a 2-D plot, exemplarily for the $41D$ state. The detailed calculation yielding these energy landscapes can be

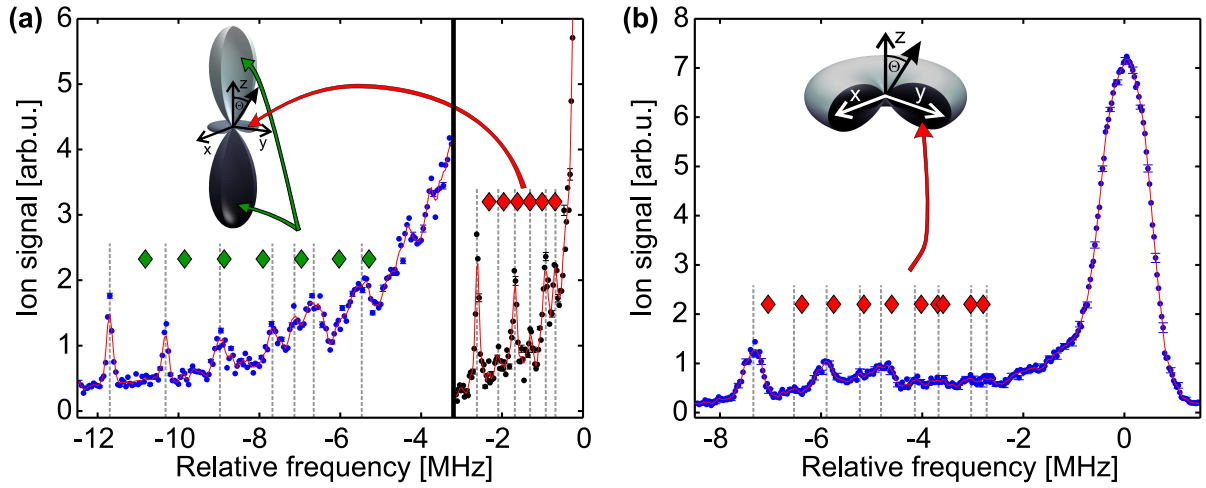

Figure 8.3: Spectra of the $44D_{5/2}$, $m_J = 1/2$ (a) and $42D_{5/2}$, $m_J = 5/2$ (b) states, where the ion detector signal is plotted against the relative frequency of the excitation laser. Apart from the photoassociation spectra the angular distribution $|Y_2^{(0,2)}|^2$ (a,b) of the atomic electron orbitals relevant for the topological structure of the APES are shown in the insets. In the spectrum of (a) we depict two individual spectra taken with different laser intensities which are separated by a black line at -3.2 MHz: the left one (blue) was taken at a high intensity to resolve the axial molecules and the right one (black) at a low intensity to decrease the power broadening of the atomic line such that the toroidal molecules can be resolved. For better visibility a moving average (red line) is included and the data is scaled by a factor of three. The dashed lines (gray) mark the experimental peak positions of the molecules whereas colored diamonds indicate the calculated binding energies of the axial (green) and toroidal (red) molecular states. In (b) only molecules in the toroidal configuration were detected. For both spectra the error bars (standard deviation) are determined from 20 independent measurements and only every fifth error bar is shown so that the plots do not get overcrowded.

found in the theory section 2.2. In case of the $J = 5/2$, $m_J = 1/2$ state, the adiabatic potential energy surface (APES) shows series of potential wells with minima localized in the $\Theta = 0, \pi$ (axial states) and $\Theta = \pi/2$ (toroidal states) direction. For $m_J = 5/2$ the APES only possesses a purely toroidal structure with minima in the $\Theta = \pi/2$ direction. The topology of the APES can be understood qualitatively by considering the atomic electron orbital which dominates the specific potential surface. For $m_J = 1/2$ and $m_J = 5/2$ this is $|Y_2^0|^2$ and $|Y_2^2|^2$, shown in Figure 8.1(b) and (c), respectively. In general the potential energy surfaces confine the rovibrational dynamics in the radial as well as in the angular direction. Due to the additional confinement in Θ-direction, the rovibrational level spacing increases and we resolve a larger number of molecular lines in contrast to previous S-state measurements [6, 45], clearly visible in the spectra depicted in Figure 8.3. Since the major properties and behaviors of the two different m_J configurations are the same for all our studied principal quantum numbers n, only two states are shown exemplarily here: the $44D_{5/2}, m_J = 1/2$ (a) and the $42D_{5/2}, m_J = 5/2$ state (b). We observe that the molecular lines appear energetically below the dissociation limit of the molecules which defines the origin in these plots. The energy difference is the binding energy of the molecule which is necessary to form the bond between the Rydberg and ground state atom.

For the $m_J = 5/2$ state the molecular states are aligned toroidal as depicted in the inset

of Figure 8.3(b). The molecular ground state, the deepest bound state, has a binding energy of about $-7.4\,\mathrm{MHz}$. The other peaks on its right side in the spectrum, also indicated by gray dotted lines, are higher excited toroidal molecules. If we now compare the depth of the molecular potential with that of a S-state we get a factor of $|Y_2^2(\Theta = \pi/2)|^2/|Y_0^0|^2 = 1.88$. This factor explains well the deeper bound D-state molecules, since the radial part of the electron wavefunction is about the same as for the S-states. Furthermore the calculated values of the binding energies depicted as red diamonds in Figure 8.3(b) reproduce the measured data very well.

For the $m_J = 1/2$ state in Figure 8.3(a), two spectra are plotted, separated by a black line at $-3.2\,\mathrm{MHz}$: the blue one was taken with high laser power to resolve the outer molecules, which provide a low ion count signal due to their smaller Franck-Condon factors, and for the black spectrum only little laser power was used to resolve the inner lying molecular states. Two classes of molecular states are appearing in the spectra: the outer molecules with large binding energies are the ones localized at $\Theta = 0, \pi$ (see Figure 8.2(a)) in the axial lobes of the electron orbit (green) and the second ones with only a few MHz binding energies belong to the shallow potential wells at $\Theta = \pi/2$ bound in the toroidal configuration (red). The $m_J = 1/2$ state is a superposition of a singlet and triplet state, where the singlet contribution can be neglected due to its small scattering length [93]. Including the Clebsch-Gordan coefficient the angular part of the corresponding molecular potential thus scales as $3/5|Y_2^0(\Theta)|^2$. As a result the deepest bound axial molecular state at $\Theta = 0, \pi$ for $m_J = 1/2$ shows a binding energy four times larger than the one for the toroidal case at $\Theta = \pi/2$ for $m_J = 1/2$ and five times larger than for the corresponding S-state molecules. Both estimates are in quite good agreement with the experimental results.

So far an analysis which compares the signal strengths of the molecules in one spectrum to obtain information about the Franck-Condon factors has not been carried out yet. For example in Figure 8.3(b) it can clearly be seen that every second molecular line has a weaker signal, which is closely connected to their antisymmetric molecular wavefunctions. A theoretical calculation of the Franck-Condon factors is very demanding, because one has to think about the correct distribution function of the ground state atoms and how this affects the overlap integral between the excited Rydberg and ground state atom wavefunction.

The agreement between theoretical and experimental values for the binding energies over a wide range of principal quantum numbers can best be seen in Figures 8.4 and 8.5. Since the rotational and vibrational modes are of the same order of magnitude (in the MHz regime) we cannot distinguish them from each other because they are intermixed. Thus we use the rovibrational excitation number κ to describe the bound molecular states. The numbering starts from 0 with the deepest bound ground state and increases with decreasing molecular binding energy (absolute number). This stands in stark contrast to the S-state molecules where the rotational states are of the order of $\sim 10\,\mathrm{kHz}$ [92] and could not be resolved in previous measurements [6, 45]. Considering the volume of the Rydberg atom, one obtains, in a first approximation, a scaling of the potential depth with the effective principal quantum number as $n^{\star -6}$. The binding energy, however, also depends on the shape of the potential, so that the scaling law does not describe our high resolution data sufficiently. With increasing principal quantum number n, the molecular binding energies get lower and lower, implying that the spectral molecular lines move nearer to the atomic line, until at high principal quantum

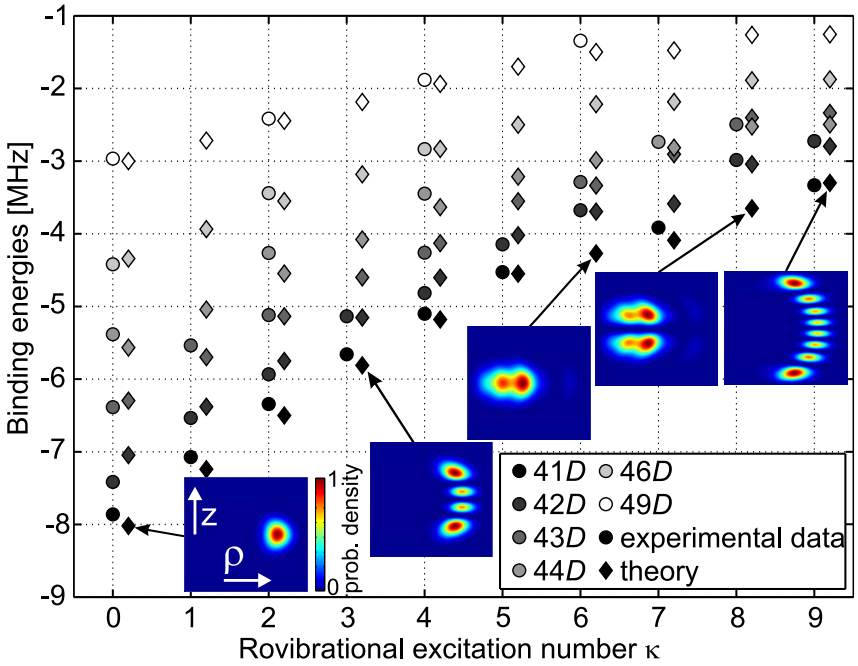

Figure 8.4: Molecular binding energies for the $m_J = 5/2$ states plotted against the rovibrational excitation numbers κ for principal quantum numbers n ranging from 41 to 49. For increasing n the states are colored brighter. The calculated binding energies (diamonds) are plotted with a horizontal offset to the experimental ones (circles) to improve readability. The insets depict the scaled probability densities of certain rovibrational states for ρ and z ranging from $2000\,\mathrm{a_0}$ to $3300\,\mathrm{a_0}$ and from $-1500\,\mathrm{a_0}$ to $1500\,\mathrm{a_0}$, respectively.

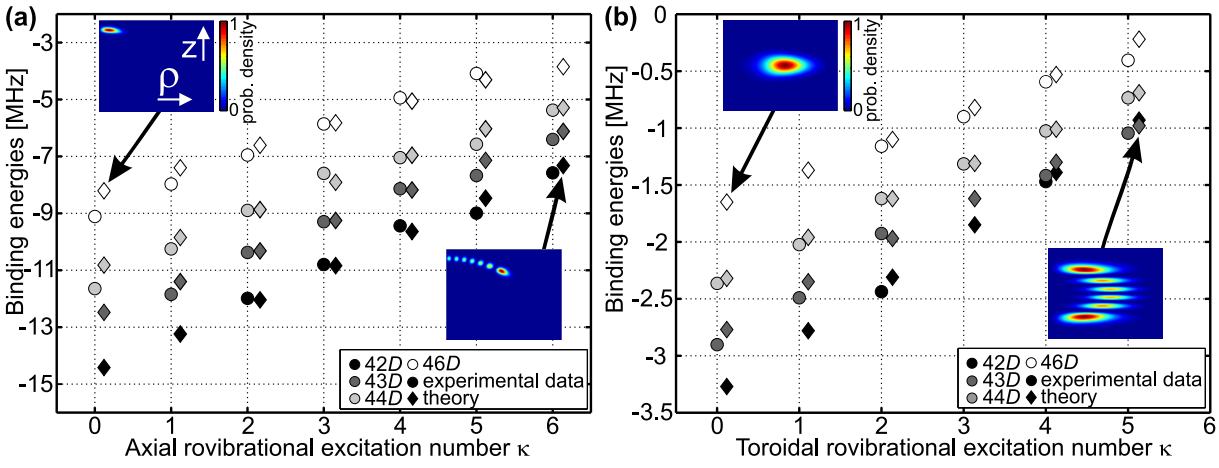

Figure 8.5: Molecular binding energies for the $m_J = 1/2$ states plotted against the axial rovibrational excitation numbers (a) and the toroidal rovibrational excitation numbers (b), respectively, for principal quantum numbers n ranging from 42 to 46. For increasing n the states are colored brighter. The calculated binding energies (diamonds) are plotted with a horizontal offset to the experimental ones (circles) to improve readability. The insets depict the scaled probability densities in z- and ρ-direction of selected rovibrational states. For the axial rovibrational excitation numbers (a) ρ ranges from 0 to $3500\,\mathrm{a_0}$ and z from 0 to $3500\,\mathrm{a_0}$, whereas for the toroidal rovibrational excitation numbers (b), ρ ranges from $2700\,\mathrm{a_0}$ to $3500\,\mathrm{a_0}$ and z from $-2250\,\mathrm{a_0}$ to $2250\,\mathrm{a_0}$.

numbers we end up with a non-resolvable flank on the red side of the atomic line, as observed for the S-states recently [9]. That is the reason why for high n in Figure 8.4 only every second molecular peak could be resolved.

It is clearly visible that the largest difference between theoretical calculated and experimental values for the binding energies can be found for the axial molecules (see Figure 8.5(a)). On the experimental side one possible reason is the uncertainty of determining the atomic and molecular line positions, which define the binding energies of the molecules. Especially the broadening of the atomic line caused by the high laser power, needed to resolve the outermost axial states, exacerbates the exact determination of the binding energies for the axial molecules. On the theory side one possible explanation is the uncertainty of the B-field of $\pm 0.1\,\mathrm{G}$, which results in a small change of the computed binding energies in the calculations. Another reason could be the problems in the convergence of the molecular wavefunctions for higher excitations numbers κ in the theoretical calculations. We introduced an artificial border to avoid that the probability density of the molecular states is larger than zero in the area which is influenced by the p-wave shape resonance (see section 2.1 for details). This causes problems in the convergence if the wavefunction is located near to this cutoff border leading to less trustworthy results. In the experiments we could only measure molecular lines down to binding energies of around $-12\,\mathrm{MHz}$, since at $-13.3\,\mathrm{MHz}$ the atomic line of the transition $(5S_{1/2}, F = 2, m_F = 1) \rightarrow (nD_{5/2}, m_J = 1/2)$ is localized (see Figure 1.3). Thus the outermost axial molecular lines of the $m_J = 1/2$ state for low principal quantum numbers and cannot be resolved since they start to overlap with this atomic line. In the insets of Figures 8.4 and 8.5 the scaled probability densities of specific rovibrational states in z- and ρ-direction are shown. The reason why these plots are of importance are connected to the alignment of the D-state molecules and are discussed in detail in the next section.

Concerning the D-state molecules, related work was recently conducted in the group of G. Raithel [143] who compared $D_{3/2}$ with $D_{5/2}$ states for $n = 32 - 40$ at almost zero magnetic field ($B < 1\,\mathrm{G}$).

8.2 Alignment of *D*-state molecules

Angular confinement of molecules, referred to as alignment (see Figure 8.6(b)), represents an unique way of influencing molecular motions, whereas orientation defines a preferred up and down direction of the molecules (Figure 8.6(c)). Alignment is of major importance for the control of a number of molecular processes and properties, such as the pathways of chemical reactions including stereo-chemistry [147, 148, 149, 150], photoelectron angular distributions [151, 152, 153, 154], dissociation of molecules [155, 156, 157, 158] and diffractive imaging of molecules [159, 160]. In the case of ultracold alkali dimers, the quantum stereodynamics (the orientation and movement of molecules in three-dimensional space) of ultracold bimolecular reactions has been probed recently [161].

In the field-free case molecules do not have a preferred direction (see Figure 8.6(a)). Molecular alignment (see Figure 8.6(b)) can be achieved by creating angular-dependent potentials through electric, magnetic and light fields. This has been used in a variety of experimental configurations such as, e.g., the brute force orientation [162], hexapole focusing [163, 164, 165],

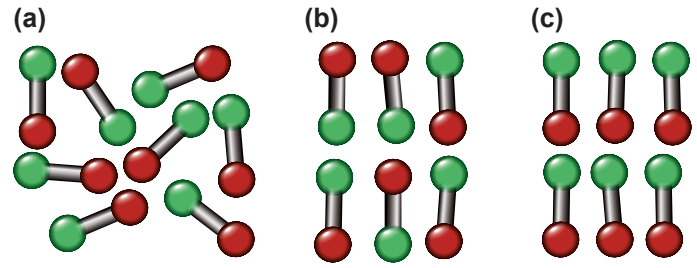

Figure 8.6: (a) no order present; (b) aligned molecules along the z-axis; (c) aligned and oriented molecules in z-direction.

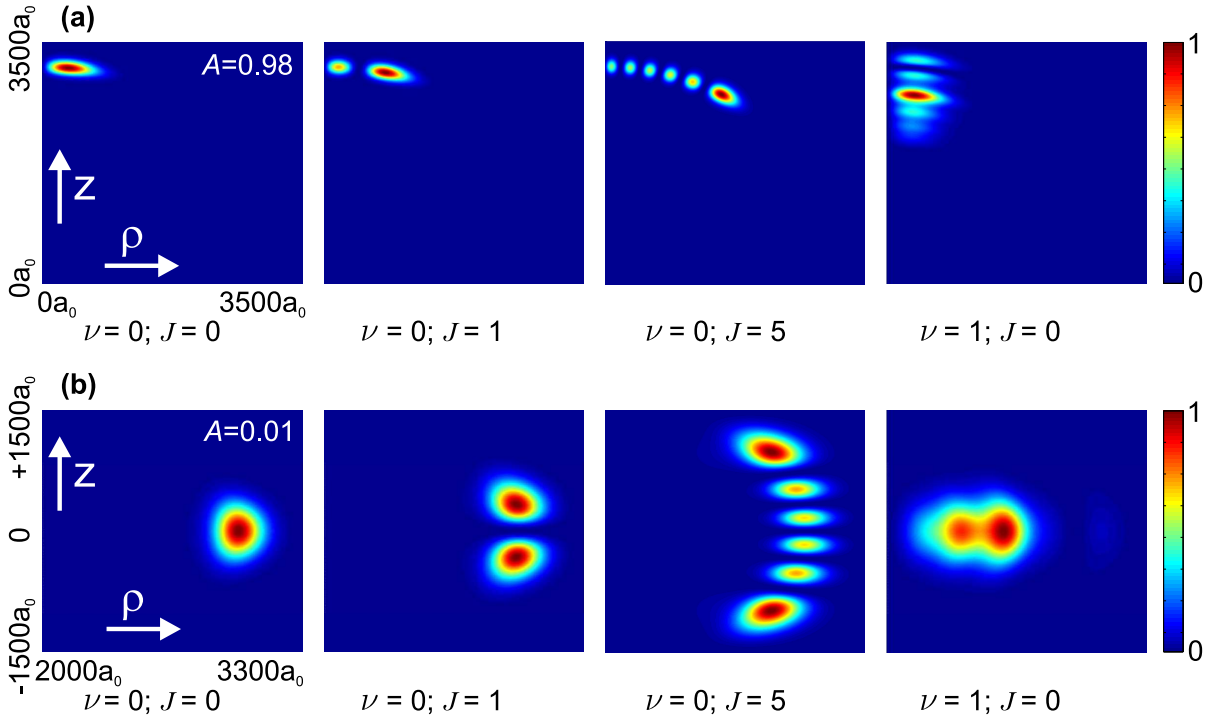

Figure 8.7: Scaled probability densities of specific rovibrational $42D$, $m_J = 1/2$ molecular states. Here we split the rovibrational states κ into vibrational excitation number ν and rotational excitation number J. In (a) the axial molecules are depicted whereas in (b) the toroidal molecules of this state can be seen. From left to right the states are spreading in Θ-direction until in the last column the jump to the first excited vibrational state occurs. In the ground state plot, the dimensions and the value of the alignment A is given.

strong ac pulsed fields [166] or combined ac and dc electric fields [167, 168, 169, 170, 171]. Furthermore strong magnetic fields crucially influence the topology of the the corresponding adiabatic potential energy surfaces (APES). The latter accommodate the nuclear motion and are responsible for a plethora of equilibrium positions [172], novel bonding and chemical reaction mechanisms [173, 174] as well as field-induced vibronic interactions via e.g. conical intersections of the APES [175, 176].

In contrast to the aforementioned cumbersome experimental efforts to bring molecules into alignment, for our Rydberg molecules it is simply done via the two-photon excitation process in a weak magnetic field of about 14 G. By changing the detuning and polarization of our lasers we can selectively excite a specific molecular state in a distinct alignment. Another advantage of our technique is that we create stationary states which stay in this configuration for their

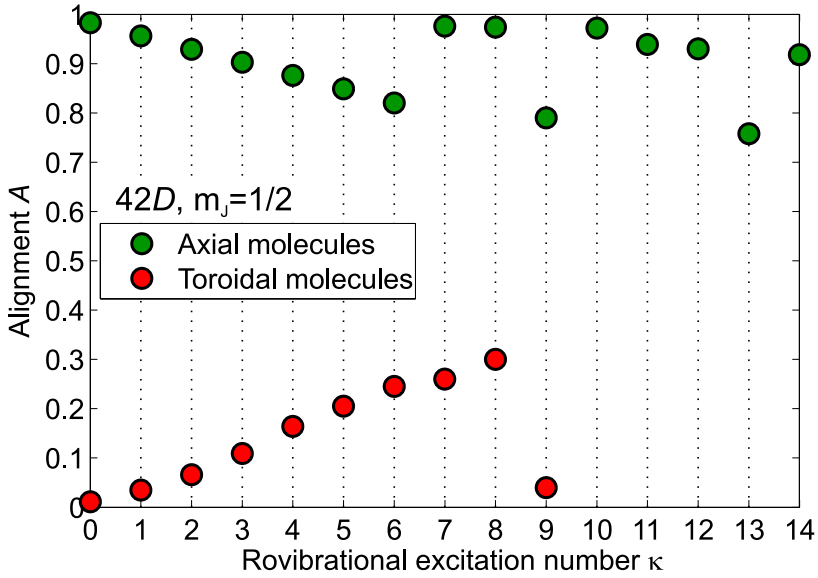

Figure 8.8: Molecular alignment plotted against the rovibrational excitation number κ for the axial (green) and toroidal (red) molecules of the $42D, m_J = 1/2$ state.

lifetime of several µs.

Mathematically the alignment of our molecules can be calculated by

$$A = \left\langle \cos^2(\Theta) \right\rangle , \tag{8.1}$$

which specifies how well the molecules are pointing into z-direction, in which our magnetic field and light fields of the lasers are directed. The quality of the alignment or antialignment (aligned perpendicular to the z-axis) of the created ground and excited state molecules can be clearly seen in Figure 8.7, where exemplarily the scaled probability density of certain rovibrational $42D$, $m_J = 1/2$ states in axial (a) and toroidal (b) configuration is displayed. Here we split the rovibrational excitation number κ into the vibrational ν and rotational excitation number J to illustrate better how the probability density is spreading in ρ- or z-direction. From this plot on can directly see that the ground state (outermost left column) of the axial (a) or toroidal (b) molecules are perfectly aligned or antialigned, respectively. If we increase the rotational excitation number J, the molecular wavefunction begins to spread in ρ-direction for the axial and in z-direction for the toroidal molecules and the alignment/antialignment gets worse. At a specific rovibrational excitation number between $\kappa = 6 - 9$, depending on the quantum numbers n and m_J, we reach a binding energy where the first vibrational mode $\nu = 1$ is excited (outermost right column) and the probability density stretches towards the origin. In the 3-D plots in Figure 2.4 we illustrated where the different molecules are formed qualitatively.

A more quantitative picture of the alignment is given in Figure 8.8 for the $42D, m_J = 1/2$ state. If we increase the rovibrational quantum number κ the alignment decreases for the axial molecules, whereas it increases for the toroidal molecules. At certain values of κ, we observe a sudden jump in the alignment, which indicates that this rovibrational state possesses a higher vibrational component, where the molecular wavefunction spreads into the direction of the origin instead of the ρ- or z-direction (c.p. Figure 8.7), giving rise to an alignment which is close

to the value at $\kappa = 0$. For low excitation numbers the alignment increases/decreases almost linearly for the toroidal/axial states, respectively.

8.3 Molecules at an $\mathcal{E}$-field induced crossing of the m_J = 5/2 and m_J = 1/2 levels

By applying a weak electric field parallel to our magnetic offset field in z-direction in the order of a few $\mathrm{V/cm}$ we can shift the position of our Zeeman split states via the Stark effect (see subsection 1.3.1) so that different m_J states show a crossing or anti-crossing behavior, depending on their coupling to each other. The idea behind this is to observe newly emerging molecular states stemming from the mixed electron orbitals of two different m_J components.

8.3.1 Analysis of the high resolution spectra

For our measurements we exemplarily picked the $42D_{5/2}$ state, for which the molecular states could be resolved for both m_J states ($5/2$ and $1/2$) very well (cp. Figures 8.4 and 8.5). Recording the Stark maps of Figure 8.9, a $\chi = \frac{1}{\sqrt{2}}(\alpha\sigma^+ + \beta\sigma^-)$ laser polarization was chosen for the blue $480\,\mathrm{nm}$ laser. The variables α and β were determined experimentally by choosing the polarization so that both $m_J = 5/2$ and $m_J = 1/2$ states have approximately the same signal height slightly detuned from the crossing where the states are not overlapping yet. This guarantees that we excite each m_J state equally. Due to the dipole transition rules there is no transition between these two states possible. Only quadrupolar or higher order transitions would be allowed, but they are too weak so that we can neglect them. This means these two lines do not 'see' each other and cross, as directly observable in the Stark map in Figure 8.9(a) and in the spectrum taken directly at the crossing at an $\mathcal{E}$-field of $1.08\,\mathrm{V/cm}$ in Figure 8.9(c). In contrast to this, the $m_J = 5/2$ and $m_J = 3/2$ atomic lines can couple via the magnetic dipole interaction and thus show an avoided crossing [59] in Figure 8.9(a). The white lines in this plot are the theory calculations for the different m_J states based on the program of B. Butscher [57]. At and near the anticrossing the spectral lines get a bit broader, due to stray electric fields or electric field gradients. The different molecular states appearing on the red side of the crossing of the $m_J = 5/2$ and $m_J = 1/2$ states can be traced back to the zero $\mathcal{E}$-field configuration of the $m_J = 1/2$ state, visible in Figure 8.9 (b). At the zero electric field position, the binding energies of the $42D_{5/2}, m_J = 1/2$ state are known from the theory calculations in section 2.3 and the measurements from section 8.1. Thus we can identify several toroidal molecules and the axial ground state molecule (cp. Figure 8.5) and trace them all the way to the crossing where they show different behaviors. While the axial molecule follows the bending of the atomic line and is not disturbed by the crossing, the toroidal states increase their binding energies at the crossing, clearly visible in Figure 8.9 (b). After the crossing the toroidal states follow the $m_J = 5/2$ atomic line, asymptotically converging to a constant binding energy. The reasons for the behavior of the molecular lines are explained in detail in the next subsection 8.3.2.

To answer the question if new molecular lines appear at the crossing because of the intermixing of the two different m_J wavefunctions, we took spectra for three different polarization

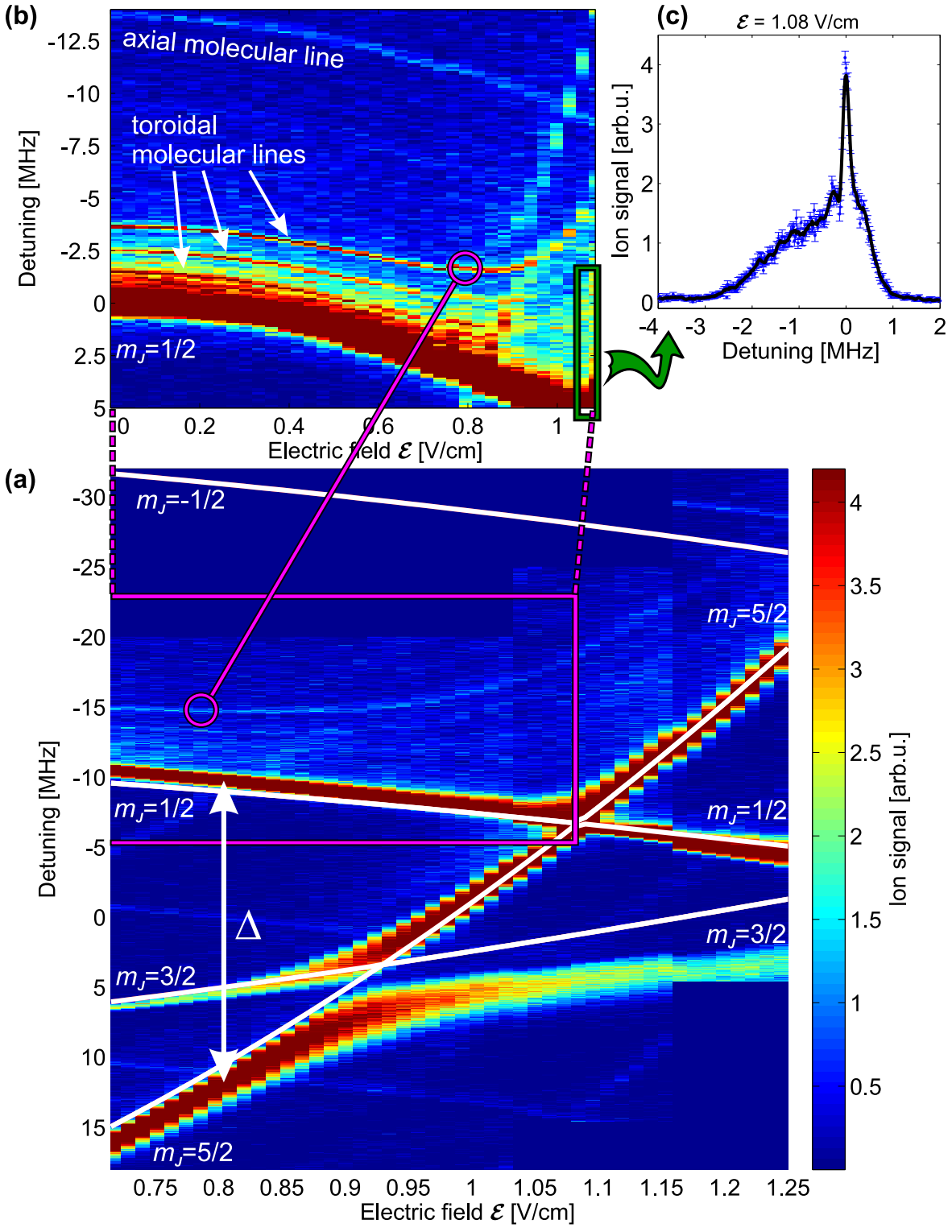

Figure 8.9: Stark map showing the crossings between different m_J levels of the Stark split $42D_{5/2}$ state. The polarization of the 480 nm laser was set to $\chi = \frac{1}{\sqrt{2}}(\alpha\sigma^+ + \beta\sigma^-)$ polarized light by using a $\lambda/4$ plate so that the ion count of the $m_J = 1/2$ and $m_J = 5/2$ state were about the same. In (a) the anticrossing between the $m_J = 5/2$ and $3/2$ as well as the crossing between the $m_J = 5/2$ and $1/2$ can clearly be seen. The white lines are theoretical calculations which match the experimental data. Tracing the molecular lines back to the zero field configuration (b), we can attribute them to toroidal and axial molecular states of $m_J = 1/2$. The spectrum taken directly at the crossing at $E = 1.08\,\mathrm{V/cm}$ is depicted in (c). The black line is a runmean shown as a guide to the eye.

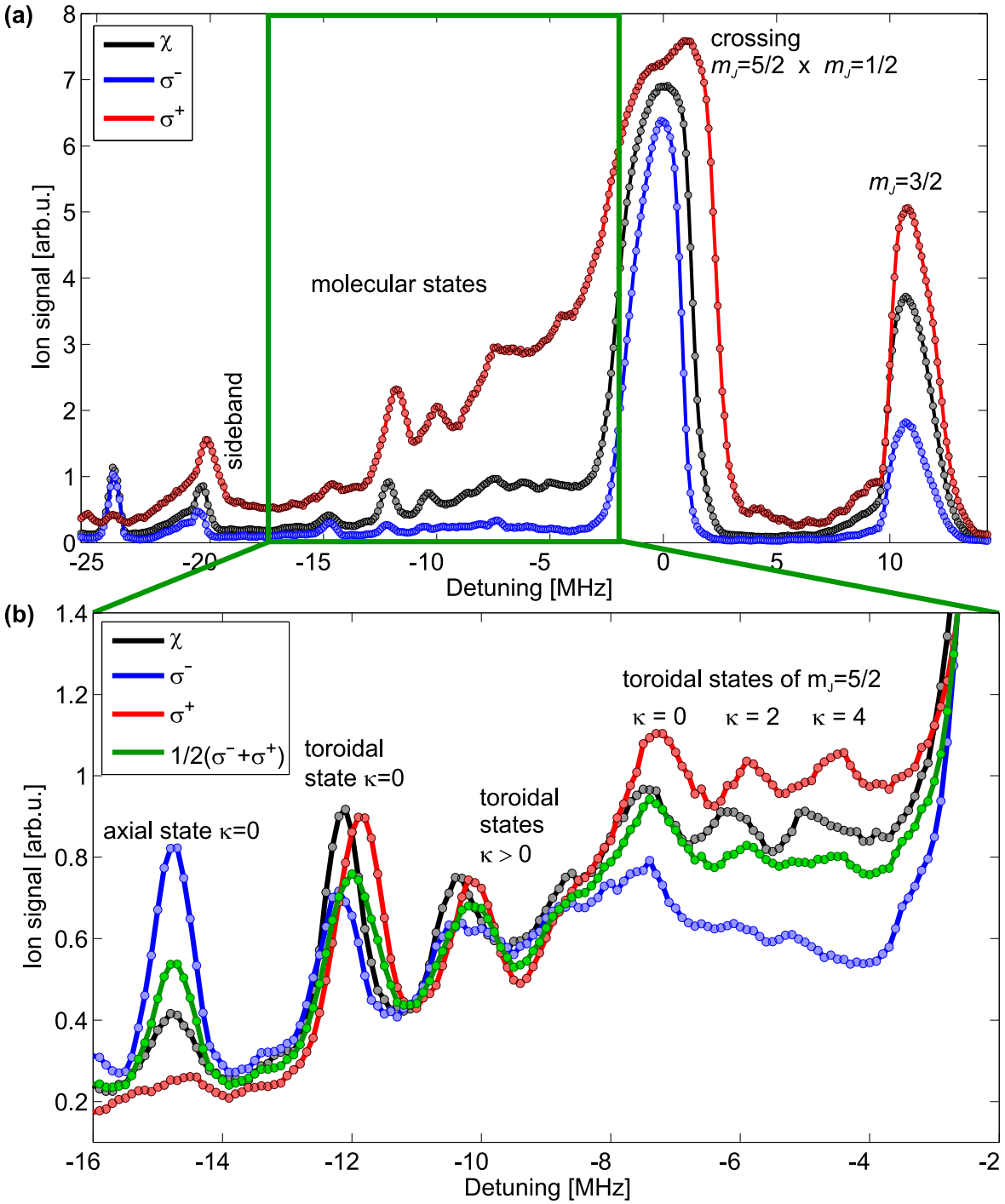

Figure 8.10: Spectra of the molecules taken at the specific electric field $\mathcal{E}$=1.08 V/cm where the $42D_{5/2}, m_j = 5/2$ and $m_j = 1/2$ atomic lines cross each other. The frequency origin is exactly placed at the crossing position. All spectra were measured for three different polarizations of the 480 nm laser: σ^- (blue), σ^+ (red) and $\chi = \frac{1}{\sqrt{2}}(\alpha\sigma^+ + \beta\sigma^-)$ (black), where α and β were determined experimentally by choosing the polarization so that both $m_J = 5/2$ and $m_J = 1/2$ states have approximately the same off-resonant signal height. The green spectrum in (b), which is an average of the σ^-- and σ^+-polarization data, is shown to highlight its resemblance to the χ-polarization spectrum. In (a) all three spectra were taken with the same laser powers, whereas in (b) different red laser powers were employed so that the ion count signal at the crossing was approximately the same for all three polarizations. In (b), the zoom into the green-rimmed area shows several molecular lines of different signal heights for the three polarizations. The identified signal peaks are labeled in the figure. The lines connecting the measured values are guides to the eye.

configurations of our blue Rydberg excitation laser (see Figure 8.10): χ (black), σ^- (blue) and σ^+ (red). Figure 8.10 (a) displays an overview of the crossing region, whereas the zoom into the green-rimmed area in Figure 8.10 (b) reveals several molecular lines on the red side of the crossing. For panel (b), the power of the red 780 nm laser was adjusted for each polarization individually so that the ion signal at the crossing was approximately the same. We observe that the molecular lines for the χ-polarization are at the same position as for the σ^-- and σ^+-polarization. In fact, if we calculate the mean value of the σ^-- and σ^+-polarization data (green), we end up nearly with the same spectrum as for the χ-polarization (black). So there are no 'new' molecular lines appearing for the χ-polarization, but we detect that some molecules change their binding energies on the way to the crossing and beyond adiabatically. Tracking back the molecular lines to the zero $\mathcal{E}$-field configuration, we can clearly identify two lines (see Figure 8.9(b)): The line at $-11.9\,\mathrm{MHz}$ at the crossing is the toroidal $m_J = 1/2$ ground state ($\kappa = 0$) corresponding to the binding energy of $-3.6\,\mathrm{MHz}$ at the zero $\mathcal{E}$-field position, whereas the line at $-14.7\,\mathrm{MHz}$ at the crossing can be assigned to the axial ground state, which features a binding energy of $-13.7\,\mathrm{MHz}$ at $\mathcal{E} = 0$. The other visible molecular states between the atomic line and the toroidal ground state are probably also toroidal states, but higher excited ones, which cannot be correlated to a certain rovibrational state, since for them the backtracking to the zero $\mathcal{E}$-field configuration is not possible. Theoretical calculations, which could be done in the future, incorporating a finite $\mathcal{E}$-field, could help in assigning these molecular states. However an analysis of the molecular lines for the different polarizations yields new insights about the molecular states which are nearest to the atomic line.

It is worth comparing the signal strengths of the molecular lines taken with σ^-- and σ^+-polarization in the spectra of Figure 8.10(b). Only the σ^--polarization allows the creation of an axial molecule at $-14.7\,\mathrm{MHz}$ in contrast to the σ^+-polarization, since axial molecules only exist in the axial lobes of the electron orbit of the $m_J = 1/2$ state, which can only be addressed by our σ^--polarized blue laser light. On the contrary, toroidal molecules can be created for the $m_J = 1/2$ and the $m_J = 5/2$ state, thus they appear in both polarization configurations, explicitly visible for the molecules at -12 and $-10.2\,\mathrm{MHz}$ in Figure 8.10(b). The toroidal molecules close to the atomic line (detuning $> -8\,\mathrm{MHz}$) are only visible in the σ^+-polarization, hinting to a connection to the $m_J = 5/2$ toroidal molecules in the zero $\mathcal{E}$-field case. If we compare the binding energies of the three peaks in the σ^+-polarization (-7.2, -5.8 and $-4.5\,\mathrm{MHz}$) with the experimental and theory values (see Table 2.1) for the zero $\mathcal{E}$-field configuration from section 8.1 we find that they match well and can be identified as the $\kappa = 0, 2$ and 4 toroidal rovibrational states of $42D_{5/2}, m_J = 5/2$. Since the electron orbits forming the potential for the Rydberg molecules admix to the probability density

$$|\Psi_{\text{tot}}|^2 = \left| \frac{1}{\sqrt{2}} \left(\Psi_{1/2} + \Psi_{5/2} \right) \right|^2 , \tag{8.2}$$

containing the square of the sum of the pure state wavefunctions of $m_J = 1/2$ and $m_J = 5/2$, we end up with the sum of three terms: one intermixing term $|\Psi_{1/2}\Psi_{5/2}|$ and two pure terms $1/2|\Psi_{1/2}|^2$ and $1/2|\Psi_{5/2}|^2$. Thus the observed toroidal molecules for σ^+-polarization are indeed the same as the zero $\mathcal{E}$-field toroidal molecules of the $m_J = 5/2$ state. Unfortunately, we cannot trace them back to the $\mathcal{E} = 0$ position for the $m_J = 5/2$ state to have an additional prove, since the nearby anticrossing of the $m_J = 3/2$ level with the $m_J = 5/2$ disturbs them significantly.

Another reason is that the data were acquired at high laser intensities to resolve the molecular lines more clearly. Since the red laser was scanned from negative to positive detunings the molecules on the red side of the first appearing atomic line are clearly visible (see Figure 8.9(a)). However, after scanning over the atomic line a lot of atoms are lost and the density is decreased, reducing the signal strengths of the detected molecules drastically.

To entirely explain the behavior of the molecules in the electric field we use a two level model, which is in detail presented in the next subsection.

8.3.2 Modeling the crossing between m_J = 5/2 and m_J = 1/2 as a two level system

The starting point leading to a simple two-level system to describe the change of the molecular binding energy in vicinity to the crossing for the toroidal molecules, is a general Hamiltonian for the three involved particles: the ionic core, the Rydberg electron and the ground state atom. All three are treated as point-like particles and give rise to the Hamiltonian

$$H = \frac{\vec{P}^2}{2M} + H_0 + H_B + H_{\mathcal{E}} + V_{n,e} \ , \tag{8.3}$$

in which $\vec{P}^2/(2M)$ is the kinetic energy of the ground state atom, H_0 is the field-free Hamiltonian (2.10), H_B is the Zeeman shift due to a magnetic field, $H_{\mathcal{E}}$ is the Stark effect caused by the electric field and $V_{n,e}$ is the scattering potential between Rydberg electron and ground state atom, described as Fermi-pseudopotential (2.1). Following closely the theoretical treatment of the same problem without $\mathcal{E}$-field in section 2.2, we apply the Born-Oppenheimer approximation to split our total wavefunction into two parts $\Psi(\vec{r};\vec{R}) = \psi(\vec{r};\vec{R})\phi(\vec{R})$. The first one describes the relative motion of the electron and the second one the relative motion of the ground state atom. The vector $\vec{r}$ denotes the relative position of the Rydberg electron to the ionic core, whereas $\vec{R}$ stands for the relative position of the ground state atom to the ionic core. Now we have to solve the time independent Schrödinger equation of the electronic Hamiltonian

$$(H_0 + H_B + H_{\mathcal{E}} + V_{n,e}(\vec{r};\vec{R}))\psi(\vec{r};\vec{R}) = E(\vec{R})\psi(\vec{r};\vec{R}), \tag{8.4}$$

in which E is the corresponding energy of this system. In a first estimate we treat the problem in first order perturbation theory taking the electronic wavefunctions of our states $42D_{5/2}, m_J = 1/2$ and $42D_{5/2}, m_J = 5/2$ as our basis, which consist of the same radial, but different angular parts:

$$\begin{aligned} \psi_{1/2}(\vec{r}) &= R_{42D}(\vec{r}) \cdot Y_{1/2}(\Theta); \\ \psi_{5/2}(\vec{r}) &= R_{42D}(\vec{r}) \cdot Y_{5/2}(\Theta,\varphi). \end{aligned} \tag{8.5}$$

Here $R_{42D}(\vec{r})$ is the radial wavefunction of the $42D$ state whereas $Y_{1/2}(\Theta)$ and $Y_{5/2}(\Theta,\varphi)$ are the modified spherical harmonics of the $m_J = 1/2$ and $m_J = 5/2$ states, respectively, taking

into account the Clebsch-Gordan coefficients for the triplet scattering:

$$Y_{1/2}(\Theta) = \underbrace{\sqrt{\frac{3}{5}}}_{\substack{\text{Clebsch-Gordan}\\ \text{coefficient}}} \cdot \underbrace{\sqrt{\frac{5}{16\pi}}\left(3\cos^2\Theta - 1\right)}_{Y_2^0(\Theta)}; \quad Y_{5/2}(\Theta,\varphi) = \underbrace{\sqrt{\frac{15}{32\pi}}\sin^2\Theta \cdot \mathrm{e}^{2i\varphi}}_{Y_2^2(\Theta,\varphi)}. \tag{8.6}$$

For $Y_{1/2}(\Theta)$ we neglected the contribution of the singlet scattering term, where the spin of the Rydberg electron is antiparallel to the spin of the ground state atom, because it is small compared to the triplet scattering term (see section 2.1 for details). The full expression can be found in equation (2.15). For this simple first approach we only take into account the pure wavefunctions (8.5) and no admixtures, which is the reason why the dependance of $\vec{R}$ drops out. In first order perturbation theory the Hamiltonian has the form $H_{i,j}(\vec{R}) = \langle\psi_i(\vec{r})\,|H|\,\psi_j(\vec{r})\rangle$. Exemplarily calculating the first element $H_{1,1}(\vec{R})$ yields

$$\begin{aligned} H_{1,1}(\vec{R}) &= \left\langle\psi_{1/2}(\vec{r})\,|H_0 + H_B + H_{\mathcal{E}}|\,\psi_{1/2}(\vec{r})\right\rangle + \left\langle\psi_{1/2}(\vec{r})\left|V_{n,e}(\vec{r};\vec{R})\right|\psi_{1/2}(\vec{r})\right\rangle \\ &= \underbrace{\Delta_1(\vec{R})}_{\text{energy shift}} + \underbrace{\int d\vec{r}\,\frac{2\pi\hbar^2 a(\vec{R})}{m_e}\left|R_{42D}\right|^2}_{p(\vec{R})} \cdot \left|Y_{1/2}(\Theta)\right|^2 = \Delta_1(\vec{R}) + p(\vec{R})\left|Y_{1/2}(\Theta)\right|^2. \end{aligned} \tag{8.7}$$

Here we summed up the total energy shift caused by the electric and magnetic Hamiltonian by the variable $\Delta_1(\vec{R})$. The variable $p(\vec{R})$ we introduced contains the information of the radial wavefunction and the scattering process and will be fitted as a constant value to the experimental data (we will neglect the $\vec{R}$ dependency once more). With no energy shifts present in the off-diagonal terms, the total Hamiltonian reads (here we omitted the dependencies of the variables for better readability)

$$H = p\begin{pmatrix} \left|Y_{1/2}\right|^2 + \Delta_1/p & Y_{1/2}^* Y_{5/2} \\ Y_{1/2}Y_{5/2}^* & \left|Y_{5/2}\right|^2 + \Delta_2/p \end{pmatrix} = \Delta_1 \cdot \mathbb{1} + p\begin{pmatrix} \left|Y_{1/2}\right|^2 & Y_{1/2}^* Y_{5/2} \\ Y_{1/2}Y_{5/2}^* & \left|Y_{5/2}\right|^2 + \Delta/p \end{pmatrix}. \tag{8.8}$$

As a simplification, we introduced the new variable $\Delta = \Delta_2 - \Delta_1$. Diagonalizing the Hamiltonian (8.8) and calculating the eigenvalues, excluding the energy offset $\Delta_1 \cdot \mathbb{1}$, yields

$$E_\pm = \frac{1}{2}\left(p \cdot \left(\left|Y_{1/2}\right|^2 + \left|Y_{5/2}\right|^2\right) + \Delta \pm \sqrt{\left(p \cdot \left(\left|Y_{5/2}\right|^2 - \left|Y_{1/2}\right|^2\right) + \Delta\right)^2 + 4p^2\left|Y_{1/2}\right|^2\left|Y_{5/2}\right|^2}\right). \tag{8.9}$$

Note that this energy was calculated with respect to the energy offset Δ_1, which represents the energy of our $42D_{5/2}, m_J = 1/2$ state. Only the solution E_+ for the binding energy of the molecules is of relevance for us, since it represents the binding energy of our Rydberg molecule. The energy shift Δ is the difference in energy between the states $42D_{5/2}, m_J = 1/2$ and $42D_{5/2}, m_J = 5/2$, caused by the Hamiltonians H_0, H_B and $H_{\mathcal{E}}$ and is depicted in Figure 8.9(a). This energy shift is exactly zero at the crossing point of these lines. When Δ approaches large negative values, it adopts the value of $45.6\,\mathrm{MHz}$ for the Zeeman splitting

between the $m_J = 5/2$ and $m_J = 1/2$ in the zero field case, calculated in subsection 1.3.1. In this case the theoretical value for the ground state toroidal molecule is $-3.27\,\mathrm{MHz}$ (see Table 2.1) and $-3.55\,\mathrm{MHz}$ in the measurement. Note that this state could not be detected in the previous measurements performed in section 8.1. In the measurement in Figure 8.9(b) only two distinct molecular lines can be traced from the crossing back to the zero field configuration of the $42D_{5/2}, m_J = 1/2$ state: the strongest bound toroidal state with an unperturbed binding energy of $-3.6\,\mathrm{MHz}$ and the axial ground state molecules ($\kappa = 0$) with a binding energy of $-13.7\,\mathrm{MHz}$. There are additional toroidal molecules of higher excitation numbers κ at lower binding energies visible, but their intensities vanish in vicinity to the crossing. Thus only two molecular states can be compared to our simple model. This is sufficient, since they contain the two different molecular species which we are interested in.

Equation (8.9) is a pure analytical expression depending on the energy difference Δ, which is our variable, and parameter p, which will be determined by a fit to the experimental data at zero electric field (large negative Δ). For the calculation of the binding energy of the toroidal molecule $\Theta = \pi/2$ was used and φ was chosen to maximize the angular wavefunction $|Y_{5/2}(\Theta, \varphi)|^2$, whereas for the axial state Θ was set to 0. In the experimental data, Gaussian fits were used to extract the maximum positions of the atomic lines to determine Δ and the molecular binding energies. The reference for these binding energies is always the atomic line, which changes at the crossing from the $m_J = 1/2$ to the $m_J = 5/2$ state. At the crossing the determination of those peak values is challenging due to the overlapping lines. In order to get rid of these disturbances at the crossings, parabolas were fitted to the Gaussian maxima to gain a smoother peak function. For the molecular lines, it turned out that a peak finding algorithm yielded better results than a Gaussian fit.

In Figure 8.11 the experimental values for the binding energies of the molecules are plotted as colored circles whereas the blue and red lines correspond to the theoretical two-level model. For the toroidal $42D_{5/2}, m_J = 1/2$ state two different datasets were used (black and blue) while for the axial state only one measurement run scanned the appropriate region (yellow filled circles). For the toroidal state the absolute binding energy increases to its maximum value of around $13\,\mathrm{MHz}$ at the crossing ($\Delta = 0$) and then decreases again, showing an asymptotic behavior. It is crucial that the asymptotic values on both sides are not the same. The reason for this behavior is the transformation of the electronic orbit from the $m_J = 1/2$ to the $m_J = 5/2$ state by the interference of their electron wavefunctions, as illustrated in Figure 8.12. The toroidal ground state molecule is formed in the outermost lobe in the $\Theta = \pi/2$ plane of the electronic orbitals. During this transformation process the toroidal lobes of the angular part of the electron wavefunction grow while the axial probability density shrinks (see Figure 8.12). This gives rise to the increasing binding energy of the toroidal molecule due to the deepening of the outermost potential wells until the electronic configuration of Figure 8.12 for $\epsilon = 0.5$ is reached, in which the two lobes in the x-y-plane are nearly maximized. From this intermediate state the electron orbit changes to a doughnut shape, reducing the extents of the two lobes in the toroidal plane. In the $m_J = 5/2$ configuration, the angular part of the electron orbit in $\Theta = \pi/2$ direction is still about a factor of 3 larger than in its initial $m_J = 1/2$ configuration, causing the two different asymptotic binding energy values. The signal intensity of the measured toroidal ground state molecule, which changes its binding energy according to the two-level model, is quite large (c.p. Figure 8.9), suggesting that this admixture process of the electronic wavefunctions is highly probable. Due to the simplifications made in our model the theoretical

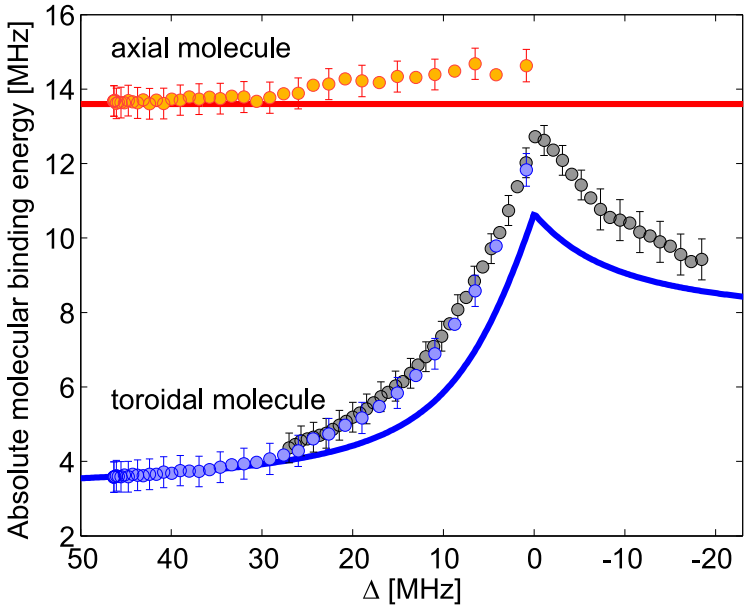

Figure 8.11: Binding energy of the toroidal and axial molecule in vicinity to the crossing of the levels $42D_{5/2}, m_J = 1/2$ and $m_J = 5/2$. The reference for this binding energy is always the atomic line, which changes at the crossing from the $m_J = 1/2$ to the $m_J = 5/2$ state. This is the reason for the kink appearing at $\Delta = 0$. The value of Δ in the x-axis is the energy difference between the two levels so that the crossing happens exactly at $\Delta = 0$. The black and blue circles indicate that two different datasets for the toroidal state were used whereas only one dataset (yellow circles) was available for the axial molecule. The red and blue lines are the calculations by the two-level model, for which the parameter p was fitted to the experimental data. The error bars result from the uncertainty of estimating the peak positions of the atomic and molecular lines.

binding energy curve (E_+) only describes the experimental data qualitatively correct. It does not take into account any other neighboring m_J states (e.g. the close-by $m_J = -1/2$ state), which can deform the electronic wavefunctions because they also admix to the wavefunctions of the two considered m_J states.

The behavior of the axial molecule, which only slightly increases its binding energy at the crossing, is completely different. In the model the angular part of the $m_J = 5/2$ wavefunction $Y_{5/2}(\Theta, \varphi)$ becomes zero for the axial state at $\Theta = 0, \pi$. Thus all coupling terms in the off-diagonal matrix elements vanish and the model predicts that the energy of the axial molecule stays constant for all values of Δ. The slight increase in binding energy at the crossing position could be caused by the uncertainty of determining the peak positions of the molecular line and atomic reference line. Another reason could be the influence of other nearby levels (e.g. the $m_J = -1/2$ state). Note that the non-intermixing probability densities of the pure electron orbits of $m_J = 1/2, 5/2$ are also present at the crossing, giving rise to this axial molecule and also to additional toroidally bound molecules in the pure $m_J = 5/2$ state (see subsection 8.3.1).

There are a lot of improvements that could be done to enhance our model and reduce the deviation to the measured data. The first deficit is that our model just uses the simple electronic wavefunctions of the non-perturbed states $m_J = 1/2$ and $m_J = 5/2$, not taking into account the admixing of other nearby levels as for example the $m_J = 3/2$ or $m_J = -1/2$ state, which

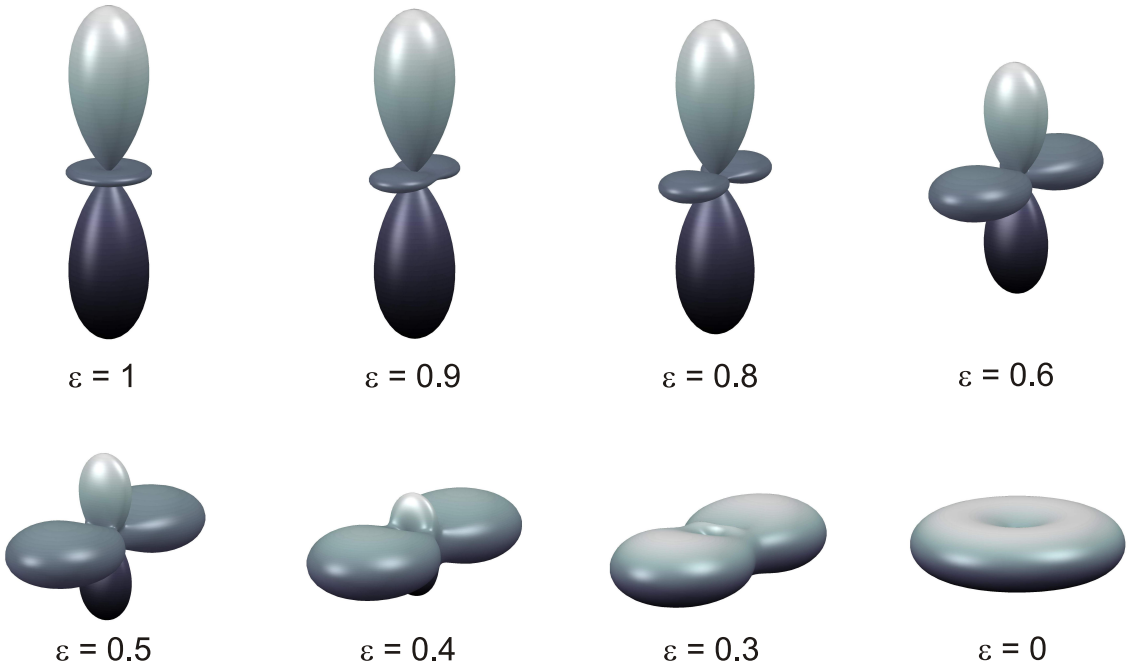

Figure 8.12: Transformation of the electron orbital of the $D_{5/2}, m_J = 1/2$ state to the $D_{5/2}, m_J = 5/2$ state. The shown orbits are given by the probability density $|Y_{\text{tot}}|^2 = \left| \frac{1}{N} \left(\epsilon \sqrt{\frac{3}{5}} \cdot Y_2^0(\Theta) + (1-\epsilon) Y_2^2(\Theta, \varphi) \right) \right|^2$, where N is the normalization constant and ϵ is the contribution of the angular part of the $D_{5/2}, m_J = 1/2$ state to the combined orbit. The parameter ϵ is scanned from 1 to 0, corresponding to a sweep of the electric field from one side to the other side of the crossing in the experiment. One observes that the electron orbit directly at the crossing ($\epsilon = 0.5$) and during the whole transformation shows a dependance on φ, in contrast to electron orbits of the pure m_J states for $\epsilon = 1$ and $\epsilon = 0$. Furthermore the maxima of the lobes in the x-y-plane directly at the crossing position ($\epsilon = 0.5$) are a factor of 3.33 larger than those of the pure $m_J = 1/2$ orbit ($\epsilon = 1$).

could slightly change the binding energies of the molecules. Another improvement would be to calculate the 3-D potential energy landscape and the corresponding molecular binding energy using the full Hamiltonian of the problem. This could be done again in a collaboration with the theory group of P. Schmelcher in Hamburg who recently already calculated the 3-D potential energy landscapes for Rydberg molecules in crossed electric and magnetic fields for $n = 30 - 50$ [177]. This way, no fitting parameter p would be necessary. A further step would be to determine all molecular binding energies at the crossing in this 3-D potential energy landscape and compare them to the measured ones from Figure 8.10.

The most crucial observation in this whole section is that the molecular wavefunctions intermix, whereas their atomic lines do not interact at all and show a nearly perfect crossing behavior (see Figure 8.9). In comparison to the D-state molecules at zero $\mathcal{E}$-field, the toroidal molecules at the crossing show a new φ-dependence emerging from the intermixing of the different angular parts of the wavefunctions (see Figure 8.12). This creates a new, but weak electric quadrupole moment for the toroidal molecules. In the outlook in section 11.3 we will propose a way to admix high-l electronic wavefunctions to our S-state electron orbits in order

to create molecules with large permanent dipole moment.

9 Single Rydberg electron in a BEC

In this chapter the measurement results of the D-state Rydberg atoms, interacting with a Bose-Einstein condensate, are presented and discussed. The main goal of these investigations is to discover differences between the excitation of S- and D-state Rydberg atoms inside the condensate, which possess the same radial, but different angular wavefunctions. In the first section 9.1 of this chapter a short summary of the previous S-state measurement results is given, which should remind the reader of the important findings which were made in [10, 11] and also apply for D-state Rydberg atoms. We then split the investigations of the D-state electrons in a BEC into section 9.2, where a pulsed laser sequence was used, and section 9.3, in which we introduced an adiabatic ramp of the red laser to minimize off-resonant background oscillations. In section 9.2 we present a detailed study of the lifetimes of the D- and S-state Rydberg atoms and discuss possible decay mechanisms. Furthermore, measurements of the atom losses in the condensate by the successive excitation of Rydberg atoms for principal quantum numbers n around 110 and 180 are reviewed. Additionally, we show that with a pulsed excitation sequence the effect of the Rydberg atom on the condensate oscillations compared to the background oscillations is very small, whereas with the adiabatic ramping sequence in section 9.3 the mechanical effect on the BEC is distinctly visible. For the adiabatic sequence we also studied the differences in the BEC atom losses and the condensate aspect ratio between S- and D-states.

9.1 Single *S*-state Rydberg electron in a BEC

A huge success was the extension of the investigation of Rydberg atoms to high densities ($\rho \approx 10^{14}\,\mathrm{cm}$) and to high principal quantum numbers $n > 100$. So far only single S-state Rydberg atoms in a BEC were investigated, but in the framework of this thesis the research was expanded to D-states. Before we delve into the new topic, we first briefly summarize the crucial findings for the S-state Rydberg atoms in a condensate, which lay the foundation for the work on the D-states and can be found in detail in [10, 11].

Let us start with a simplified scheme of this system, depicted in Figure 9.1, where the extent of the Rydberg electron wavefunctions for the $110S$ (blue) and $202S$ (red) states are visible as spheres inside the gray shaded condensate. The diameter of our typical cigar-shaped condensate is $8\,\mu\mathrm{m}$ in the radial direction and about $40\,\mu\mathrm{m}$ in the axial direction. Already for the $110S$ state the blockade radius exceeds the extent of the condensate in all spatial directions. Therefore only one single Rydberg excitation in the BEC at a time is possible. Since the wavefunctions of the D-states are angular-dependent and not spherically symmetric, their blockade radius becomes dependent on the angle Θ, but unfortunately the calculation of the blockade radius turned out to be very involved going beyond the scope of this thesis (see section 1.5 for details). Thus we have to assume that there is also only one excitation possible at the same time for the D-states

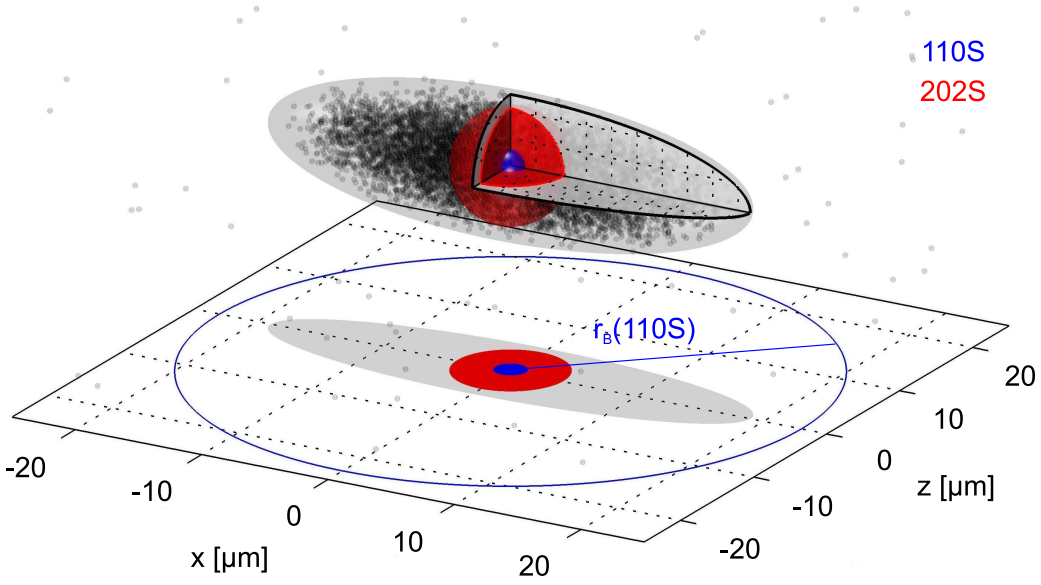

Figure 9.1: Size comparison of the single Rydberg electron−BEC system. Above the x-y-plane a cigar shaped BEC (gray) of 40 µm diameter in axial and 8 µm in radial direction, consisting of about $N = 8 \times 10^4$ ground state atoms, is depicted. It contains, as comparison, two Rydberg atoms of different sizes: The blue sphere defines the radius of the $110S$ state, whereas the red sphere displays the about 4 times larger radius of the $202S$ Rydberg atom. In the projection of the shapes of the condensate and Rydberg atoms on the x-y-plane their different sizes can be compared. Additionally the blockade radius r_B of the $110S$ state is shown, which already extends beyond the size of the whole condensate. That is the reason why only one single excitation at a time is possible in the BEC. The blockade radius of the $202S$ state is too big to fit into the scale of this scheme. This figure was taken from [11].

as for the S-state Rydberg atoms, due their same radial wavefunctions and similar measurement results (see next sections). Noteworthy is that in case of the $202S$ state the Rydberg electron probes already the outer zones of the condensate in the radial direction where the density is much lower. For this state there are several tens of thousands of ground state atoms within the radius of the Rydberg atom, tremendously increasing interaction effects between the ground state atoms and the Rydberg electron.

Systematic measurements of Rydberg S-states were conducted for principal quantum numbers n ranging from 110 to 202 in the thermal cloud as well as in the BEC regime [11]. From these measurements we can summarize the five essential results:

1. The first important result is the observed frequency mean shift: this is the frequency deviation between the spectral position of the atomic line in the thermal cloud and the position of maximum atom losses in the BEC. It was found that this frequency shift can be explained by the density dependent scattering of the electron from the huge number of surrounding ground state atoms. This density dependent shift was in fact first observed in 1934 by E. Amaldi and E. Segrè [36, 37]. They experimentally discovered a line shift in sodium of 0.22 THz when they brought these atoms into a very dense hydrogen background gas ($\rho = 4.8 \times 10^{19}\,\mathrm{cm}^{-3}$). In our case the background gas is equivalent

to the ground state rubidium atoms and the shift can be described by the formula (cp. equation (2.2))

$$\Delta E = \frac{2\pi\hbar^2 a}{m_e}\bar{\rho}. \tag{9.1}$$

In this equation $a = -16.1\,\mathrm{a_0}$ is the triplet scattering length of rubidium [93], m_e is the mass of the electron and $\bar{\rho}$ is the mean effective density of the condensate atoms, which can be calculated by taking into account the Thomas-Fermi density distribution (3.14). Eventually we end up with a decreasing line shift for increasing principal quantum numbers, shown in Figure 3.4(b). The reason for this behavior is that the size of the excited Rydberg atom grows with $n^{\star 2}$, probing on average more of the lower density parts away from the center of the condensate. This energy shift could also be reproduced very well by our stochastic model using the Gross-Pitaevskii equation, presented in section 3.3. This whole discussion about the density dependent line shift leads to an interesting consequence: we can spectroscopically probe and address different density regions in the condensate by changing the detuning of our laser. The densest region is addressed with the highest detuning where we still see some small atom losses in the condensate. So we could exchange our detuning axis in the plots to a density axis pointing to the red detuned side.

2. The second important result is the observed atom losses in the Bose-Einstein condensate per laser excitation pulse. They decrease with increasing principal quantum number n and can be explained illustratively by the fact that for higher n the Rydberg electron radius is bigger and it thus probes more the outer zones of the condensate where the density is lower. There are two reasons for these losses: the Rydberg electron kicks out condensate atoms, which are then lost to the thermal cloud and the coupling of the Rydberg electron to phonons, density ripples in the BEC, inducing shape oscillations. During our time of flight absorption imaging (see section 6.2) these phononic excitations are transferred into condensate atom losses as well, so that we cannot distinguish between these two processes in our measurements. In [10] we described this atom loss process by introducing Bogoliubov excitations in our BEC. These theoretical calculations reproduced our data for all n very well. Additionally, we show in Figure 3.4(a) that the atom losses per pulse in the condensate can also be described accurately with our stochastic excitation model (see theory section 3.3). Here the different losses occur due to the detuning dependent excitation probability, including the density shift, the different effective resonant two-photon Rabi frequencies and the different electron wavefunctions.

3. The third crucial result is the line broadening in the atom loss curve. One reason for this could be the excitation of the Rydberg atoms at random positions in the condensate. According to the simulations of the stochastic model in section 3.3 the highest condensate atom losses are expected to come mainly from the high density region in the center of the condensate (see Figure 3.3(c)). If we go to larger absolute detunings, the probability to excite Rydberg atoms gets quite low due to the large effective off-resonant two-photon Rabi frequencies (see equation (3.28)), resulting in fewer atom losses (see Figure 3.3(b)). If we go to small absolute detunings, we excite Rydberg atoms evenly distributed over the whole condensate (see Figure 3.3(d)), leading again to fewer atom losses, since on average the density in the orbit of the Rydberg electrons is lower. Thus we end up with a

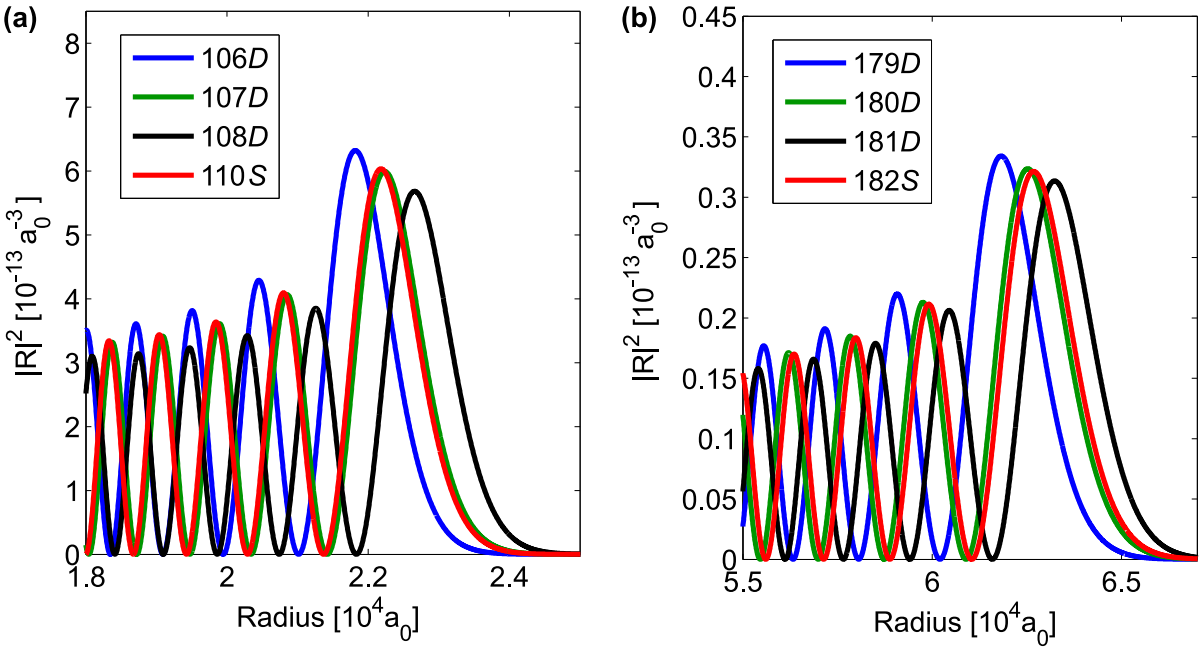

Figure 9.2: Calculated probability densities of the radial part of the electron wavefunctions of the states $110S$, 106 to $108D_{5/2}$ (a) and of the states $182S$, 179 to $181D_{5/2}$ in (b), plotted as a function of the radius. Only the outermost slopes of the probability densities are shown. The calculations of the wavefunctions were done with the program of B. Butscher [57].

Gaussian shaped loss curve. Another source of the broadening could be that the ground state atom is scattered at a random position in the electron scattering potential or is broadened by the scattering process itself (collisional broadening). In the stochastic model in section 3.3 only the excitation at random positions was taken into account, yielding a good agreement of the FWHM to our experimental data in Figure 3.4(c). Thus this effect seems to be the dominant broadening mechanism.

4. The forth important observation is that via the consecutive excitation of Rydberg atoms, the BEC starts to oscillate in the slow quadrupole oscillation mode (see section 3.4). By creating single electron impurities in the BEC we can bring the whole condensate into motion. In our measurements so far, the dominant effect was not caused by the excitation of Rydberg atoms in the condensate itself, but by the pulsing of the red excitation laser. This issue will be discussed in the next sections where we will present a different excitation sequence with which we can eliminate this background oscillation.

5. Another interesting result came up when we investigated the lifetimes of the S-state Rydberg atoms at principal quantum numbers n ranging from 110 to 202. In the lifetime measurements in the thermal cloud (see experimental sequence in subsection 6.1) we find a rather constant value of about $780 \pm 80\,\mu s$, almost independent of n, whereas the lifetime in the condensate (see experimental sequence in subsection 6.2) is much shorter, up to $10\,\mu s$. So there seems to be a limiting process which is connected to the ground state atom density. A detailed discussion about possible decay mechanisms and a comparison to the D-state data can be found in subsection 9.2.1.

9.2 Investigation of a single *D*-state electron in a BEC with a pulsed laser sequence

In this section we investigate D-states of principal quantum number $n = 106$ and 180 using a pulsed laser sequence (see section 6.2 and Figure 6.1(b) for details) and compare the measurements with those of the S-states possessing approximately the same radial extent of their electron wavefunction, so that they only differ in the angular part. The goal for the measurements is to see a difference in condensate atom losses, shape oscillations and lifetimes due to the different angular dependency of the D-states. To visualize which D-state has the best matching radial extent of the electron wavefunction we plot the outermost slopes of the probability density of the radial electron wavefunctions of these states in Figure 9.2, calculated with the program `rydLib` [57]. The $107D$ state has nearly the same radial extent as the $110S$ state, but unfortunately we took the $106D$ state for our comparison measurements. Since the difference between the $106D$ and the $107D$ state is small and experimentally it is only possible to identify specific Rydberg states $n > 100$ with an error of ± 1 in principal quantum numbers, we are going to compare the $106D$ with the $110S$ state in the following sections. The reason of this error stems from the $\sim 0.8\,\mathrm{GHz}$ precision of our spectrometer[1], which we use as a rough frequency reference. For the high principal quantum numbers, we compare the $180D$ state with the $182S$ state, since here again the radial extent is almost the same (see Figure 9.2(b)). In the following subsection we compare the lifetimes, atom losses and aspect ratios of the condensate and discuss BEC shape oscillation measurements.

9.2.1 Decay of *D*-state Rydberg atoms

Rydberg atoms are an intriguing species because of their enhanced radiative lifetimes which scale with $n^{\star\,3}$ [31], taking into account only spontaneous decay to lower energy levels. Spontaneous decay is dominant for small angular momenta $l \ll n$. Additional finite temperature effects lead to transitions to neighboring states which open up new decay channels, increasing the total decay rate of the Rydberg atom (see section 1.4). The black-body radiation induced decay results in a scaling of the lifetime with $n^{\star\,2}$ [31]. These two mechanisms are the main source for the shortened lifetime of Rydberg atoms (for details see theory section 1.4).

We measured the lifetimes of the D-states and S-states with comparable extent of the radial wavefunction in two different regimes: the thermal cloud where we achieve peak densities of $10^{12}\,\mathrm{cm}^{-3}$, and the condensate with peak densities of $10^{14}\,\mathrm{cm}^{-3}$. The two different measurement techniques are in detail described in section 6.1 and 6.2. The measurements were always conducted at the specific detunings where the highest losses in the condensate have been observed (see subsection 9.2.2).

We use equation (1.44) with the fitting parameters from I. Beterov and coworkers [64] and a temperature of $300\,\mathrm{K}$ to estimate the effective lifetime of our Rydberg atoms at high principal quantum numbers (see section 1.4). We end up with lifetimes of $411\,\mu\mathrm{s}$ for the $110S$, $379\,\mu\mathrm{s}$ for the $106D_{5/2}$, $1.20\,\mathrm{ms}$ for the $182S$, and $1.17\,\mathrm{ms}$ for the $180D_{5/2}$ state. If we compare the lifetime of the measured $n = 106D_{5/2}$, $m_L = 2$ state of $577 \pm 27\,\mu\mathrm{s}$ in Figure 9.3 in a thermal

[1] Advantest Wavelength Meter TQ8325

cloud with the theoretically calculated one, we detect a discrepancy, but they are in the same order of magnitude. In our previous work [10, 11] S-state lifetimes were measured for principal quantum numbers n ranging from 110 to 202 and it turned out that they were more or less constant ($780 \pm 80\,\mu s$), whereas the theoretically calculated values by equation (1.44) increase with principal quantum number. Thus there must be other mechanisms hindering us to observe the predicted increase. Possible candidates for these processes are discussed later. The lifetime of the D-state (see Figure 9.3) is in the same order of magnitude as for the $110S$-state, which is not surprising since the angular dependence of the wavefunction does not play a role in a huge thermal cloud where more than one Rydberg excitation is possible at the same time. Therefore we shift our focus now to the lifetime measurements in a Bose-Einstein condensate with a single Rydberg atom.

In Figures 9.4 and 9.5 we compare D- and S-state lifetime measurements in the BEC regime. In contrast to the thermal cloud measurement the lifetimes in the BEC are about two orders of magnitude smaller, corresponding to the difference in peak densities between these two regimes. Going from lower to higher principal quantum numbers the lifetime of the S- and D-states increases slightly from about $7\,\mu s$ to $10\,\mu s$, as observed in previous systematic studies for the S-states [11]. The measured lifetimes for the $182S$ and the $180D$ states are the same within the error bars (see Figure 9.5). The change of the angular part of the wavefunctions between the different D- and the S-states does not show any influence here. In case of the $110S$ state, we observe a $2.5\,\mu s$ shorter lifetime compared to the two different m_L $106D$ states, which show exactly the same lifetime of $7.3\,\mu s$ within their error bars (see Figure 9.4). An explanation for this small effect is still elusive. All lifetimes obtained from the BEC measurements are summarized in Table 9.1.

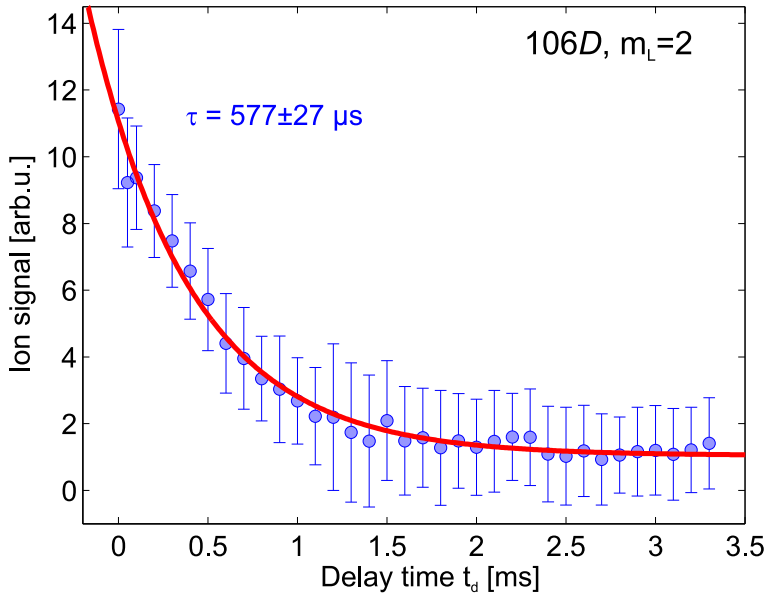

Figure 9.3: Lifetime measurement taken in a thermal cloud for the $106D_{5/2}, m_L = 2$ state. The exponential fit to the decaying data yields a lifetime of $577 \pm 27\,\mu s$. The error bars (standard deviation) were determined from 5 independent measurements.

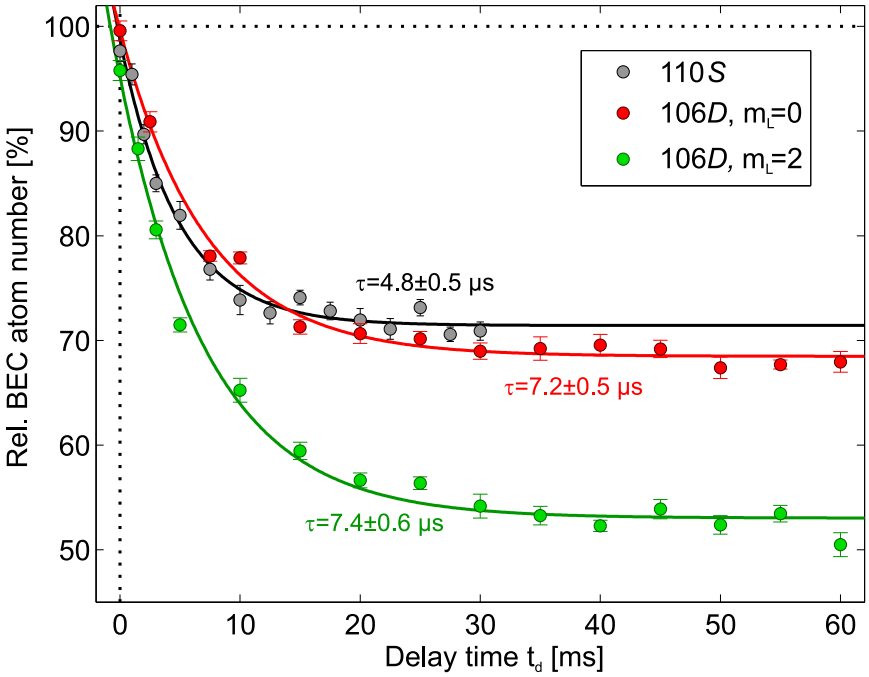

Figure 9.4: Lifetime measurements in the BEC regime for the states $110S$ (gray), $106D$, $m_L = 0$ (red) and $m_L = 2$ (green). Exponential fits to the three data sets yield the lifetimes of the Rydberg atoms, always taken at the detuning where maximum atom losses were detected (cp. Figure 9.6). For all data sets the error bars (standard deviation) were determined from 20 independent measurements.

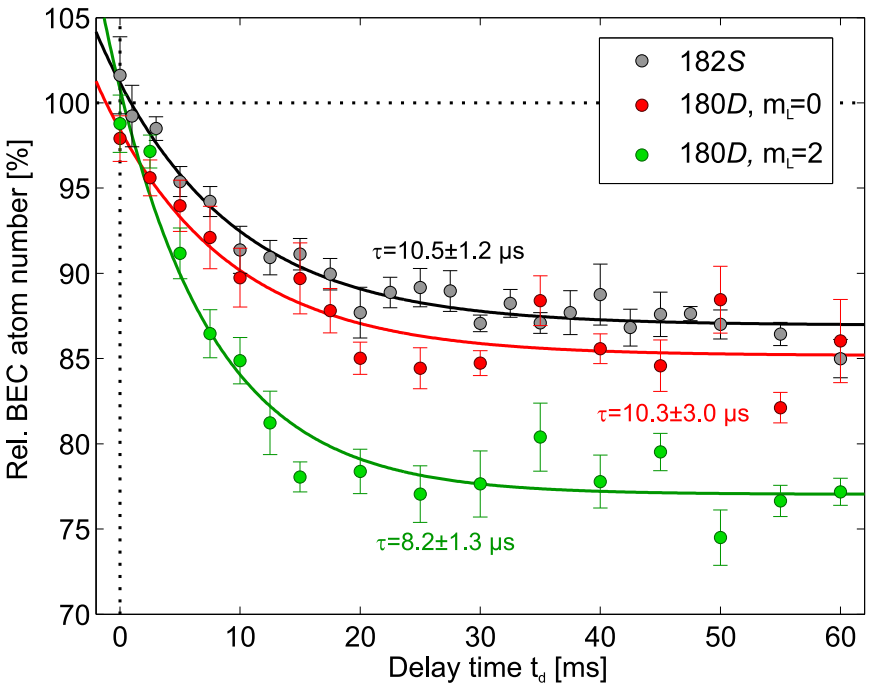

Figure 9.5: Lifetime measurements in the BEC regime for the states $182S$ (gray), $180D$, $m_L = 0$ (red) and $m_L = 2$ (green). Exponential fits to the three data sets yield the lifetimes of the Rydberg atoms, always taken at the detuning where maximum atom losses were detected (cp. Figure 9.7). For all data sets the error bars (standard deviation) were determined from 20 independent measurements.

Rydberg state	$110S$	$106D, m_L$=0	m_L=2	$182S$	$180D, m_L$=0	m_L=2
BEC lifetime τ [µs]	4.8 ± 0.5	7.2 ± 0.5	7.4 ± 0.6	10.5 ± 1.2	10.3 ± 3	8.2 ± 1.3
Two-photon Rabi frequency [2π kHz]	5.8	5.5	12.2	2.1	2.9	5.5
Line shift [MHz]	-8.4 ± 0.2	-8.0 ± 0.4	-8.9 ± 0.3	-6.0 ± 0.3	-7.6 ± 0.3	-6.9 ± 0.2
FWHM [MHz]	12.6 ± 0.5	7.2 ± 1.1	15.7 ± 0.9	6.7 ± 0.7	7.1 ± 1.0	7.2 ± 0.8
Lost atoms per excitation pulse	48 ± 2.0	41 ± 4.2	71 ± 3.5	8.4 ± 0.7	5.6 ± 0.6	12 ± 0.8

Table 9.1: Summary of the important parameters and results obtained by the pulsed excitation measurements from section 9.2. The given lifetimes for the Rydberg states in the BEC were measured independently at the specific detuning where the maximum atom losses had been detected. The two-photon Rabi frequencies were calculated by using the red laser power determined from the saturation curve measurements (see appendix B.1). The line shift, FWHM and atom losses per excitation pulse were obtained from Gaussian fits to relative BEC atom number data from Figures 9.6 and 9.7.

To sum up, other sources of decay processes have to be taken into account to explain the deviation from the theoretically predicted lifetimes, where only spontaneous decay and black-body radiation induced decay have been considered. Reasons for this may be ionization [178, 179], superradiance [180, 181] or plasma formation [182, 183]. Since the condensate density is two orders of magnitude larger than the thermal cloud density and the lifetime of the Rydberg atom in the BEC is two orders of magnitude smaller than in the thermal cloud, there is evidence that the dominant decay process depends on the number of ground state atoms inside the wavefunction of the Rydberg atom. If we assume that the density in the thermal cloud is homogenous based on its large size compared to the extent of a Rydberg atom, the number of atoms inside the electron wavefunction is constant [11]. Thus this could explain that the lifetime of the Rydberg atom in the thermal cloud is nearly independent on the principal quantum number n. In contrast to this, in a BEC, the average density of ground state atoms inside the Rydberg wavefunction decreases for increasing principal quantum number n, since the radius of the Rydberg atoms starts to extend to the lower density regions at the outer zones of the condensate. This could explain the slightly increased lifetime for higher n.

Effects of superradiance occur if the density of the excited state atoms is on the order of 10^8 to $10^{10}\,\mathrm{cm}^{-3}$ [180, 181], which is clearly not the case in our measurements. Another idea is that the Rydberg electron in a classical picture would constantly loose energy due to scattering processes with ground state atoms and would slowly cascade to lower Rydberg states. In this regard an important observation about the lifetime of S-state Rydberg atoms in the BEC was made in [10, 11] where it had been shown that the high n Rydberg state does not decay to states with significantly lower principal quantum number within 3 µs. Thus the Rydberg atom has to cascade either to lower Rydberg states after 3 µs, or decay to the ground state via spontaneous decay or it directly ionizes.

Two possible ionization processes can be found in the literature, starting with a rubidium $5S$ ground state atom and an excited rubidium atom. The first is the so-called Hornbeck-Molnar ionization or autoionization [178], in which a positively charged molecular ion Rb_2^+ is formed, while an electron is ejected. In the second one the ground state rubidium atom

snatches the Rydberg electron leading to the formation of a negatively charged Rb^- and a positively charged ion Rb^+, thus called ion-pair formation process [179]. Both processes have been experimentally observed in high pressure rubidium vapor cells for very low principal quantum numbers [179, 184, 185] and are good candidates for the decay process of Rydberg molecules [92].

The conclusion of the lifetime measurements is that the dominant effect reducing and limiting the observed lifetimes drastically is linked to the number of ground state atoms inside the Rydberg wavefunction. The angular dependance of D-states compared to the S-states does not play a role here, since the D-states are equally effected by this process. That is the reason why they have such similar lifetimes. Just recently in the other rubidium BEC apparatus in our institute, lifetimes of hundreds of µs were measured via single ion detection in the condensate in contrast to our 10 µs measurements with time of flight imaging. A possible explanation would be that the Rydberg atom leaves the BEC on short time scales ($< 10\,\mu s$), preventing further losses of condensate atoms and allowing the measurement of longer lifetimes as expected in a low density regime (thermal cloud). Still, for a full understanding of the decay mechanism, additional measurements are required.

9.2.2 Rydberg electron induced losses of condensate atoms and aspect ratio changes

In the following measurements a pulsed excitation sequence as depicted in Figure 6.1(b) was used to obtain information about the losses and aspect ratio changes of the condensate after time of flight absorption imaging (see section 6.2 for details). The power of the blue 480 nm laser was always kept at the highest technically possible value (around $110 \pm 5\,\mathrm{mW}$) to maximize the effective resonant two-photon Rabi frequency (1.24) and thus the probability to excite a Rydberg atom. We adjusted the power of the red 780 nm laser to the value for which the BEC atom losses begin to saturate, so that we do not get into the regime, in which the scattering of photons at the intermediate state becomes dominant and reduces the total number of BEC atoms. These saturation curve measurements can be found in the appendix B.1. The effective resonant two-photon Rabi frequencies are summarized in Table 9.1 and are all in the order of a few kHz. They were calculated from the measured laser powers and beam waists using the dipole matrix elements from reference [128]. The difference between the Rabi frequencies arises only from their different dipole matrix elements. The parameters for the experimental sequence used for the measurements in this subsection can be found in section 6.1.

In Figures 9.6 and 9.7 the relative BEC atom numbers (a) and the relative aspect ratios (b) are plotted as functions of the blue laser detuning. For the measurements at lower n in the first figure, 300 excitation pulses were sufficient to obtain significant losses in the BEC, whereas for the high n states in the second figure 500 pulses were needed. The aspect ratio is defined as the quotient of the radial and the axial extent of the condensate after the time of flight imaging $\epsilon = r_r/r_z$. As already mentioned in section 9.1, in which the crucial results from the former S-state measurements were presented, the larger radii of the Rydberg atoms for higher n are responsible for the fewer atom losses in the BEC, since the Rydberg electron is probing the less dense outer parts of the condensate. This is also the case for the D-state measurements because

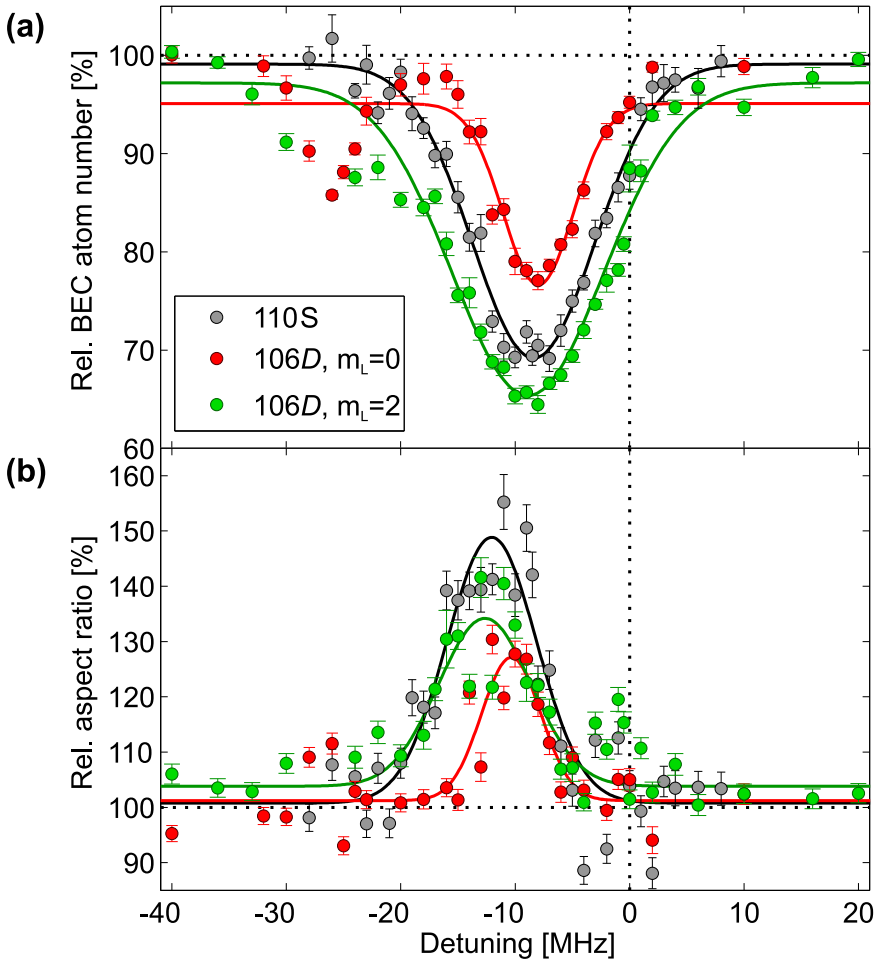

Figure 9.6: Measurements of the relative BEC atom number (a) and change of aspect ratio (b) for different laser detunings for the $110S$ (gray), $106D_{5/2}$, $m_L = 0$ (red) and $m_L = 2$ (green) state after a 50 ms time of flight for the pulsed laser sequence. For these measurements always 300 successive excitation pulses were used. The zero position was determined as the position of the Rydberg line in a spectrum measured in a thermal cloud. We obtained the error bars of the data from 20 independent measurements and fitted Gaussian functions to these points.

they have nearly the same radial wavefunctions as the S-states which were chosen for this comparison. In Table 9.1 we summed up the absolute losses per excitation pulse, line shifts, and FWHM obtained by Gaussian fits to the data. A comparison of the line shifts between the low and high D-states with their respective corresponding S-states reveals only small differences. Since according to equation (9.1) the line shift is only depending on the mean density of the ground state atoms, the slightly different condensate densities in combination with our small error in positioning the origin (determined by the spectral line in the thermal cloud) explain these observed differences well. Due to the density inhomogeneity and Rydberg excitations at random positions in the condensate, it is impossible to detect an influence of the different electron orbits of the D-states here. After the discussion about the reasons for the broadening of the atom-loss curves in section 9.1 we concluded that the dominant broadening mechanism is the excitation of Rydberg atoms at random positions (weighted with the density) in the condensate. Since the excitation probability (3.28) of the Rydberg atom depends on the

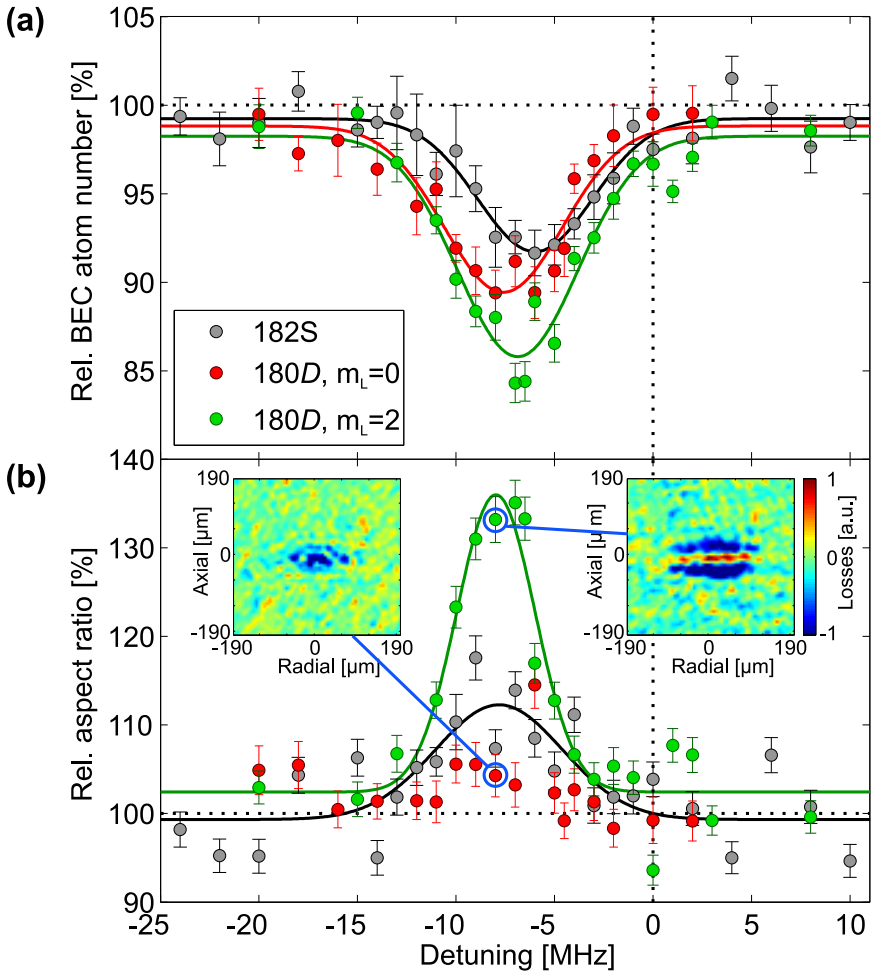

Figure 9.7: Measurements of the relative BEC atom number (a) and change of aspect ratio (b) for different laser detunings for the $182S$ (gray), $180D_{5/2}, m_L = 0$ (red) and $m_L = 2$ (green) state after a 50 ms time of flight for the pulsed laser sequence. For the Rydberg excitation 500 pulses were used to obtain a sufficiently large atom loss signal. The two insets depict the atom losses in the condensate at -8 MHz for the two different D-states. The zero position was determined as the position of the Rydberg line in a spectrum measured in a thermal cloud. We obtained the error bars of the data from 20 independent measurements and fitted Gaussian functions to these points.

two-photon Rabi frequency, which was not constant for the measurements, (see Table 9.1), it is not possible to extract information about the influence of the different electron orbits from these line broadenings. Concerning the atom losses per excitation pulse, we identify a trend that the $m_L = 2$ state for $n = 106$ and $n = 180$ has a higher atom loss per excitation pulse than the other D- and S-states. This is caused by the much larger two-photon Rabi frequencies (see Table 9.1), allowing more Rydberg excitations during the 300/500 pulses. Contradictory to the previous statement is the observation that, although the two-photon Rabi frequency for the $180D, m_L = 0$ state is higher than for the $182S$ state, granting a two times higher Rydberg excitation probability (3.28), there are fewer atoms lost in each excitation pulse for the $180D, m_L = 0$ state. Thus there needs to be another mechanism at work leading to this discrepancy. Possible reasons for this behavior could be the different electron orbits, state

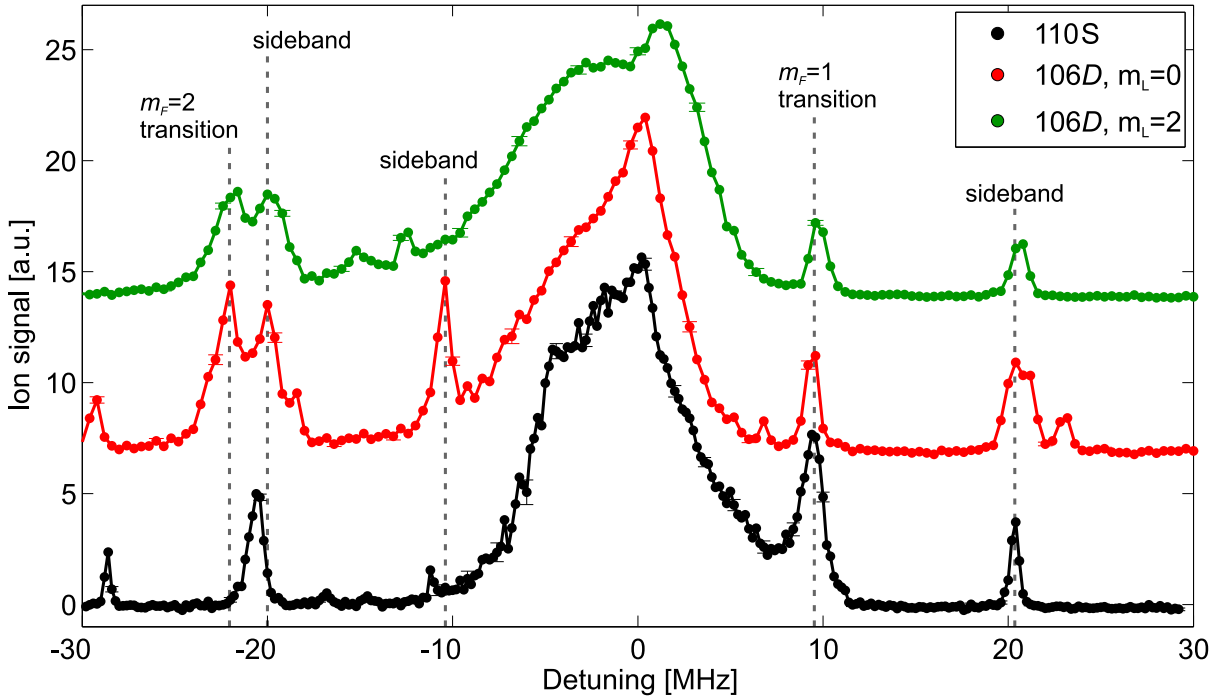

Figure 9.8: Spectra of the Rydberg states $110S$ (black), $106D_{5/2}, m_L = 0$ (red) and $106D_{5/2}, m_L = 2$ (green) taken at a magnetic offset field of 13.55 G. The zero position is set to these main transitions from the $5S_{1/2}(F = 2, m_F = 2)$ ground state. We also observe a spectral line stemming from the small $5S_{1/2}(F = 2, m_F = 1)$ ground state population at around 10 MHz. Additionally modulated sidebands are visible $\pm$ 20 MHz apart from the transition lines, generated by our Pound-Drever-Hall locking scheme (see chapter 5). The lines connecting the data points are guides to the eye whereas the gray dashed lines mark the features in the spectra. The three spectra have an offset in y-direction to improve the visibility of the peaks. Only a few error bars are exemplarily shown which were determined from 20 independent measurements.

changing collisions [94, 186] and three-body recombination processes [187, 188, 189, 190]. A scaling with the ground state atom density of $\propto \rho^2$ would provide evidence that a three-body recombination process is involved. Further measurements, currently carried out in the 'new' BEC setup, and especially a deeper theoretical understanding for the underlying loss process is needed to explain these findings.

Another visible feature in the atom loss measurements for low n is the shoulder for the $106D, m_L = 2$ state, which is at the same position as the dip for the $106D, m_L = 0$ state at a laser detuning of around -25 MHz (see Figure 9.6). The reason for this is visible in the spectra depicted in Figure 9.8: both D-states possess the next spectral line at around -22 MHz, stemming from the next m_L-transition. Due to the line shift this feature is moved to around -25 to -30 MHz in the BEC measurement (see Figure 9.6). The reason why we see a broad shoulder in one case and a peak in the other case is still unknown.

The relative aspect ratio change of the $180D_{5/2}, m_L = 2$ state is huge compared to the nearly non-existing change for the $m_L = 0$ configuration, whereas in the relative BEC number there is only a small difference of 5 % between them (see Figure 9.7). From the insets in Figure 9.7(b) it is visible that the atom losses are more or less equally distributed for the

$m_L = 0$ case, while for the $m_L = 2$ state they are split into two, meaning that we obtain an elongated BEC undergoing shape oscillations. The reason why a change in aspect ratio is only detectable for the $180D_{5/2}, m_L = 2$ state is probably the nearly doubled effective two-photon Rabi frequency (see Table 9.1), which increases the probability to excite a Rydberg atom by a factor of about 3.6. More interesting is the comparison of the $180D_{5/2}, m_L = 0$ with the $182S$ state. Although the D-state has a factor of 2 higher probability to excite Rydberg atoms, a larger change in aspect ratio can be observed for the S-state (see Figure 9.7(b)). For the measurements at lower n it is puzzling that the $106D_{5/2}, m_L = 2$ state shows a lower relative aspect ratio than the $110S$-state (see Figure 9.6(b)), despite having a much larger effective two-photon Rabi frequency and many more lost atoms per pulse (see Table 9.1). We cannot provide an explanation for this but it might be again linked to the different electron orbits, state changing collisions [94, 186] or three-body recombination processes [187, 188, 189, 190].

We conclude that further measurements and theoretical modeling of the D-state measurements are needed to get more insight into the underlying physical processes. So far our collaborators from the group of K. Rzążewski have just begun to work on simulations for the D-states.

9.2.3 Shape oscillations in the condensate

In the aspect ratio measurements from the previous subsection 9.2.2, we have already seen that the condensate gets deformed. For further analysis we fixed the laser detuning to the position with the highest aspect ratio change and introduced an additional variable hold time t_h before the time of flight imaging (see Figure 6.1(b) and section 6.1). Scanning this waiting time, we observe shape oscillations in the radial axis of the condensate after the time of flight, shown in Figure 9.9. Unfortunately this sinusoidal oscillation is not only visible at the detuning where we excite Rydberg atoms in our condensate, but also in a reference measurement conducted 50 MHz detuned from this point. There is clearly a larger oscillation effect present for the non-detuned case but still the background oscillation provides the dominant contribution. The frequency of this oscillation is around $2\pi \cdot (34 \pm 0.4)$ Hz and matches well to the prevailing slow quadrupole oscillation $L = 2, m_L = 0$ with $\omega \approx \sqrt{5/2}\ \omega_z = 2\pi \cdot 34.8$ Hz (see section 3.4). An additional measurement revealed that the background oscillation stems from the pulsed red laser. In the next section we show an altered sequence with which we were able to get rid of this problem.

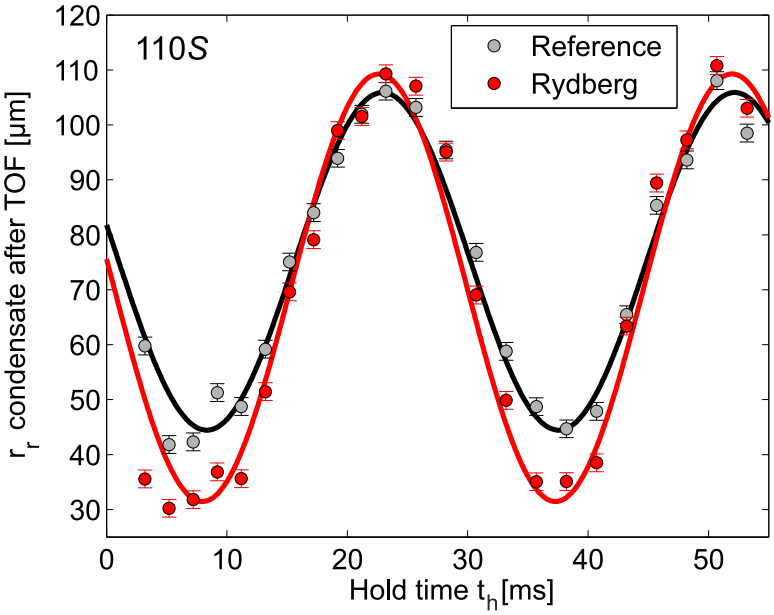

Figure 9.9: Oscillation measurement observing the slow quadrupole oscillation in the radial axis after time of flight imaging for the $110S$-state, using the pulsed excitation sequence. The 'Rydberg' labeled measurement was conducted at a laser detuning of $-14\,\mathrm{MHz}$ whereas the reference measurement was done $50\,\mathrm{MHz}$ detuned from this value. To extract the oscillation period sinusoidal fits to the data were performed. The error bars (standard deviation) were determined from 20 independent measurements.

9.3 Investigation of a single *D*-state electron in a BEC with an adiabatic ramping sequence

In this section we changed our Rydberg excitation sequence from the previously pulsed one (section 9.2) to an adiabatic ramping sequence of the red laser, which is shown in Figure 6.2 and discussed in detail at the end of section 6.2. The reason why we introduced this sequence is to get rid of the background oscillations caused by the red pulsed laser, shown in subsection 9.3.2. The red laser is now switched on via an about $37\,\mathrm{ms}$ long s-shaped adiabatic ramp and is then kept on for $0.8\,\mathrm{ms}$ at its maximum level, for the measurements at the principal quantum numbers $n = 106$ and 110. We set the maximum red laser power to a very low value of $25\,\mathrm{nW}$ to minimize the photon scattering rate at the intermediate level. For a better comparison of the D- and S-states we fixed the resonant two-photon Rabi frequencies to $0.41\,\mathrm{kHz}$ for all measurements around $n = 110$ by adjusting the power of the blue laser for each state individually. In the following two subsections we show measurements of atom losses in the condensate and of the BEC shape oscillations. Table 9.2 summarizes the important results and parameters from the measurements conducted with the adiabatic sequence.

Rydberg state	$110S$	$106D, m_L$=0	$106D, m_L$=2
Blue laser power [mW]	83	104	17.3
Two-photon Rabi frequency [2π kHz]	0.41	0.41	0.41
Line shift [MHz]	-8.0 ± 0.2	-7.8 ± 0.2	-11 ± 1.0
FWHM [MHz]	10.8 ± 0.7	10.4 ± 0.6	12 ± 1.0
Maximum atom losses [%]	43.0 ± 1.7	40.2 ± 1.5	34.0 ± 1.5
Maximum absolute atom losses [10^4]	2.33 ± 0.85	2.42 ± 0.61	2.04 ± 0.62
Oscillation frequency [2π Hz]	33.3 ± 0.8	31.2 ± 1.6	32.4 ± 1.1
Oscillation amplitude [arb.u.]	16.5 ± 1.1	14.3 ± 2.1	12.1 ± 1.1

Table 9.2: Summary of the important parameters and results obtained by the adiabatic ramping measurements from section 9.3. To keep the two-photon Rabi frequencies constant the red power was fixed at 25 nW while the blue power was adapted for the different states. The line shift and full width half maximum (FWHM) were extracted from Gaussian fits to the relative BEC atom number data from Figure 9.10, except for the $106D, m_L = 2$ state, whose shape is not Gaussian at all. Still we roughly estimated the line shift and FWHM for this state. The maximum atom losses in the BEC were also obtained from this measurement, whereas the oscillation frequency and amplitude were extracted from sinusoidal fits to the oscillation measurements from Figure 9.12.

9.3.1 Rydberg electron induced losses of condensate atoms and aspect ratio changes

In contrast to the pulsed measurements of subsection 9.2.2 we now present similar measurements done with the adiabatic ramping sequence and a constant two-photon Rabi frequency. In Figure 9.10 the relative BEC atom losses (a) and the relative aspect ratio changes (b) are depicted. The $106D, m_L = 0$ state features nearly the same shape of the atom loss curve as the $110S$ state, whereas the $106D, m_L = 2$ state shows a completely different behavior. We fitted Gaussian functions to the atom losses of these states except for the $106D, m_L = 2$ state, where we estimated the line shift and FWHM manually. The resulting values for the fits are summarized in Table 9.2.

We detect a dip at a laser detuning of around -1 to -2 MHz which is caused by the $5S_{1/2}(F = 2, m_F = 1)$ transition to the different m_L-states which can be clearly seen at around 10 MHz in the spectra of these states (see Figure 9.8). The reason why we also trap a small population of this ground state in our cold atom cloud is the evaporative cooling process and is explained in detail in chapter 4. Due to the density dependent line shift this transition is shifted to around -1 MHz in the atom-loss curves. In contrast to the measurements with the pulsed sequence in Figure 9.6, where the effect of this transition can hardly be seen, it is very prominent in the measurement with the adiabatic sequence (Figure 9.10). Another huge difference is that the other $5S_{1/2}(F = 2, m_F = 2)$ transition at around -25 MHz, clearly visible in the pulsed sequence measurements (Figure 9.6) cannot be seen in the adiabatic measurements (Figure 9.10). The reasons for the discrepancies in those measurements are still unclear. It might be connected to the different durations of the two sequences: the adiabatic sequence takes about 38 ms from the start of the red laser ramp to the time of flight imaging,

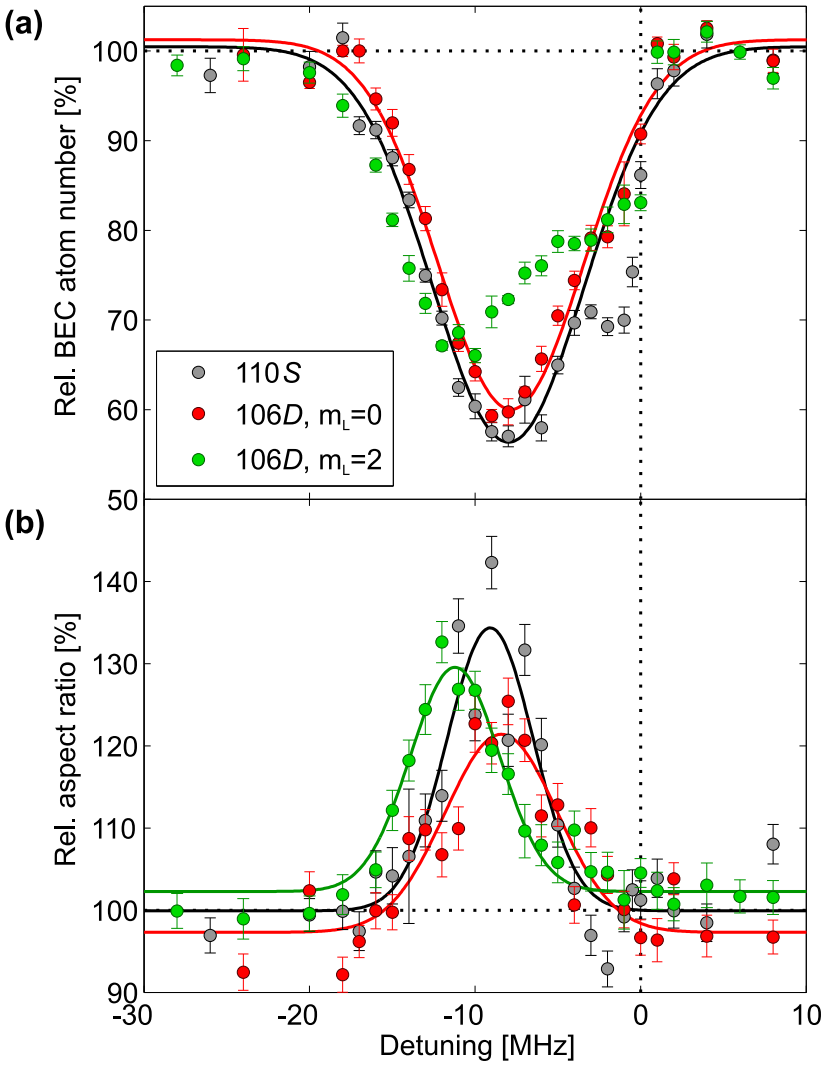

Figure 9.10: Measurements of the relative BEC atom number (a) and the change of aspect ratio (b) for different laser detunings for the $110S$ (gray), $106D_{5/2}, m_L = 0$ (red) and $m_L = 2$ (green) state after a 50 ms time of flight for an adiabatic ramping sequence of the red laser (see Figure 6.2). The zero position was determined as the position of the Rydberg line in a spectrum measured in a thermal cloud. We obtained the error bars of the data from 16 independent measurements and fitted Gaussian functions to the data points.

while the pulsed sequence only lasts for 4.8 ms. Another reason could be the much smaller two-photon Rabi frequency of the adiabatic measurement or the ionization process: for the pulsed measurement we always ionize our cloud for 2 µs after the red laser pulse (with a delay time of 10 µs), whereas for the adiabatic measurement we do not use any ionization pulse. Due to the completely different sequences it is hard to draw conclusions comparing these measurements with each other. Furthermore, for the adiabatic measurement, there is no explanation yet why the maximum line shift of the $106D, m_L = 2$ state is about 3 MHz larger than for the other two states and why the atom loss curve has this different shape compared to the other two states (see Figure 9.10).

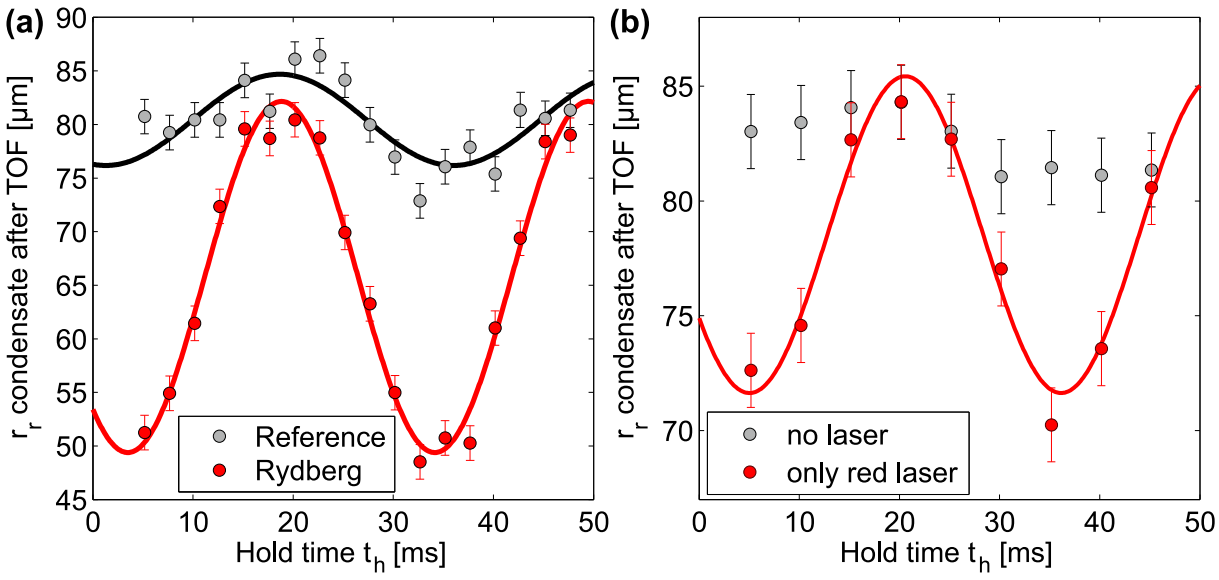

Figure 9.11: Measurement of the oscillations in the radial condensate axis after time of flight imaging for the $110S$ (a) and the $106D, m_L = 2$ state (b), using the adiabatic ramping sequence. In (a) the 'Rydberg' labeled measurement was conducted at a laser detuning of $-8.5\,\mathrm{MHz}$ whereas the reference measurement was done 50 MHz detuned from this value. In (b) the blue laser was always switched off while the red laser was one time switched on (red dots) and the other time off (gray dots). This measurement clearly shows that the adiabatic ramping of the red laser still causes oscillations in the BEC, but significantly fewer than in the pulsed measurement, clearly visible in a direct comparison with Figure 9.9. To extract the oscillation period sinusoidal fits to the data were performed. The error bars (standard deviation) were determined from 20 independent measurements.

Although the $110S$ and $106D, m_L = 0$ states feature nearly the same relative atom losses (Figure 9.10(a)), the S-state exhibits an around 13 % higher change in aspect ratio (see Figure 9.10(b)), comparing the maxima of the fitted Gaussian functions. Possible reasons for this behavior might be the different electron orbits, state changing collisions [94, 186] or three-body recombination processes [187, 188, 189, 190]. Another interesting observation is that the change in aspect ratio for the $106D, m_L = 2$ state is higher than for the $106D, m_L = 0$ state (see Figure 9.10), despite showing the opposite behavior when comparing the relative atom losses in the BEC. An explanation to this fact is still elusive.

To summarize we detect differences between these three states, but so far we cannot explain our observations sufficiently. Further measurements and a simulation of this altered sequence using the stochastic model explained in section 3.3 is needed to get a better understanding of the underlying physical processes.

9.3.2 Shape oscillations in the condensate

The reason we introduced the adiabatic ramping sequence was to get rid of the oscillations caused by pulsing the red laser. As we can see in Figure 9.11(a) exemplarily for the $110S$ state, the background oscillation in the reference measurement could be tremendously decreased compared to the pulsed sequence in Figure 9.9. The signal amplitude of the sinusoidal fit at resonance (red) is a factor 3.8 higher than the reference signal (black). The measurement in Figure 9.11(b) proves that the red laser is still causing background oscillations in the adiabatically ramped sequence. One time the oscillation measurement for the $106D, m_L = 2$ state was done without any laser (gray dots) and the other time only with the red laser switched on using the adiabatic ramp (red dots). We observe that there is still a very small oscillation visible in the red sinusoidal fit even for the adiabatic sequence, but it is negligible compared to the Rydberg signal (see Figure 9.9).

In Figure 9.12 we compare the oscillation measurements of the states $110S$, $106D, m_L = 0$ and $106D, m_L = 2$. Each measurement was conducted with the same two-photon Rabi frequency of $2\pi \cdot 0.41\,\mathrm{kHz}$ and at a blue laser detuning of $-8.5\,\mathrm{MHz}$. We always normalized each measurement point to the reference measurement, taken $50\,\mathrm{MHz}$ detuned from resonance, by dividing these two values. Additionally sinusoidal functions were fitted to all three data sets yielding values for the amplitude and frequency of the oscillations, summarized in Table 9.2.

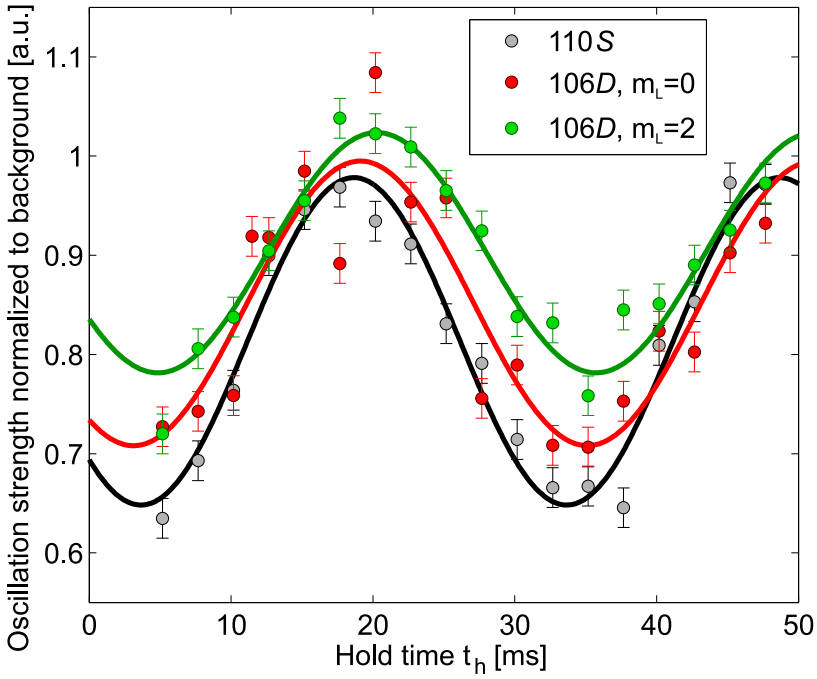

Figure 9.12: Comparison of the quadrupole oscillations of the states $110S$ (gray), $106D, m_L = 0$ (red) and $106D, m_L = 2$ (green), using the adiabatic ramping sequence. The oscillation strengths were always normalized to the reference measurements taken $50\,\mathrm{MHz}$ away from the detuning of $-8.5\,\mathrm{MHz}$, at which all oscillation measurements were conducted. To extract the oscillation period sinusoidal fits to the data were performed. The error bars (standard deviation) were determined from 20 independent measurements.

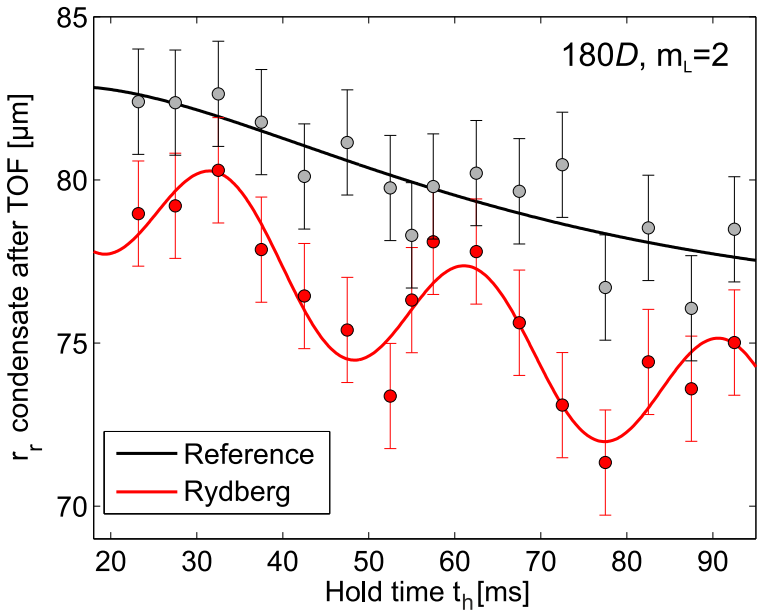

Figure 9.13: Oscillation measurement for the $180D$, $m_L = 2$ state, using the adiabatic ramping sequence at a laser detuning of $-7.5\,\mathrm{MHz}$. To induce an oscillation at this high n, the time for which the red laser is on its final value after the adiabatic ramp was increased from $0.8\,\mathrm{ms}$ to $24\,\mathrm{ms}$, employing a two-photon Rabi frequency of $2\pi \cdot 0.39\,\mathrm{kHz}$ to drive the Rydberg transition. For these long hold times the condensate gets depleted quickly, as can be seen by the decay of the reference signal, taken $60\,\mathrm{MHz}$ detuned from resonance and the resonant signal. We use a decaying sinusoidal fit function to describe the signal on resonance. The error bars (standard deviation) were determined from 20 independent measurements.

The observed frequencies of $2\pi\cdot$ (31 - 33) Hz are close to the calculated slow quadrupole oscillation frequency $\omega \approx \sqrt{5/2}\,\omega_z = 2\pi \cdot 34.8\,\mathrm{Hz}$ and demonstrate that additional effects from finite temperature and influences of the thermal cloud can be mostly neglected. The very small differences in the phases between the three states can be completely omitted since they are the same within the error bars. The amplitude of the $110S$ state is around 13.1 % higher than for the $106D, m_L = 0$ state and 26.6 % higher than for the $106D, m_L = 2$ state. The random excitation positions, the different angular wavefunctions, three-body recombination processes [187, 188, 189, 190] or maybe state changing collisions [94, 186] might be the reason for these differences in the amplitudes.

We furthermore conducted measurements for the $180D, m_L = 2$ state. Due to the far fewer atom losses compared to the low n measurements we needed to increase the duration of the red laser shining on the rubidium atoms tremendously from $0.8\,\mathrm{ms}$ to $24\,\mathrm{ms}$ to see an effect stemming from the excitation of Rydberg atoms. The result of this measurement can be seen in Figure 9.13. We again compare the resonance position at a blue laser detuning of $-7.5\,\mathrm{MHz}$ with a reference measurement recorded $60\,\mathrm{MHz}$ detuned from this position and drive the transition with a resonant two-photon frequency of $2\pi \cdot 0.39\,\mathrm{kHz}$. The first observation is the decay of the oscillatory signal for the measurement on resonance as well as for the reference measurement, stemming from the atom losses of the condensate over the total sequence time of $61\,\mathrm{ms}$, from the beginning of the adiabatic ramping of the red laser to the time of flight detection. Moreover the signal amplitude of the measurement for the $180D$ state is very small compared

to the measurements at low n. The reason is the smaller depth of the electron−ground state atom scattering potential created by the Rydberg electron wavefunction. Therefore the coupling to the BEC atoms is reduced, decreasing the strength of the shape oscillations. Although we excite Rydberg atoms for such a long time, the positions where we excite the Rydberg atoms are still random (the highest density region in the middle of the condensate has still the highest probability to get excited) and thus the oscillation signal gets washed out. The measured frequency of the oscillations is $2\pi \cdot (34.1 \pm 2.1)\,\mathrm{Hz}$ and thus agrees well with the theoretical value of the slow quadrupole oscillation of $2\pi \cdot 34.8\,\mathrm{Hz}$.

All in all the measurement at this high quantum number is not favorable for the oscillation measurement. To understand the different behaviors in the oscillations for the low n measurements we need to compare our results with theory simulations which could be done in the group of K. Rzążewski using the stochastic model presented in section 3.3.

Conclusion and Outlook

It is always wise to look ahead, but
difficult to look further than you can see.

Winston Churchill

10 Conclusion

As already mentioned in the title of this thesis, the goal of this dissertation was to study the interaction between D-state Rydberg electrons and ultracold atoms. This was carried out in two different density regimes of the ^{87}Rb ground state atoms. In the thermal cloud with densities of $10^{12}\,\mathrm{cm}^{-3}$ we created Rydberg molecules, consisting of a D-state Rydberg electron and one ground state rubidium atom, which was the topic of the first part of my thesis. In the second one we excited single D-state Rydberg electrons in a Bose-Einstein condensate with densities of $10^{14}\,\mathrm{cm}^{-3}$.

Rydberg molecules are an intriguing kind of species which inherit their exceptional properties from their constituent Rydberg atom. They can have sizes of several $\mu\mathrm{m}$ which is the size of bacteria or large viruses. Furthermore due to their high polarizability ($\propto n^{\star\,7}$) they can be easily controlled by electric fields, changing their properties. A novel chemical binding mechanism is responsible for the creation of Rydberg molecules, which differs from the covalent van der Waals and the ionic binding. The Rydberg electron creates an attractive potential for the ground state atoms, trapping them and forming a bound molecular state. This binding mechanism can be described with the so-called Fermi pseudopotential. It was introduced already in 1934 by Fermi and coworkers [12, 91] and is proportional to the negative triplet scattering length $a = -16.1\,\mathrm{a}_0$ and the squared electron wavefunction. This type of molecule has been predicted by C. Greene in 2000 [13] and has been created for the first time in 2009 by V. Bendkowsky and coworkers [6]. These studies were conducted for S-state Rydberg molecules which possess a spherical symmetric electron orbit. In this thesis we extended this study to D-state molecules, which feature a Θ-dependent electron orbit. Two types of D-state molecules were investigated, the $D_{5/2}, m_J = 1/2$ and the $D_{5/2}, m_J = 5/2$ for principal quantum numbers n from around 40 to 50. A magnetic field of $13.55\,\mathrm{G}$ was used to energetically split the m_J sublevels. In a collaboration with M. Kurz from the University of Hamburg the potential energy surfaces and the binding energies of these molecules were calculated and compared with the experimental findings. We discovered two different types of molecules, the axial ones, which are formed in the outermost potential wells along the z-axis of the electron orbits of the $m_J = 1/2$ states, and the toroidal states, which are created in x-y-plane for both m_J states. The measured binding energies of these molecules match well to the theoretically calculated ones, although we only used the B-field value from the experiment ($13.55\,\mathrm{G}$) and no other free parameters. We also detected several higher excited rovibrational states which we can selectively excite by choosing the appropriate laser detuning. Since the vibrational and rotational states of these Rydberg D-state molecules have the same order of magnitude we used rovibrational excitation numbers to characterize them.

The angular confinement of molecules, the alignment, is of importance because it influences their chemical reaction dynamics. To create alignment usually strong magnetic, electric or light fields are necessary, while our Rydberg molecules are already aligned by their creation process

in a weak magnetic field. The axial molecules possess a very high alignment along the z-axis whereas the toroidal molecules are antialigned since they are formed perpendicular to the z-axis in the x-y-plane. Another advantage of our technique is that these molecules are stationary and do not rotate in their short lifetime of around 10 µs. All in all, we showed that we can address specific molecular states by changing our laser detuning and thus create perfectly aligned axial or antialigned toroidal molecules, in good agreement with the theoretical calculations.

To alter the potential surfaces and properties of these molecules we conducted further measurements in an electric field. Here we investigated the crossing of the atomic lines of the $42D_{5/2}, m_J = 1/2$ and $m_J = 5/2$ states. Due to the dipole coupling rules these states do not interact with each other, however their molecular states do. Since the electronic wavefunctions of the two states intermix, the trapping potentials as well as the binding energies for these molecules are changed. Continuously increasing the electric field, we can trace the ground state molecular lines from the previously studied zero field case to the crossing of the two m_J states and beyond. While the binding energy of the axial molecule is nearly unchanged during this ramp, the binding energy of the toroidal state increases to its maximum at the crossing and then decreases again. These different behaviors can be understood by a simple two level model, taking the unperturbed Rydberg electron wavefunctions of the $m_J = 1/2$ and $m_J = 5/2$ states as a basis. The change of the electron orbit, starting from the $m_J = 1/2$ state, advancing to an equal mixture of both m_J states at the crossing and ending with the electron orbit of the $m_J = 5/2$ state after the crossing, explains well the behavior of the molecules. The toroidal state alters its energy according to this intermixing of the electron orbits, whereas the axial does not change its binding energy due to the fact that the $m_J = 5/2$ state has no axial contribution in its electron orbit. There are quantitative differences between model and experimental data which stem from the oversimplification of the used model. We did not take into account any admixtures of other nearby m_J states. Instead we used just the unperturbed wavefunctions for the two m_J states in the calculations. Note that the toroidal molecules now possess a φ-dependance at the crossing which is not the case for the non-intermixed toroidal molecules, which are isotropic in the azimuthal angle φ. To summarize we can explain the altered binding energies of the toroidal molecules and showed that the electric field permits us to create new potential energy landscapes with novel molecular states, showing a different angular dependance and alignment. Based on this measurement for the $42D$-state, we came up with the idea to create Rydberg molecules with large permanent dipole moments by mixing S- and high-l state wavefunctions, the so-called trilobite molecules [13]. This idea is discussed in detail in the outlook in section 11.3.

The second part of this thesis deals with D-state Rydberg electrons in Bose-Einstein condensates for high principal quantum numbers $n > 100$. The foundation for this work was laid by the previous investigation of the successive excitation of single S-state Rydberg atoms in a Bose-Einstein condensate [10, 11]. Due to the large size of the Rydberg atoms their blockade radii exceed the dimensions of the condensate, giving rise to only one excited Rydberg atom in the condensate at a time. In these measurements we discovered that the atomic losses in the condensate are due to electron−phonon coupling and expelled atoms into the surrounding thermal cloud. Furthermore, we observed the maximum losses detuned from the expected resonance position, based on spectral measurements in the thermal cloud. This line shift is caused by the scattering between the Rydberg electron and the many ground state

atoms inside the large radius of the Rydberg atom. The shift, which is linearly dependent on the density, was already observed in measurements of E. Amaldi and E. Segré in 1934, who conducted experiments with alkali atoms in dense background gases [36, 37]. This feature allows us to probe different density regions in our condensate just by changing the detuning of our excitation lasers. In this thesis we extended the measurements from S-state to D-state Rydberg electrons and investigated the differences arising from their different electron orbits. For comparison we chose D-states, which possess nearly the same radial wavefunctions as their S-state counterparts. In the lifetime measurements no noticeable differences between the two different $D_{5/2}, m_J = 1/2$ and $m_J = 5/2$ states and the S-state could be seen. It is still elusive why the lifetimes measured in the condensate (around $7 - 10\,\mu\mathrm{s}$) are two orders of magnitude smaller than in the measurements conducted in the thermal cloud (around $780\,\mu\mathrm{s}$). We concluded that the ground state density is involved in the explanation of the decay mechanism since it differs also two orders of magnitude between the thermal cloud and the condensate, and that this process limiting the lifetime in the condensate affects D- and S-states equally. The formation of ions or the fast ejection of the Rydberg atom out of the condensate could be possible explanations. However further measurements are needed to understand and explain the underlying physical processes.

In the measurements of the condensate atom losses we first adopted the same experimental pulsed sequence which was used for the S-state measurements. The conducted measurements of the condensate losses and aspect ratios for different laser detunings show that there are differences between the S- and D-states, which cannot be explained by the different used two-photon Rabi frequencies. In the measurements of the condensate shape oscillations we found that the pulsing of our red $780\,\mathrm{nm}$ Rydberg excitation laser is the main source for the oscillations, not the excitation of Rydberg atoms in the condensate. Therefore we changed our experimental sequence and introduced an adiabatic ramp for the red laser. By finding the optimal parameters for the ramping length and red excitation laser power we managed to minimize the oscillation signal coming from the red laser and showed that we can bring the condensate into motion by the excitation of Rydberg atoms. We confirmed the generation of slow quadrupole shape oscillations, but did not find an explanation for the different oscillation amplitudes of the S-state compared to the two D-state measurements yet. We also repeated the condensate atom loss and aspect ratio measurements with the new sequence and a constant two-photon Rabi frequency and found profound differences between the $106D_{5/2}, m_L = 2$ state and the $110S$ and $106D_{5/2}, m_L = 0$ states, which could not be explained so far. Especially the different shape of the loss curve is puzzling. Reasons for all these different behaviors might be state changing collisions of the Rydberg atoms [94, 186], three body recombination processes [187, 188, 189, 190] or the different angular dependance of the electron wavefunctions. Further measurements need to be conducted and theoretical work is necessary to explain these findings and understand the underlying physical processes.

In cooperation with K. Rzążewski and coworkers we developed a stochastic model, based on the evolution of the Gross-Pitaevskii equation, which could very well simulate the data of our S-state Rydberg excitation measurements in the BEC conducted previously [10]. So far the work on the D-state simulations has just begun, but first preliminary results were not as promising as excepted. Furthermore, the more interesting adiabatic ramping sequence needs to be implemented in the simulations which could give us further insight into the shape oscillation measurements.

To summarize, the work in this thesis showed the existence of D-state Rydberg molecules, which we can selectively excite and assign to specific rovibrational states. Furthermore we were able to change the properties of these molecules concerning their energy landscapes and binding energies by applying an electric field. This opens up new interesting prospects like the creation of molecules with a permanent dipole moment by mixing different electron orbits of S- and high-l states (see section 11.3 in the outlook). The study in the dense condensate for the D-state Rydberg atoms showed various, so far unexplained features with respect to the differences in atom losses in the condensate and shape oscillation amplitudes between S- and D-states. Further measurements and simulations using the stochastic model presented in this thesis are already underway and promise a deeper understanding, revealing the underlying physical processes.

11 Outlook

In the next sections several ideas about future projects and investigations that could be realized without substantial changes in our current experimental setup. The experimental realization of some of them are already underway, others are planned to do and some of them are projects for the future.

11.1 Electron orbital imaging

The goal of this idea is to image the orbital of a single electron by its imprint into the condensate. Due to the electron−atom scattering the density of the condensate is modulated in such a way that for specific experimental parameters, the observation of textbook-like electron orbital in-situ images lies within reach. In section 3.3 we have introduced a theoretical model which describes the consecutive excitation of Rydberg atoms in a condensate and their influence on the evolution of the condensate wavefunction and density. It was also shown that for the S-state Rydberg atoms, the experimental data of the atom losses in a BEC, the line width and the FWHM could be surprisingly well reproduced. After this successful utilization of the model we simulated the effect of one single Rydberg excitation on the BEC. There are several crucial issues which need to be taken into consideration in order to choose the ideal parameters which offer the best achievable image contrast of the electron orbit as an imprint into the condensate. These are the quantum number of the Rydberg state (size, potential depth, lifetime), the density of the BEC (size, lifetime, atom number fluctuations), the trap frequencies (size, aspect ratio), the time when the image is taken and the imaging resolution. First of all the excitation laser beam needs to be tightly focused on the BEC, so that the region where the excitation takes place is well defined and not at the edge of the condensate. Furthermore the quantum number of the Rydberg state n should be high enough so that the structure of

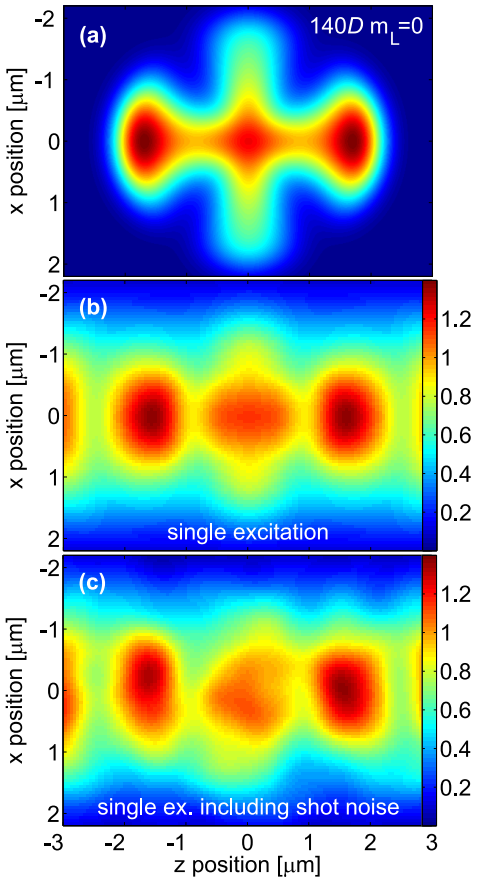

Figure 11.1: (a): Calculated orbital for the $140D, m_L = 0$ Rydberg electron convolved with a finite imaging resolution of $1\,\mu\mathrm{m}$ ($1/e^2$ width of the point spread function). (b) and (c): Simulation of the density change of a single Rydberg excitation without (b) and with (c) atom number shot noise. This figure was taken from [118].

the Rydberg atom is larger than the imaging resolution, but not too high so that the scattering potential between the electron and ground state atom is large enough to have an impact on the BEC atoms. The upper limit for the condensate density is given by the lifetime of the Rydberg atoms, which decreases for increasing density and thus reduces the time of interaction with the BEC atoms. On the other side a too small density results in higher atom number fluctuations and a smaller signal. Therefore an intermediate value of around $10^{14}\,\mathrm{cm}^{-3}$ is ideal. For choosing the trap frequencies one has to consider that the size of the condensate along the imaging direction should match the size of the Rydberg atom orbital. If the condensate is bigger in this direction, we would sum over a large region where the Rydberg atom does not affect the condensate density. This would result in a worse contrast for the imprint of the wavefunction and thus should be avoided. Another important issue is the time when the image is taken. This time should be fixed to the point where the contrast of the density change due to the imprint of the Rydberg orbital is maximum. Thus one has to wait until the BEC atoms react to the new potential, increasing the contrast of the imprint. Waiting for a too long time should be avoided since the structure begins to wash out at some point. There are various experimental techniques for imaging available, like dark ground imaging [123] or phase contrast imaging [191, 192] which can take non-destructive in-situ images of Bose Einstein condensate.

In Figure 11.1 we present the simulation for one set of parameters. It shows the $140D$, $m_L = 0$ state for a BEC atom number of $N = 50000$ and trap frequencies of $\omega_z = 2\pi \cdot 10\,\mathrm{Hz}$ in axial and $\omega_r = 2\pi \cdot 200\,\mathrm{Hz}$ in radial direction. A peak density of $10^{14}\,\mathrm{cm}^{-3}$ was assumed as well as an imaging resolution of $1\,\mu\mathrm{m}$. The simulated interaction time of the single Rydberg atom is $30\,\mu\mathrm{s}$, which should be observed every twentieth shot if we assume an exponential decay with an average lifetime of around $10\,\mu\mathrm{s}$. In Figure 11.1(a) the pure electron orbit of this Rydberg state is depicted, whereas in (b) the finite imaging resolution was taken into account and additional atom number shot noise in (c). Despite the atom number shot noise the electron orbit is still clearly visible in (c), which makes this whole idea of the electron orbital imaging a very promising candidate for realization. More details about this proposal can be found in the our recent paper [118] and its supplementary material.

11.2 Cold ion impurity and circular states

This idea came to our mind when we were realizing that for the $202S$ state, the radius of the excited Rydberg atom is nearly the same as the radial size of our condensate. We asked ourselves what would happen if we remove the Rydberg electron completely from the Bose-Einstein condensate. We would be left with an interesting system: one single ion trapped in a Bose-Einstein condensate. This ion can interact with many ground state atoms forming a so-called polaron quasi-particle. Generally the concept of the polaron is mainly used in solid state physics to describe interactions of electrons and ions in metals resulting in a bound state, lowering the energy compared to a non-interacting system. These particles play an important for the transition temperature in high temperature superconductors and for the colossal magnetoresistance in manganites [193, 194]. There are proposals which predict that with an ionic impurity in a BEC the strong coupling regime can be reached, which so far could not be accessed in solid state physics [195]. In this regime the ion impurity distorts the density of the surrounding BEC and thereby creates a self-trapping potential leading to its

localization [196, 197]. Via a standard time of flight measurement this impurity self-trapping results in a faster and further expansion in contrast to the not self-bound case.

Current experiments, realizing the ion impurity in a condensate by ion traps [103, 104] are limited by the residual micromotion of the ion in the trap [105]. This prevents them from reaching the regime of s-wave scattering, which is required for this self-trapping mechanism of the ion. In our case we excite one atom from the condensate directly into the Rydberg state where the inner shell electrons screen the ionic charge preventing it to be affected by electric fields. We therefore do not need a sophisticated trapping technique for the ion, but have to bring the Rydberg electron out of the condensate to realize the single ion−BEC entity. Otherwise the interaction is dominated by the electron−ground state interaction, as shown in this thesis. To transfer the Rydberg electron out of the BEC we could create a so-called circular state for which the Rydberg electron reaches its maximal orbital angular momentum, moving on a Bohr-like circular orbit [198, 199]. These circular states have long radiative lifetimes, a small Stark effect and large magnetic moments. Due to these advantages, they are used in cavity quantum electrodynamics [200] and in metrology [201, 202]. For a sufficiently high enough quantum number n the Rydberg electron will be located in the thermal cloud and not in the BEC any more. Since circular states cannot be directly populated from the ground state by laser excitation because only one unit of angular momentum can be transferred per photon, one first needs to excite a Rydberg atom into a S or D state in our case. After that the Rydberg electron needs to be transferred to these high-l states. There are four prominent ways to execute this: the first one is a microwave adiabatic transfer in which the electron absorbs microwave photons while an electric field is adiabatically decreased [198]. In the second method the Rydberg atom is excited in a circularly polarized microwave field which is then turned off adiabatically [203] and the third one uses an electric field ramp in a crossed electric and magnetic field configuration [199]. The last method relies on a carefully tailored series of short electric field or laser pulses, whose timings are short compared to the classical electron orbital period, to increase the angular momentum of the electron with each pulse until we end up with a circular state [204]. A review of the advantages and disadvantages of each method would go beyond the scope of this outlook. The method, which will finally be realized in the experiment is still under discussion.

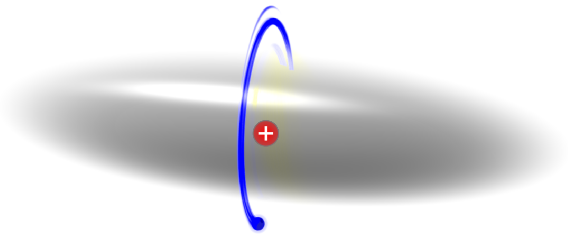

Figure 11.2: Schematic view of the circular state consisting of the Rydberg core (red) in the middle of the Bose-Einstein condensate and the Rydberg electron (blue) orbiting the condensate, interacting with the thermal cloud surrounding the BEC. This figure was taken from [11].

11.3 Rydberg molecules at the crossing of high-*l* states

This idea is directly linked to the measurements of the molecular states at the crossing between the two different $42D, m_J = 1/2$ and $m_J = 5/2$ atomic states we conducted in section 8.3. In vicinity of this crossing we managed to create a mixture between two different electronic wavefunctions which gave rise to a new potential landscape, enabling the creation of molecules with a different symmetry compared to the molecules formed in the unperturbed bare electronic wavefunctions of the $m_J = 1/2$ and $m_J = 5/2$ states. An intriguing prospect would be to use a symmetry breaking to form molecules with an extraordinary high dipole moment. This could be achieved by exciting molecular states at an $\mathcal{E}$-field induced crossing between a S-state and higher l-states ($l \geq 3$). Since these high-l states cannot be excited directly in a zero field environment by our two-photon laser excitation scheme, the crossing would play a crucial role again. Due to the intermixing of the wavefunctions, the spherical symmetric S-state is coupled to a high-l state which has its highest electron density far away from its center, generating an asymmetry and thus a large permanent dipole moment for the created molecules. In Figure 11.3 we show a Stark map in the vicinity of the $43S$ state (as an example), which crosses the high-l manifold of $n = 40$. The first crossing is at around $\mathcal{E} = 4.7\,\mathrm{V/cm}$.

Recording a high resolution Stark map at such a crossing would enable us to observe a bunch of different molecular states created by the mixing of the electronic wavefunctions of the S-state with different high-l states. Since this kind of measurement requires no change in the current setup, this idea could be realized straightforward in the experiment in the not so far future. Only the principal quantum number n has still to be chosen carefully. On the one hand it should not be too high so that molecular lines can still be resolved and the permanent dipole moment, which scales with $1/n^{\star 2}$ [8, 13], has still a large value. On the other hand for a too low n, the electric field needed to reach the crossing is much higher due to the smaller polarizability ($\propto n^{\star 7}$) of the

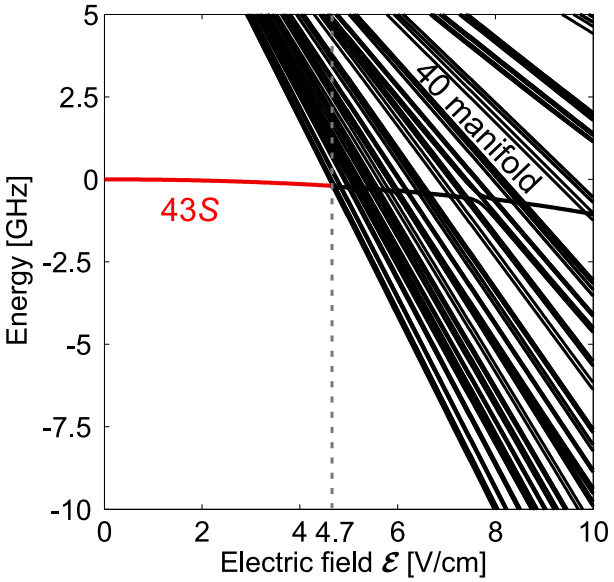

Figure 11.3: Stark map of the $43S$ state (red) crossing the high-l state manifold (black). The first crossing happens at an electric field $\mathcal{E}$ of 4.7 V/cm between the $43S$ state and a state consisting of a mixture of high-l states ($l > 2$) of the $n = 40$ manifold.

Rydberg atom. This can lead to a larger broadening of the molecular lines, as observed in [8] for the diatomic $35S$ ground state molecule. Moreover the B-field should be chosen as high as possible ($B = 13.55\,\mathrm{G}$) to split the m_J levels of the high-l states so that the different orbitals can be separated like for the D-state measurements in chapter 8. Due to the many nearby crossings it will be a challenge to assign all the different peaks in the spectra to a certain orbit and theory calculations and models will be needed to explain the findings. From the incline of the molecular lines in a recorded Stark map values for the permanent dipole moments can be extracted, subtracting the quadratic Stark effect beforehand.

If the B-field is reduced to the minimum, the high-l manifold becomes even more degenerate and the states intermix to a large extent. By coupling to the degenerate high-l state manifold we create so-called trilobite molecules, because of their excitation probability resembling the shape of a trilobite fossil, which have been predicted by C. Greene and coworkers [13]. They possess large electric dipole moments of several hundreds of Debye although consisting only of homonuclear atoms. For high principal quantum numbers n the trilobite molecules have not been observed experimentally, yet.

Appendix

A Appendix: Theory

In this chapter additional theory calculations and results are presented. In the first section A.1 we show how the rovibrational Hamiltonian used in the theory section 2.3 was calculated. The additionally computed binding energies of the toroidal and axial D-state molecules are listed in the second section of this appendix A.2.

A.1 Calculation of the rovibrational Hamiltonian

In this section we show how to derive equation (2.18) from the theory section 2.3. Throughout this section atomic units are used. To simplify the rovibrational Hamiltonian from equation (2.13)

$$\underbrace{\left(\frac{\vec{P}^2}{M} + \epsilon_{n,m_J}(\vec{R})\right)}_{H_{\text{rv}}} \phi_{\kappa u}^{(n,m_J)}(\vec{R}) = E_{\kappa u}^{(n,m_J)} \phi_{\kappa u}^{(n,m_J)}(\vec{R}), \tag{A.1}$$

we use the ansatz (2.17)

$$\phi_{\kappa u}^{(n,m_J)}(\vec{R}) := \frac{F_{\kappa u}^{(n,m_J)}(\rho, z)}{\sqrt{2\pi\rho}} \mathrm{e}^{iu\varphi}, \quad u \in \mathbb{Z},\ \kappa \in \mathbb{N}_0. \tag{A.2}$$

Here $\vec{P} = -i\vec{\nabla}$ is the momentum and M the mass of the ground state atom. The energies ϵ_{n,m_J} are the potential energy surfaces obtained by solving the electronic Hamiltonian equation (2.12). κ is the rovibrational excitation number of the molecular binding energies $E_{\kappa u}^{(n,m_J)} = E_B^{(\kappa)}$ and $F_{\kappa u}^{(n,m_J)}(\rho, z)$ the corresponding molecular wavefunctions. Furthermore we use cylindrical coordinates $\vec{R} = (\rho, \varphi, z)$ to simplify the calculation of the molecular binding energies since the APES are rotationally symmetric along the z-axis. Inserting the ansatz (A.2) into equation (A.1) yields

$$\left(-\frac{\vec{\nabla}^2}{M} + \epsilon_{n,m_J}(\vec{R})\right) \frac{F_{\kappa u}^{(n,m_J)}(\rho, z)}{\sqrt{2\pi\rho}} \mathrm{e}^{iu\varphi} = E_{\kappa u}^{(n,m_J)} \frac{F_{\kappa u}^{(n,m_J)}(\rho, z)}{\sqrt{2\pi\rho}} \mathrm{e}^{iu\varphi}. \tag{A.3}$$

Writing the Laplace operator in cylindrical coordinates

$$\vec{\nabla}^2 f = \Delta f = \frac{1}{\rho}\partial_\rho(\rho\,\partial_\rho f) + \frac{1}{\rho^2}\partial_\varphi^2 f + \partial_z^2 f = \frac{1}{\rho}\partial_\rho f + \partial_\rho^2 f + \frac{1}{\rho^2}\partial_\varphi^2 f + \partial_z^2 f \tag{A.4}$$

we can rewrite the left side of equation (A.3) as

$$\left(-\frac{1}{M}\left[\frac{1}{\rho}\partial_\rho + \partial_\rho^2 + \frac{1}{\rho^2}\partial_\varphi^2 + \partial_z^2\right] + \epsilon_{n,m_J}(\vec{R})\right)\frac{F_{\kappa u}^{(n,m_J)}(\rho,z)}{\sqrt{2\pi\rho}}\mathrm{e}^{iu\varphi}. \tag{A.5}$$

This equation can now be simplified to:

$$\begin{aligned}
&\frac{\mathrm{e}^{iu\varphi}}{\sqrt{2\pi}}\Bigg(-\frac{\partial_\rho F_{\kappa u}^{(n,m_J)}(\rho,z)}{M\rho^{3/2}} + \frac{F_{\kappa u}^{(n,m_J)}(\rho,z)}{2M\rho^{5/2}} - \frac{\partial_\rho^2 F_{\kappa u}^{(n,m_J)}(\rho,z)}{M\rho^{1/2}} + \frac{\partial_\rho F_{\kappa u}^{(n,m_J)}(\rho,z)}{M\rho^{3/2}} - \\
&- \frac{3}{4}\frac{F_{\kappa u}^{(n,m_J)}(\rho,z)}{M\rho^{5/2}} + \frac{F_{\kappa u}^{(n,m_J)}(\rho,z)}{M\rho^{5/2}}u^2 - \frac{\partial_z^2 F_{\kappa u}^{(n,m_J)}(\rho,z)}{M\rho^{1/2}} + \epsilon_{n,m_J}(\vec{R})\frac{F_{\kappa u}^{(n,m_J)}(\rho,z)}{\rho^{1/2}}\Bigg) = \\
&= \frac{\mathrm{e}^{iu\varphi}}{\sqrt{2\pi\rho}}\left(-\frac{\partial_\rho^2 + \partial_z^2}{M} + \frac{u^2+\frac{1}{4}}{M\rho^2} + \epsilon_{n,m_J}(\vec{R})\right)F_{\kappa u}^{(n,m_J)}(\rho,z).
\end{aligned} \tag{A.6}$$

This leaves use with complete Hamiltonian equation:

$$\left(-\frac{\partial_\rho^2 + \partial_z^2}{M} + \frac{u^2+\frac{1}{4}}{M\rho^2} + \epsilon_{n,m_J}(\vec{R})\right)F_{\kappa u}^{(n,m_J)}(\rho,z) = E_{\kappa u}^{(n,m_J)}F_{\kappa u}^{(n,m_J)}(\rho,z). \tag{A.7}$$

We now derived equation (2.18) from theory section 2.3.

A.2 Calculated $D_{5/2}$ state molecular binding energies for $n = 41, 43, 44, 46, 49, 50$

In this section the calculated absolute binding energies for the states $n = 41, 43, 44, 46, 49, 50$ are presented in the following Tables, including the higher excited rovibrational states $\kappa > 0$. Note that for the principal quantum numbers $n = 41$ and 49 only the binding energies of the $m_J = 5/2$ states were calculated, since only these were measured in the experiment.

$41D_{5/2}$	$m_J = 5/2$ Toroidal states
κ	$\lvert E_B^{(\kappa)}\rvert$[MHz]
0	8.02
1	7.24
2	6.50
3	5.81
4	5.18
5	4.55
6	4.27
7	4.09
8	3.65
9	3.30

Table A.1: Absolute binding energies of the $41D_{5/2}$ state, calculated by a finite element method.

$43D_{5/2}$	$m_J = 1/2$ Axial states	$m_J = 1/2$ Toroidal states	$m_J = 5/2$ Toroidal states
κ	$\lvert E_B^{(\kappa)}\rvert$[MHz]	$\lvert E_B^{(\kappa)}\rvert$[MHz]	$\lvert E_B^{(\kappa)}\rvert$[MHz]
0	12.48	2.77	6.40
1	11.40	2.35	5.70
2	10.32	1.97	5.14
3	9.25	1.62	4.60
4	8.18	1.30	4.13
5	7.14	0.98	3.55
6	6.12		3.34
7	5.95		2.90
8	5.66		2.40
9	5.13		2.34
10	5.09		
11	4.95		
12	4.61		
13	4.19		
14	4.19		
15	4.02		
16	3.97		
17	3.59		
18	3.30		
19	3.30		
20	3.09		

Table A.2: Binding energies (absolute values) of the $43D_{5/2}$ state, calculated by a finite element method. The dark red color indicates for which binding energies the numerical calculation did not converge nicely and thus these values have to be treated with caution (more details in section 2.3).

$44D_{5/2}$	$m_J = 1/2$ Axial states	$m_J = 1/2$ Toroidal states	$m_J = 5/2$ Toroidal states
κ	$\lvert E_B^{(\kappa)}\rvert$[MHz]	$\lvert E_B^{(\kappa)}\rvert$[MHz]	$\lvert E_B^{(\kappa)}\rvert$[MHz]
0	10.82	2.32	5.56
1	9.85	1.96	5.04
2	8.87	1.62	4.55
3	7.91	1.31	4.08
4	6.96	1.01	3.63
5	6.03	0.69	3.21
6	5.29		2.99
7	5.12		2.82
8	4.97		2.52
9	4.32		2.50
10	4.26		
11	4.25		
12	4.04		
13	3.73		
14	3.48		
15	3.42		
16	3.35		
17	3.08		
18	2.86		
19	2.66		
20	3.65		

Table A.3: Absolute binding energies of the $44D_{5/2}$ state, calculated by a finite element method. The dark red color indicates for which binding energies the numerical calculation did not converge nicely and thus these values have to be treated with caution (more details in section 2.3).

$46D_{5/2}$	$m_J = 1/2$ Axial states	$m_J = 1/2$ Toroidal states	$m_J = 5/2$ Toroidal states
κ	$\lvert E_B^{(\kappa)}\rvert$[MHz]	$\lvert E_B^{(\kappa)}\rvert$[MHz]	$\lvert E_B^{(\kappa)}\rvert$[MHz]
0	8.21	1.65	4.34
1	7.40	1.37	3.94
2	6.61	1.10	3.55
3	5.82	0.82	3.18
4	5.06	0.53	2.83
5	4.31	0.22	2.50
6	3.85		2.22
7	3.63		2.19
8	3.61		1.89
9	3.11		1.88
10	2.99		
11	2.92		
12	2.84		
13	2.56		
14	2.44		
15	2.29		
16	2.28		
17	2.08		
18	1.89		
19	1.79		
20	1.71		

Table A.4: Absolute binding energies of the $46D_{5/2}$ state, calculated by a finite element method. The dark red color indicates for which binding energies the numerical calculation did not converge nicely and thus these values have to be treated with caution (more details in section 2.3).

$49D_{5/2}$	$m_J = 5/2$ Toroidal states
κ	$\lvert E_B^{(\kappa)}\rvert$[MHz]
0	3.00
1	2.72
2	2.45
3	2.19
4	1.94
5	1.70
6	1.45
7	1.48
8	1.26
9	1.25

Table A.5: Binding energies (absolute values) of the $49D_{5/2}$ state, calculated by a finite element method.

$50D_{5/2}$	$m_J = 1/2$ Axial states	$m_J = 1/2$ Toroidal states	$m_J = 5/2$ Toroidal states
κ	$\lvert E_B^{(\kappa)}\rvert$[MHz]	$\lvert E_B^{(\kappa)}\rvert$[MHz]	$\lvert E_B^{(\kappa)}\rvert$[MHz]
0	4.86	0.89	2.65
1	4.31	0.72	2.40
2	3.77	0.56	2.16
3	3.25	0.38	1.92
4	2.74	0.20	1.70
5	2.27	0.02	1.49
6	2.24		1.34
7	2.10		1.29
8	1.81		1.12
9	1.75		1.10
10	1.64		
11	1.56		
12	1.40		
13	1.32		
14	1.24		
15	1.15		
16	1.05		
17	1.03		
18	0.92		
19	0.83		
20	0.81		

Table A.6: Absolute binding energies of the $50D_{5/2}$ state, calculated by a finite element method. The dark red color indicates for which binding energies the numerical calculation did not converge nicely and thus these values have to be treated with caution (more details in section 2.3).

B Appendix: Experiment

In this chapter additional experimental data and evaluations are presented, which are not essential for the understanding of chapter 9, but provide some extra details. In section B.1 the measurements of the saturation curves are presented, which were needed to determine the power of the red $780\,\mathrm{nm}$ laser and the associated effective resonant two-photon Rabi frequency (1.24). These state-dependent Rabi frequencies are summarized in Table 9.1 and were used for all measurements with the pulsed excitation sequence described in section 9.2. In the second section B.2 we show measurements in which we changed the number of pulses in order to get a better understanding of the saturation behavior and the scattering at the intermediate level.

B.1 Saturation curve measurements

In this section we present the measurements of the saturation curves for the pulsed BEC excitation sequence (see Figure 6.1(b) and section 6.2) to determine the power of the red laser and the associated effective resonant two-photon Rabi frequency (1.24), so that it is as high as possible without loosing too many atoms due to spontaneous scattering of photons at the intermediate state [205]. In Figure B.1 the relative atom losses in the BEC for different pulse areas of the red laser with the wavelength $780\,\mathrm{nm}$ are shown. The relative BEC atom losses for the states $110S$, $106D_{5/2}, m_L = 0$ and $m_L = 2$ are depicted in Figure B.1(a) whereas in (b) the states $182S$, $180D_{5/2}, m_L = 0$ and $m_L = 2$ are displayed. In these plots the onset of the saturation is indicated by blue circles. At these positions the scattering at the intermediate state, which scales as $\propto \Omega_r^2$ (5.1), starts to get relevant. Since the effective resonant Rabi frequency scales only with $\propto \Omega_r$ (1.24), this scattering process starts to dominate for large pulse areas, leading to a heating of the condensate and to more atom losses. Therefore the density of the condensate decreases and due to the density dependent line shift (9.1) we are not anymore at the detuning with the maximum losses. Thus the relative BEC number increases for high pulse areas. The ideal positions are the blue marked pulse areas where the effective resonant Rabi frequency is the highest before the scattering process becomes a problem. These values of the red laser power were used for the pulsed measurements described in section 9.2.

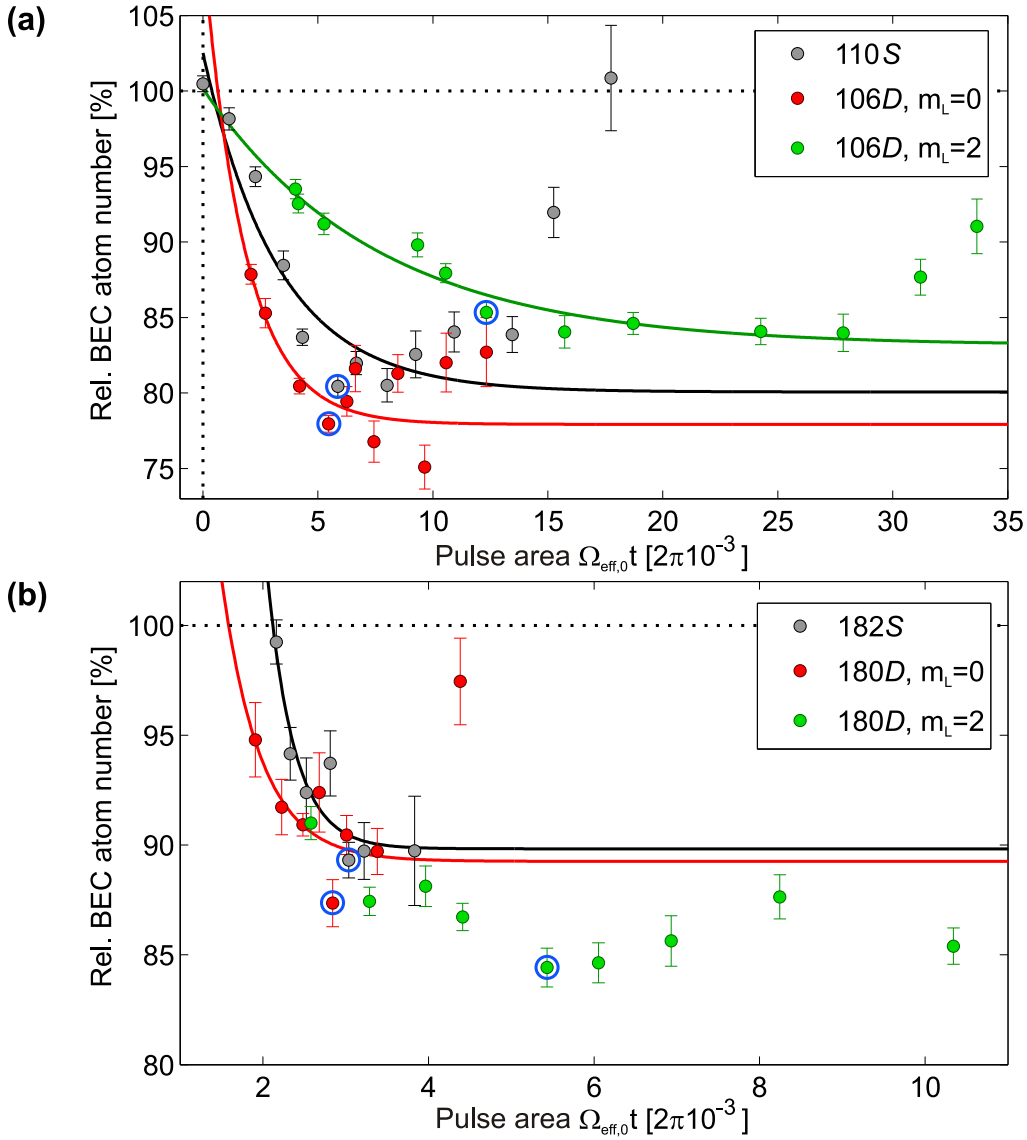

Figure B.1: Saturation curves for the states $110S$ (gray), $106D, m_L = 0$ (red), $m_L = 2$ (green) in (a) and $182S$ (gray), $180D, m_L = 0$ (red), $m_L = 2$ (green) in (b), for which the relative BEC number (in percent) is plotted against the pulse area $\Omega_{\text{eff},0}t$ (1.24). For the higher states 500 red laser excitation pulses were used whereas for the lower states 300 pulses were sufficient to observe significant losses in the BEC atom number. The blue circles mark the chosen pulse areas for the measurements in section 9.2. At these values the losses due to scattering at the intermediate level start to affect the measurements. Exponential curves are fitted to the data to show the saturation effect. The error bar for each data point was determined from 20 independent measurements.

B.2 BEC atom losses and change of aspect ratio measurements with a different number of excitation pulses

The measurements in this section were conducted in order to study the dependency of the atom number losses in the BEC and aspect ratio on the number of excitation pulses and the total

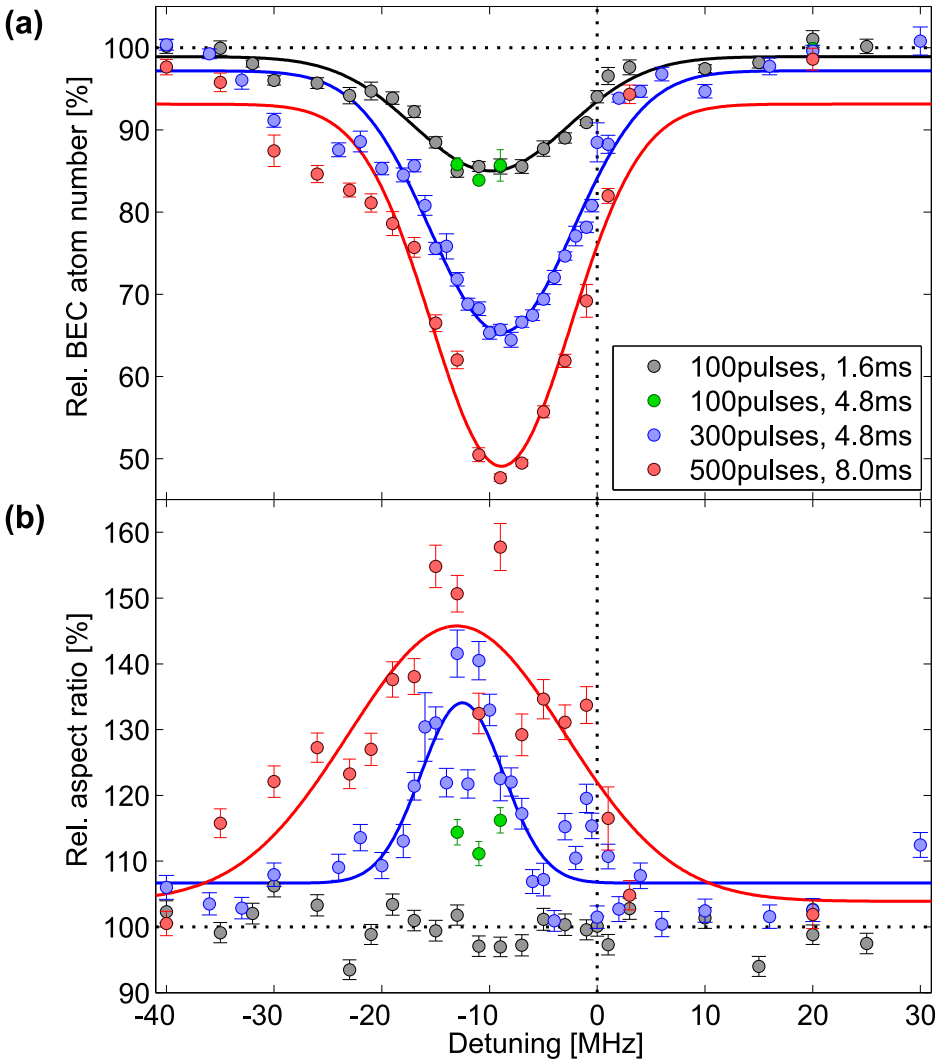

Figure B.2: Measurement of the relative BEC atom number (a) and the change of aspect ratio (b) for different laser detunings and red laser pulses for the $106D_{5/2}, m_L = 2$ state. In this measurement 100 (gray), 100 (green), 300 (blue) and 500 (red) pulses were shone onto the BEC with total excitation times of 1.6, 4.8, 4.8 and 8 ms, respectively. The green data points were taken to verify that an additional wait time does not change the BEC atom losses, but only changes the value for the aspect ratio. The zero position was determined as the position of the Rydberg line in a spectrum measured in a thermal cloud. Furthermore Gaussian functions were fitted to the data points and the error bars (standard deviation) were determined by 20 independent measurements.

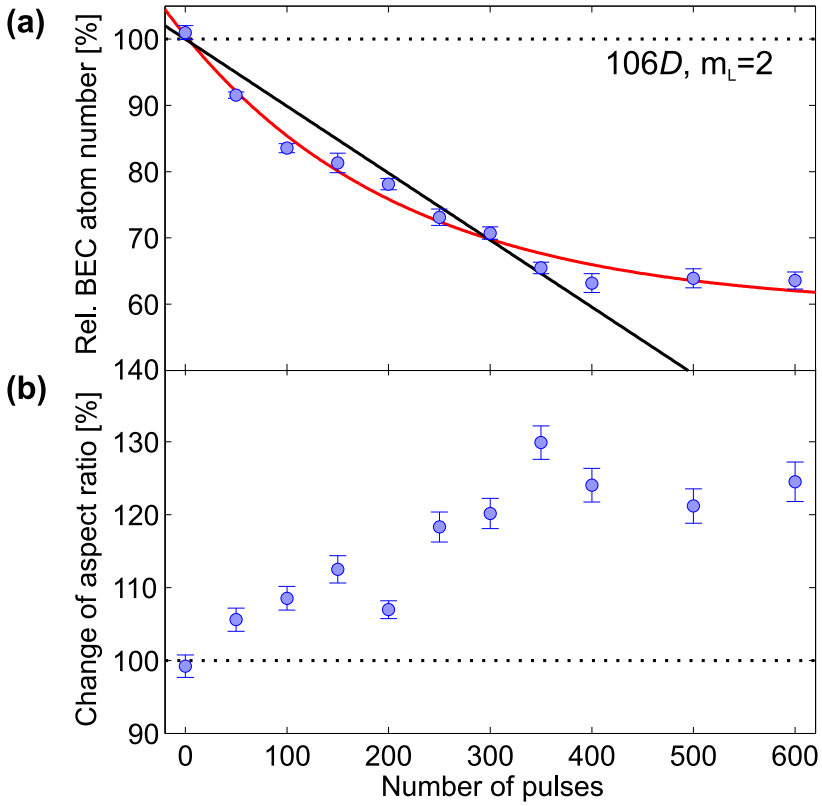

Figure B.3: Relative BEC atom number (a) and change of aspect ratio (b) for a time of flight imaging measurement for the $106D_{5/2}, m_L = 2$ state for a different number of red laser excitation pulses. The detuning of the blue laser was fixed at $-13\,\mathrm{MHz}$. A delay time of $34.5\,\mathrm{ms}$ was introduced before the TOF to be at the oscillation position where the condensate extends to its maximum radial size. An exponential curve (red) was fitted to the relative BEC atom number in (a) to show the deviation from a linear fit (black).

excitation time. In Figure B.2 the relative BEC atom numbers (a) and the relative aspect ratios (b) are depicted for the $106D_{5/2}, m_L = 2$ state. The aspect ratio is defined as the quotient of radial and axial radius of the condensate after the time of flight imaging $\epsilon = r_r/r_z$. The excitation sequence is depicted in Figure 6.1(b) with a $16\,\mu\mathrm{s}$ time between successive red laser pulses. Thus for the measurement with 100 (gray), 300 (blue) and 500 (red) pulses we get a total time for the excitation pulses of 1.6, 4.8 and $8\,\mathrm{ms}$. As the number of pulses is increased the relative BEC atom number is decreased (Figure B.2(a)) whereas the relative aspect ratio is raised (Figure B.2(b)). If we now use 100 pulses for the Rydberg excitation but introduce an additional wait time so that the total time adds up to $4.8\,\mathrm{ms}$ (three green data points), we observe within the error bars exactly the same atom losses as for the $1.6\,\mathrm{ms}$ excitation measurement (gray points). Thus an additional short wait time does not lead to more losses, but to a change in the aspect ratio in Figure B.2(b), since we probe the atoms at a different oscillation period (see subsection 9.2.3).

Another knob which we can use to tune the atom losses is the number of excitation pulses. In Figure B.3 this parameter was varied and the relative BEC atom losses (a) as well as the change of aspect ratio (b) were measured for the $106D_{5/2}, m_L = 2$ state at a blue laser detuning of $-13\,\mathrm{MHz}$. The two-photon Rabi frequency of $12.4\,\mathrm{kHz}$ was fixed by the red laser power

determined from the saturation curve measurement (see the previous section B.1). A delay time of $34.5\,\mathrm{ms}$ before the TOF was introduced to be at the second maximum position where the condensate is extended to its maximum in radial direction. Thus the aspect ratio is maximized at this position. Note that the radial axis becomes the elongated one after the TOF, due to momentum inversion (see theory section 3.2 for details). In Figure B.3(a) we can see a slight deviation from a linear drop of the relative BEC atom number until saturation sets in when the number of pulses reaches around 350. The reason for this small deviation could be the scattering of photons at the intermediate level. If we would rescale the x-axis to pulse area we get a similar curve as the green data points in Figure B.1(a). The aspect ratio also shows this saturation behavior.

Bibliography

[1] A. Einstein, *Über die Entwicklung unserer Anschauungen über das Wesen und die Konstitution der Strahlung*, Physik Journal, **25**, 386–391 (1969).

[2] M. H. Anderson, J. R. Ensher, M. R. Matthews, C. E. Wieman and E. A. Cornell, *Observation of Bose-Einstein condensation in a Dilute Atomic Vapor*, Science, **269**, 198–201 (1995).

[3] K. B. Davis, M. O. Mewes, M. R. Andrews, N. J. van Druten, D. S. Durfee, D. M. Kurn and W. Ketterle, *Bose-Einstein Condensation in a Gas of Sodium Atoms*, Phys. Rev. Lett., **75**, 3969–3973 (1995).

[4] M. J. Seaton, *Quantum defect theory*, Rep. Prog. Phys., **46**, 167 (1983).

[5] S. Haroche, *Nobel Lecture: Controlling photons in a box and exploring the quantum to classical boundary*, Rev. Mod. Phys., **85**, 1083–1102 (2013).

[6] V. Bendkowsky, B. Butscher, J. Nipper, J. P. Shaffer, R. Löw and T. Pfau, *Observation of ultralong-range Rydberg molecules*, Nature, **458**, 1005–1008 (2009).

[7] B. Butscher, J. Nipper, J. B. Balewski, L. Kukota, V. Bendkowsky, R. Löw and T. Pfau, *Atom-molecule coherence for ultralong-range Rydberg dimers*, Nat. Phys., **9**, 970–974 (2010).

[8] W. Li, T. Pohl, J. M. Rost, S. T. Rittenhouse, H. R. Sadeghpour, J. Nipper, B. Butscher, J. B. Balewski, V. Bendkowsky, R. Löw and T. Pfau, *A Homonuclear Molecule with a Permanent Electric Dipole Moment*, Science, **334**, 1110–1114 (2011).

[9] A. Gaj, A. T. Krupp, J. B. Balewski, R. Löw, S. Hofferberth and T. Pfau, *From molecular spectra to a density shift in dense Rydberg gases*, Nat. Commun., **5** (2014).

[10] J. B. Balewski, A. T. Krupp, A. Gaj, D. Peter, H. P. Büchler, R. Löw, S. Hofferberth and T. Pfau, *Coupling a single electron to a Bose-Einstein condensate*, Nature, **502**, 664–667 (2013).

[11] J. B. Balewski, *A single electron in a Bose-Einstein condensate*, Ph.D. thesis, Universität Stuttgart (2014).

[12] E. Fermi, *Sopra lo Spostamento per Pressione delle Righe Elevate delle Serie Spettrali*, Il Nuovo Cimento, **11**, 157–166 (1934).

[13] C. H. Greene, A. S. Dickinson and H. R. Sadeghpour, *Creation of Polar and Nonpolar Ultra-Long-Range Rydberg Molecules*, Phys. Rev. Lett., **85**, 2458–2461 (2000).

[14] T. Hänsch and A. Schawlow, *Cooling of gases by laser radiation*, Opt. Commun., **13**, 68 – 69 (1975).

[15] D. Wineland and H. Dehmelt, *Proposed* $10^{14}\ \partial\nu/\nu$ *laser fluorescence spectroscopy on* Tl^{+} *mono-ion oscillator III (sideband cooling)*, Bull. Am. Phys. Soc., **20** (1975).

[16] E. L. Raab, M. Prentiss, A. Cable, S. Chu and D. E. Pritchard, *Trapping of Neutral Sodium Atoms with Radiation Pressure*, Phys. Rev. Lett., **59**, 2631–2634 (1987).

[17] C. Adams and E. Riis, *Laser cooling and trapping of neutral atoms*, Prog. Quant. Electr., **21**, 1 – 79 (1997).

[18] S. Chu, *Nobel Lecture: The manipulation of neutral particles*, Rev. Mod. Phys., **70**, 685–706 (1998).

[19] C. N. Cohen-Tannoudji, *Nobel Lecture: Manipulating atoms with photons*, Rev. Mod. Phys., **70**, 707–719 (1998).

[20] W. D. Phillips, *Nobel Lecture: Laser cooling and trapping of neutral atoms*, Rev. Mod. Phys., **70**, 721–741 (1998).

[21] H. Deng, H. Haug and Y. Yamamoto, *Exciton-polariton Bose-Einstein condensation*, Rev. Mod. Phys., **82**, 1489–1537 (2010).

[22] M. Richard, J. Kasprzak, A. Baas, S. Kundermann, K. Lagoudakis, M. Wouters, I. Carusotto, R. André, B. Deveaud-Plédran and L. Dang, *Exciton-polariton Bose-Einstein condensation: advances and issues*, Int. J. Nanotechnology, **7**, 668–685 (2010).

[23] J. P. Eisenstein and A. H. MacDonald, *Bose-Einstein condensation of excitons in bilayer electron systems*, Nature, **432**, 0028–0836 (2004).

[24] J. Klaers, J. Schmitt, F. Vewinger and M. Weitz, *Bose-Einstein condensation of photons in an optical microcavity*, Nature, **468**, 545–548 (2010).

[25] K. Avetissian, H. K. Avetissian, A. and F. Mkrtchian, G. *Self-Amplified Gamma-Ray Laser on Positronium Atoms from a Bose-Einstein Condensate*, Phys. Rev. Lett., **113**, 023904 (2014).

[26] S. Burger, K. Bongs, S. Dettmer, W. Ertmer, K. Sengstock, A. Sanpera, G. V. Shlyapnikov and M. Lewenstein, *Dark Solitons in Bose-Einstein Condensates*, Phys. Rev. Lett., **83**, 5198–5201 (1999).

[27] K. E. Strecker, G. B. Partridge, A. G. Truscott and R. G. Hulet, *Formation and propagation of matter-wave soliton trains*, Nature, **417**, 150–153 (2002).

[28] M. R. Matthews, B. P. Anderson, P. C. Haljan, D. S. Hall, C. E. Wieman and E. A. Cornell, *Vortices in a Bose-Einstein Condensate*, Phys. Rev. Lett., **83**, 2498–2501 (1999).

[29] K. W. Madison, F. Chevy, W. Wohlleben and J. Dalibard, *Vortex Formation in a Stirred Bose-Einstein Condensate*, Phys. Rev. Lett., **84**, 806–809 (2000).

[30] I. Bloch, T. W. Hänsch and T. Esslinger, *Atom Laser with a cw Output Coupler*, Phys. Rev. Lett., **82**, 3008–3011 (1999).

[31] T. F. Gallagher, *Rydberg Atoms*, Cambridge Monographs on Atomic, Molecular, and Chemical Physics, Cambridge University Press, Cambridge (1994).

[32] J. J. Balmer, *Notiz über die Spektrallinien des Wasserstoffs*, Ann. Phys., **25**, 80–87 (1885).

[33] J. R. Rydberg, *On the structure of the line-spectra of the chemical elements*, Phil. Mag. Series 5, **29**, 331–337 (1890).

[34] N. Bohr, *On the Constitution of Atoms and Molecules*, Phil. Mag. Series 6, **26**, 1–25 (1913).

[35] N. Bohr, *Über die Serienspektra der Elemente*, Z. Phys., **2**, 423–469 (1920).

[36] E. Amaldi and E. Segrè, *Effect of Pressure on High Terms of Alkaline Spectra*, Nature, **133**, 141 (1934).

[37] E. Amaldi and E. Segrè, *Effetto della pressione sui termini elevati degli alcalini*, Nuovo Cimento, **11**, 145–156 (1934).

[38] C. Füchtbauer and F. Gössler, *Verschiebung und unsymmetrische Verbreiterung von Absorptionslinien durch Fremdgase*, Naturwissenschaften, **21**, 675–676 (1933).

[39] C. Füchtbauer and F. Gössler, *Verschiebung und unsymmetrische Verbreiterung von Absorptionslinien durch Fremdgase*, Z. Phys., **87**, 89–104 (1934).

[40] C. Füchtbauer, P. Schulz and A. F. Brandt, *Verschiebung von hohen Serienlinien des Natriums und Kaliums durch Fremdgase, Berechnung der Wirkungsquerschnitte von Edelgasen gegen sehr langsame Elektronen*, Z. Phys., **90**, 403–415 (1934).

[41] M. Saffman, T. G. Walker and K. Mølmer, *Quantum information with Rydberg atoms*, Rev. Mod. Phys., **82**, 2313–2363 (2010).

[42] V. Vuletic, *Quantum networks: When superatoms talk photons*, Nat. Phys., **2**, 801–802 (2006).

[43] K. Bergmann, H. Theuer and B. W. Shore, *Coherent population transfer among quantum states of atoms and molecules*, Rev. Mod. Phys., **70**, 1003–1025 (1998).

[44] D. Jaksch, J. I. Cirac, P. Zoller, S. L. Rolston, R. Côté and M. D. Lukin, *Fast Quantum Gates for Neutral Atoms*, Phys. Rev. Lett., **85**, 2208–2211 (2000).

[45] V. Bendkowsky, B. Butscher, J. Nipper, J. B. Balewski, J. P. Shaffer, R. Löw, T. Pfau, W. Li, J. Stanojevic, T. Pohl and J. M. Rost, *Rydberg Trimers and Excited Dimers Bound by Internal Quantum Reflection*, Phys. Rev. Lett., **105**, 163201 (2010).

[46] W. Li, I. Mourachko, M. W. Noel and T. F. Gallagher, *Millimeter-wave spectroscopy of cold Rb Rydberg atoms in a magneto-optical trap: Quantum defects of the ns, np, and nd series*, Phys. Rev. A, **67**, 052502 (2003).

[47] J. Han, Y. Jamil, D. V. L. Norum, P. J. Tanner and T. F. Gallagher, *Rb nf quantum defects from millimeter-wave spectroscopy of cold ^{85}Rb Rydberg atoms*, Phys. Rev. A, **74**, 054502 (2006).

[48] C.-J. Lorenzen and K. Niemax, *Quantum Defects of the $n^2P_{1/2,3/2}$ Levels in ^{39}K I and ^{85}Rb I*, Phys. Scr., **27**, 300 (1983).

[49] W. Ritz, *Magnetische Atomfelder und Serienspektren*, Ann. Phys., **330**, 660–696 (1908).

[50] C. J. Foot, *Atomic Physics*, Oxford Master Series in Atomic, Optical and Laser Physics, Oxford University Press, Cambridge (2005).

[51] I. Bloch, *Licht-Atom Wechselwirkung im Zwei-Niveau System*, available online at http://www.quantum.physik.uni-mainz.de/Dateien/ (2004).

[52] M. Fleischhauer, A. Imamoglu and J. P. Marangos, *Electromagnetically induced transparency: Optics in coherent media*, Rev. Mod. Phys., **77**, 633–673 (2005).

[53] S. H. Autler and C. H. Townes, *Stark Effect in Rapidly Varying Fields*, Phys. Rev., **100**, 703–722 (1955).

[54] Gardiner, D. J., Graves, P. R., & Bowley, H. J., *Practical Raman spectroscopy*, Springer-Verlag, Berlin (1989).

[55] D. A. Steck, *Rubidium 87 D Line Data*, available online at steck.us/alkalidata (revision 2.1.4) (2010), 23 December 2010.

[56] M. Mack, F. Karlewski, H. Hattermann, S. Höckh, F. Jessen, D. Cano and J. Fortágh, *Measurement of absolute transition frequencies of ^{87}Rb to nS and nD Rydberg states by means of electromagnetically induced transparency*, Phys. Rev. A, **83**, 052515 (2011).

[57] B. Butscher, *A Rydberg Interferometer*, Ph.D. thesis, Universität Stuttgart (2011).

[58] J. Nipper, *Interacting Rydberg atoms: Coherent control at Förster resonances and polar homonuclear molecules*, Ph.D. thesis, Universität Stuttgart (2012).

[59] J. R. Rubbmark, M. M. Kash, M. G. Littman and D. Kleppner, *Dynamical effects at avoided level crossings: A study of the Landau-Zener effect using Rydberg atoms*, Phys. Rev. A, **23**, 3107–3117 (1981).

[60] Gounand, F., *Calculation of radial matrix elements and radiative lifetimes for highly excited states of alkali atoms using the Coulomb approximation*, J. Phys. France, **40**, 457–460 (1979).

[61] J. S. Deech, R. Luypaert, L. R. Pendrill and G. W. Series, *Lifetimes, depopulation cross sections and hyperfine structures of some Rydberg S and D states of ^{133}Cs*, J. Phys. B: At. Mol. Phys., **10**, L137 (1977).

[62] D. B. Branden, T. Juhasz, T. Mahlokozera, C. Vesa, R. O. Wilson, M. Zheng, A. Kortyna and D. A. Tate, *Radiative lifetime measurements of rubidium Rydberg states*, Journal of Physics B: Atomic, Molecular and Optical Physics, **43**, 015002 (2010).

[63] W. E. Cooke and T. F. Gallagher, *Effects of blackbody radiation on highly excited atoms*, Phys. Rev. A, **21**, 588–593 (1980).

[64] I. I. Beterov, I. I. Ryabtsev, D. B. Tretyakov and V. M. Entin, *Quasiclassical calculations of blackbody-radiation-induced depopulation rates and effective lifetimes of Rydberg nS, nP, and nD alkali-metal atoms with $n \leq 80$*, Phys. Rev. A, **79**, 052504 (2009).

[65] D. Comparat and P. Pillet, *Dipole blockade in a cold Rydberg atomic sample*, J. Opt. Soc. Am. B, **27**, A208–A232 (2010).

[66] A. Reinhard, T. C. Liebisch, B. Knuffman and G. Raithel, *Level shifts of rubidium Rydberg states due to binary interactions*, Phys. Rev. A, **75**, 032712 (2007).

[67] T. G. Walker and M. Saffman, *Consequences of Zeeman degeneracy for the van der Waals blockade between Rydberg atoms*, Phys. Rev. A, **77**, 032723 (2008).

[68] E. Altiere, D. P. Fahey, M. W. Noel, R. J. Smith and T. J. Carroll, *Dipole-dipole interaction between rubidium Rydberg atoms*, Phys. Rev. A, **84**, 053431 (2011).

[69] J. Nipper, J. B. Balewski, A. T. Krupp, B. Butscher, R. Löw and T. Pfau, *Highly Resolved Measurements of Stark-Tuned Förster Resonances between Rydberg Atoms*, Phys. Rev. Lett., **108**, 113001 (2012).

[70] J. Nipper, J. B. Balewski, A. T. Krupp, S. Hofferberth, R. Löw and T. Pfau, *Atomic Pair-State Interferometer: Controlling and Measuring an Interaction-Induced Phase Shift in Rydberg-Atom Pairs*, Phys. Rev. X, **2**, 031011 (2012).

[71] I. I. Ryabtsev, D. B. Tretyakov, I. I. Beterov and V. M. Entin, *Observation of the Stark-Tuned Förster Resonance between Two Rydberg Atoms*, Phys. Rev. Lett., **104**, 073003 (2010).

[72] A. Reinhard, K. C. Younge, T. C. Liebisch, B. Knuffman, P. R. Berman and G. Raithel, *Double-Resonance Spectroscopy of Interacting Rydberg-Atom Systems*, Phys. Rev. Lett., **100**, 233201 (2008).

[73] K. Afrousheh, P. Bohlouli-Zanjani, J. A. Petrus and J. D. D. Martin, *Determination of the ^{85}Rb ng-series quantum defect by electric-field-induced resonant energy transfer between cold Rydberg atoms*, Phys. Rev. A, **74**, 062712 (2006).

[74] K. Afrousheh, P. Bohlouli-Zanjani, D. Vagale, A. Mugford, M. Fedorov and J. D. D. Martin, *Spectroscopic Observation of Resonant Electric Dipole-Dipole Interactions between Cold Rydberg Atoms*, Phys. Rev. Lett., **93**, 233001 (2004).

[75] A. Tauschinsky, C. S. E. van Ditzhuijzen, L. D. Noordam and H. B. v. L. van den Heuvell, *Radio-frequency-driven dipole-dipole interactions in spatially separated volumes*, Phys. Rev. A, **78**, 063409 (2008).

[76] D. Tretyakov, I. Beterov, V. Entin, E. Yakshina, I. Ryabtsev, S. Dyubko, E. Alekseev, N. Pogrebnyak, N. Bezuglov and E. Arimondo, *Effect of photoions on the line shape of the Förster resonance lines and microwave transitions in cold rubidium Rydberg atoms*, J. Exp. Theor. Phys., **114**, 14–24 (2012).

[77] M. Şener, J. Strümpfer, J. Hsin, D. Chandler, S. Scheuring, C. N. Hunter and K. Schulten, *Förster Energy Transfer Theory as Reflected in the Structures of Photosynthetic Light-Harvesting Systems*, ChemPhysChem, **12**, 518–531 (2011).

[78] G. Günter, H. Schempp, M. Robert-de Saint-Vincent, V. Gavryusev, S. Helmrich, C. S. Hofmann, S. Whitlock and M. Weidemüller, *Observing the Dynamics of Dipole-Mediated Energy Transport by Interaction-Enhanced Imaging*, Science, **342**, 954–956 (2013).

[79] S. Weber, private communication.

[80] A. Gaëtan, Y. Miroshnychenko, T. Wilk, A. Chotia, M. Viteau, D. Comparat, P. Pillet, A. Browaeys and P. Grangier, *Observation of collective excitation of two individual atoms in the Rydberg blockade regime*, Nature Physics, **5**, 115–118 (2009).

[81] Y. O. Dudin, L. Li, F. Bariani and A. Kuzmich, *Observation of coherent many-body Rabi oscillations*, Nat. Phys., **8**, 790–794 (2012).

[82] T. Pohl and P. R. Berman, *Breaking the Dipole Blockade: Nearly Resonant Dipole Interactions in Few-Atom Systems*, Phys. Rev. Lett., **102**, 013004 (2009).

[83] E. R. Hudson, C. Ticknor, B. C. Sawyer, C. A. Taatjes, H. J. Lewandowski, J. R. Bochinski, J. L. Bohn and J. Ye, *Production of cold formaldehyde molecules for study and control of chemical reaction dynamics with hydroxyl radicals*, Phys. Rev. A, **73**, 063404 (2006).

[84] R. V. Krems, *Molecules near absolute zero and external field control of atomic and molecular dynamics*, Int. Rev. Phys. Chem., **24**, 99–118 (2005).

[85] R. V. Krems, *Cold controlled chemistry*, Phys. Chem. Chem. Phys., **10**, 4079–4092 (2008).

[86] A. Pe'er, E. A. Shapiro, M. C. Stowe, M. Shapiro and J. Ye, *Precise Control of Molecular Dynamics with a Femtosecond Frequency Comb*, Phys. Rev. Lett., **98**, 113004 (2007).

[87] L. Bomble, P. Pellegrini, P. Ghesquière and M. Desouter-Lecomte, *Toward scalable information processing with ultracold polar molecules in an electric field: A numerical investigation*, Phys. Rev. A, **82**, 062323 (2010).

[88] D. Petrosyan and K. Mølmer, *Binding Potentials and Interaction Gates between Microwave-Dressed Rydberg Atoms*, Phys. Rev. Lett., **113**, 123003 (2014).

[89] K.-A. B. Soderberg, N. Gemelke and C. Chin, *Ultracold molecules: vehicles to scalable quantum information processing*, New J. Phys., **11**, 055022 (2009).

[90] B. Butscher, V. Bendkowsky, J. Nipper, J. B. Balewski, L. Kukota, R. Löw, T. Pfau, W. Li, T. Pohl and J. M. Rost, *Lifetimes of ultralong-range Rydberg molecules in vibrational ground and excited states*, J. Phys. B: At. Mol. Opt. Phys., **44**, 184004 (2011).

[91] E. Fermi, *Sul moto dei neutroni nelle sostanze idrogenate*, Ric. Scientifica, **7**, 13–52 (1936), translated by G. M. Temmer in Enrico Fermi, *Collected Papers Volume I*, university of Chicago press, 1962.

[92] V. Bendkowsky, *Ultralong-range Rydberg molecules: Investigation of a novel binding*, Ph.D. thesis, Universität Stuttgart (2010).

[93] C. Bahrim, U. Thumm and I. I. Fabrikant, *$^3S^e$ and $^1S^e$ scattering lengths for e^- + Rb, Cs and Fr collisions*, J. Phys. B: At. Mol. Opt. Phys., **34**, L195–L201 (2001).

[94] I. Beigman and V. Lebedev, *Collision theory of Rydberg atoms with neutral and charged particles*, Physics Reports, **250**, 95 – 328 (1995).

[95] O. Hinckelmann and L. Spruch, *Low-Energy Scattering by Long-Range Potentials*, Phys. Rev. A, **3**, 642–648 (1971).

[96] T. F. O'Malley, L. Spruch and L. Rosenberg, *Modification of Effective-Range Theory in the Presence of a Long-Range (r^{-4}) Potential*, J. Math. Phys., **2**, 491–498 (1961).

[97] Omont, A., *On the theory of collisions of atoms in Rydberg states with neutral particles*, J. Phys. France, **38**, 1343–1359 (1977).

[98] M. I. Chibisov, A. A. Khuskivadze and I. I. Fabrikant, *Energies and dipole moments of long-range molecular Rydberg states*, J. Phys. B: At. Mol. Opt. Phys., **35**, L193 (2002).

[99] M. Kurz and P. Schmelcher, *Electrically dressed ultra-long-range polar Rydberg molecules*, Phys. Rev. A, **88**, 022501 (2013).

[100] E. L. Hamilton, C. H. Greene and H. R. Sadeghpour, *Shape-resonance-induced long-range molecular Rydberg states*, J. Phys. B: At. Mol. Opt. Phys., **35**, L199 (2002).

[101] C. H. Greene, E. L. Hamilton, H. Crowell, C. Vadla and K. Niemax, *Experimental Verification of Minima in Excited Long-Range Rydberg States of Rb_2*, Phys. Rev. Lett., **97**, 233002 (2006).

[102] F. Hildebrand, *Finite-difference equations and simulations*, Prentice-Hall (1968).

[103] C. Zipkes, S. Palzer, C. Sias and M. Köhl, *A trapped single ion inside a Bose-Einstein condensate*, Nature, **464**, 388–391 (2010).

[104] S. Schmid, A. Härter and J. H. Denschlag, *Dynamics of a Cold Trapped Ion in a Bose-Einstein Condensate*, Phys. Rev. Lett., **105**, 133202 (2010).

[105] A. Härter, A. Krükow, A. Brunner and J. H. Denschlag, *Minimization of ion micromotion using ultracold atomic probes*, Appl. Phys. Lett., **102**, 221115 (2013).

[106] D. J. Berkeland, J. D. Miller, J. C. Bergquist, W. M. Itano and D. J. Wineland, *Minimization of ion micromotion in a Paul trap*, J. Appl. Phys., **83**, 5025–5033 (1998).

[107] L. H. Nguyên, A. Kalev, M. D. Barrett and B.-G. Englert, *Micromotion in trapped atom-ion systems*, Phys. Rev. A, **85**, 052718 (2012).

[108] W. Ketterle, D. S. Durfee and D. M. Stamper-Kurn, *Making, probing and understanding Bose-Einstein condensates*, Proceedings of the International School of Physics "Enrico Fermi", Course CXL, IOS Press, Amsterdam (1999).

[109] M.-C. Combourieu and H. Rauch, *The wave-particle dualism in 1992: A summary*, Foundations of Physics, **22**, 1403–1434 (1992).

[110] C. J. Pethik and H. Smith, *Bose-Einstein condensation in dilute gases*, Cambridge University Press, Cambridge, 2nd edition (2008).

[111] A. Einstein, *Quantentheorie des einatomigen idealen Gases*, Sitzungsberichte der Preußischen Akademie der Wissenschaften, pages 261–267 (1924).

[112] S. N. Bose, *Plancks Gesetz und Lichtquantenhypothese*, Z. Phys., **26**, 178–181 (1924).

[113] D. E. Pritchard, *Cooling Neutral Atoms in a Magnetic Trap for Precision Spectroscopy*, Phys. Rev. Lett., **51**, 1336–1339 (1983).

[114] K. B. Davis, M.-O. Mewes, M. A. Joffe, M. R. Andrews and W. Ketterle, *Evaporative Cooling of Sodium Atoms*, Phys. Rev. Lett., **74**, 5202–5205 (1995).

[115] F. Dalfovo, S. Giorgini, L. P. Pitaevskii and S. Stringari, *Theory of Bose-Einstein condensation in trapped gases*, Rev. Mod. Phys., **71**, 463–512 (1999).

[116] L. Pitaevskii and S. Stringari, *Bose-Einstein Condensation*, Oxford University Press, Oxford (2003).

[117] Y. Castin and R. Dum, *Bose-Einstein Condensates in Time Dependent Traps*, Phys. Rev. Lett., **77**, 5315–5319 (1996).

[118] T. Karpiuk, M. Brewczyk, K. Rzążewski, J. B. Balewski, A. T. Krupp, A. Gaj, R. Löw, S. Hofferberth and T. Pfau, *Detecting and imaging single Rydberg electrons in a Bose-Einstein condensate*, arXiv:1402.6875 (2014).

[119] O. Penrose and L. Onsager, *Bose-Einstein Condensation and Liquid Helium*, Phys. Rev., **104**, 576–584 (1956).

[120] T. Karpiuk, M. Brewczyk, M. Gajda and K. Rzążewski, *Constructing a classical field for a Bose-Einstein condensate in an arbitrary trapping potential: Quadrupole oscillations at nonzero temperatures*, Phys. Rev. A, **81**, 013629 (2010).

[121] K. Goral, M. Gajda and K. Rzążewski, *Multi-mode description of an interacting Bose-Einstein condensate*, Opt. Express, **8**, 92–98 (2001).

[122] S. Stringari, *Collective Excitations of a Trapped Bose-Condensed Gas*, Phys. Rev. Lett., **77**, 2360–2363 (1996).

[123] M. R. Andrews, M.-O. Mewes, N. J. van Druten, D. S. Durfee, D. M. Kurn and W. Ketterle, *Direct, Nondestructive Observation of a Bose Condensate*, Science, **273**, 84–87 (1996).

[124] D. S. Jin, J. R. Ensher, M. R. Matthews, C. E. Wieman and E. A. Cornell, *Collective Excitations of a Bose-Einstein Condensate in a Dilute Gas*, Phys. Rev. Lett., **77**, 420–423 (1996).

[125] J. E. Lye, L. Fallani, M. Modugno, D. S. Wiersma, C. Fort and M. Inguscio, *Bose-Einstein Condensate in a Random Potential*, Phys. Rev. Lett., **95**, 070401 (2005).

[126] T. Kuwamoto and T. Hirano, *Collective Excitation of Bose-Einstein Condensates Induced by Evaporative Cooling*, J. Phys. Soc. Jpn., **81**, 074002 (2012).

[127] R. Löw, *A versatile setup for experiments with rubidium Bose-Einstein condensates: From optical lattices to Rydberg matter*, Ph.D. thesis, Universität Stuttgart (2006).

[128] R. Heidemann, *Rydberg excitation of Bose-Einstein condensates: Coherent collective dynamics*, Ph.D. thesis, Universität Stuttgart (2008).

[129] U. Krohn, *Universal scaling and coherence properties of an ultracold Rydberg gas*, Ph.D. thesis, Universität Stuttgart (2008).

[130] E. W. Streed, A. P. Chikkatur, T. L. Gustavson, M. Boyd, Y. Torii, D. Schneble, G. K. Campbell, D. E. Pritchard and W. Ketterle, *Large atom number Bose-Einstein condensate machines*, Rev. Sci. Instrum., **77**, 023106 (2006).

[131] W. D. Phillips and H. Metcalf, *Laser Deceleration of an Atomic Beam*, Phys. Rev. Lett., **48**, 596–599 (1982).

[132] W. Ketterle, K. B. Davis, M. A. Joffe, A. Martin and D. E. Pritchard, *High densities of cold atoms in a dark spontaneous-force optical trap*, Phys. Rev. Lett., **70**, 2253–2256 (1993).

[133] D. Boiron, A. Michaud, P. Lemonde, Y. Castin, C. Salomon, S. Weyers, K. Szymaniec, L. Cognet and A. Clairon, *Laser cooling of cesium atoms in gray optical molasses down to 1.1 μK*, Phys. Rev. A, **53**, R3734–R3737 (1996).

[134] M.-O. Mewes, M. R. Andrews, N. J. van Druten, D. M. Kurn, D. S. Durfee and W. Ketterle, *Bose-Einstein Condensation in a Tightly Confining dc Magnetic Trap*, Phys. Rev. Lett., **77**, 416–419 (1996).

[135] R. Grimm, M. Weidemüller and Y. B. Ovchinnikov, *Optical dipole traps for neutral atoms*, Adv. At. Mol. Opt. Phys., **42**, 95–170 (2000).

[136] C. Tresp, *A setup for highly precise excitation and detection of Rydberg atoms*, Master Thesis, Universität Stuttgart (2012).

[137] E. Courtade, M. Anderlini, D. Ciampini, J. H. Müller, O. Morsch, E. Arimondo, M. Aymar and E. J. Robinson, *Two-photon ionization of cold rubidium atoms with a near resonant intermediate state*, J. Phys. B: At. Mol. Opt. Phys., **37**, 967–979 (2004).

[138] M. Anderlini, E. Courtade, D. Ciampini, J. H. Müller, O. Morsch and E. Arimondo, *Two-photon ionization of cold rubidium atoms*, J. Opt. Soc. Am. B, **21**, 480–485 (2004).

[139] J. Balewski, *Hochauflösende Photoassoziationsspektroskopie von Rydberg-Dimeren und Trimeren*, Diplomarbeit, Universität Stuttgart (2009).

[140] M. S. O'Sullivan and B. P. Stoicheff, *Scalar polarizabilities and avoided crossings of high Rydberg states in Rb*, Phys. Rev. A, **31**, 2718–2720 (1985).

[141] M. A. Bellos, R. Carollo, J. Banerjee, E. E. Eyler, P. L. Gould and W. C. Stwalley, *Excitation of Weakly Bound Molecules to Trilobitelike Rydberg States*, Phys. Rev. Lett., **111**, 053001 (2013).

[142] J. Tallant, S. T. Rittenhouse, D. Booth, H. R. Sadeghpour and J. P. Shaffer, *Observation of Blueshifted Ultralong-Range Cs_2 Rydberg Molecules*, Phys. Rev. Lett., **109**, 173202 (2012).

[143] D. A. Anderson, S. A. Miller and G. Raithel, *Photoassociation of Long-Range nD Rydberg Molecules*, Phys. Rev. Lett., **112**, 163201 (2014).

[144] S. T. Rittenhouse and H. R. Sadeghpour, *Ultracold Giant Polyatomic Rydberg Molecules: Coherent Control of Molecular Orientation*, Phys. Rev. Lett., **104**, 243002 (2010).

[145] S. T. Rittenhouse, M. Mayle, P. Schmelcher and H. R. Sadeghpour, *Ultralong-range polyatomic Rydberg molecules formed by a polar perturber*, J. Phys. B: At., Mol. Opt. Phys., **44**, 184005 (2011).

[146] A. T. Krupp, A. Gaj, J. B. Balewski, P. Ilzhöfer, S. Hofferberth, R. Löw, T. Pfau, M. Kurz and P. Schmelcher, *Alignment of D-State Rydberg Molecules*, Phys. Rev. Lett., **112**, 143008 (2014).

[147] P. R. Brooks and E. M. Jones, *Reactive Scattering of K Atoms from Oriented CH_3I Molecules*, J. Chem. Phys., **45**, 3449–3450 (1966).

[148] S. Stolte, *Reactive Scattering Studies on Oriented Molecules*, Ber. Bunsen. Phys. Chem., **86**, 413–421 (1982).

[149] R. N. Zare, *Laser Control of Chemical Reactions*, Science, **279**, 1875–1879 (1998).

[150] V. Aquilanti, M. Bartolomei, F. Pirani, D. Cappelletti, F. Vecchiocattivi, Y. Shimizu and T. Kasai, *Orienting and aligning molecules for stereochemistry and photodynamics*, Phys. Chem. Chem. Phys., **7**, 291–300 (2005).

[151] L. Holmegaard, J. L. Hansen, L. Kalhøj, S. L. Kragh, H. Stapelfeldt, F. Filsinger, J. Küpper, G. Meijer, D. Dimitrovski, M. Abu-samha, C. P. J. Martiny and L. B. Madsen, *Photoelectron angular distributions from strong-field ionization of oriented molecules*, Nat. Phys., **6**, 428 (2010).

[152] J. L. Hansen, L. Holmegaard, L. Kalhøj, S. L. Kragh, H. Stapelfeldt, F. Filsinger, G. Meijer, J. Küpper, D. Dimitrovski, M. Abu-samha, C. P. J. Martiny and L. B. Madsen, *Ionization of one- and three-dimensionally-oriented asymmetric-top molecules by intense circularly polarized femtosecond laser pulses*, Phys. Rev. A, **83**, 023406 (2011).

[153] A. Landers, T. Weber, I. Ali, A. Cassimi, M. Hattass, O. Jagutzki, A. Nauert, T. Osipov, A. Staudte, M. H. Prior, H. Schmidt-Böcking, C. L. Cocke and R. Dörner, *Photoelectron Diffraction Mapping: Molecules Illuminated from Within*, Phys. Rev. Lett., **87**, 013002 (2001).

[154] C. Z. Bisgaard, O. J. Clarkin, G. Wu, A. M. D. Lee, O. Geßner, C. C. Hayden and A. Stolow, *Time-Resolved Molecular Frame Dynamics of Fixed-in-Space CS_2 Molecules*, Science, **323**, 1464–1468 (2009).

[155] M. Wu, R. J. Bemish and R. E. Miller, *Photodissociation of molecules oriented by dc electric fields: Determining photofragment angular distributions*, J. Chem. Phys., **101**, 9447–9456 (1994).

[156] N. H. Nahler, R. Baumfalk, U. Buck, Z. Bihary, R. B. Gerber and B. Friedrich, *Photodissociation of oriented HXeI molecules generated from HI-Xe_n clusters*, J. Chem. Phys., **119**, 224–231 (2003).

[157] A. J. van den Brom, T. P. Rakitzis and M. H. M. Janssen, *Photodissociation of laboratory oriented molecules: Revealing molecular frame properties of nonaxial recoil*, J. Chem. Phys., **121**, 11645–11652 (2004).

[158] M. L. Lipciuc, A. J. van den Brom, L. Dinu and M. H. M. Janssen, *Slice imaging of photodissociation of spatially oriented molecules*, Rev. Sci. Instrum., **76**, 123103 (2005).

[159] J. C. H. Spence and R. B. Doak, *Single Molecule Diffraction*, Phys. Rev. Lett., **92**, 198102 (2004).

[160] F. Filsinger, G. Meijer, H. Stapelfeldt, H. N. Chapman and J. Küpper, *State- and conformer-selected beams of aligned and oriented molecules for ultrafast diffraction studies*, Phys. Chem. Chem. Phys., **13**, 2076–2087 (2011).

[161] M. H. G. de Miranda, A. Chotia, B. Neyenhuis, D. Wang, G. Quéméner, S. Ospelkaus, J. L. Bohn, J. Ye and D. S. Jin, *Controlling the quantum stereodynamics of ultracold bimolecular reactions*, Nat. Phys., **7**, 502–507 (2011).

[162] H. J. Loesch and A. Remscheid, *Brute force in molecular reaction dynamics: A novel technique for measuring steric effects*, J. Chem. Phys., **93**, 4779–4790 (1990).

[163] P. R. Brooks, *Reactions of Oriented Molecules*, Science, **193**, 11–16 (1976).

[164] D. H. Parker and R. B. Bernstein, *Oriented Molecule Beams Via the Electrostatic Hexapole: Preparation, Characterization, and Reactive Scattering*, Annu. Rev. Phys. Chem., **40**, 561 (1989).

[165] T. D. Hain, R. M. Moision and T. J. Curtiss, *Hexapole state-selection and orientation of asymmetric top molecules: CH_2F_2*, J. Chem. Phys., **111**, 6797–6806 (1999).

[166] H. Stapelfeldt and T. Seideman, *Colloquium : Aligning molecules with strong laser pulses*, Rev. Mod. Phys., **75**, 543–557 (2003).

[167] B. Friedrich and D. R. Herschbach, *Enhanced orientation of polar molecules by combined electrostatic and nonresonant induced dipole forces*, J. Chem. Phys., **111**, 6157 (1999).

[168] B. Friedrich and D. R. Herschbach, *Manipulating Molecules via Combined Static and Laser Fields*, J. Phys. Chem. A, **103**, 10280 (1999).

[169] R. Baumfalk, N. H. Nahler and U. Buck, *Photodissociation of oriented HXeI molecules in the gas phase*, J. Chem. Phys., **114**, 4755 (2001).

[170] H. Sakai, S. Minemoto, H. Nanjo, H. Tanji and T. Suzuki, *Controlling the Orientation of Polar Molecules with Combined Electrostatic and Pulsed, Nonresonant Laser Fields*, Phys. Rev. Lett., **90**, 083001 (2003).

[171] H. Tanji, S. Minemoto and H. Sakai, *Three-dimensional molecular orientation with combined electrostatic and elliptically polarized laser fields*, Phys. Rev. A, **72**, 063401 (2005).

[172] U. Kappes and P. Schmelcher, *On the topology of the adiabatic potential energy surfaces of the $H_2{}^+$-ion in a strong magnetic field*, Phys. Lett. A, **210**, 409 – 415 (1996).

[173] T. Detmer, P. Schmelcher and L. S. Cederbaum, *Hydrogen molecule in a magnetic field: The lowest states of the Π manifold and the global ground state of the parallel configuration*, Phys. Rev. A, **57**, 1767–1777 (1998).

[174] K. K. Lange, E. I. Tellgren, M. R. Hoffmann and T. Helgaker, *A Paramagnetic Bonding Mechanism for Diatomics in Strong Magnetic Fields*, Science, **337**, 327–331 (2012).

[175] U. Kappes and P. Schmelcher, *Adiabatic potential-energy surfaces of the $H_2{}^+$ ion in a strong magnetic field*, Phys. Rev. A, **53**, 3869–3883 (1996).

[176] P. Schmelcher and L. S. Cederbaum, *Crossings of potential-energy surfaces in a magnetic field*, Phys. Rev. A, **41**, 4936–4943 (1990).

[177] M. Kurz and P. Schmelcher, *Ultralong-range Rydberg molecules in combined electric and magnetic fields*, J. Phys. B: At., Mol. Opt. Phys., **47**, 165101 (2014).

[178] A. Kumar, B. C. Saha, C. A. Weatherford and S. K. Verma, *A systematic study of Hornbeck Molnar ionization involving Rydberg alkali atoms*, Journal of Molecular Structure: THEOCHEM, **487**, 1 – 9 (1999).

[179] L. Barbier, M. T. Djerad and M. Chéret, *Collisional ion-pair formation in an excited alkali-metal vapor*, Phys. Rev. A, **34**, 2710–2718 (1986).

[180] F. Gounand, M. Hugon, P. R. Fournier and J. Berlande, *Superradiant cascading effects in rubidium Rydberg levels*, J. Phys. B: At. Mol. Opt. Phys., **12**, 547 (1979).

[181] T. Wang, S. F. Yelin, R. Côté, E. E. Eyler, S. M. Farooqi, P. L. Gould, M. Koštrun, D. Tong and D. Vrinceanu, *Superradiance in ultracold Rydberg gases*, Phys. Rev. A, **75**, 033802 (2007).

[182] M. P. Robinson, B. L. Tolra, M. W. Noel, T. F. Gallagher and P. Pillet, *Spontaneous Evolution of Rydberg Atoms into an Ultracold Plasma*, Phys. Rev. Lett., **85**, 4466–4469 (2000).

[183] M. Robert-de Saint-Vincent, C. S. Hofmann, H. Schempp, G. Günter, S. Whitlock and M. Weidemüller, *Spontaneous Avalanche Ionization of a Strongly Blockaded Rydberg Gas*, Phys. Rev. Lett., **110**, 045004 (2013).

[184] M. Chéret, L. Barbier, W. Lindinger and R. Deloche, *Penning and associative ionisation of highly excited rubidium atoms*, J. Phys. B: At. Mol. Phys., **15**, 3463 (1982).

[185] L. Barbier and M. Chéret, *Experimental study of Penning and Hornbeck−Molnar ionisation of rubidium atoms excited in a high s or d level ($5d \leq nl \leq 11s$)*, J. Phys. B: At. Mol. Phys., **20**, 1229 (1987).

[186] V. S. Lebedev, *Theory of the orbital angular momentum and energy transfer processes in collisions involving Rydberg atoms*, J. Phys. B: At. Mol. Opt. Phys., **31**, 1579 (1998).

[187] A. Härter, A. Krükow, M. Deisz, B. Drews, E. Tiemann and J. H. Denschlag, *Population distribution of product states following three-body recombination in an ultracold atomic gas*, Nat. Phys., **9**, 1745–2473 (2013).

[188] A. Härter, A. Krükow, A. Brunner, W. Schnitzler, S. Schmid and J. H. Denschlag, *Single Ion as a Three-Body Reaction Center in an Ultracold Atomic Gas*, Phys. Rev. Lett., **109**, 123201 (2012).

[189] A. Zenesini, B. Huang, M. Berninger, S. Besler, H.-C. Nägerl, F. Ferlaino, R. Grimm, C. H. Greene and J. von Stecher, *Resonant five-body recombination in an ultracold gas of bosonic atoms*, New J. Phys., **15**, 043040 (2013).

[190] J. Pérez-Ríos, S. Ragole, J. Wang and C. H. Greene, *Comparison of classical and quantal calculations of helium three-body recombination*, J. Chem. Phys., **140**, 044307 (2014).

[191] M. R. Andrews, D. M. Kurn, H.-J. Miesner, D. S. Durfee, C. G. Townsend, S. Inouye and W. Ketterle, *Propagation of Sound in a Bose-Einstein Condensate*, Phys. Rev. Lett., **79**, 553–556 (1997).

[192] C. C. Bradley, C. A. Sackett and R. G. Hulet, *Bose-Einstein Condensation of Lithium: Observation of Limited Condensate Number*, Phys. Rev. Lett., **78**, 985–989 (1997).

[193] M. Koschorreck, D. Pertot, E. Vogt, B. Fröhlich, M. Feld and M. Köhl, *Attractive and repulsive Fermi polarons in two dimensions*, Nature, **485**, 619–622 (2012).

[194] J. T. Devreese and A. S. Alexandrov, *Fröhlich polaron and bipolaron: recent developments*, Rep. Prog. Phys., **72**, 066501 (2009).

[195] J. Tempere, W. Casteels, M. K. Oberthaler, S. Knoop, E. Timmermans and J. T. Devreese, *Feynman path-integral treatment of the BEC-impurity polaron*, Phys. Rev. B, **80**, 184504 (2009).

[196] F. M. Cucchietti and E. Timmermans, *Strong-Coupling Polarons in Dilute Gas Bose-Einstein Condensates*, Phys. Rev. Lett., **96**, 210401 (2006).

[197] W. Casteels, J. Tempere and J. Devreese, *Polaronic Properties of an Ion in a Bose-Einstein Condensate in the Strong-Coupling Limit*, J. Low Temp. Phys., **162**, 266–273 (2011).

[198] R. G. Hulet and D. Kleppner, *Rydberg Atoms in "Circular" States*, Phys. Rev. Lett., **51**, 1430–1433 (1983).

[199] D. A. Anderson, A. Schwarzkopf, R. E. Sapiro and G. Raithel, *Production and trapping of cold circular Rydberg atoms*, Phys. Rev. A, **88**, 031401 (2013).

[200] M. Brune, E. Hagley, J. Dreyer, X. Maître, A. Maali, C. Wunderlich, J. M. Raimond and S. Haroche, *Observing the Progressive Decoherence of the "Meter" in a Quantum Measurement*, Phys. Rev. Lett., **77**, 4887–4890 (1996).

[201] J. Hare, A. Nussenzweig, C. Gabbanini, M. Weidemuller, P. Goy, M. Gross and S. Haroche, *Toward a Rydberg constant measurement on circular atoms*, IEEE Transactions on Instrumentation and Measurement, **42**, 331–334 (1993).

[202] R. Lutwak, J. Holley, P. P. Chang, S. Paine, D. Kleppner and T. Ducas, *Circular states of atomic hydrogen*, Phys. Rev. A, **56**, 1443–1452 (1997).

[203] C. H. Cheng, C. Y. Lee and T. F. Gallagher, *Production of Circular Rydberg States with Circularly Polarized Microwave Fields*, Phys. Rev. Lett., **73**, 3078–3081 (1994).

[204] F. B. Dunning, J. J. Mestayer, C. O. Reinhold, S. Yoshida and J. Burgdörfer, *Engineering atomic Rydberg states with pulsed electric fields*, J. Phys. B: At., Mol. Opt. Phys., **42**, 022001 (2009).

[205] R. Löw, H. Weimer, J. Nipper, J. B. Balewski, B. Butscher, H. P. Büchler and T. Pfau, *An experimental and theoretical guide to strongly interacting Rydberg gases*, J. Phys. B: At. Mol. Opt. Phys., **45**, 113001 (2012).

Danksagung

An dieser Stelle möchte ich allen Personen danken, die mich auf dem Weg meiner Doktorarbeit auf alle nur erdenkliche Weise unterstützt und damit einen Beitrag zum Gelingen der Dissertation beigesteuert haben.

Allen voran gebührt mein Dank Professor Pfau, der mich in seine Arbeitsgruppe aufgenommen hat, obwohl ich mit ultrakalten Gasen bisher nicht in Berührung gekommen bin, da ich meine Diplomarbeit im Bereich der Festkörperphysik anfertigte. Er unterstützte uns fortwährend mit neuen Ideen und brachte in Diskussionen immer die richtigen Impulse, um das Experiment auf Erfolgskurs zu steuern.

Als nächstes möchte ich dem Team am kalten Rydberg Experiment danken, namentlich Johannes, Jonathan, Anita, Thomas, Philipp und Bernd, die alle zum Erfolg des Experiments beigetragen haben. Den Anfang machte Johannes, der der Erfahrenste von uns Doktoranden und erster Ansprechpartner bei Fragen über unseren experimentellen Aufbau, die Steuerung und die kalte Atomphysik im Allgemeinen war. Er hat mir sehr geholfen und stand mir bei dem Aufbau des DFB-Diodenlasers jederzeit hilfreich zur Seite (auch wenn sich leider am Schluss herausstellte, dass der Laser doch nicht gebraucht wurde, da die neue Klimaanlage dafür sorgte, dass der 'alte' Repumper Diodenlaser stabil lief). Mit Jonathan habe ich sowohl die schwierigste Zeit am Experiment durchgemacht, wo wir fast ein Jahr erfolglos versucht haben einen Effekt des Dressings auf die Rydbergatome zu sehen, als auch die Wende zur erfolgreichsten Zeit, in der wir mit der einzelnen Rydbergatomanregung im Kondensat ein komplett neues Themengebiet pionierten. Vor allem dein Durchhaltevermögen und unermüdlicher Arbeitseinsatz waren mir stets ein Vorbild. Dem jetzigen Team mit Anita, Thomas und Philipp wünsche ich, dass das Experiment weiterhin so interessante Daten abwirft und, dass ihr euch von Rückschlägen nicht entmutigen lassen und eure Dissertationen bzw. Masterarbeit auch erfolgreich abschließen werdet. Anita möchte ich vor allem für ihren Mut loben, dass sie sich in der Zeit der Dressing-Messungen, dem Tiefpunkt unserer experimentellen Versuchszeit, unserem Team angechlossen und uns seitdem tatkräftig unterstützt hat.

Des Weiteren sei Robert an dieser Stelle mein Dank für den Aufbau der Rydberg Apparatur vor 10 Jahren ausgesprochen, sowie für Hilfestellungen, wenn mal wieder etwas am Experiment nicht so tat, wie es tun sollte.

Als Sebastian sich vor drei Jahren dem Institut anschloss und den Aufbau der beiden Experimente im 5. Stock koordinierte, bereicherte er vor allem die beiden Rydberg Gruppen mit seinem Knowhow und seiner Kompetenz in der ultrakalten Atomphysik. Bei Theoriefragen war er die Ansprechstation Nummer Eins, und in Besprechungen steuerte er hilfreiche Lösungsvorschläge und Ideen bei. Besonders die ausführlichen Diskussionen in unserem Büro

werde ich vermissen.

Weiterhin möchte ich mich bei dem Rydberg und RQO Team im 5.Stock bedanken, namentlich Huan, Stephan, Michael, Tara, Graham, Udo, Hannes, Christoph und Johannes. Positiv hervorheben möchte ich hier, dass wir euer Lasersystem für lange Zeit benutzen durften, ohne das wir nicht so erfolgreich die Experimente bei hohen Quantenzahlen im Bose-Einstein Kondensat hätten durchführen können (Danke Christoph für den Aufbau!). Michael ist uns mit seiner Kompetenz in Sachen Elektronikbauteilen unersetzlich gewesen und Graham 'the magnificent' wurde von mir immer wegen seines britischen Humors und seiner Kompetenz auf dem Gebiet der Rydberg Physik geschätzt. Tara möchte ich besonders für die sprachlichen und grammatikalischen Korrekturen zu meiner Dissertation an dieser Stelle herzlich danken.

Außerdem möchte ich mich an dieser Stelle bei Markus und Professor Schmelcher aus Hamburg für die erfolgreiche und fruchtbare Zusammenarbeit bedanken; besonders Markus, für die durcharbeiteten Nächte vor der kurzfristigen Einreichung unseres gemeinsamen, in Eiltempo verfassten Papers. Auch bei dem Team von Professor Rzążewski möchte ich mich für unsere erfolgreiche Kooperation bedanken.

Weiterhin gilt mein Dank Harald, unserem Systemadministrator, der die erste Anlaufstation war, wenn die Steuercomputer plötzlich mal wieder die Zusammenarbeit verweigerten, und die Mainboards ausgetauscht werden mussten.

Außerdem möchte ich mich bei all den restlichen Mitgliedern des Instituts bedanken. Die Atmosphäre und gegenseitige Hilfsbereitschaft war unter allen Mitgliedern des PI5 einfach hervorragend und bespielhaft. Des Weitern gilt mein Dank Astrid, Bea, den beiden Karins, Oli und Nadine, die mir großteils die zeitraubenden organisatorischen Tätigkeiten abnahmen und bei Verwaltungsangelegenheiten immer geduldig meine Fragen beantworteten.

Ebenso möchte ich Professor Keimer für die Übernahme des Mitberichts und Professor Wunner für die Übernahme des Prüfungsvorsitzes danken.

Meinen Freunden aus dem Münchner Raum sei gedankt, dass ihr mich immer wieder aufgemuntert habt. An unsere lustigen Video- und Spieleabende, die die nötige Abwechslung zum physikalischen Alltag im Labor schafften, werde ich mich immer gerne zurückerinnern.

Ohne den Rückhalt meiner Eltern und meines Bruders Hans-Jürgen wäre diese Doktorarbeit nicht möglich gewesen und ich möchte mich inbesondere für all die Unterstützung in den letzten $3^1/_2$ Jahren bedanken.

Ganz zum Schluss möchte ich allen Personen danken, die ihre wertvolle Zeit geopfert haben, um meine Arbeit Korrektur zu lesen und damit zur Verbesserung und Vollendung dieser Dissertation nicht unwesentlich beigetragen haben.